Modelling glacial erosional landform development

Hindmarsh, R.C.A.

MODELLING GLACIAL EROSIONAL LANDFORM DEVELOPMENT

VOLUME 2

BY

R. C. A. HINDMARSH

A thesis presented for the degree of
Doctor of Philosophy in the
University of Durham

Graduate Society

January 1935

LIST OF FIGURES

LIST OF OVERLAYS

FIGURE 2.1 DEVELOPMENT OF GLACIALLY ERODED SURFACES BY SCRATCHING AND POLISHING

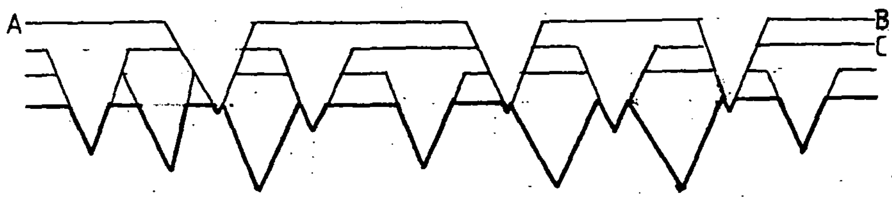

(a) 3 scratches/unit area/unit time

KEY

AB = UNIT WIDTH

BC = POLISHING EFFECTED IN UNIT TIME

V UNIT SCRATCH

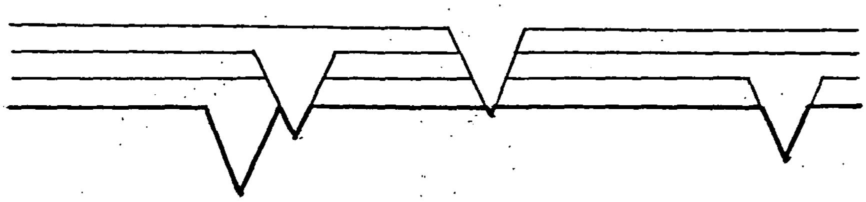

(b) 1 scratch/unit area/unit time

FIGURE 2.2 DERIVATION OF THE ABRASION EQUATION

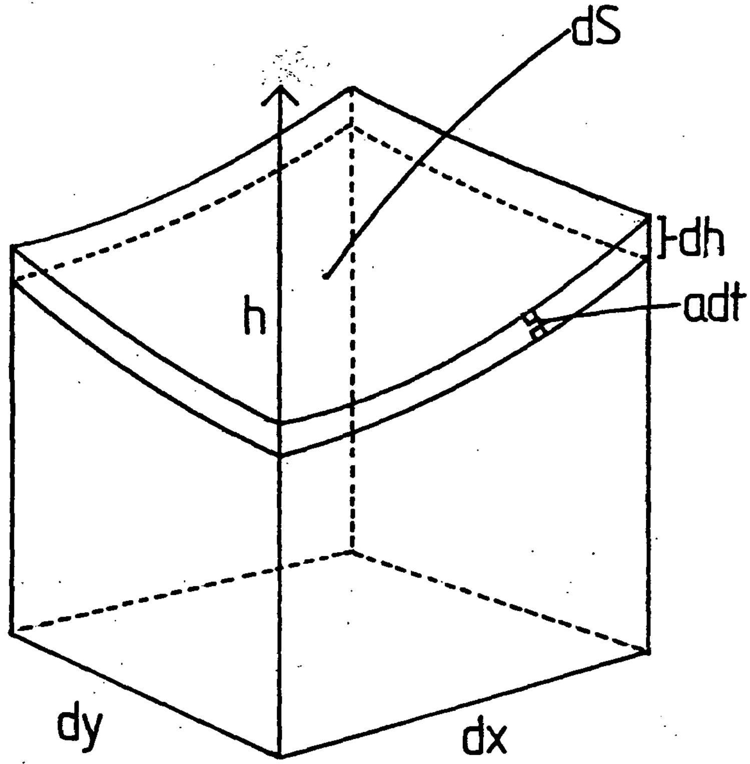

Figure 2.3 Contour plot of surface persistent under constant abrasion: $a = 1$, $\ell = 2$, $m_x = m_y = 0$.

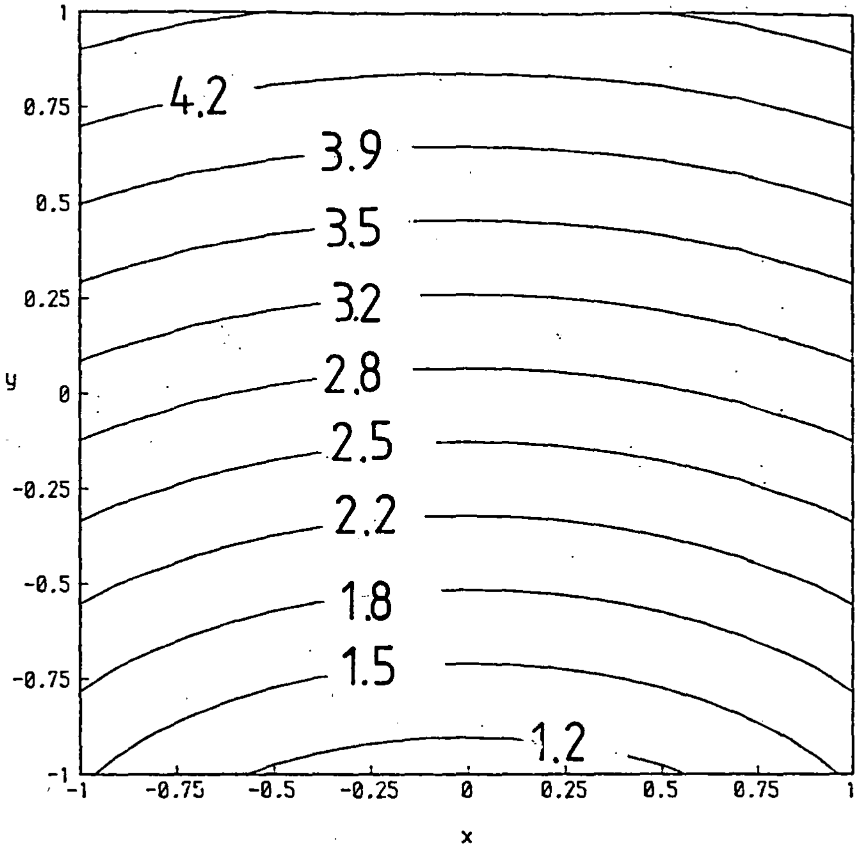

Figure 2.4 Contour plot of surface persistent under constant abrasion: $a = 1$, $\ell = 2$, $m_x = 0{\cdot}0$, $m_y = -0{\cdot}5$.

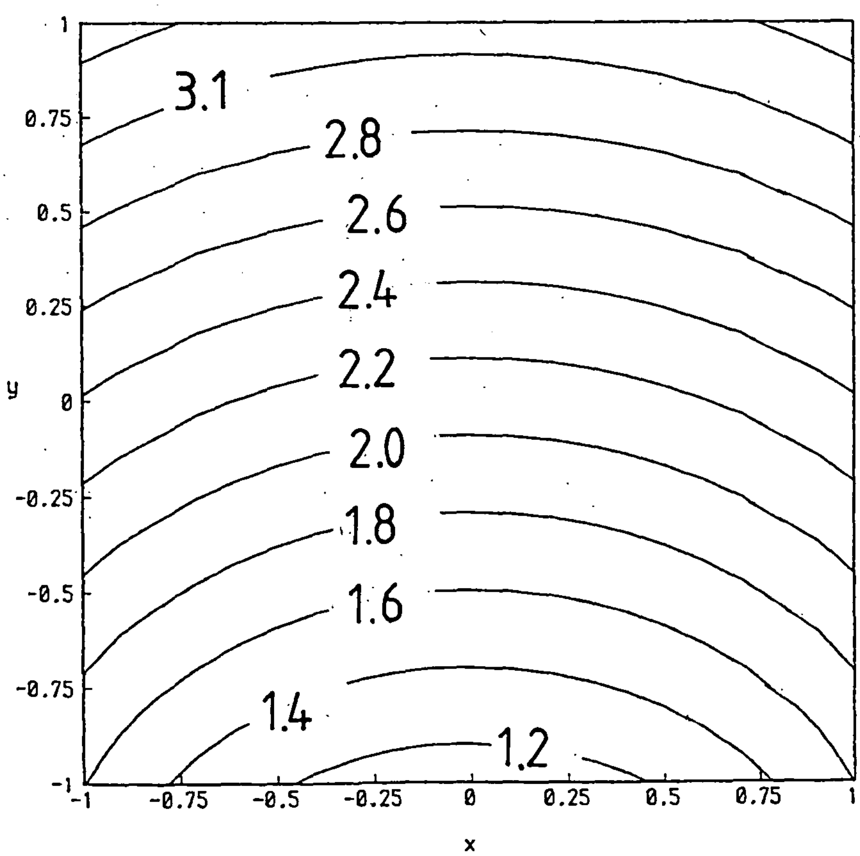

Figure 2.5 Contour plot of surface persistent under constant abrasion: $a = 1$, $\ell = 2$, $m_x = m_y = -0\cdot5$.

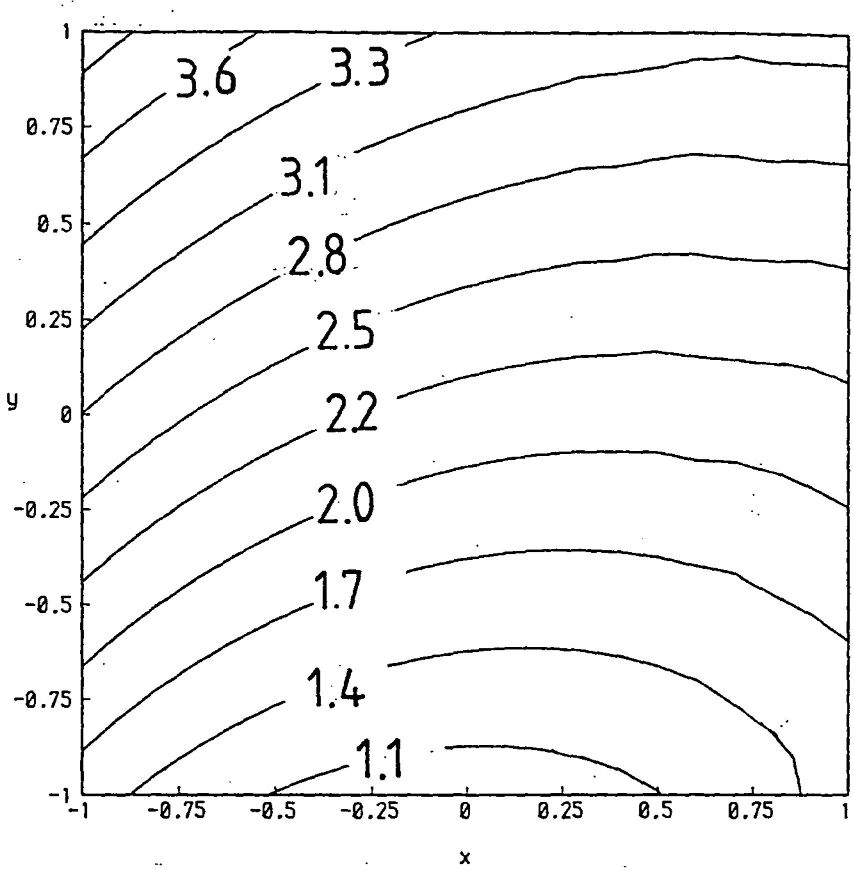

Figure 2.6 Contour plot of surface persistent under constant abrasion: $a = 1$, $\ell = 2$, $m_x = m_y = -0\cdot9$.

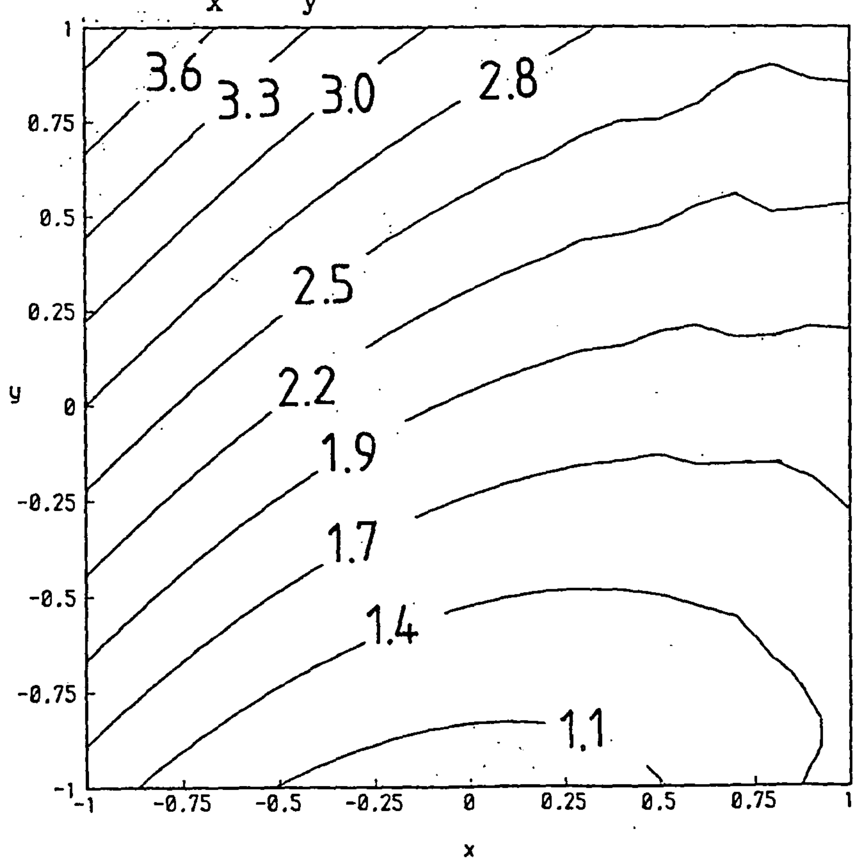

Figure 2.7 Dependence of abrasion on position for persistence of a sine-wave under lowering.

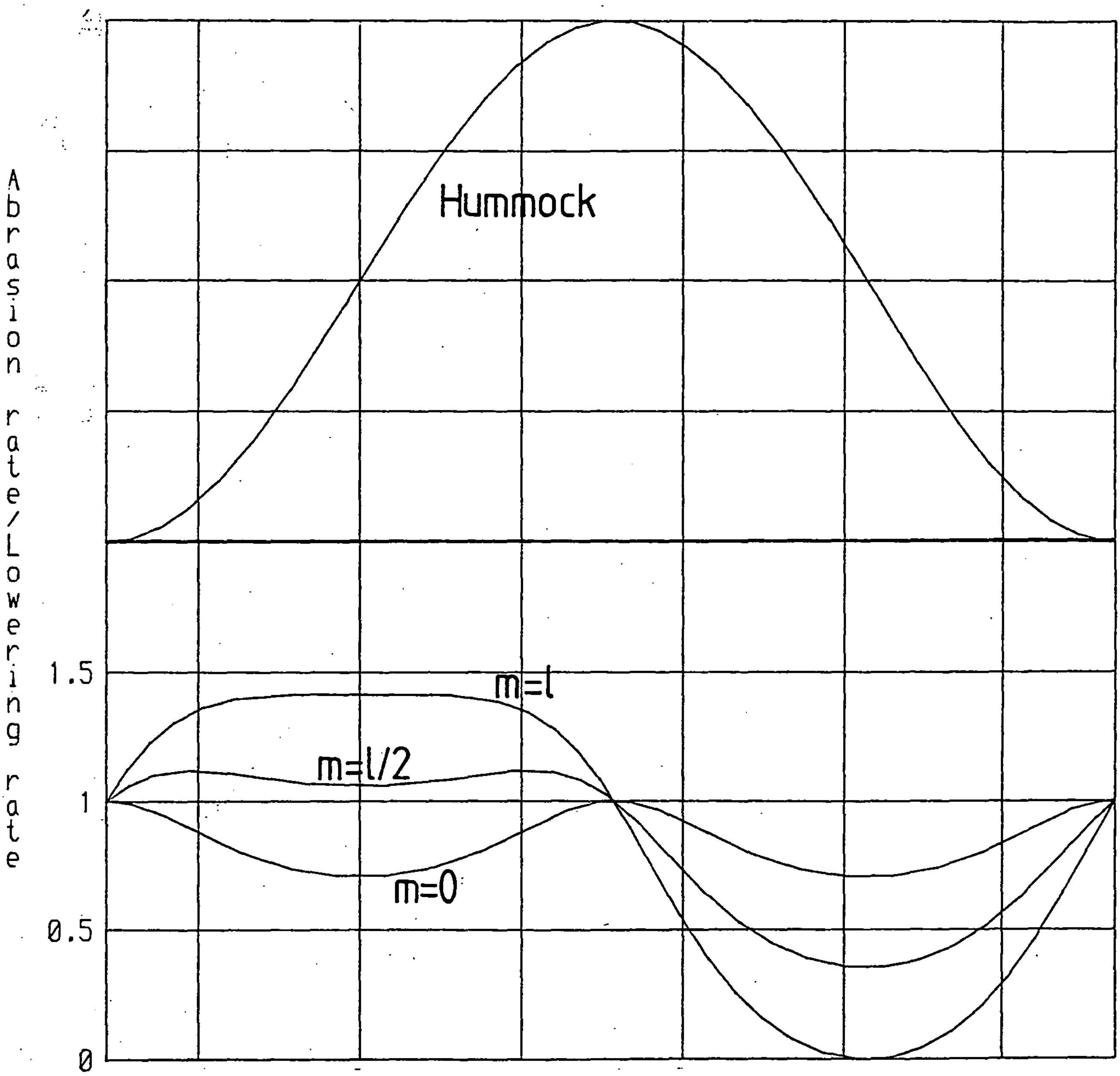

Figure 2.8 Evolution of a slope and plateau under constant abrasion using the method of characteristics.

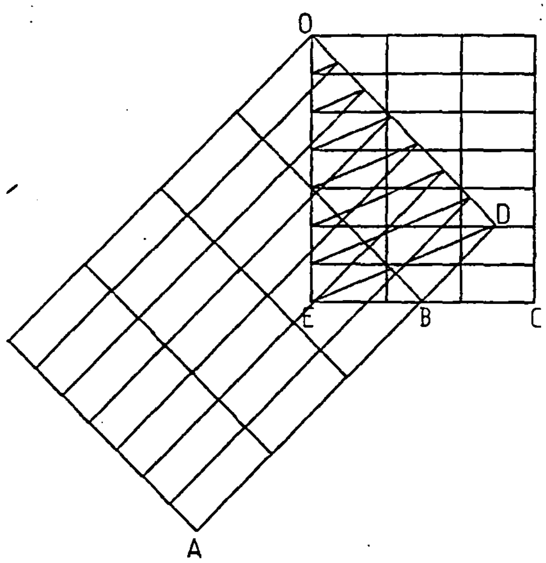

Figure 2.9 Evolution of a bell-shape under constant abrasion using the method of characteristics.

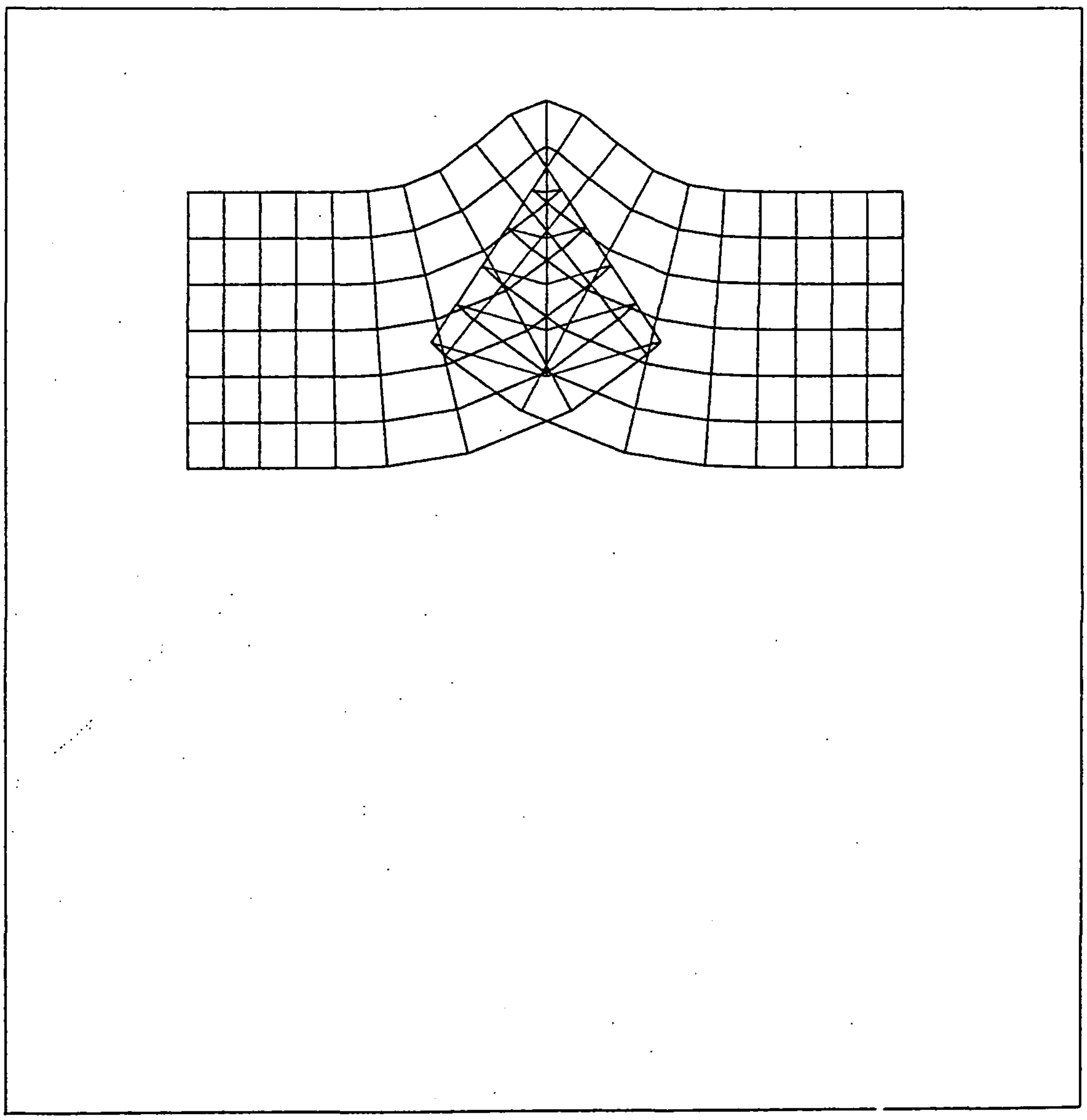

Figure 2.10 Evolution of a V-shaped valley under constant abrasion using a direct finite-difference formulation of the abrasion equation.

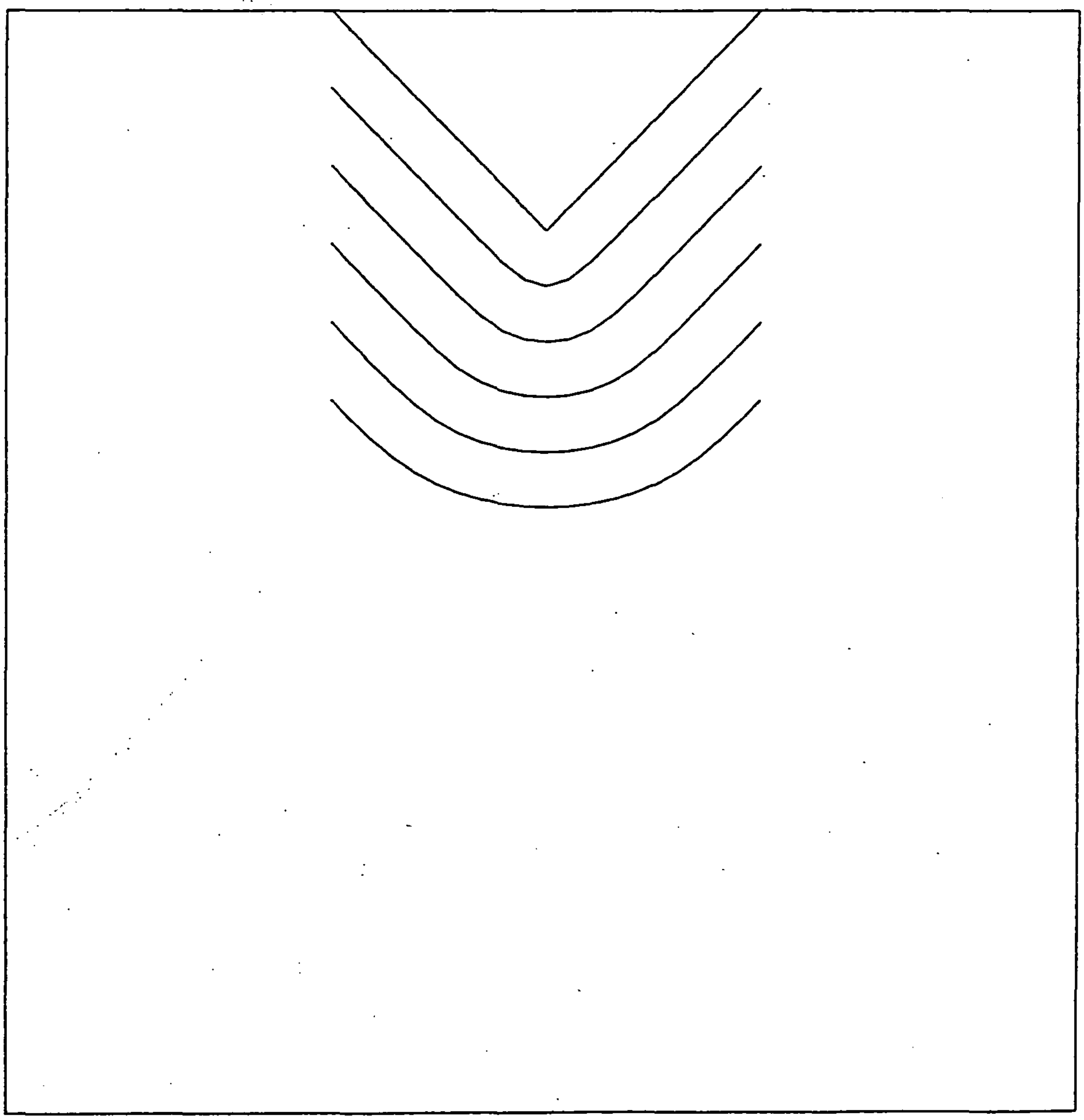

Figure 2.11 Evolution of a bell-shape under constant abrasion using a direct finite-difference formulation of the abrasion equation.

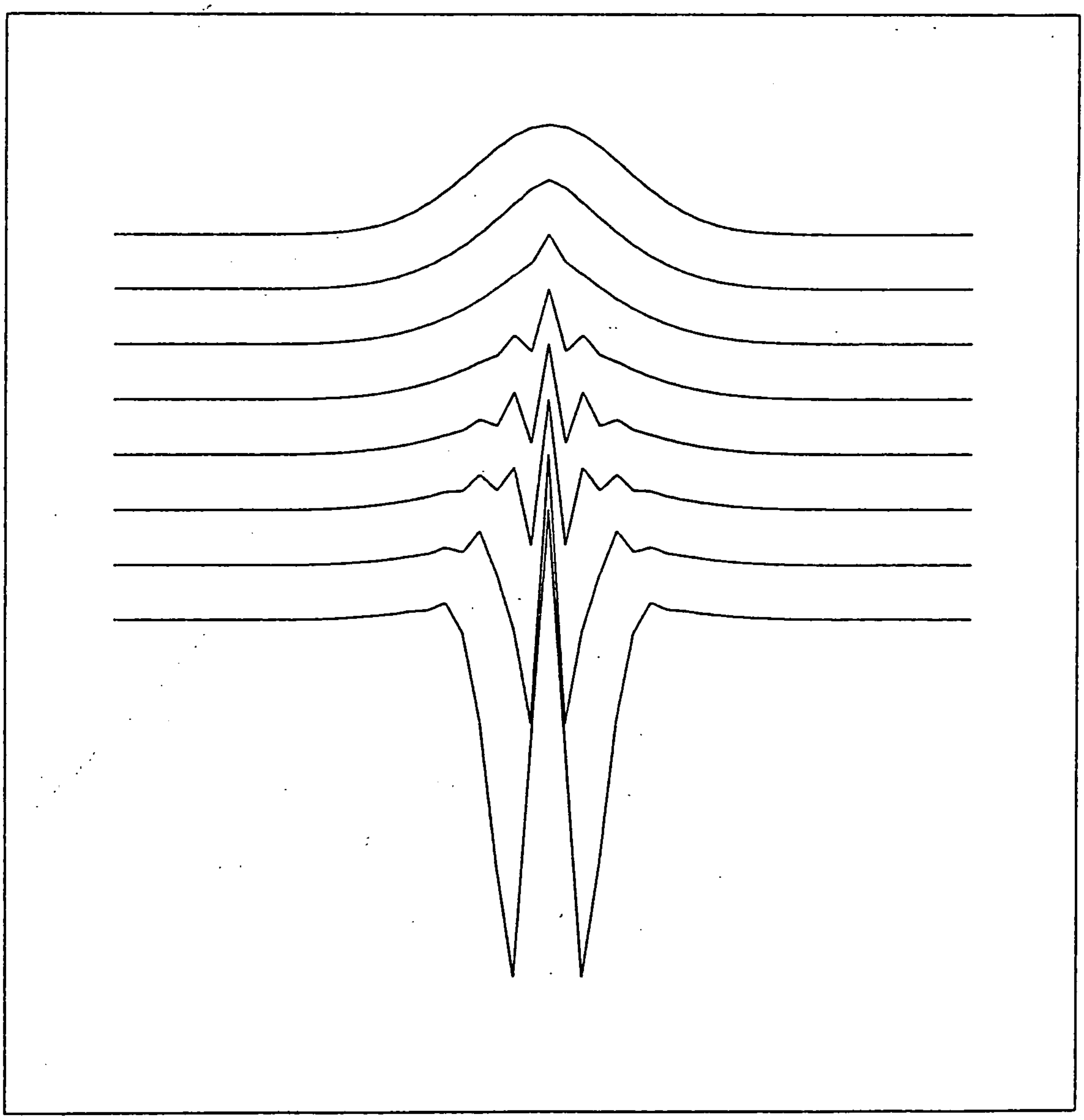

Figure 2.12 Evolution of a V-shaped valley under constant abrasion using the Farmer formulation with a coarse mesh.

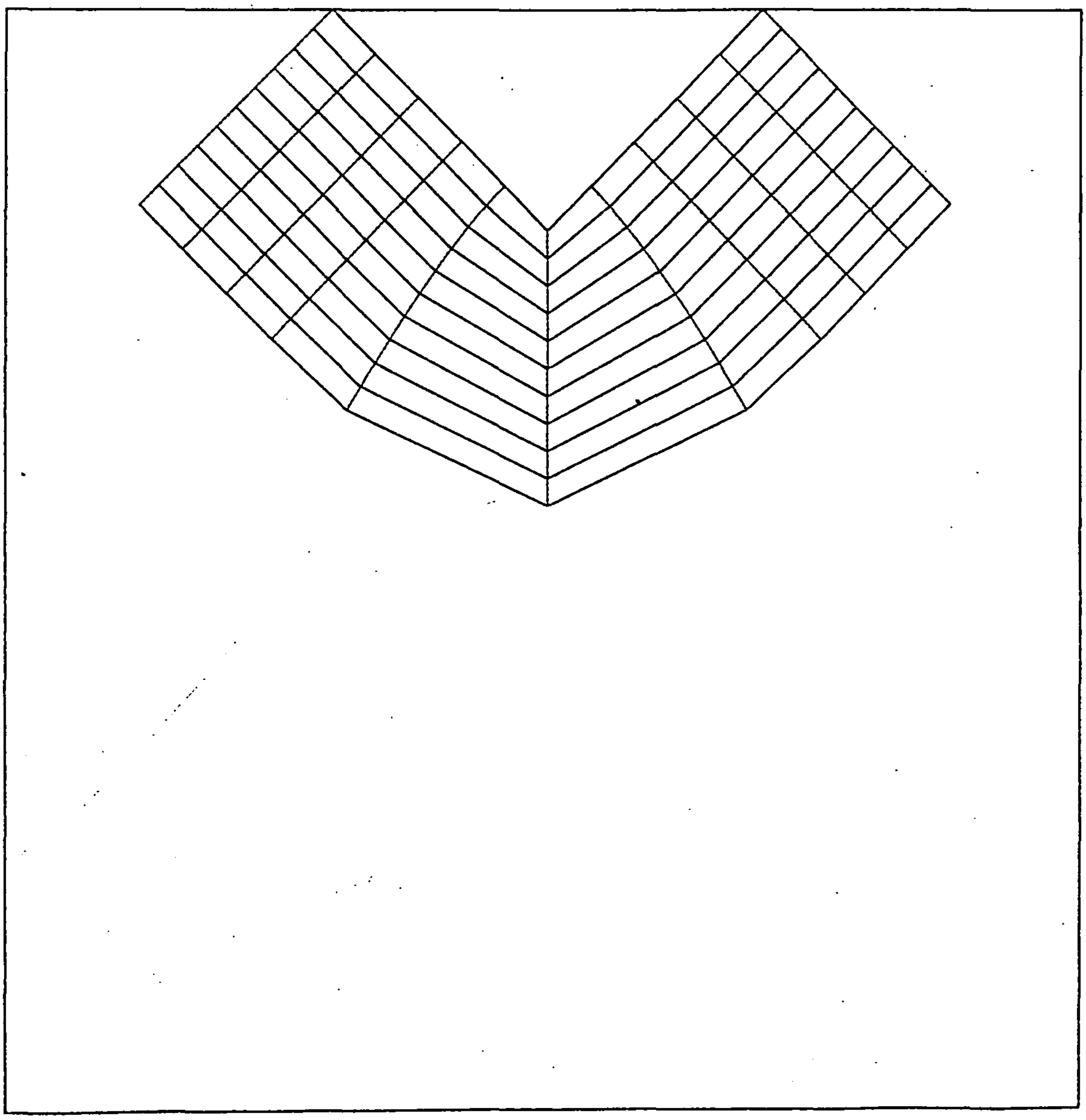

Figure 2.13 Evolution of a V-shaped valley under constant abrasion using the Farmer formulation with a fine mesh.

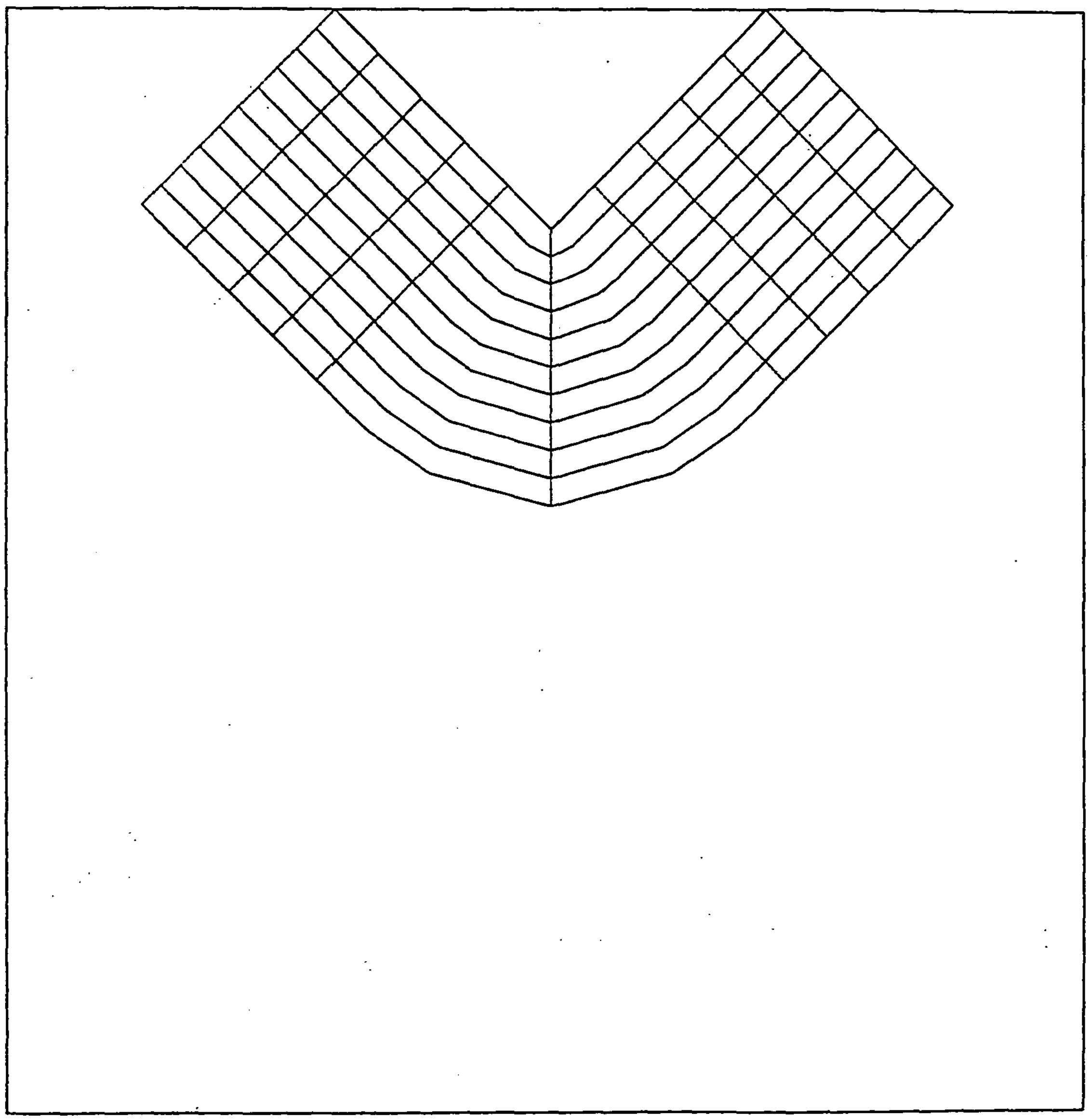

Figure 2.14 Evolution of a bell-shape under constant abrasion using the Farmer formulation.

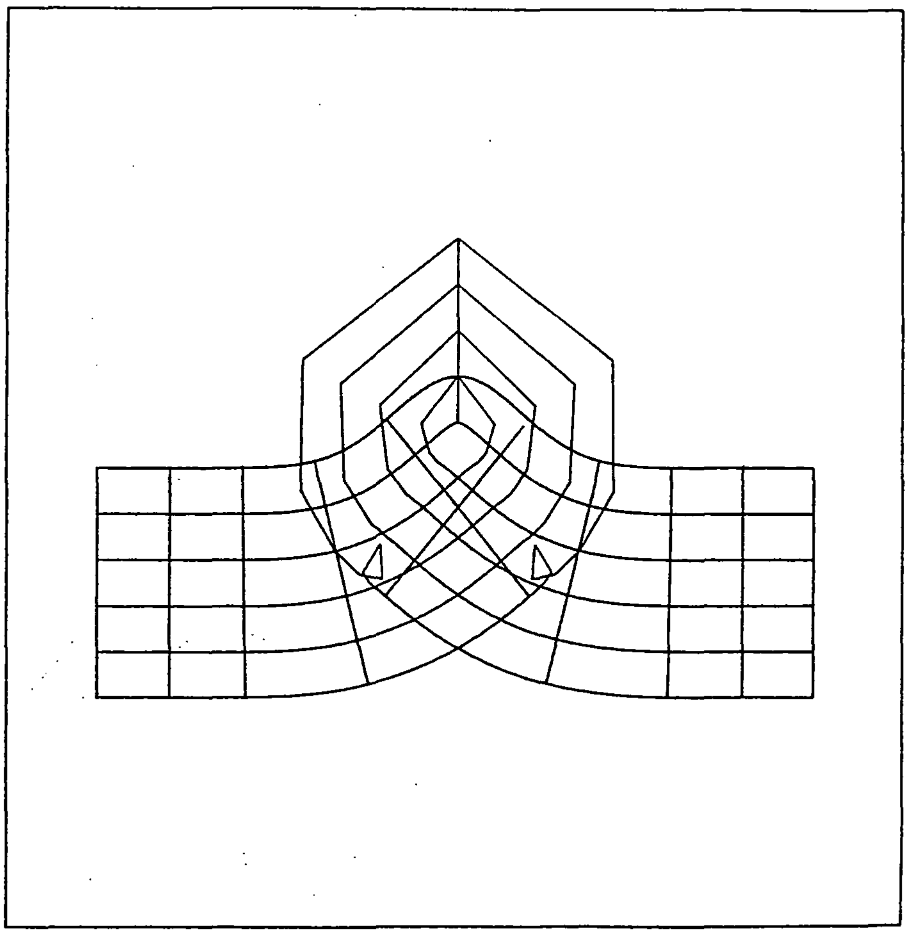

Figure 2.15 Persistence without migration of a bell-shape with lowering.

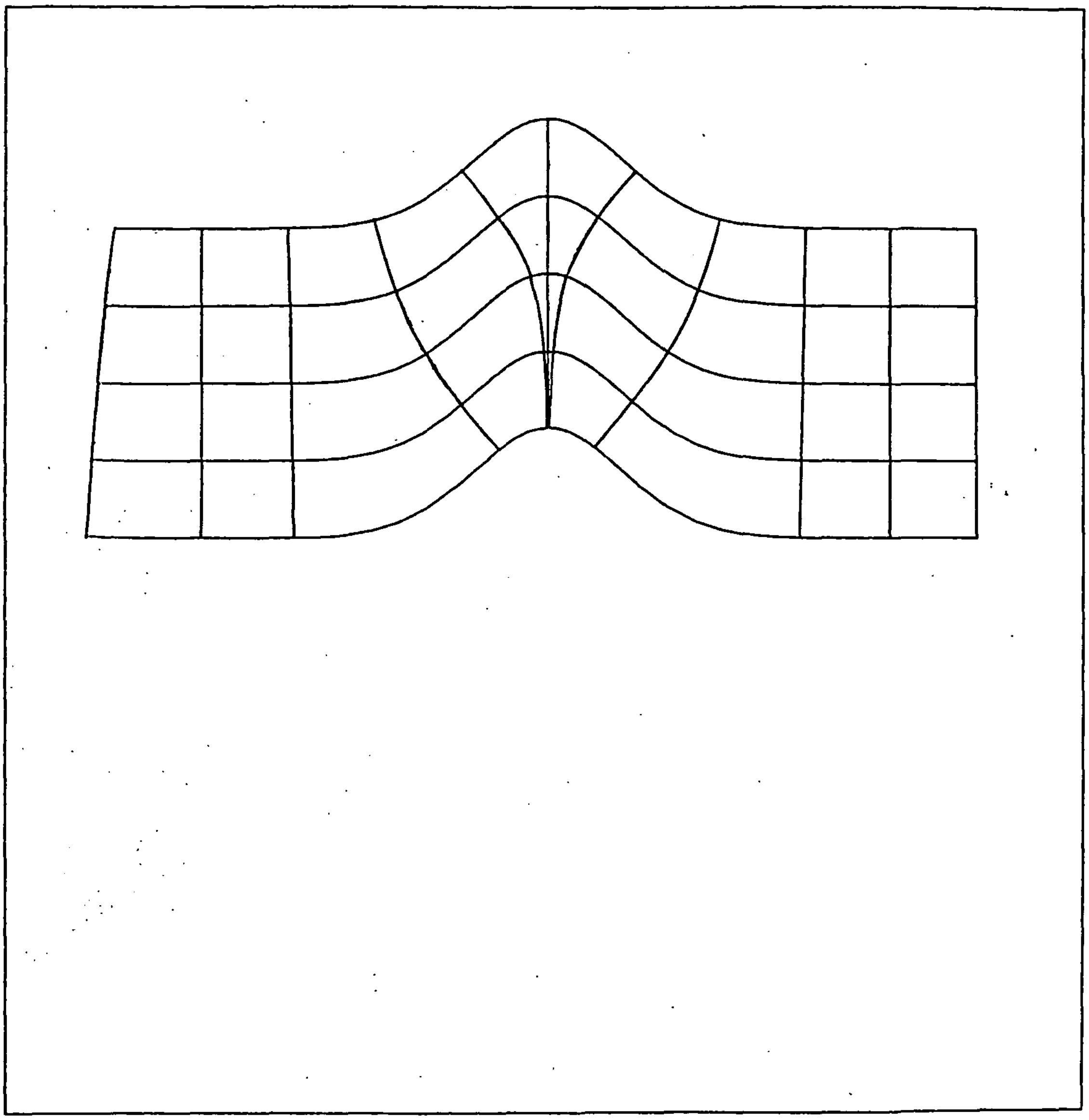

Figure 2.16 Persistence with migration of a bell-shape with lowering.

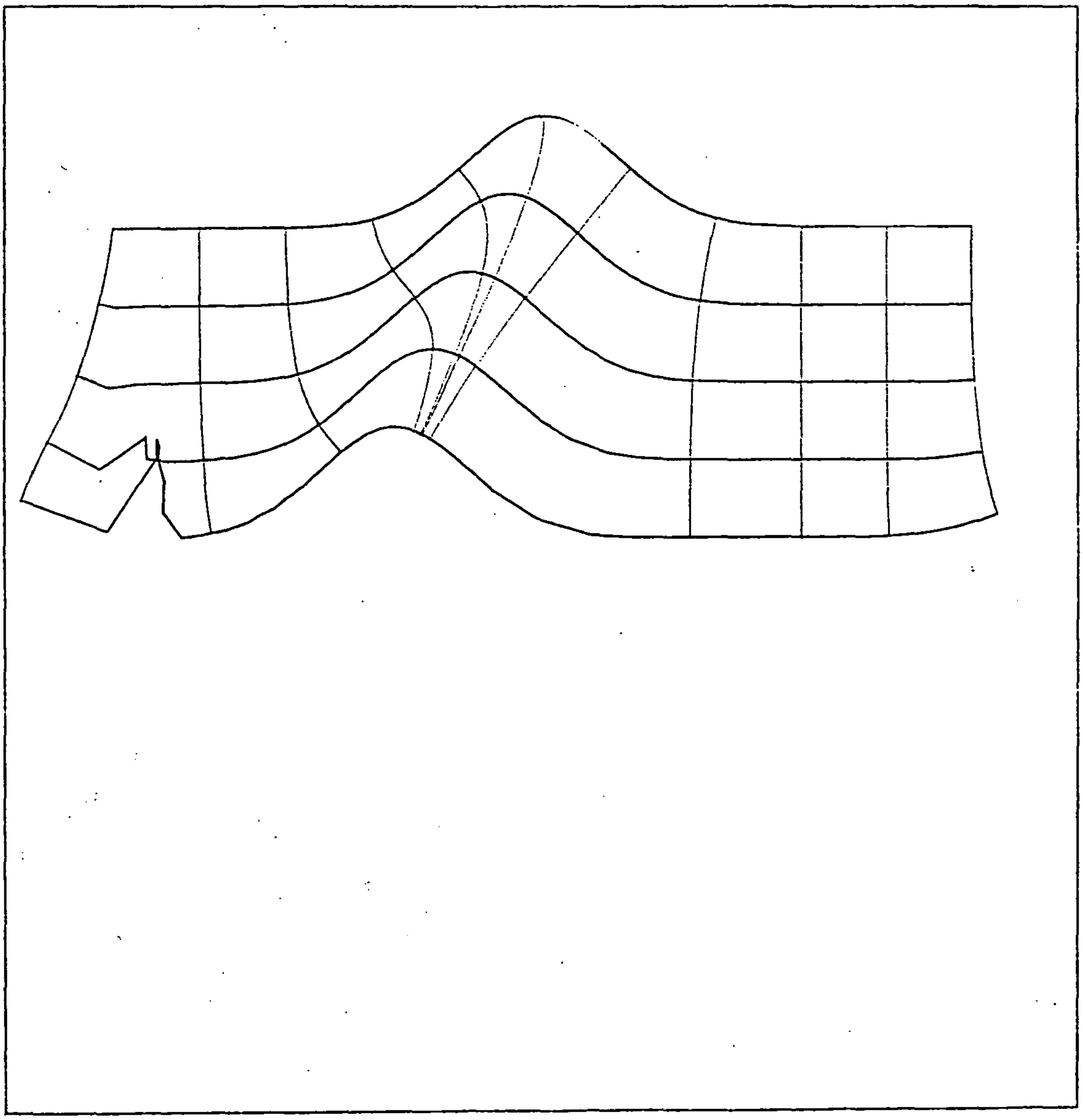

Figure 2.17 Evolution of a V-shaped valley under constant abrasion using the method of characteristics: no definition of point.

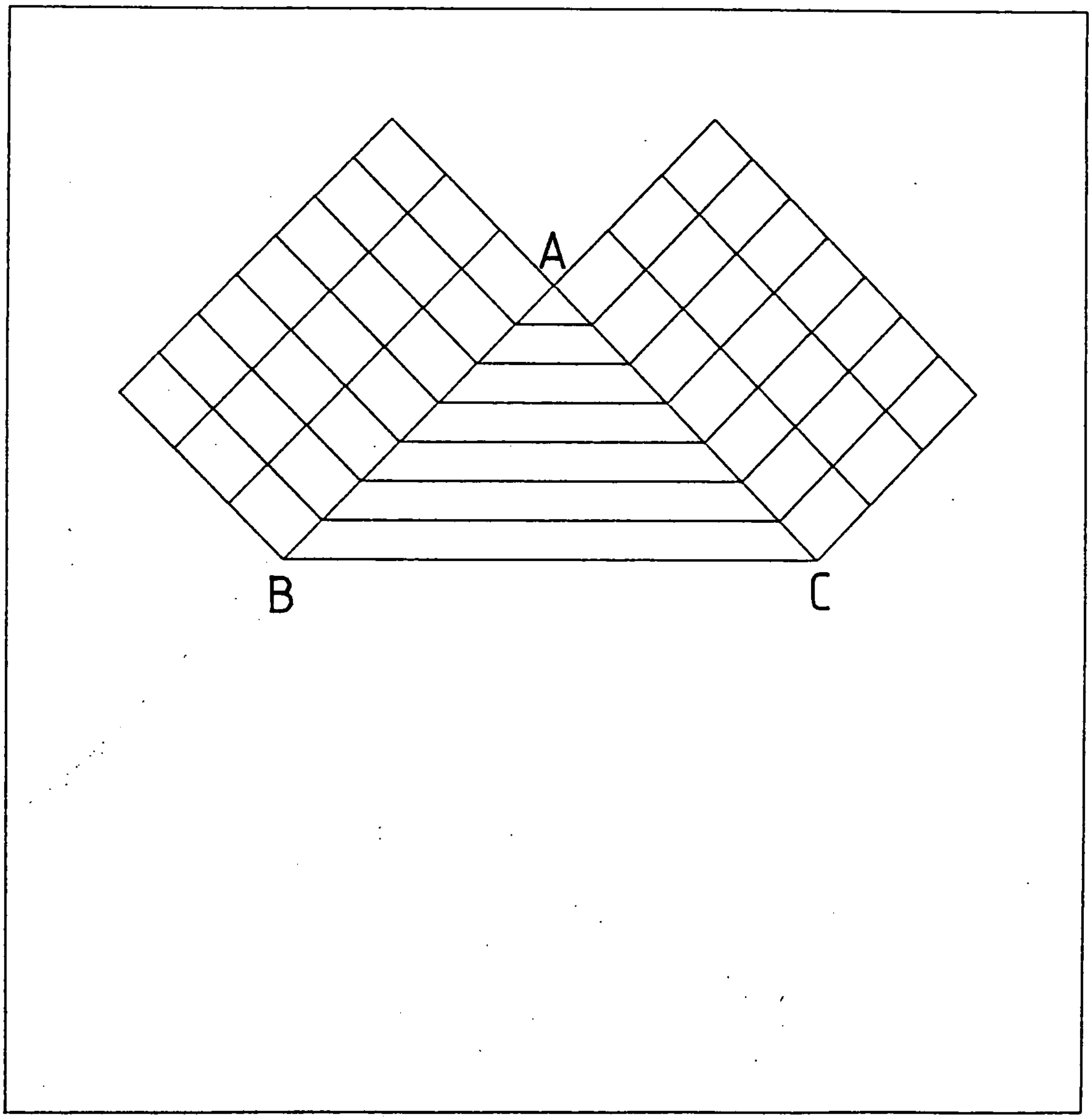

Figure 2.18 Evolution of a V-shaped valley under constant abrasion using the method of characteristics: smooth definition of point.

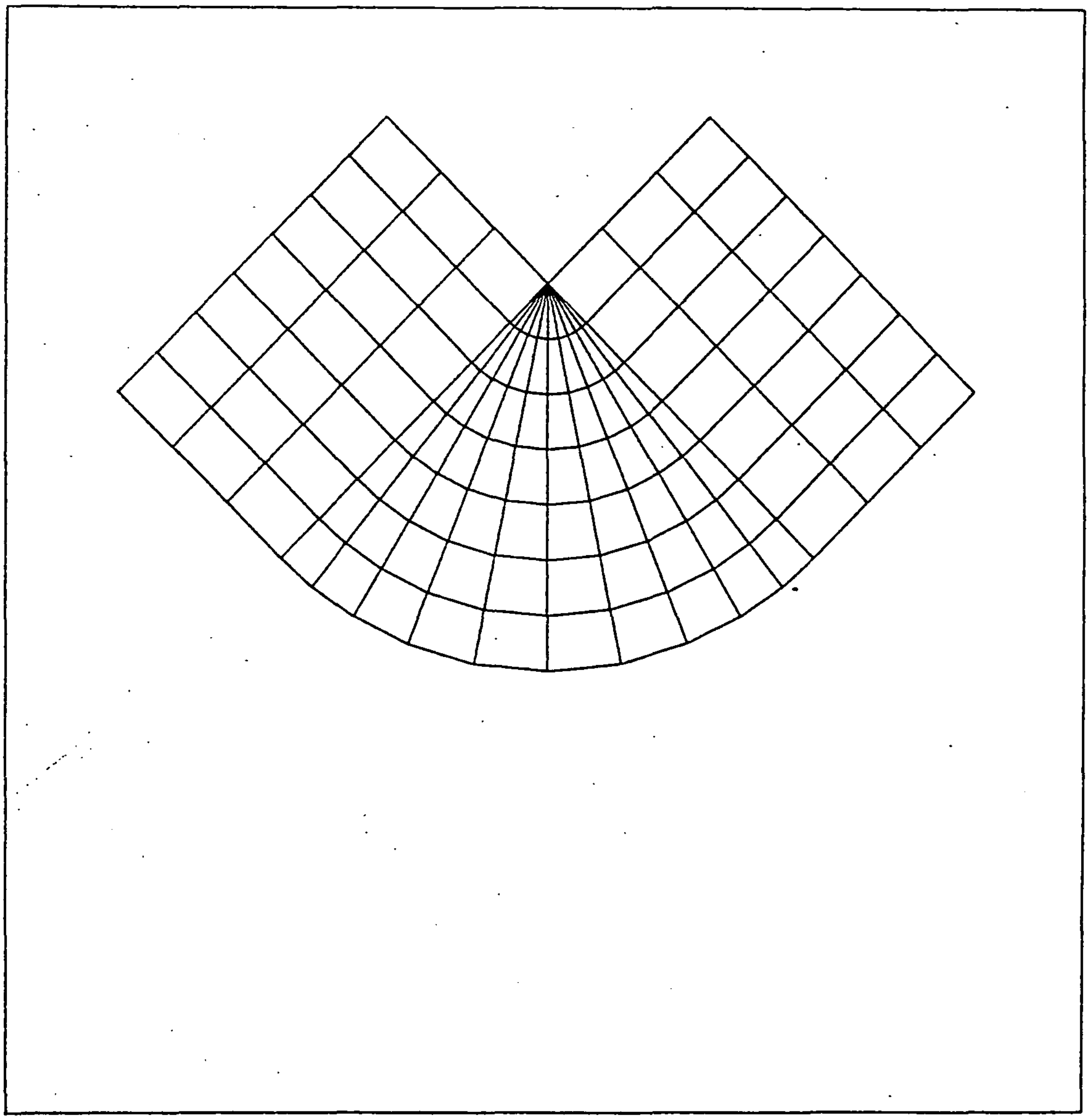

Figure 2.19 Evolution of a V-shaped valley under constant abrasion using the method of characteristics: random definition of point.

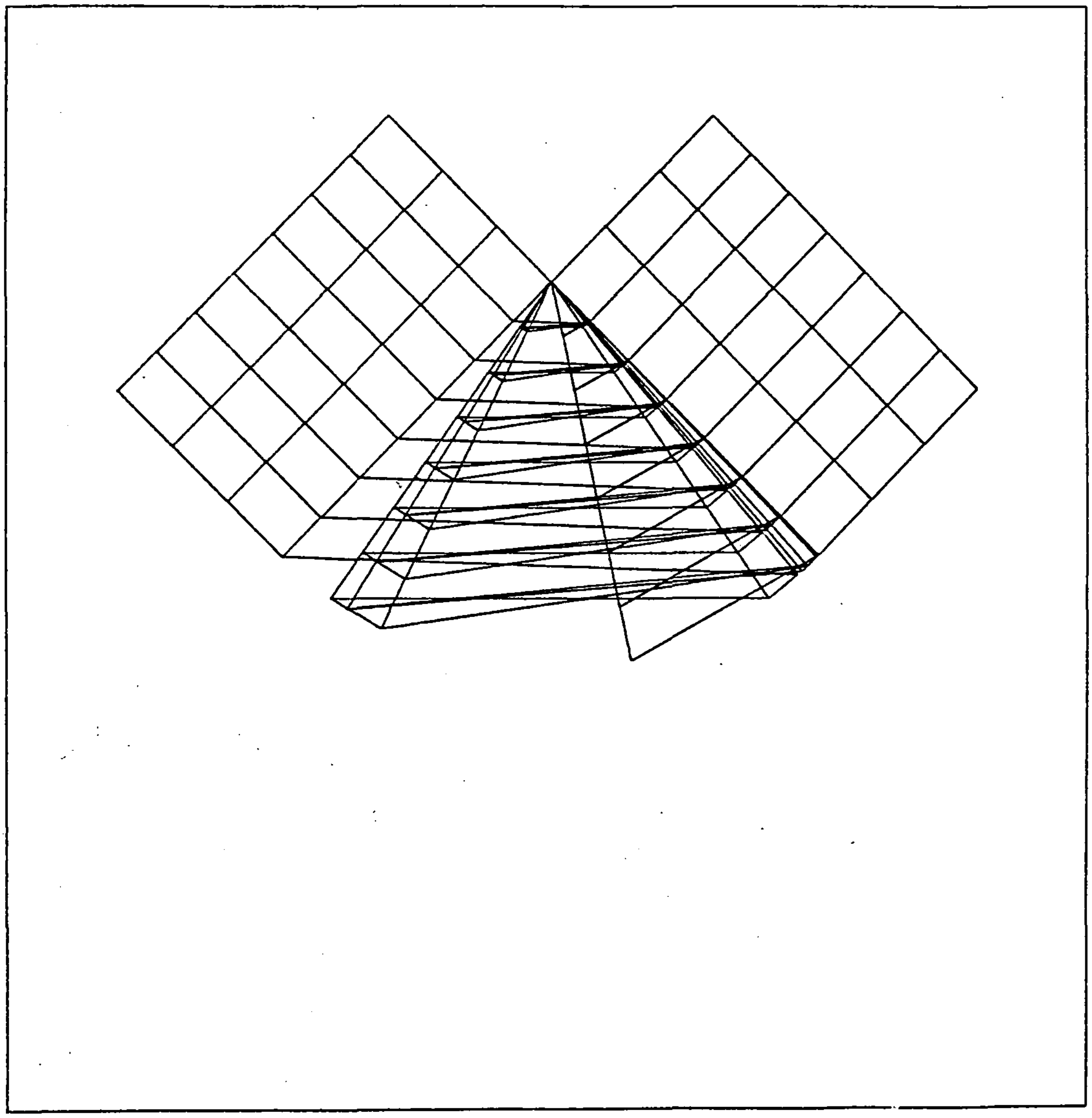

Figure 2.20 Evolution of slope and plateau with curvature dependent abrasion rate using the Farmer formulation.

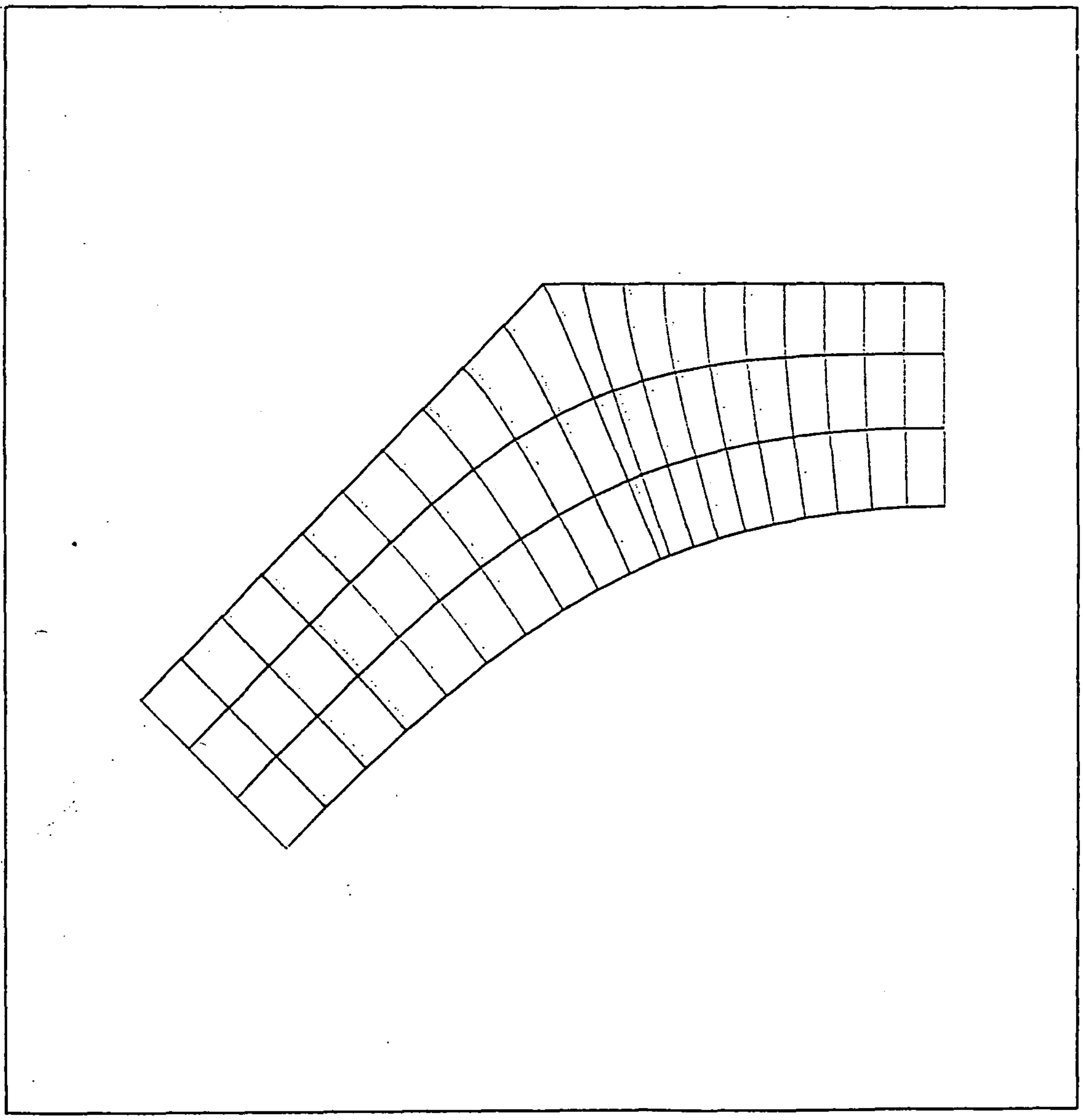

Figure 2.21 Evolution of V-shaped valley with abrasion inhibited by concavity using the Farmer formulation.

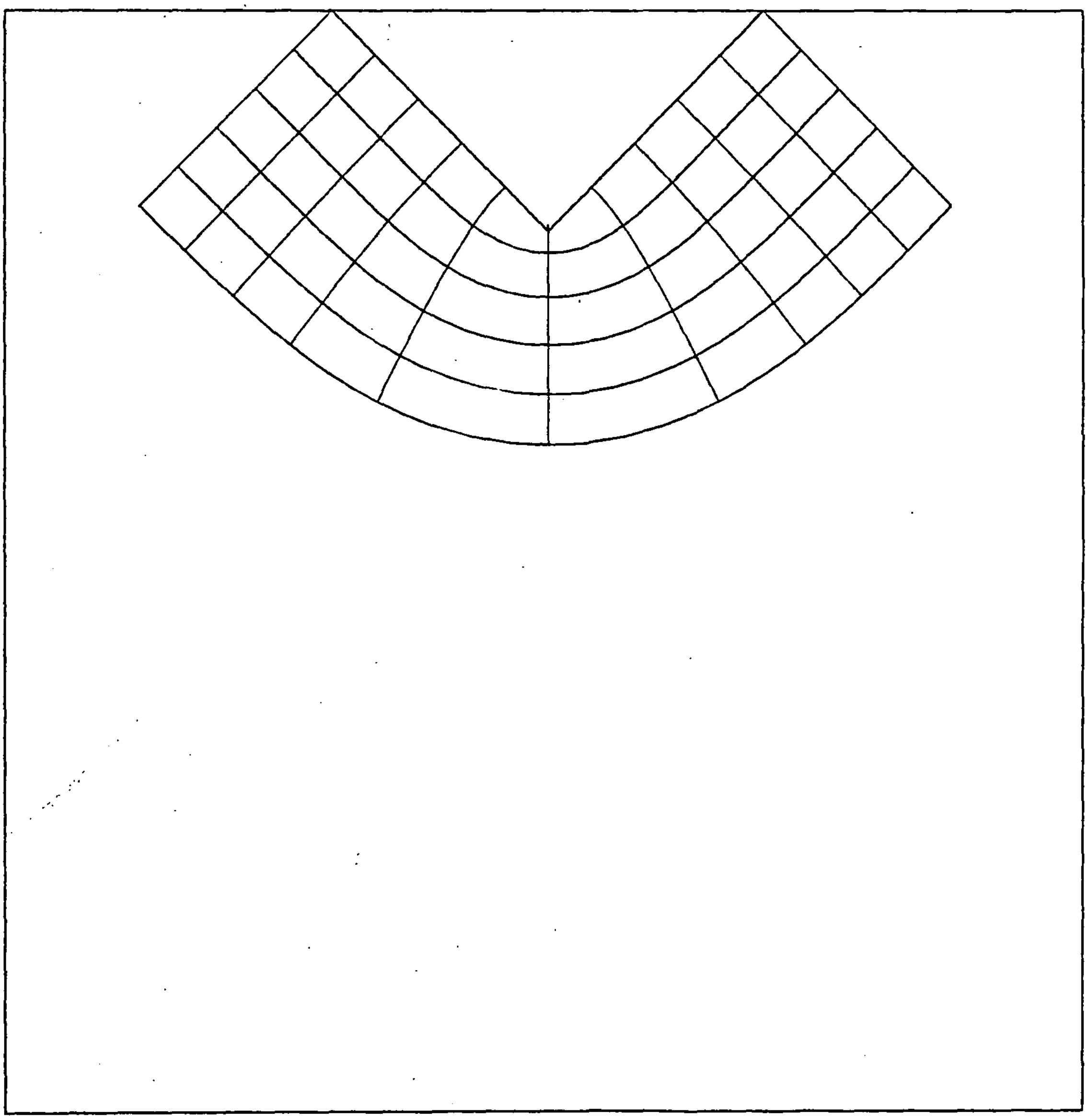

Figure 2.22 Evolution of V-shaped valley with abrasion enhanced by concavity using the Farmer formulation.

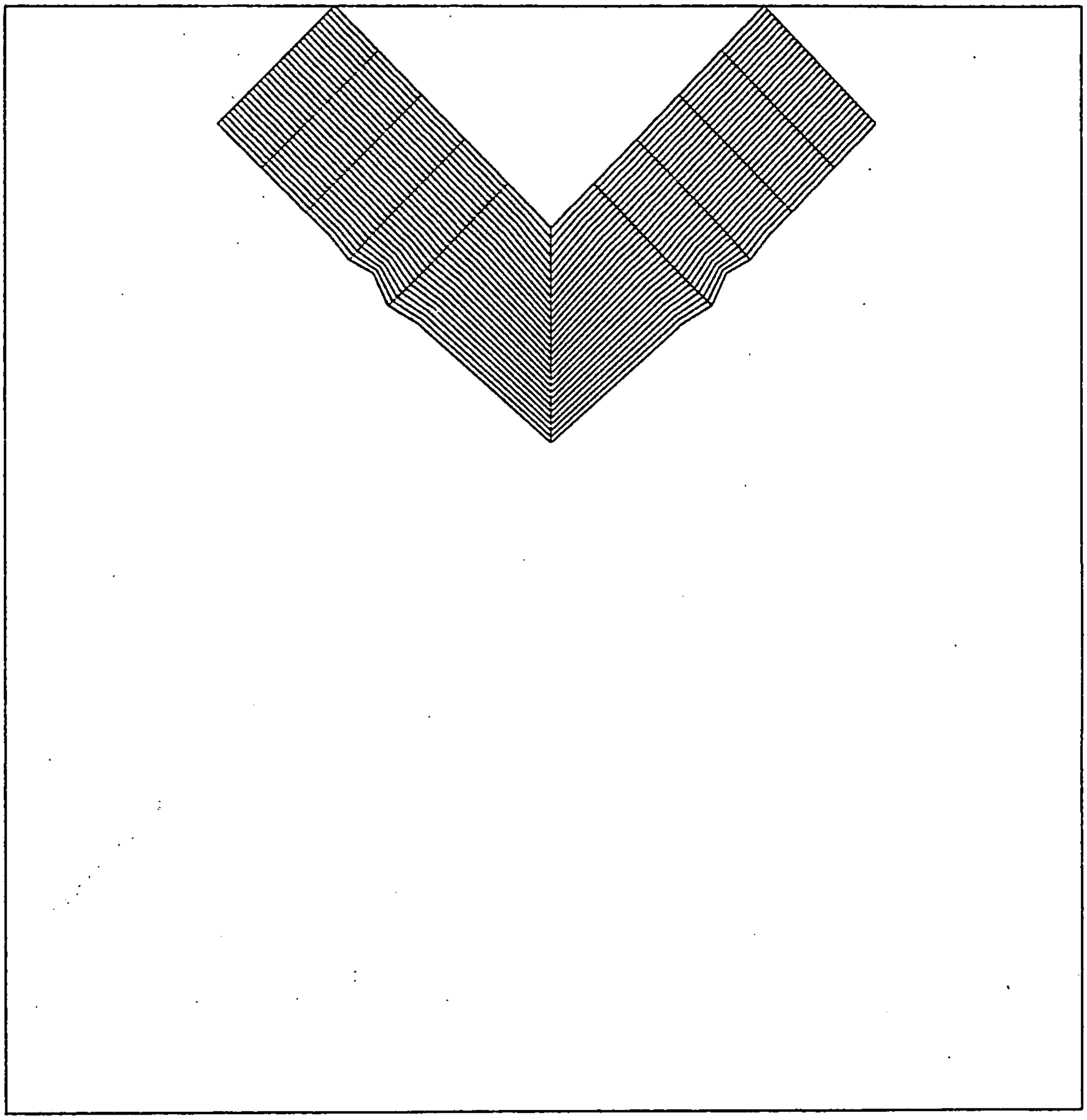

Figure 2.23 Evolution of a V-shaped valley with a Gaussian abrasion function.

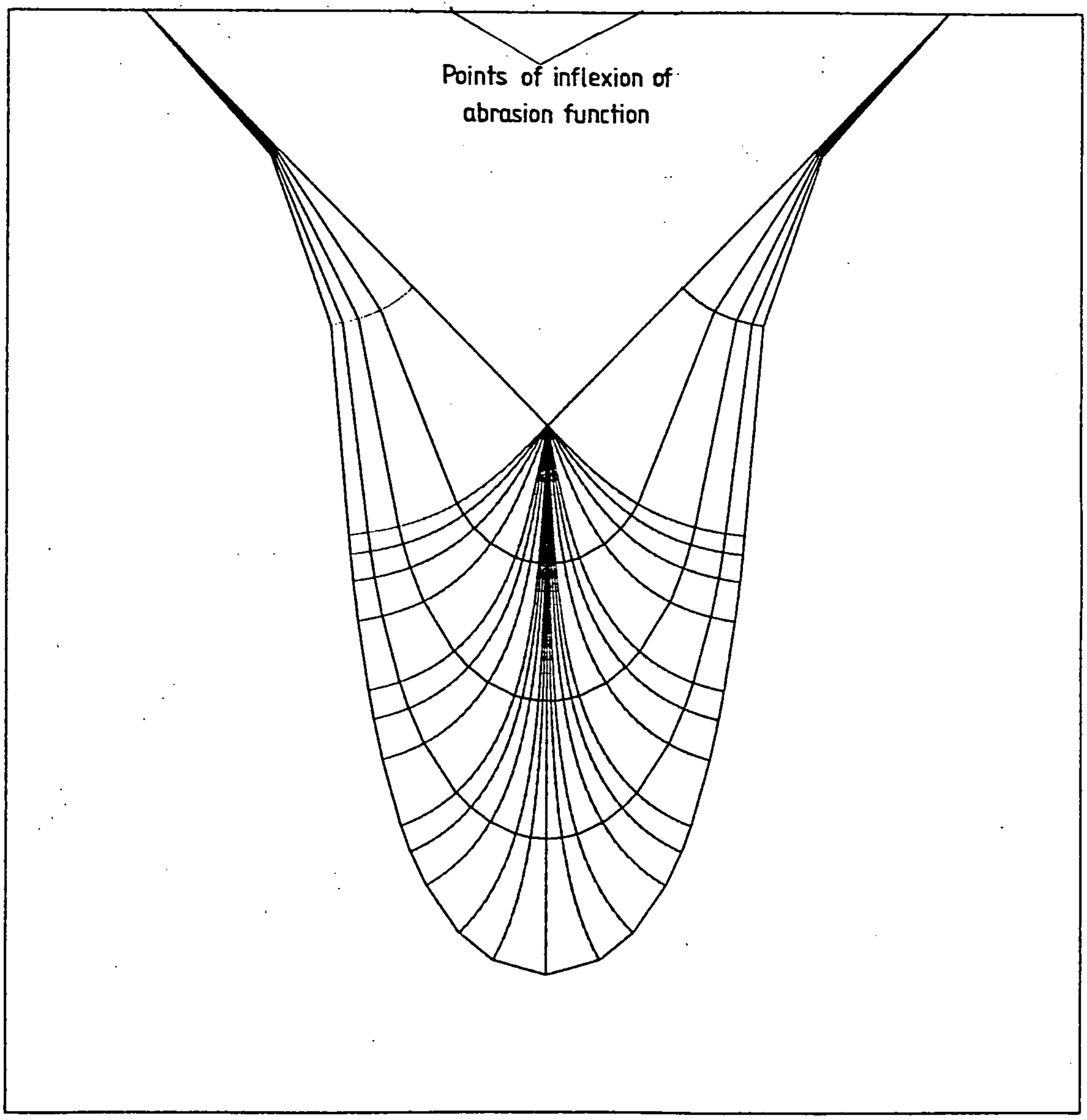

Figure 2.24 Evolution of a V-shaped valley with rocks of different hardness.

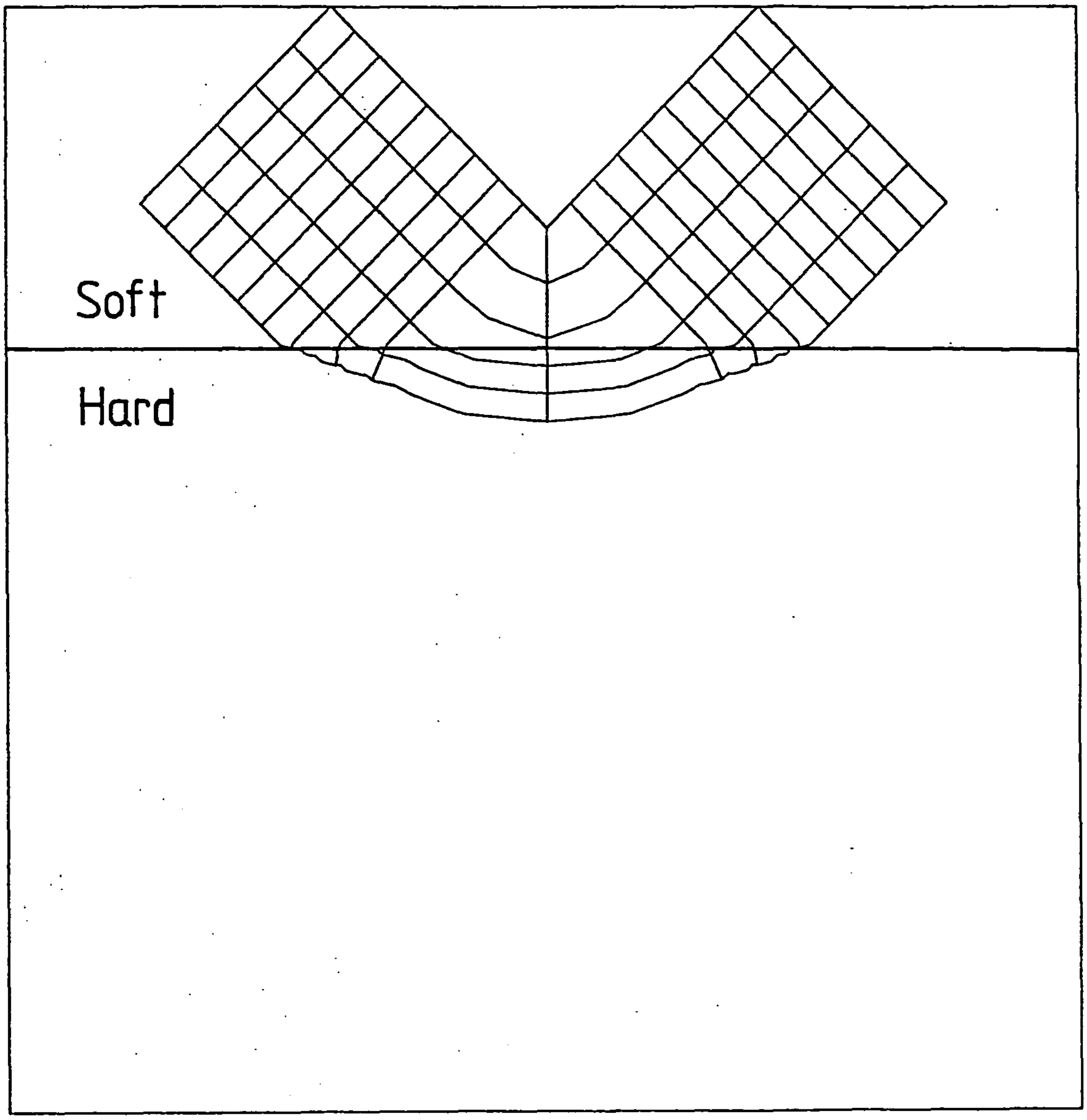

Figure 2.25 Trough persistent under lowering with $a \propto 1/h$: hyberbolic cosine.

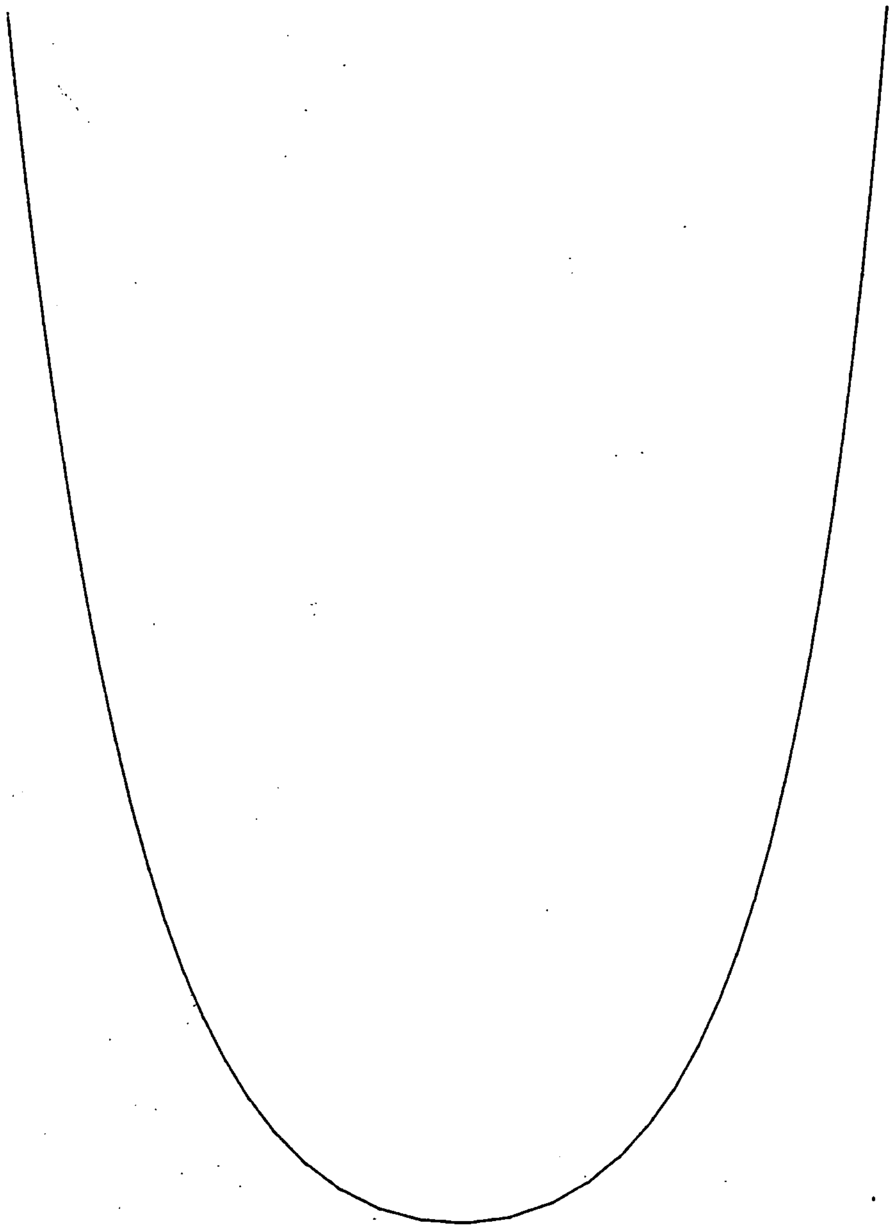

Figure 2.26 Troughs persistent under lowering with abrasion a function of a curvature.

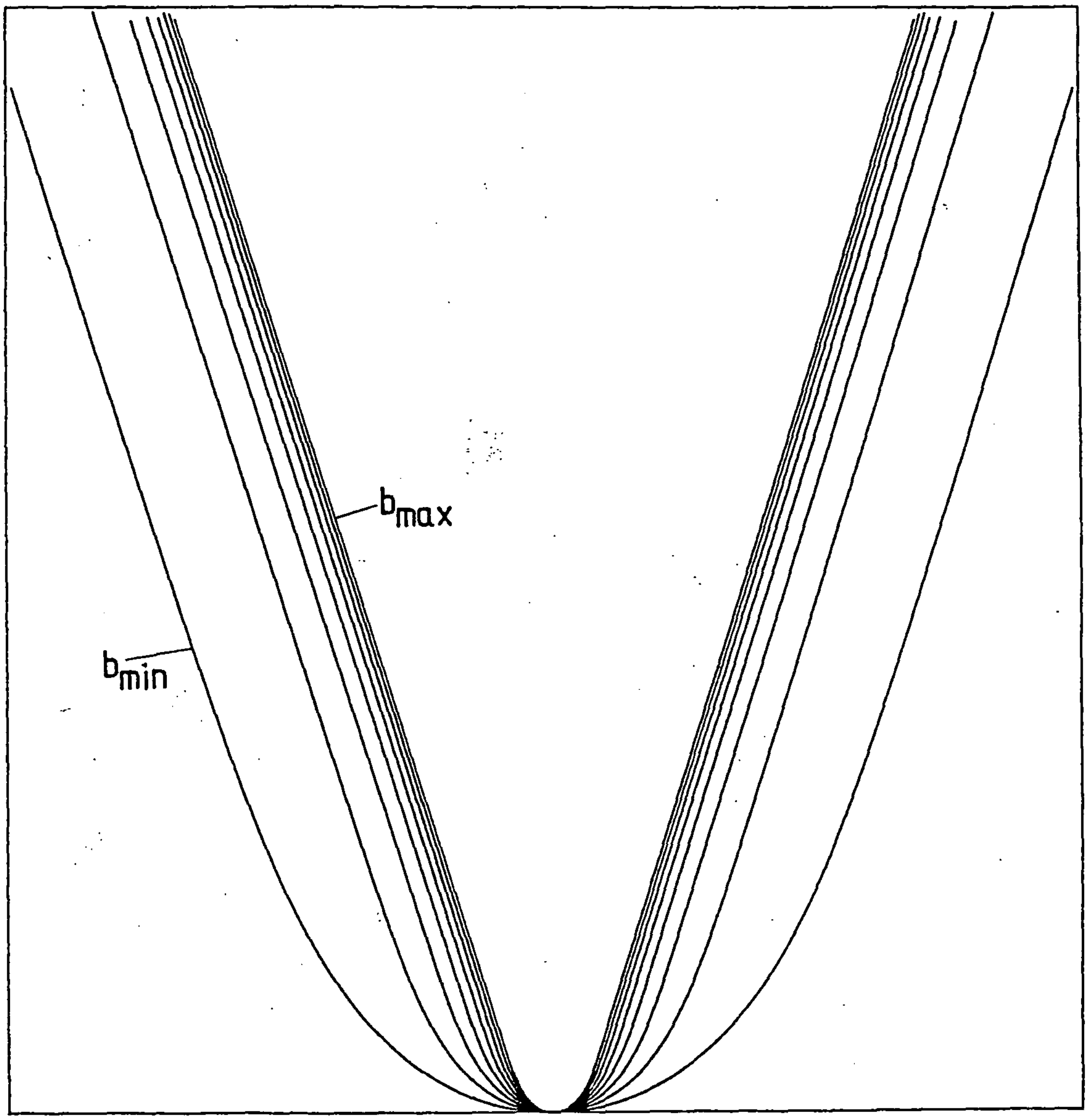

Figure 2.27 Abrasion of a weak zone.

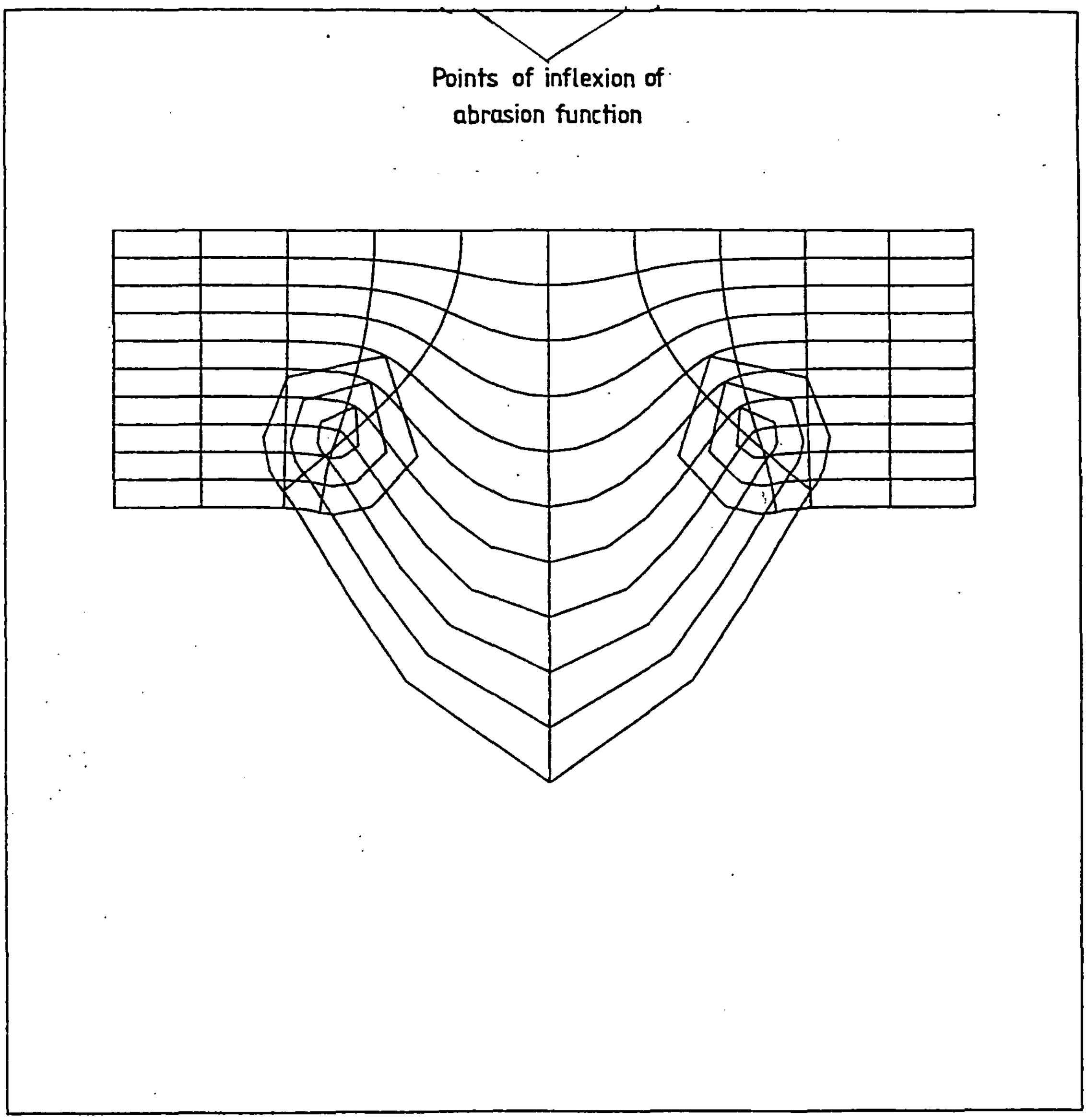

FIGURE 4.1 TWO ELEMENT TEST MODEL

o–Node at which velocity and pressure are solved for

x–Node at which velocity only is solved for

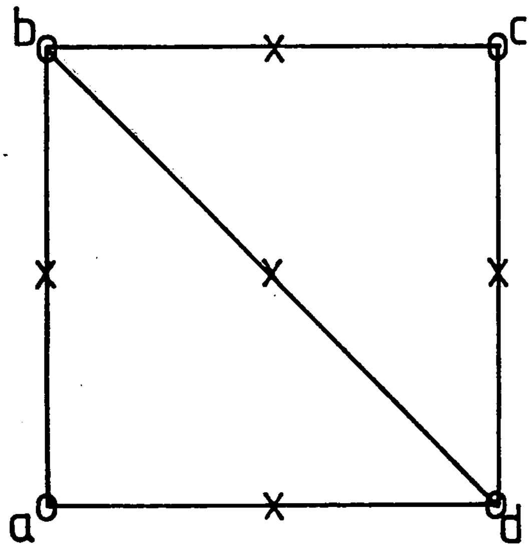

Boundary Conditions

ad – Fixed bed or Weertman

abcd–Prescribed velocity or traction

abd,bcd are the finite elements

Figure 4.2 Inclined plane problem-nine nodes.

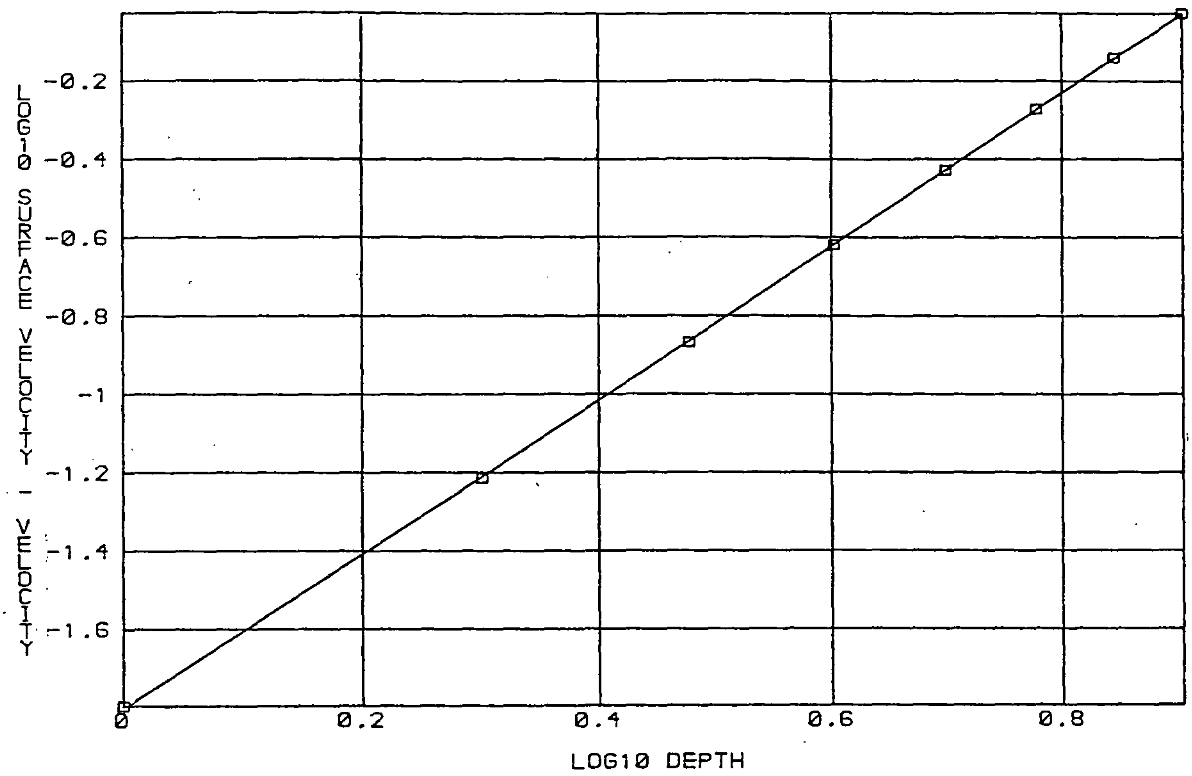

Figure 4.3 Inclined plane problem-seventeen nodes.

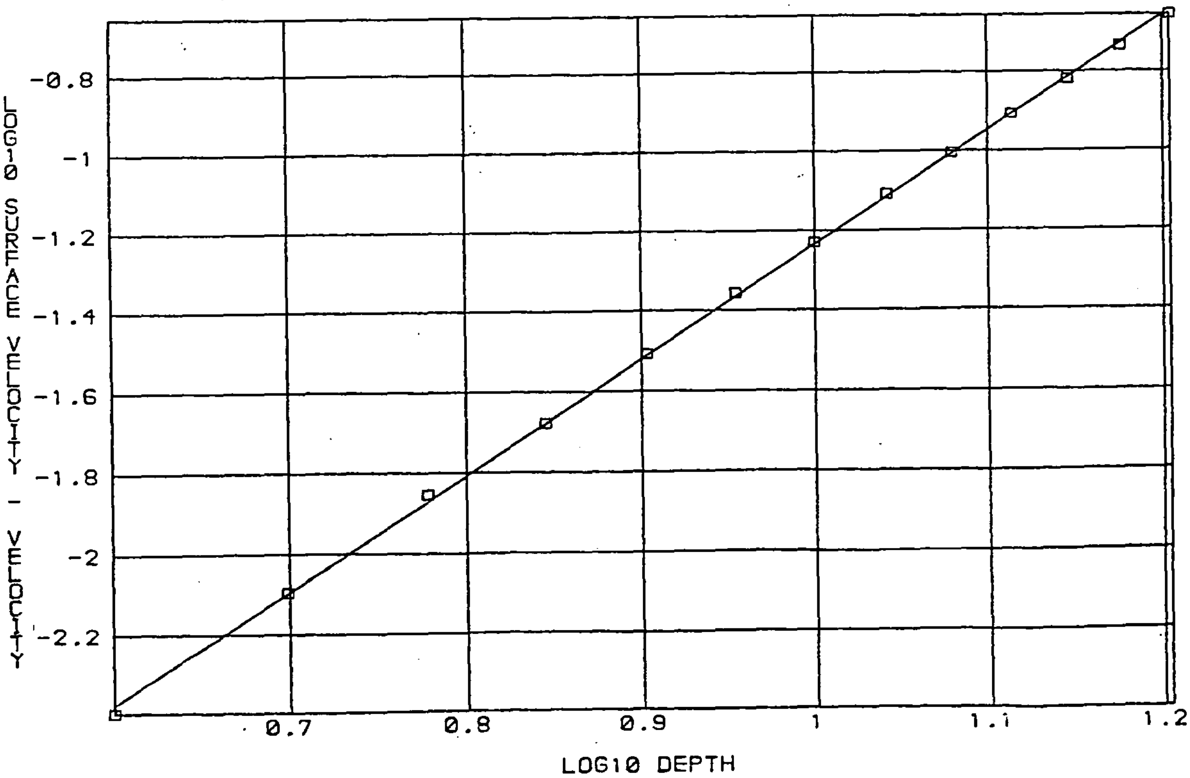

Figure 4.4 Rotating Couette flow.

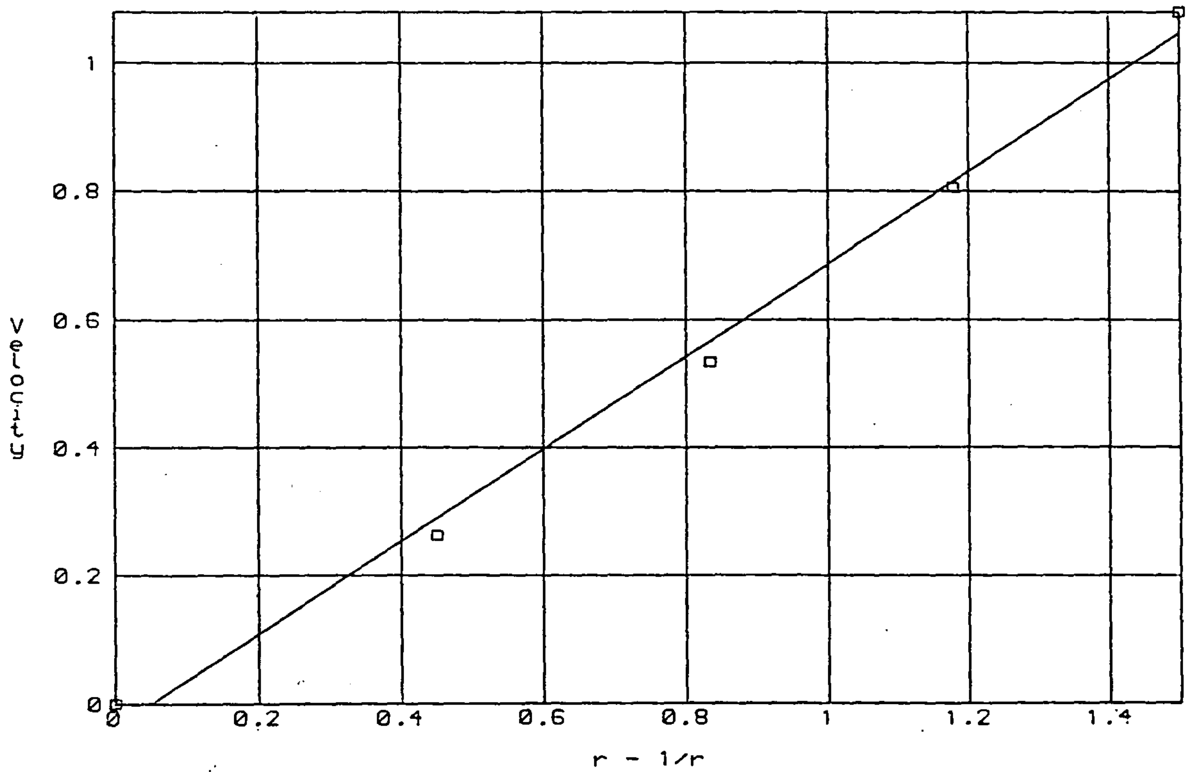

Figure 5.1 View of finite element mesh showing the nesting scheme.

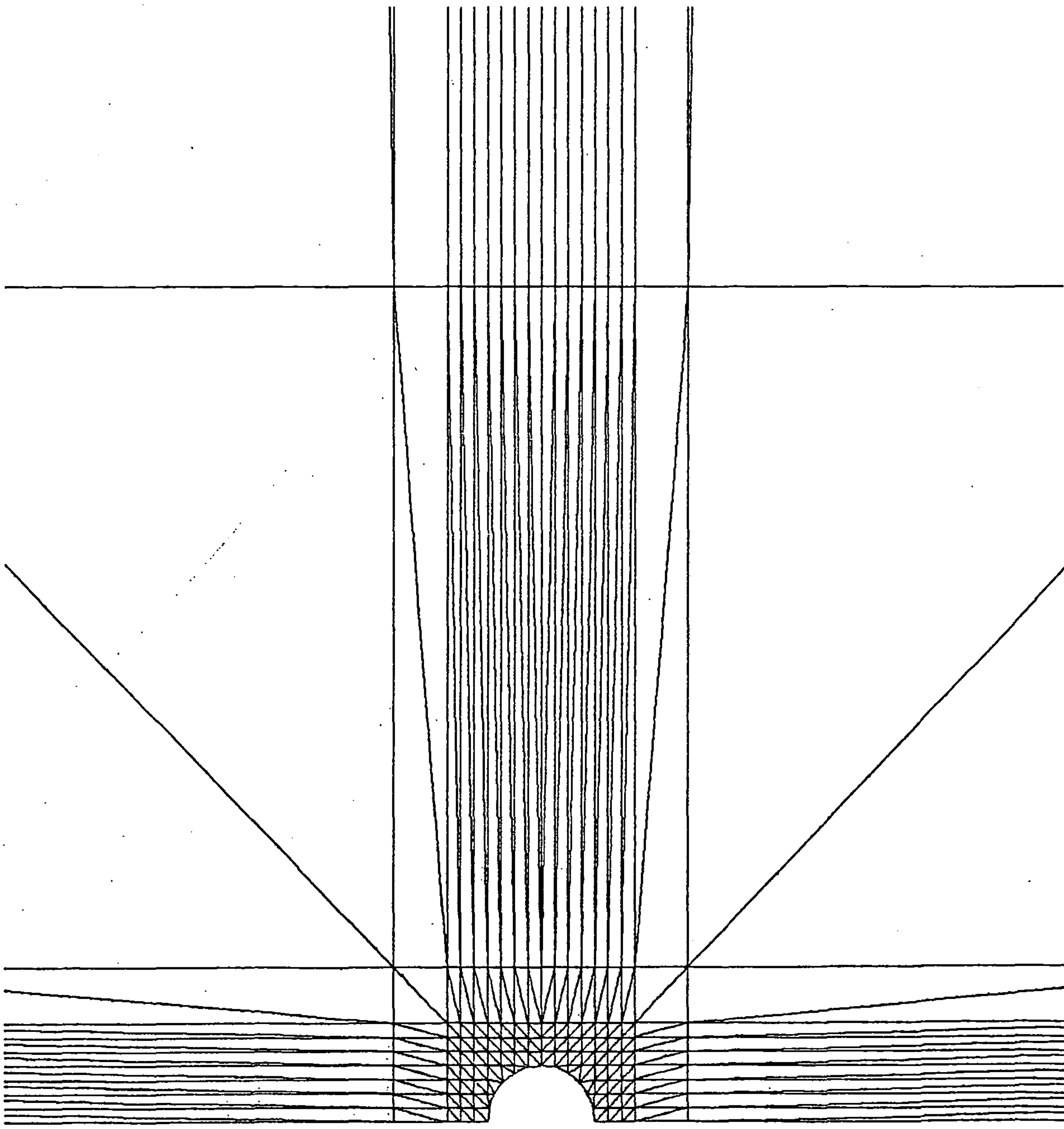

Figure 5.2 Detail from finite element mesh for modelling flow over a semi-cylindrical ridge.

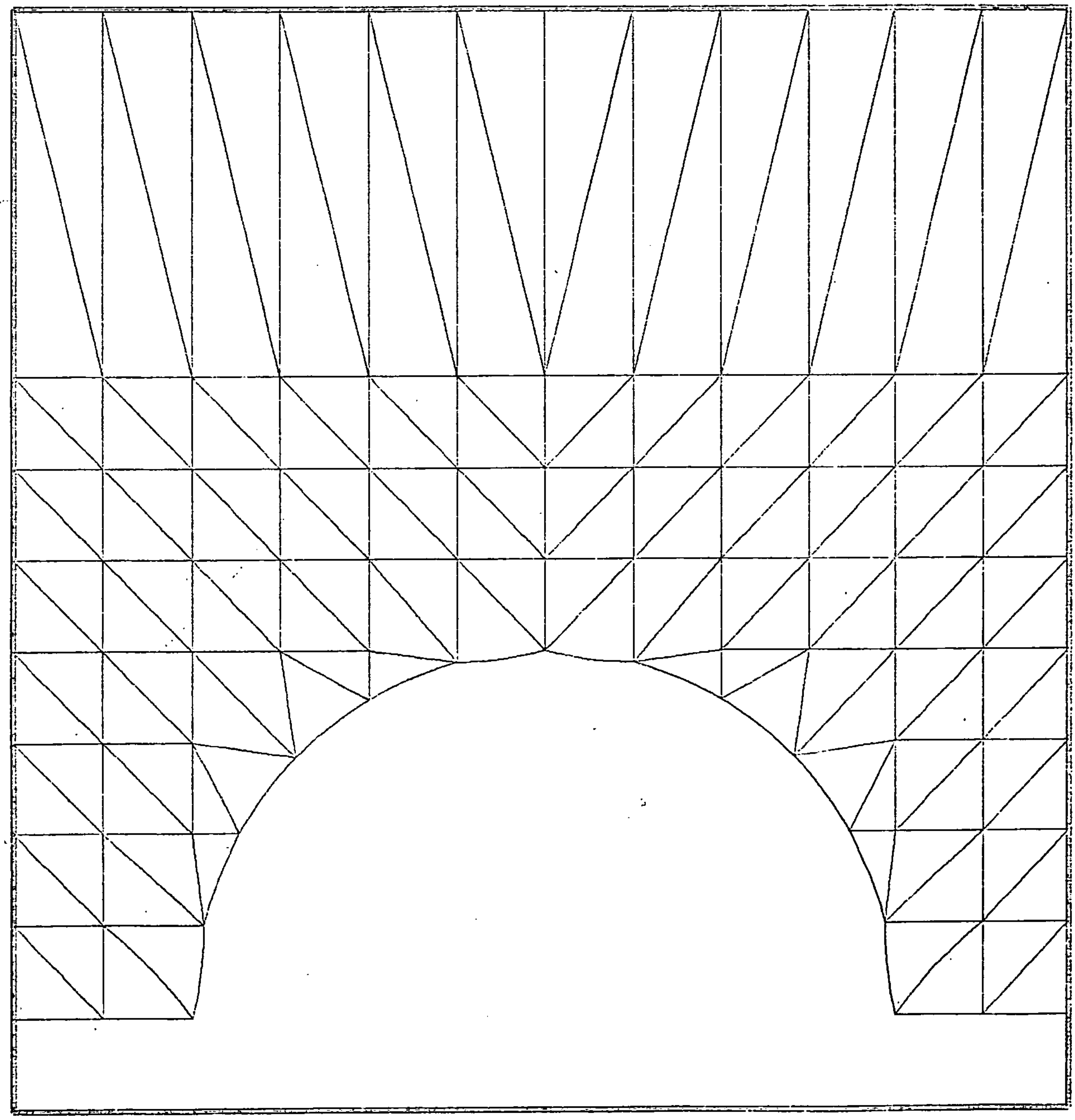

Figure 5.3 Detail from finite element mesh for modelling flow over a truncated sine ridge.

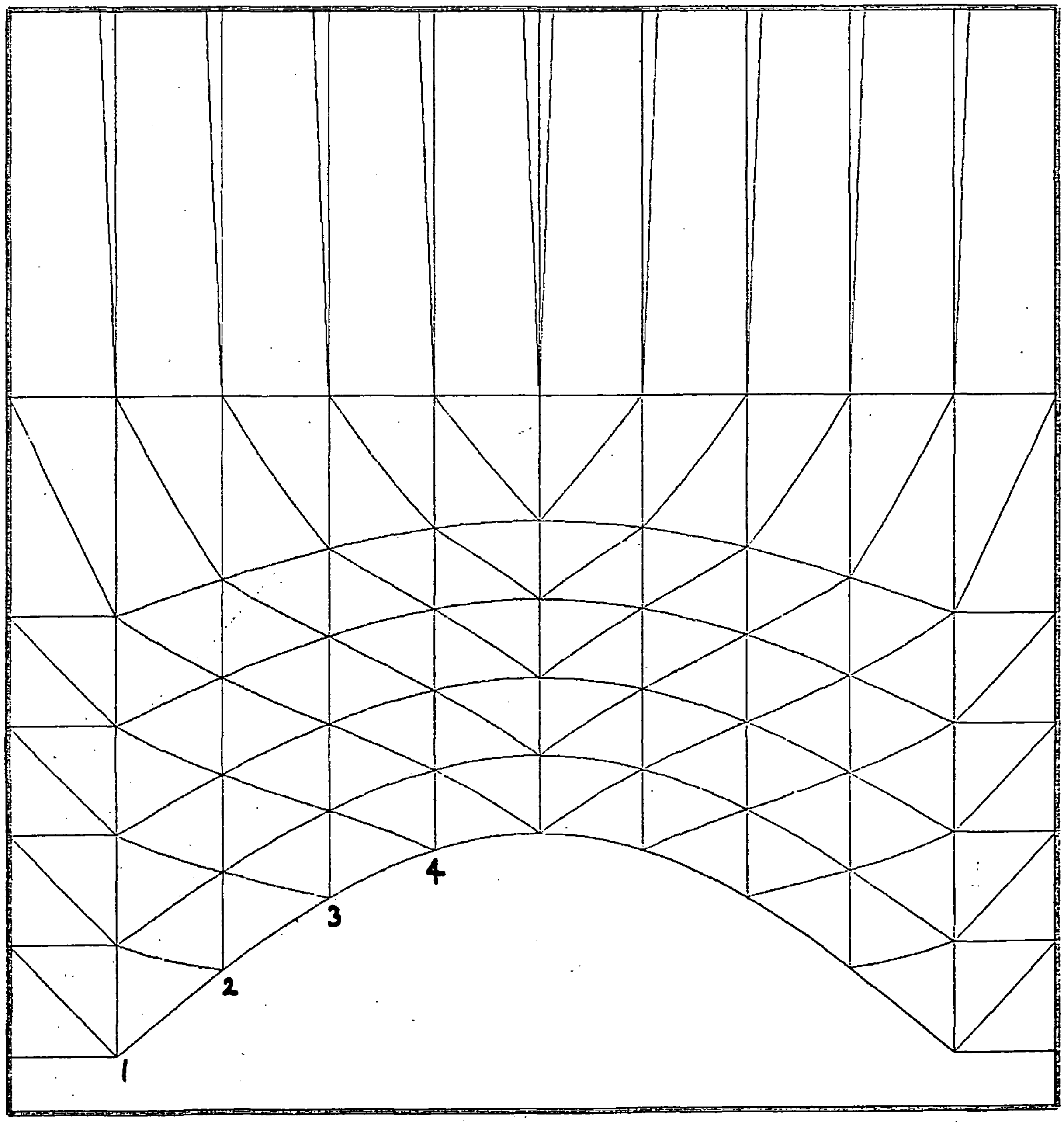

FIGURE 5.4 SCHEMATIC DIAGRAM OF BOUNDARY CONDITIONS FOR PLANE-STRAIN

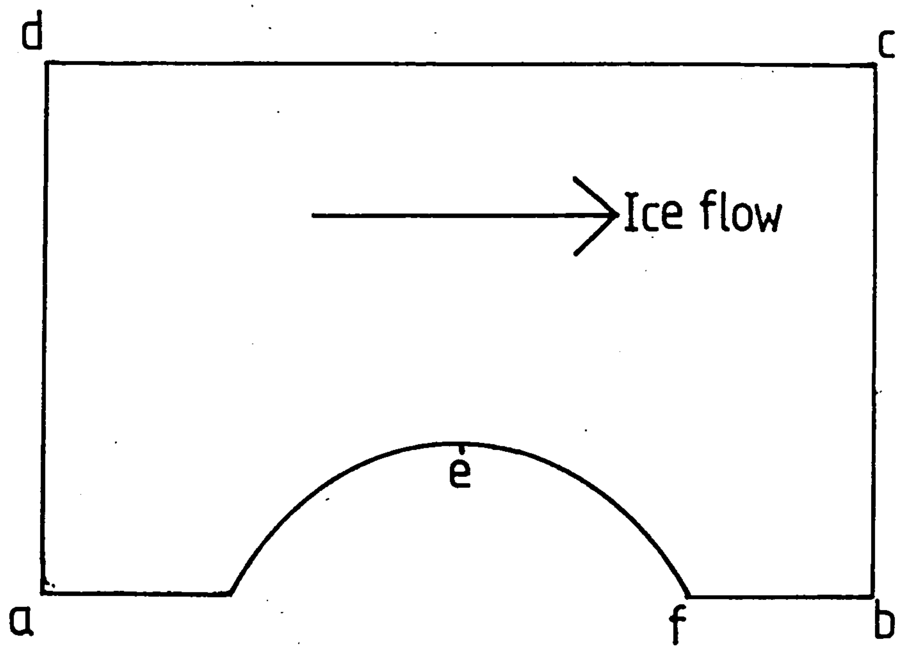

adcb - Tractions at infinity

ab - Zero normal velocity, perfect slip or Weertman; if cavity exists, then tractions along ef

a,b - Slip velocity at infinity

Figure 5.5 Velocity vector plot for an incompressible linear rheology with v_d = 100 alu/a (Case 3).

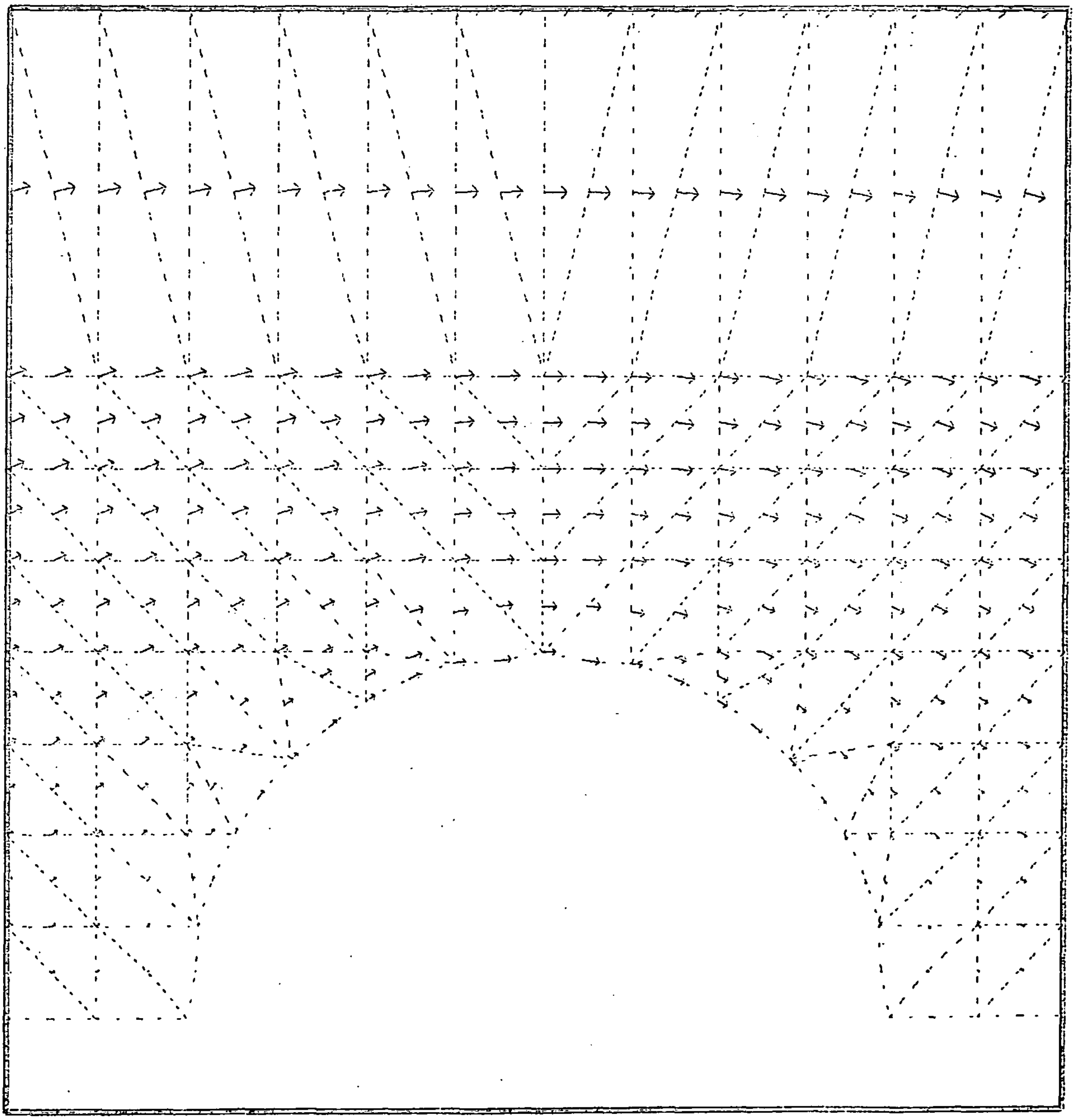

Figure 5.6 Larger view of velocity vector plot for an incompressible linear rheology with v_d = 100 alu/a (Case 3).

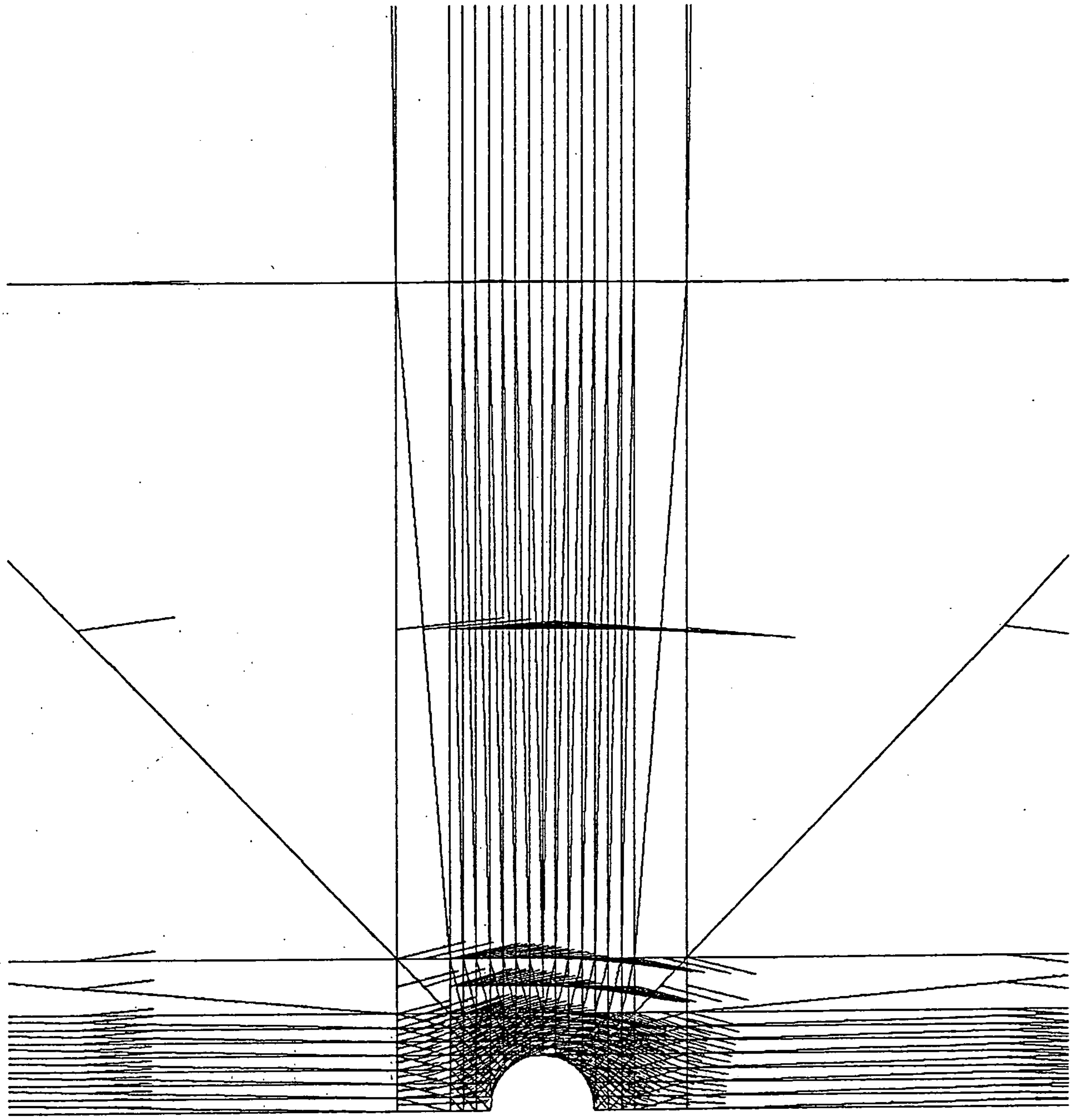

Figure 5.7 v_τ against $\sin\gamma$ for an incompressible linear rheology with v_d = 10 alu/a (Case 1).

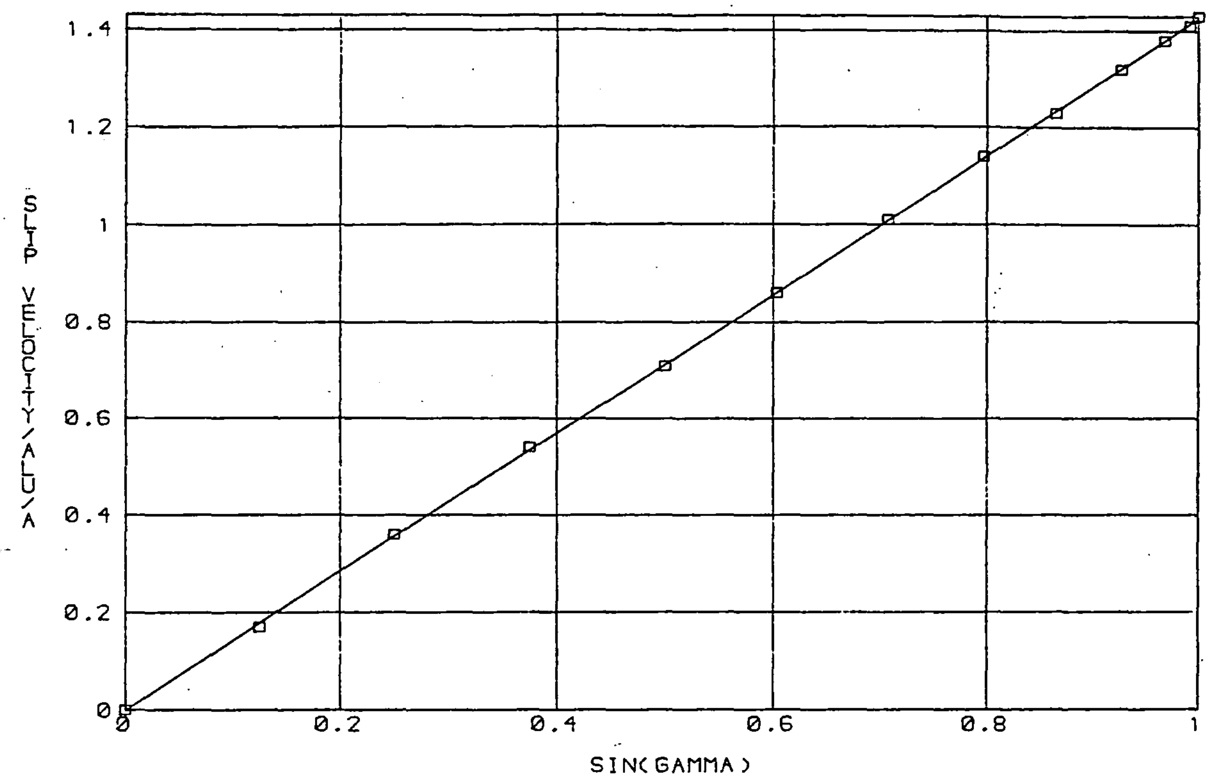

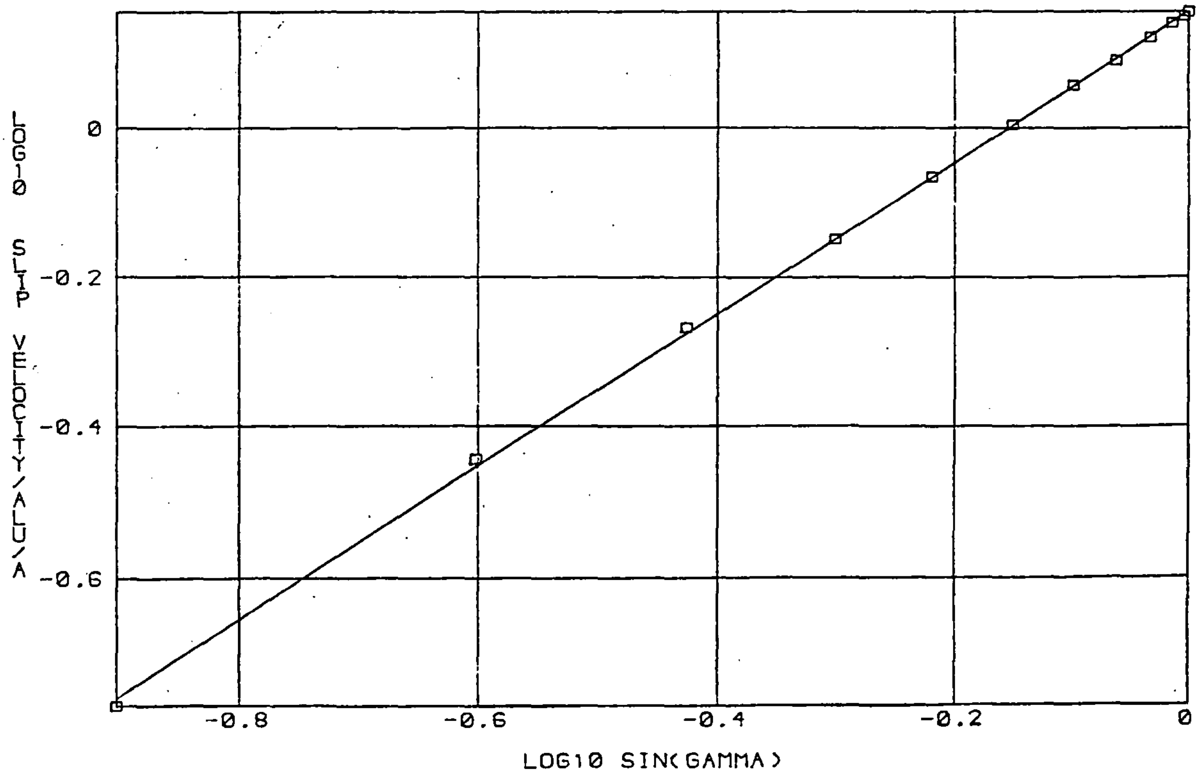

Figure 5.8 v_τ against $\sin\gamma$ for an incompressible linear rheology with a cavity and v_d = 400 alu/a (Case 7).

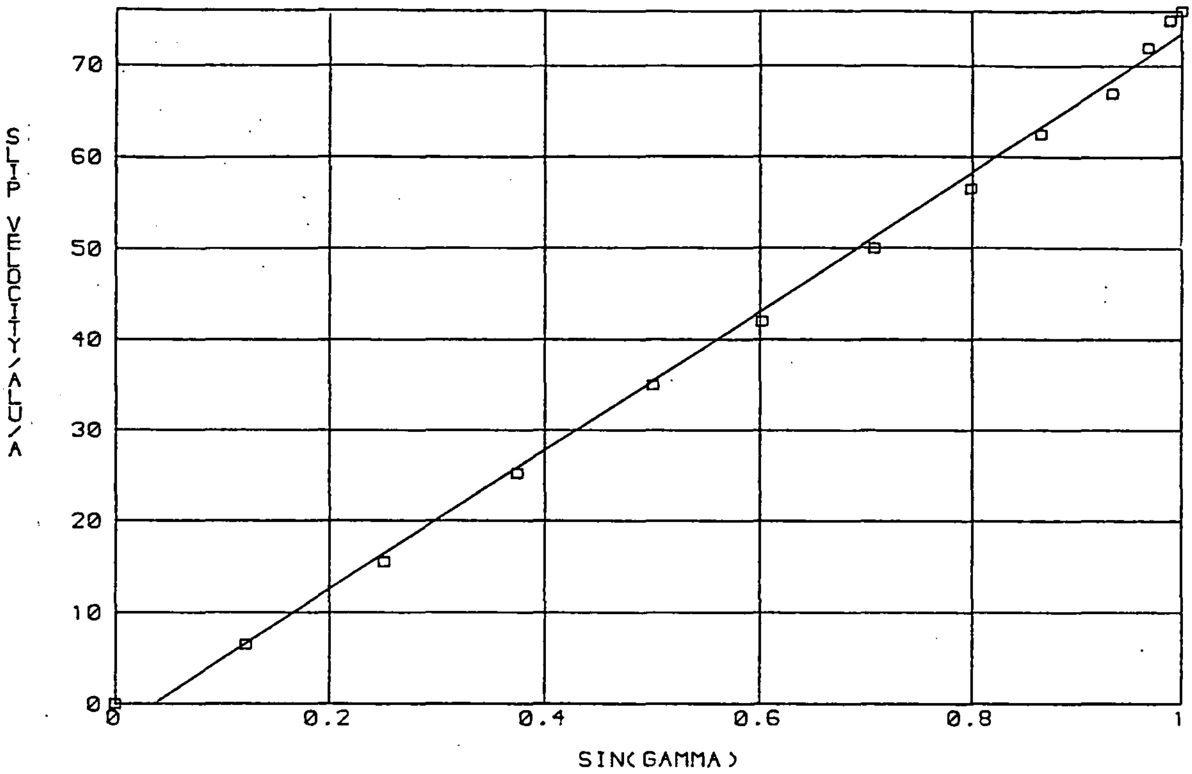

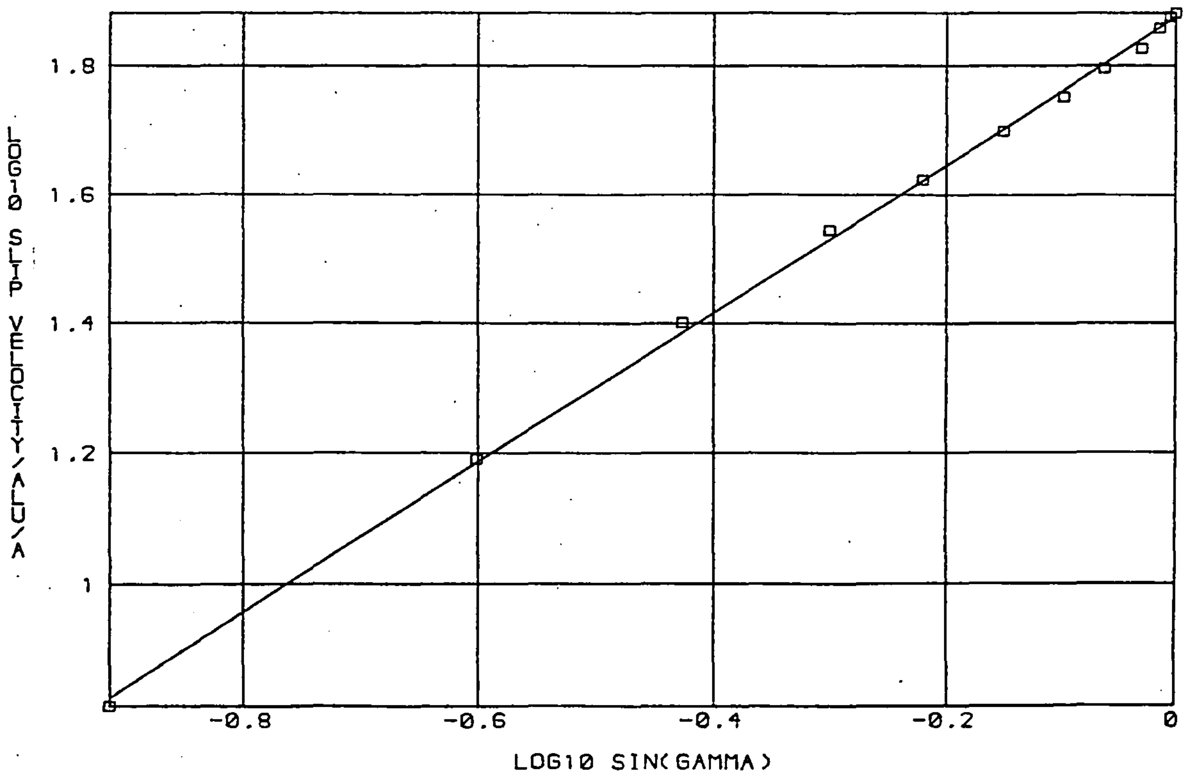

Figure 5.9 v_τ against $\sin\gamma$ for an incompressible linear rheology with a cavity and v_d = 10 alu/a (Case 6).

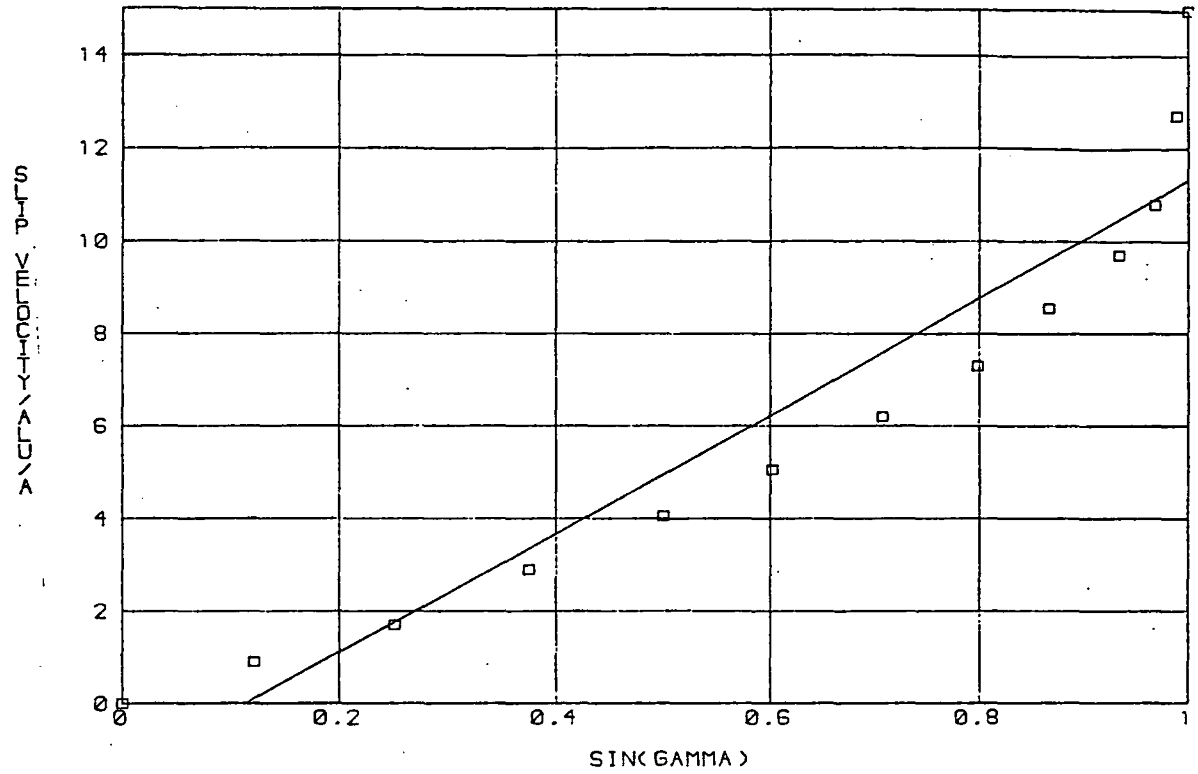

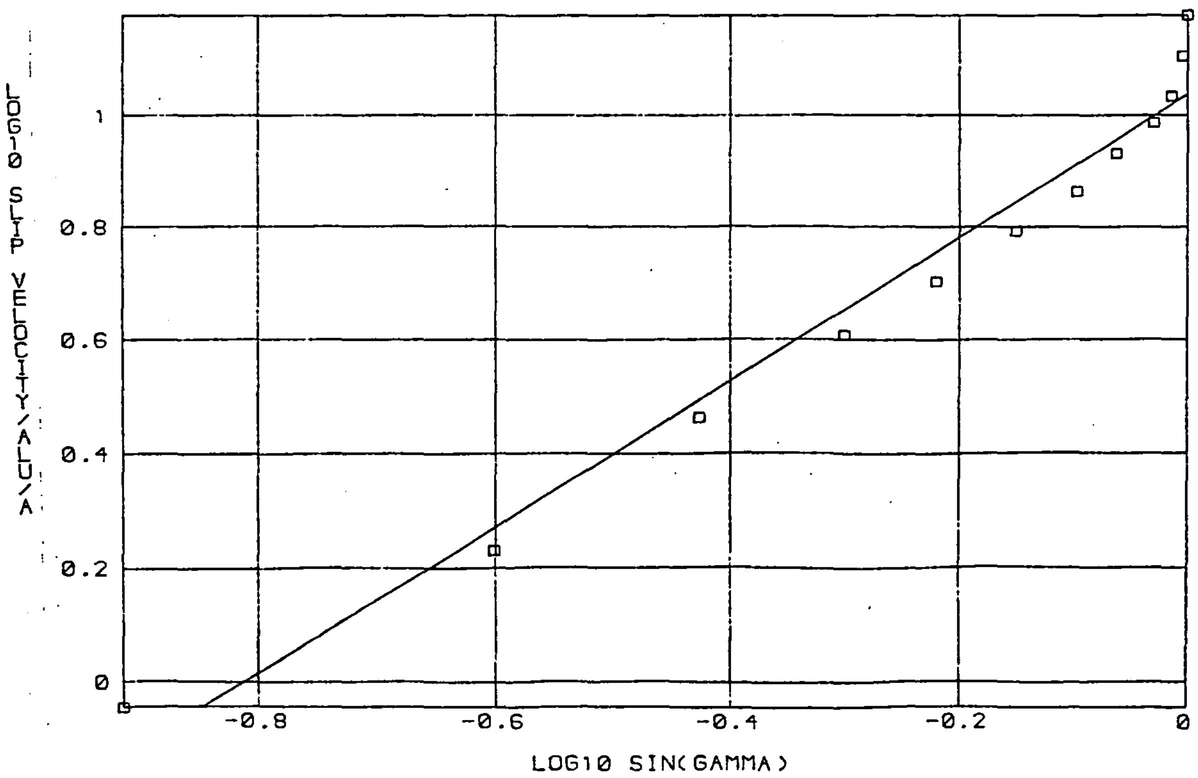

Figure 5.10 v_τ against $\sin\gamma$ for a compressible linear rheology with χ = 1 alu²/bar.a and v_d = 10 alu/a (Case 8).

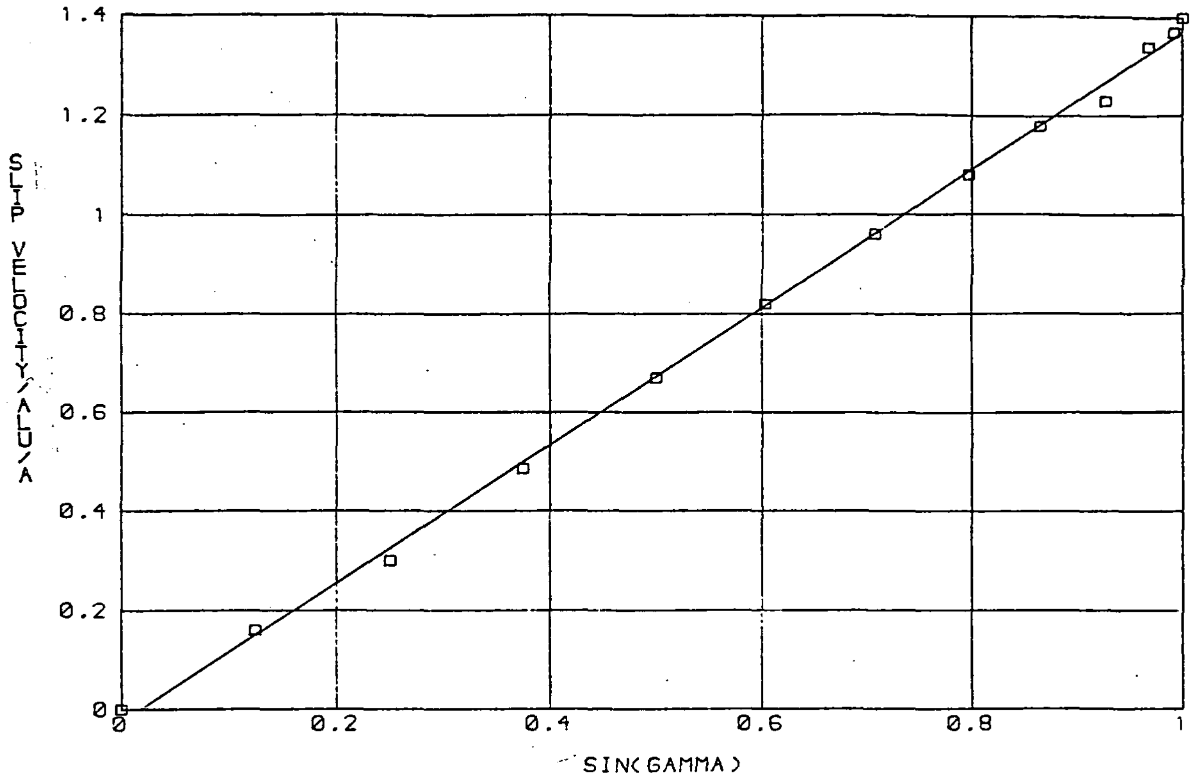

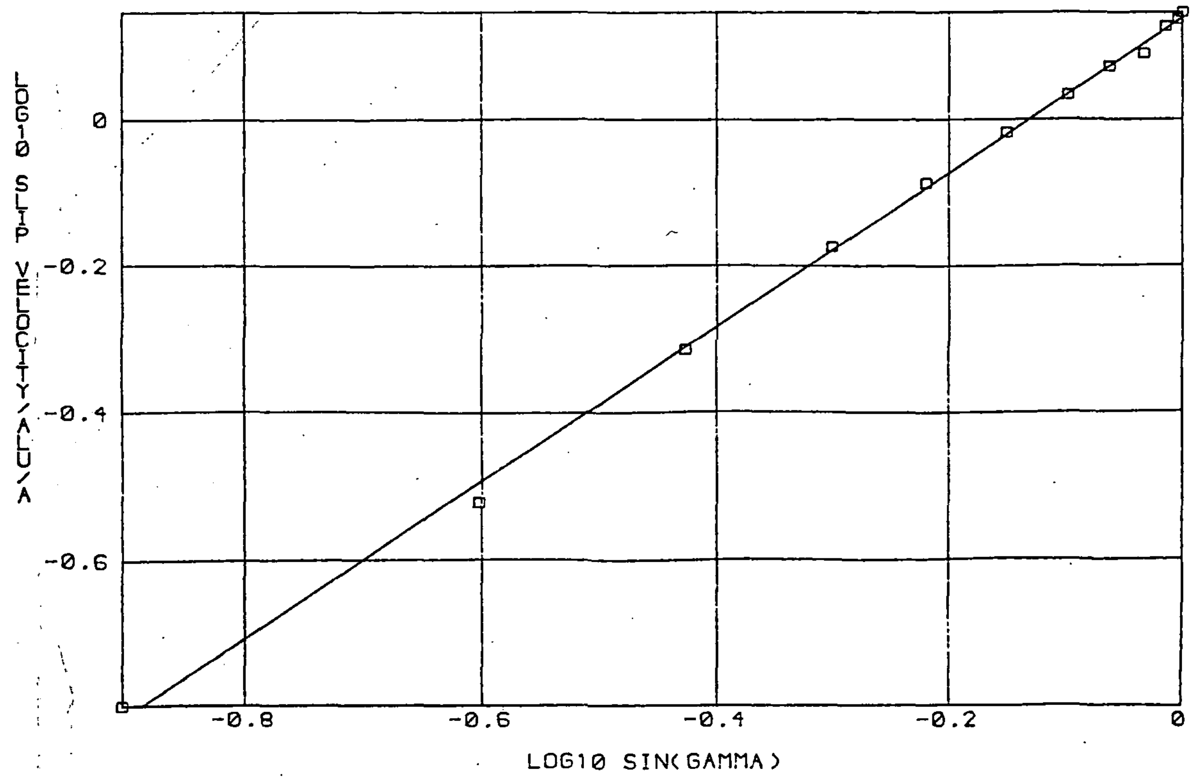

Figure 5.11 Velocity vector plot for a compressible linear rheology with χ = 10 alu²/bar.a and v_d = 200 alu/a (Case 16).

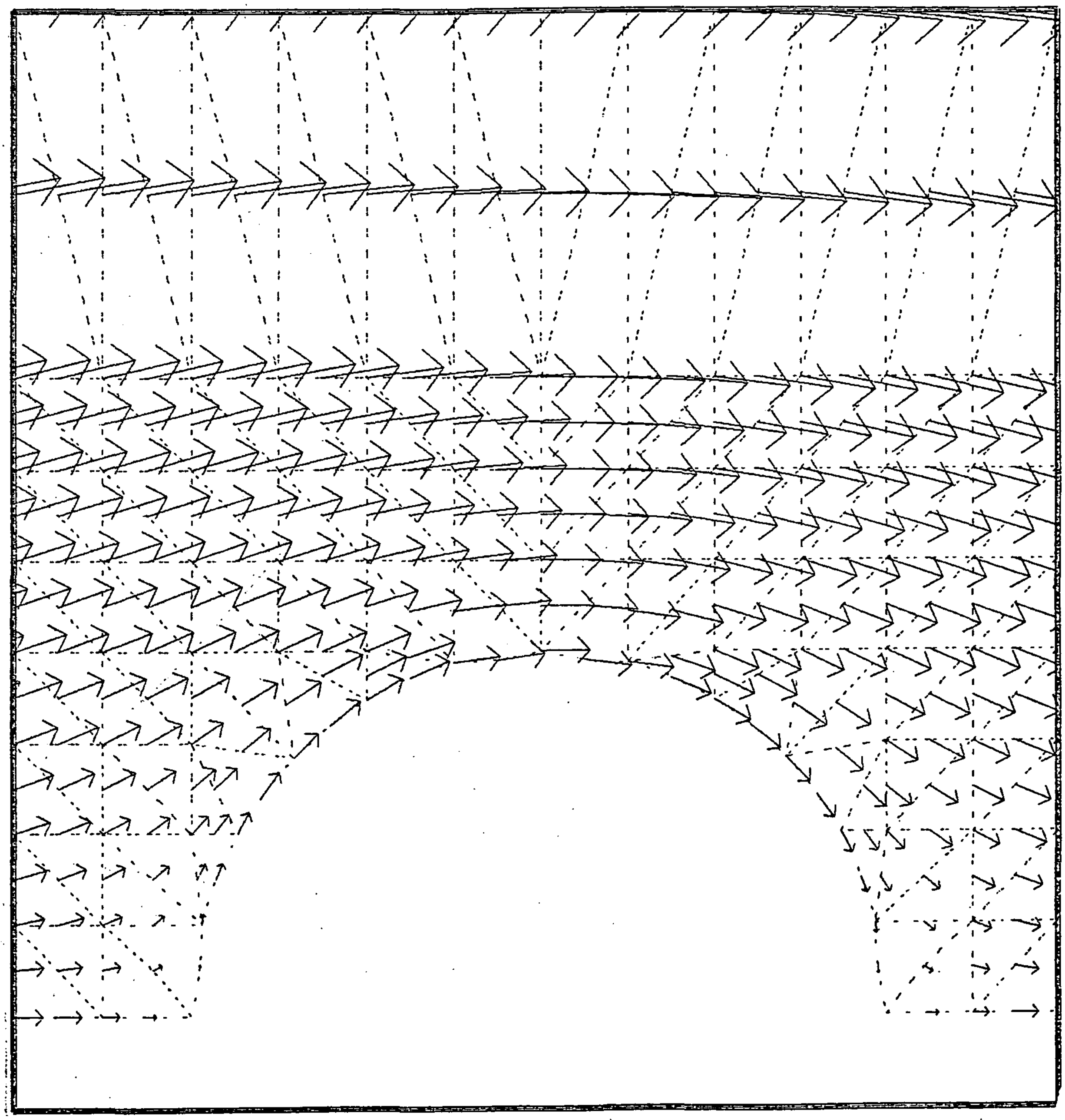

Figure 5.12 v_τ against $\sin\gamma$ for a compressible linear rheology with χ = 10 alu² /bar.a and v_d = 200 alu/a (Case 16).

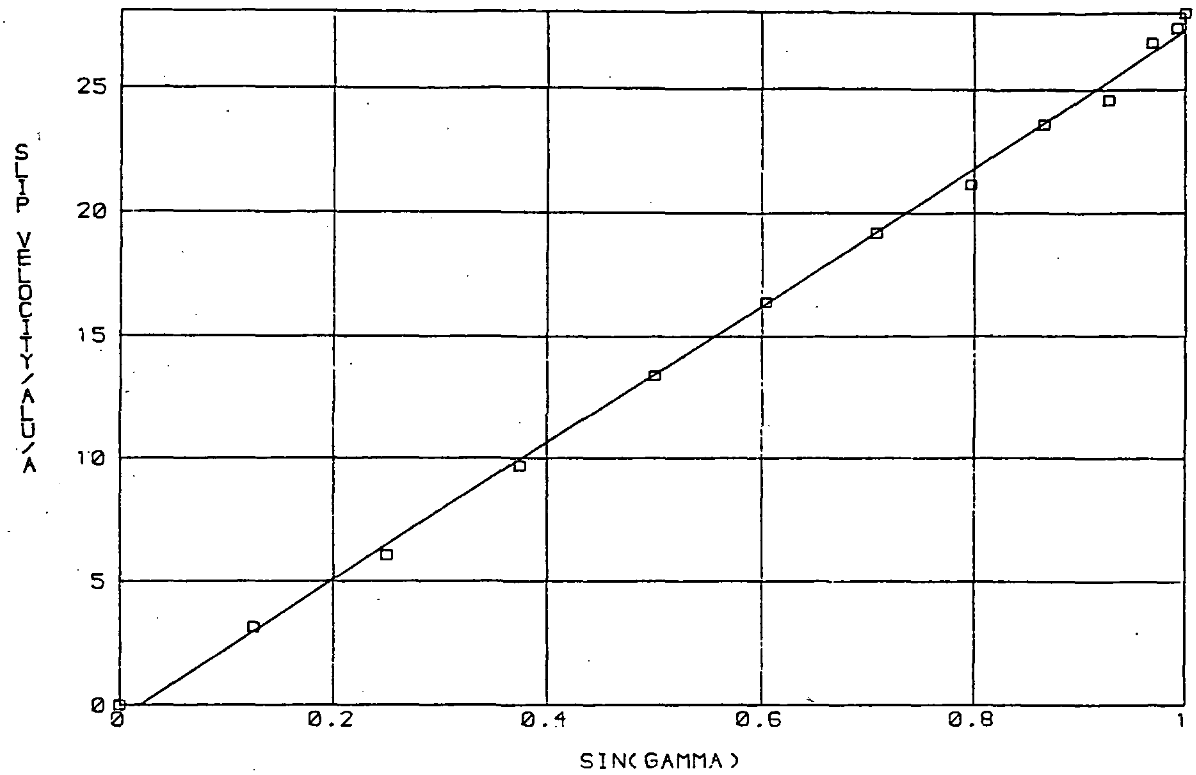

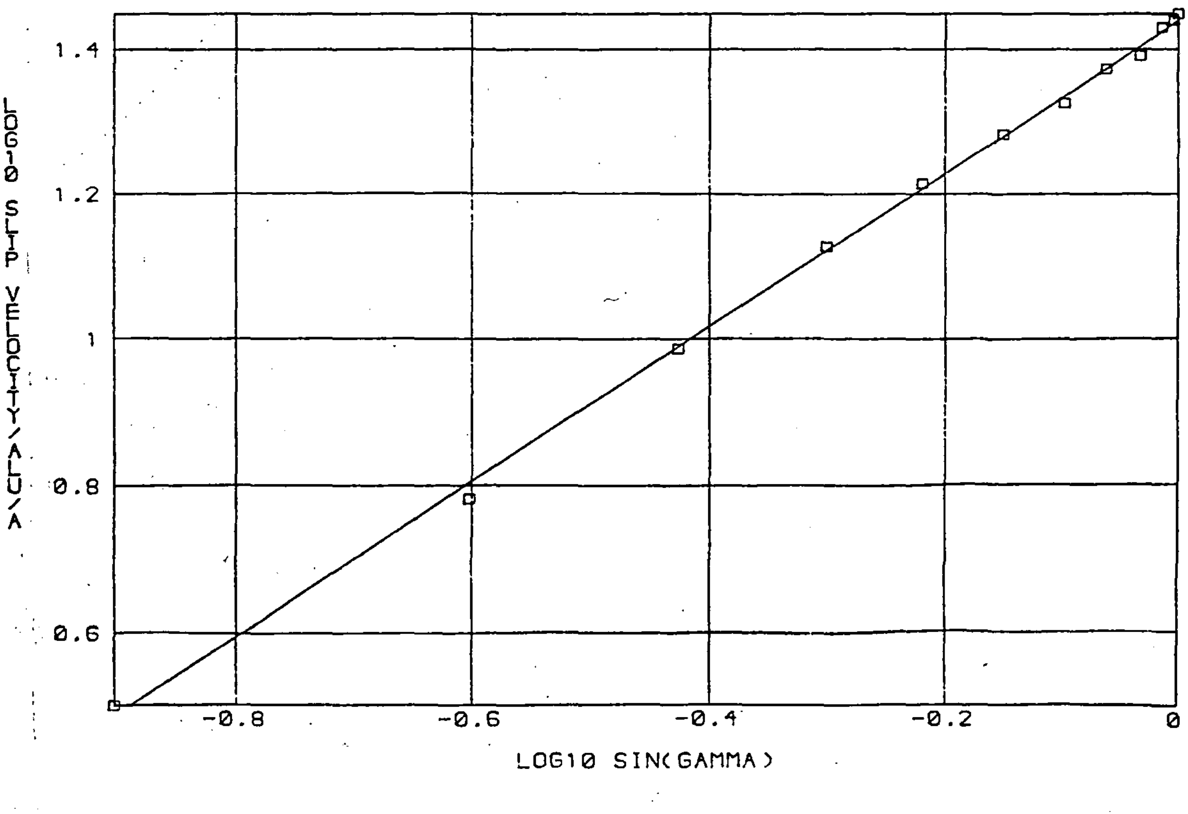

Figure 5.13 Velocity vector plot for an incompressible linear rheology with bed of S = 100 alu/bar.a and v_d = 100 alu/a (Case 20).

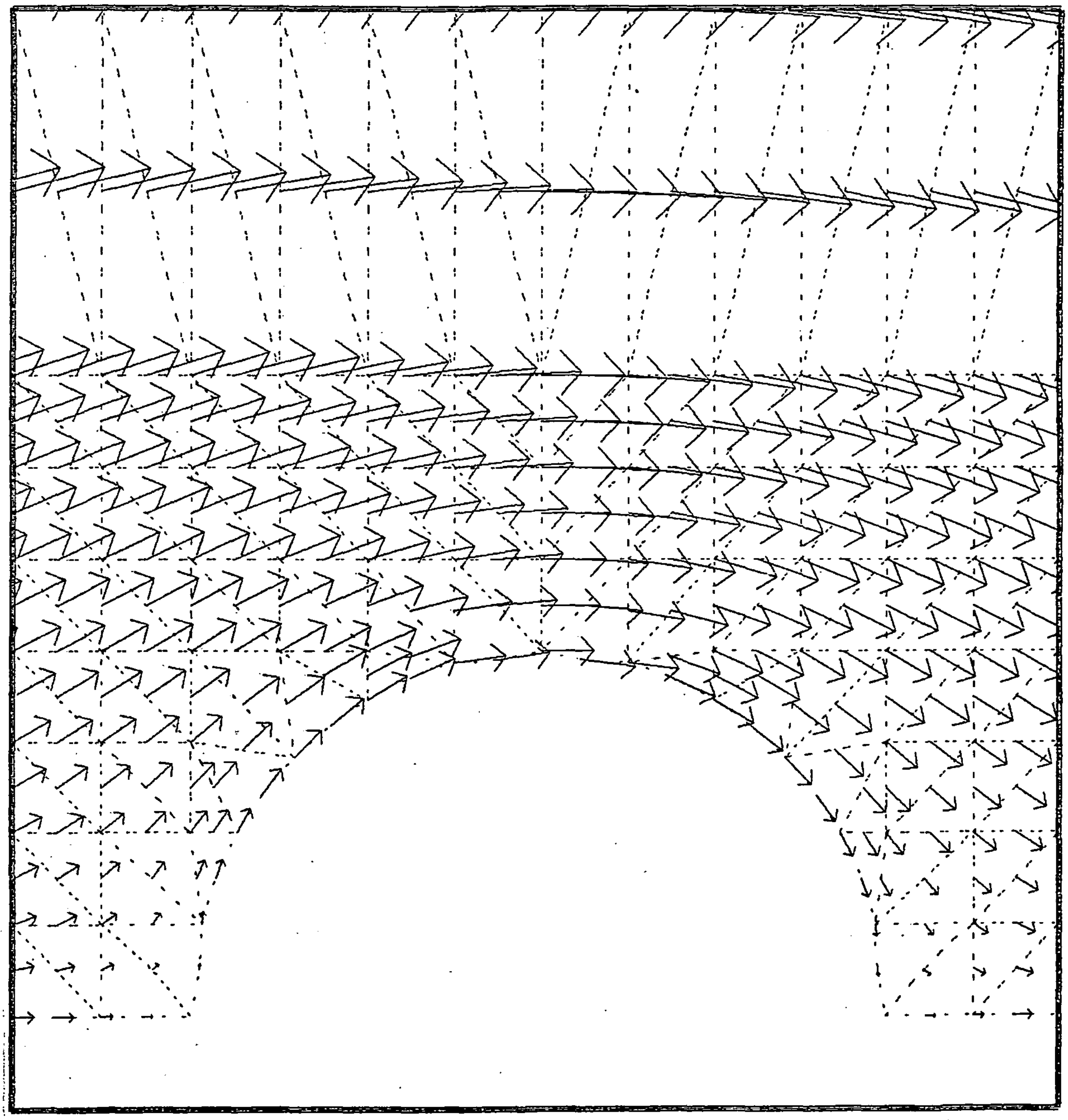

Figure 5.14 v_τ against $\sin\gamma$ for an incompressible linear rheology with bed of $S = 10$ alu/bar.a, $v_d = 10$ alu/a (Case 18)

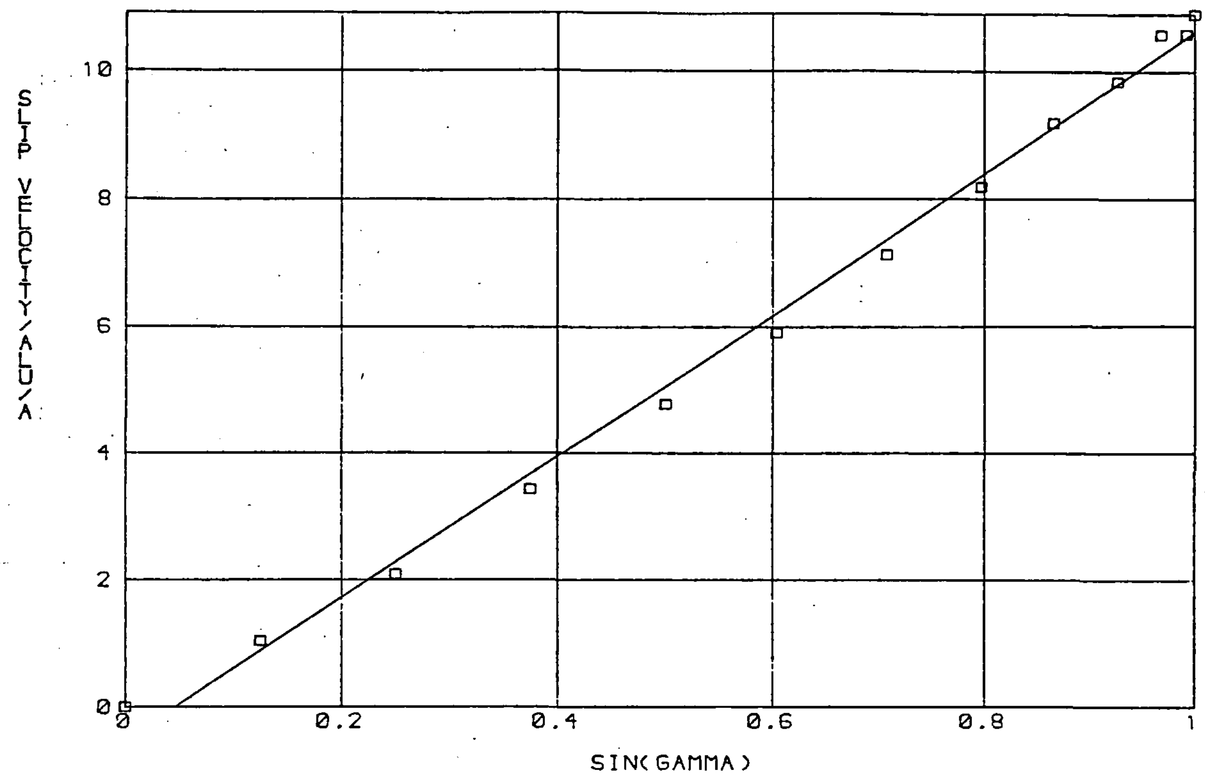

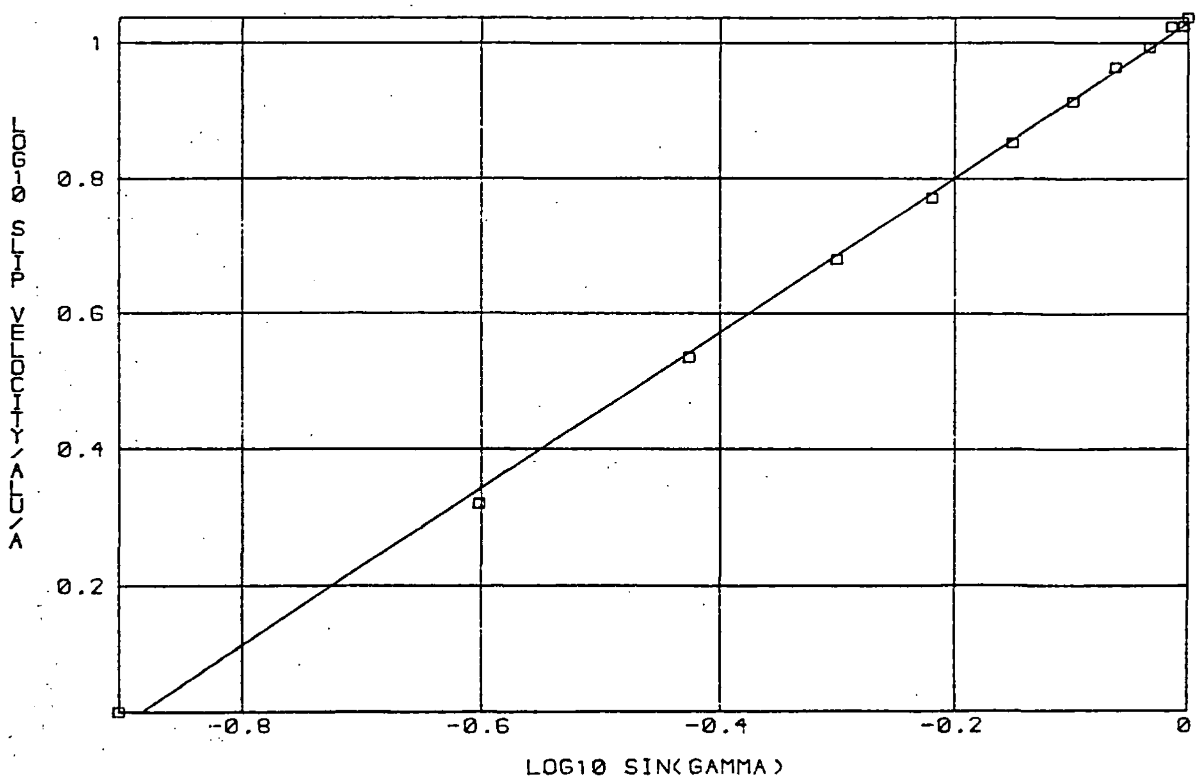

Figure 5.15 v_τ against $\sin\gamma$ for an incompressible linear rheology with bed of S = 400 alu/bar.a, v_d = 400 alu/a (Case 22).

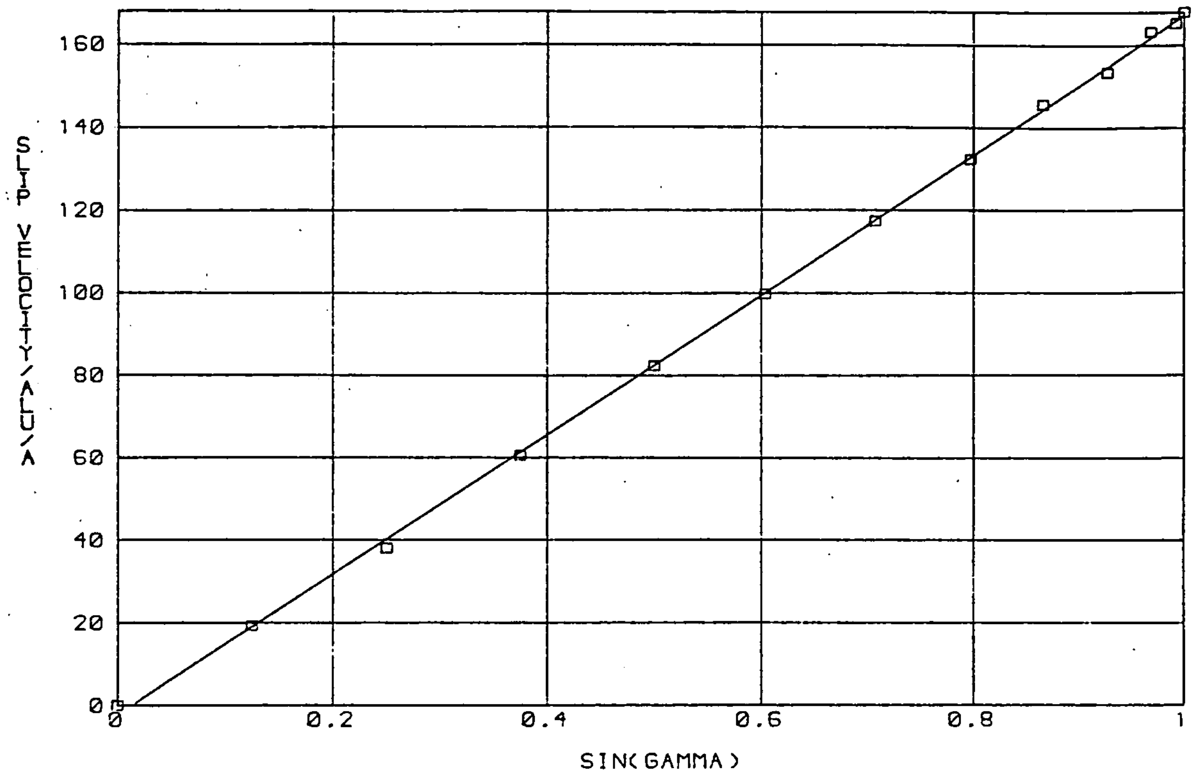

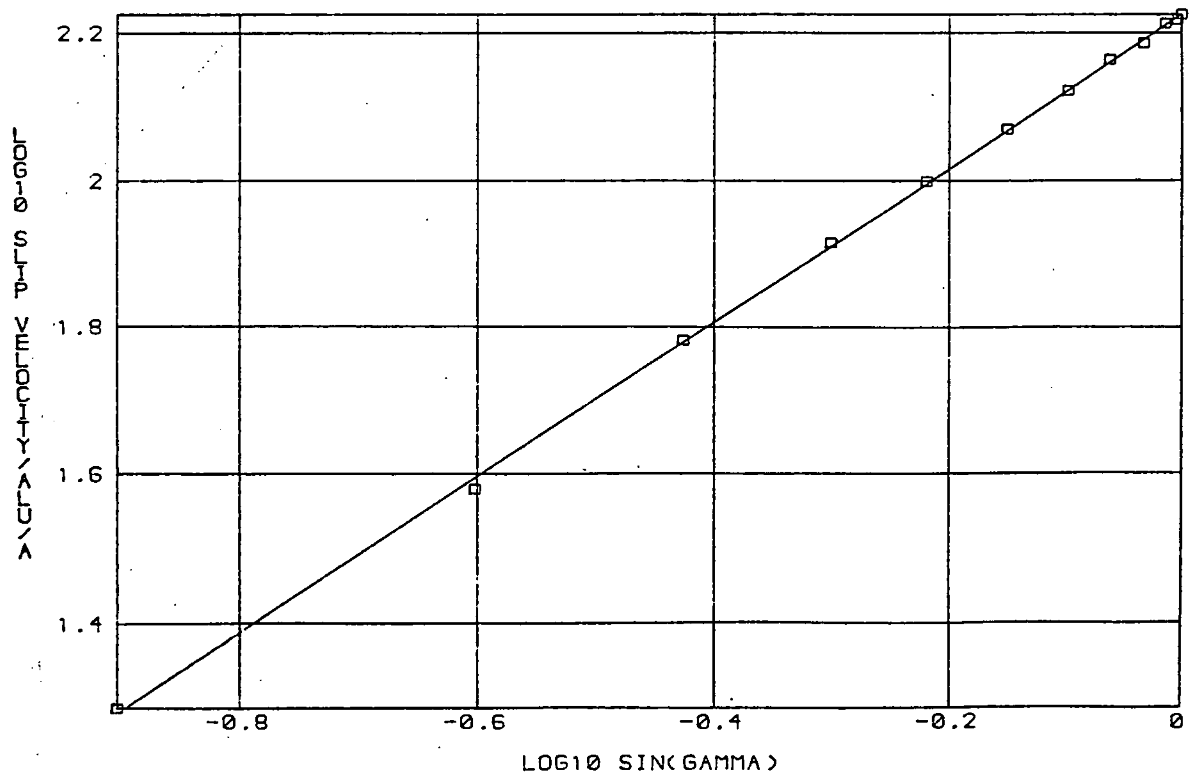

Figure 5.16 Velocity vector plot for an incompressible Glen rheology with v_d = 100 alu/a (Case 25).

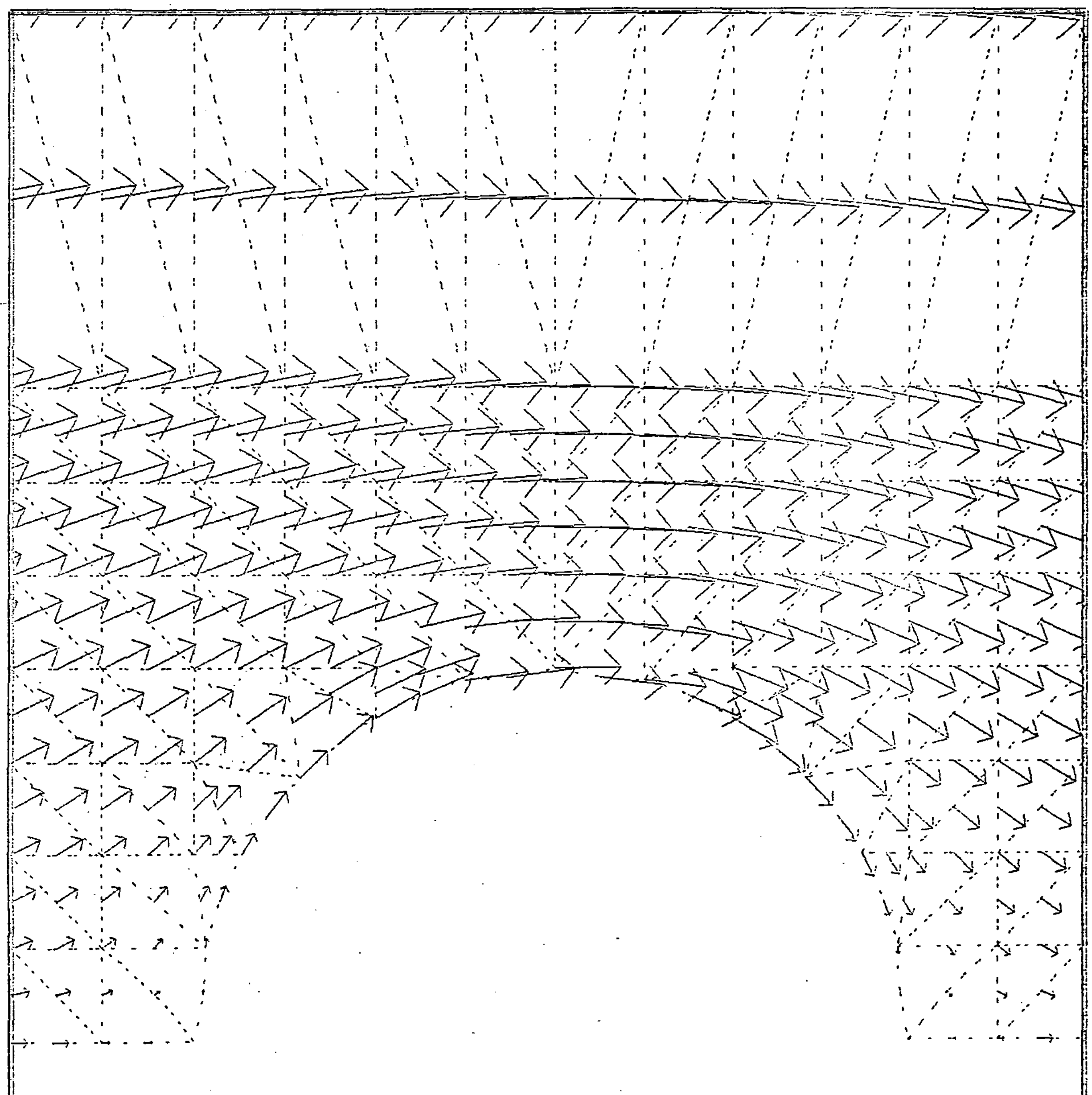

Figure 5.17 v_τ against $\sin\gamma$ for an incompressible Glen rheology with v_d = 10 alu/a (Case 23).

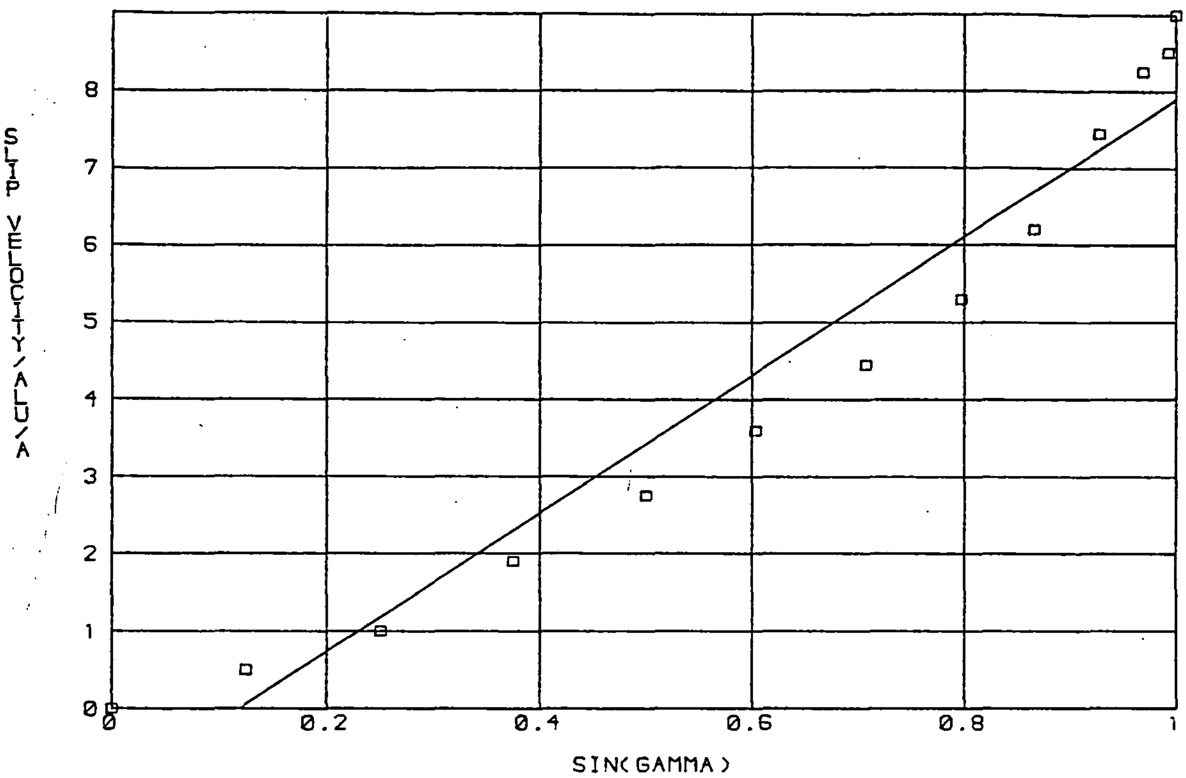

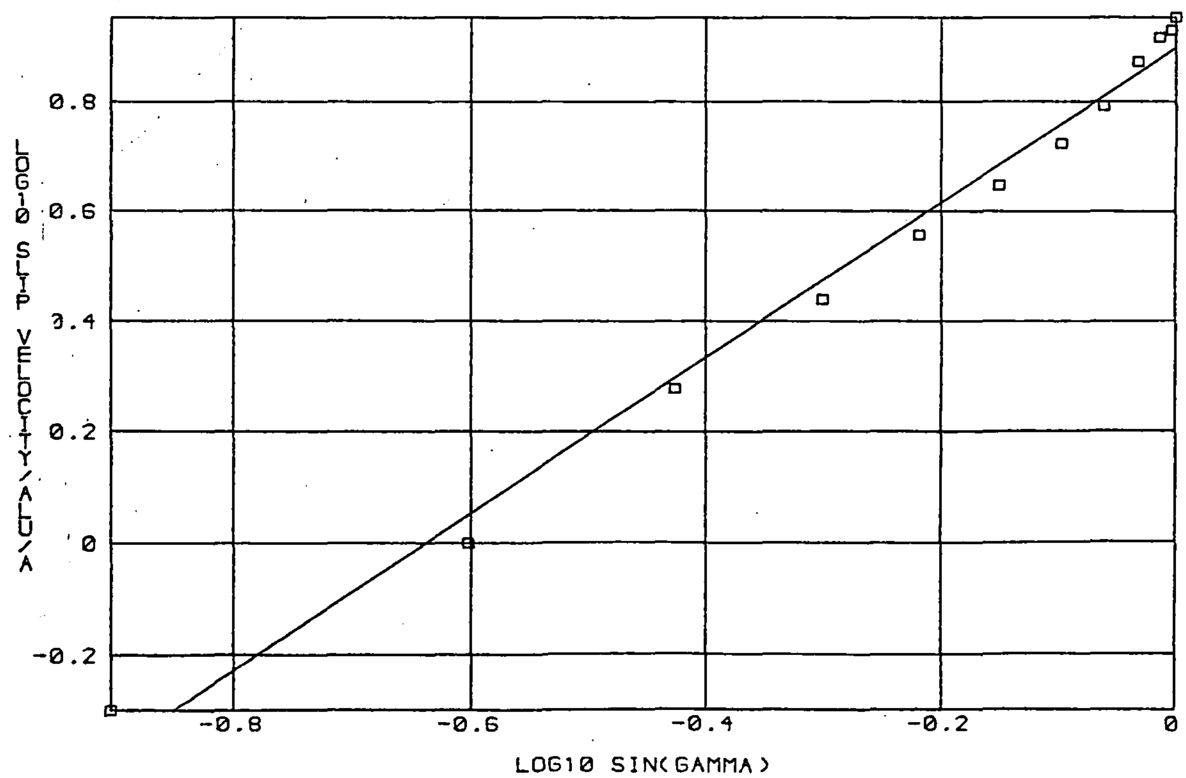

Figure 5.18 v_τ against $\sin\gamma$ for an incompressible Glen rheology with v_d = 400 alu/a (Case 25).

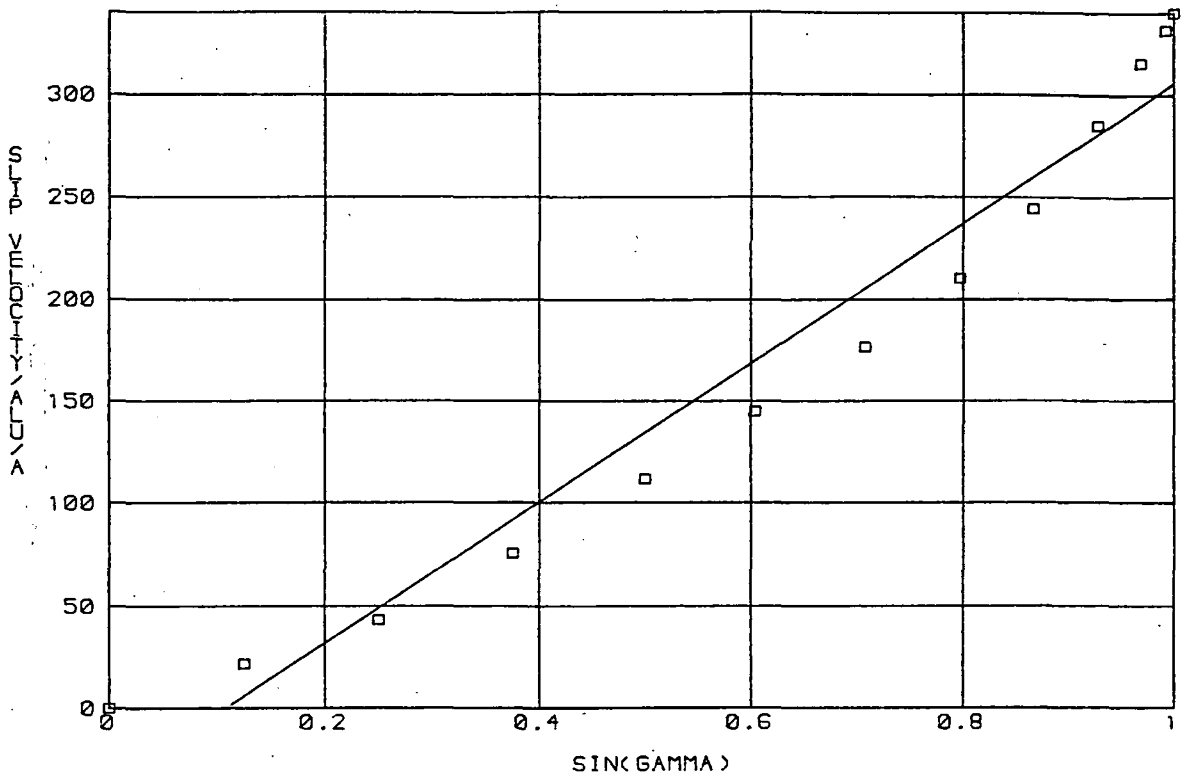

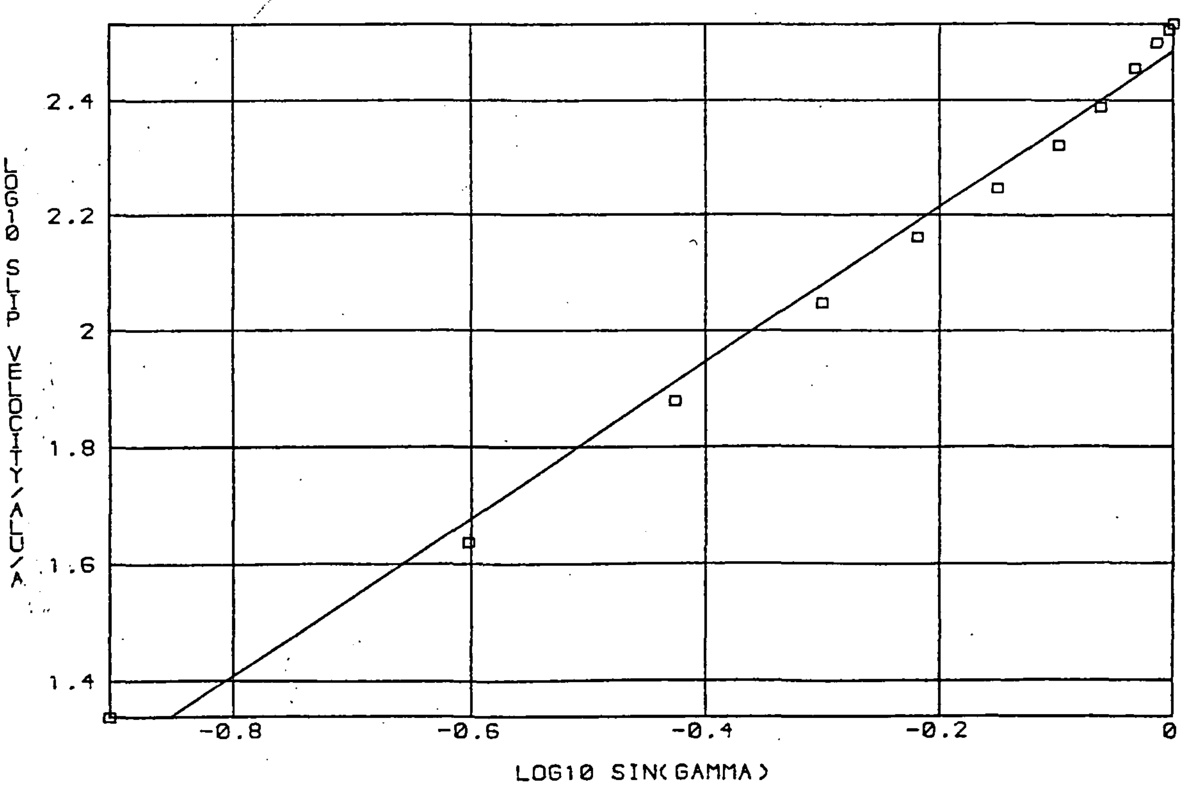

Figure 5.19 Velocity vector plot for an incompressible Glen rheology with a cavity and v_d = 400 alu/a (Case 28).

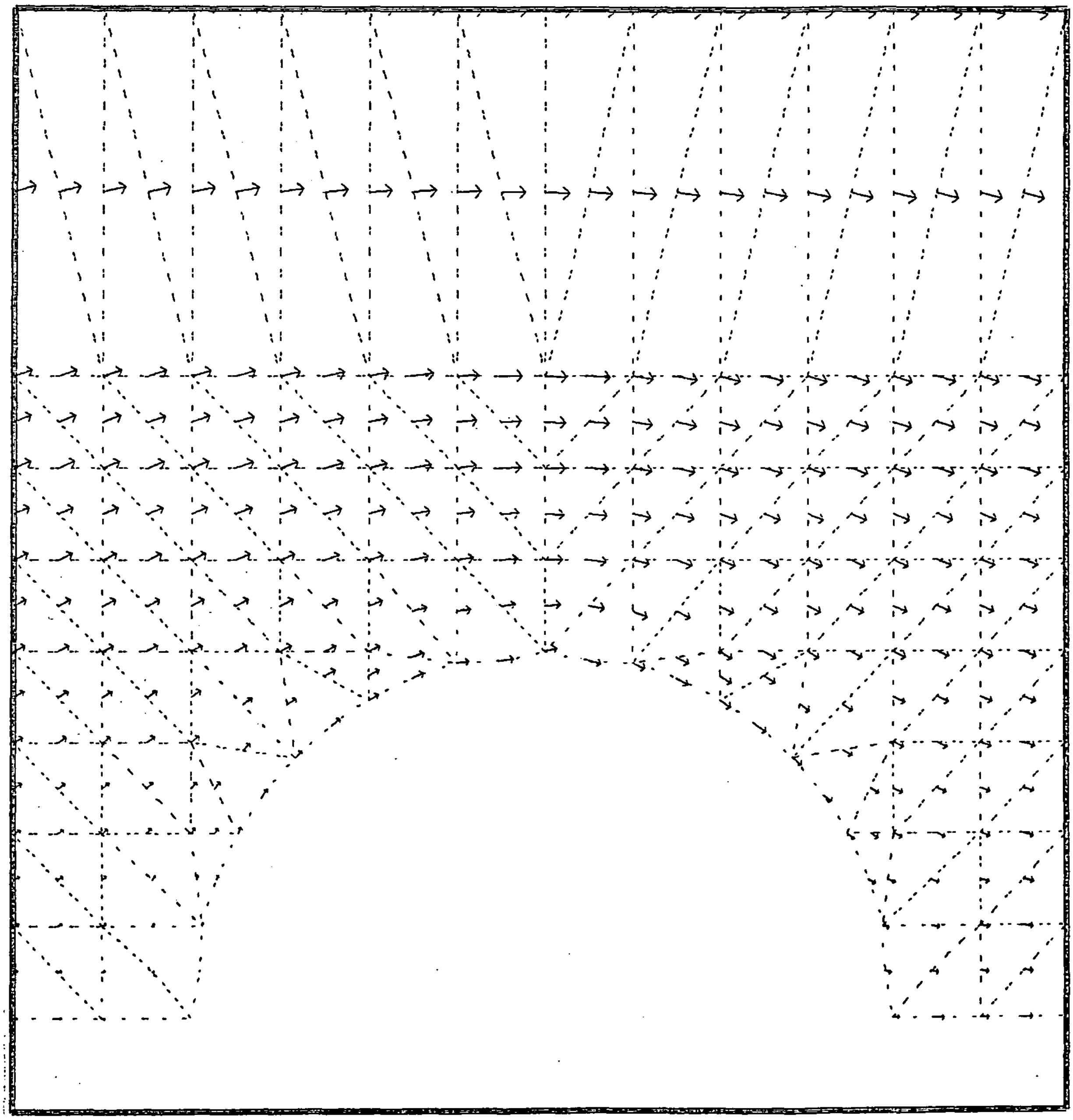

Figure 5.20 v_τ against $\sin\gamma$ for an incompressible Glen rheology with a cavity and v_d = 400 alu/a (Case 28).

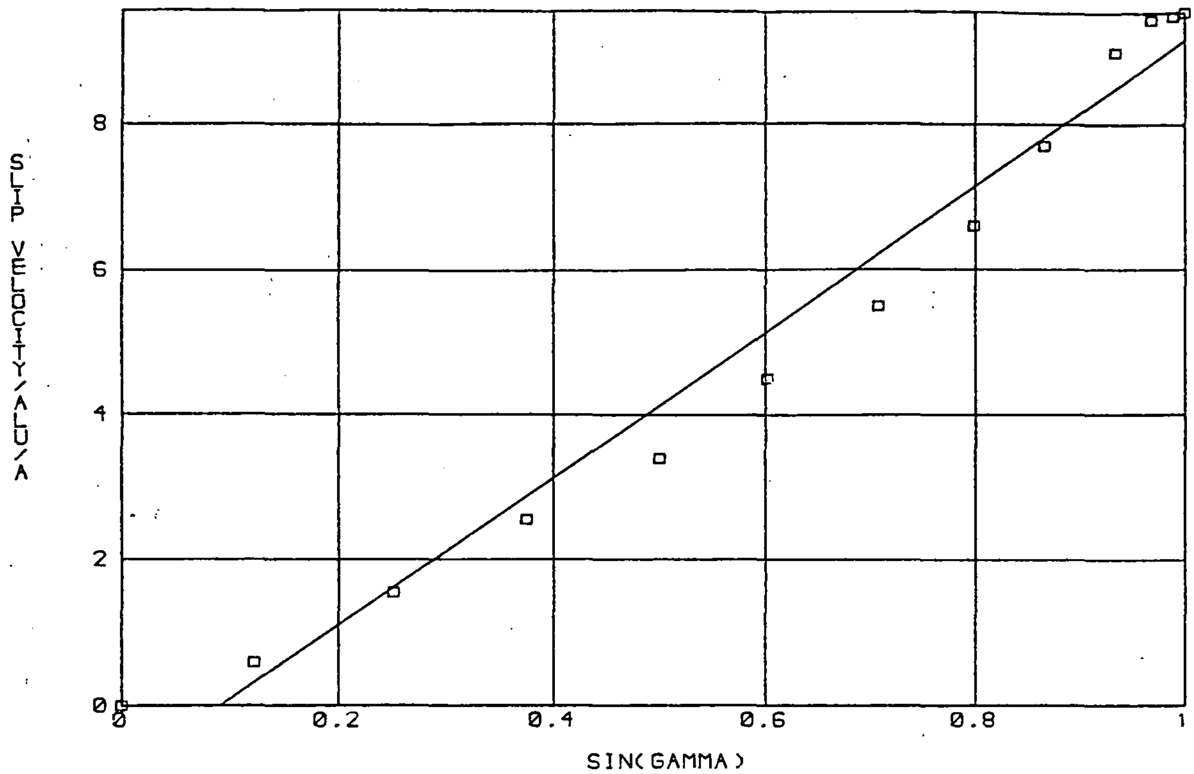

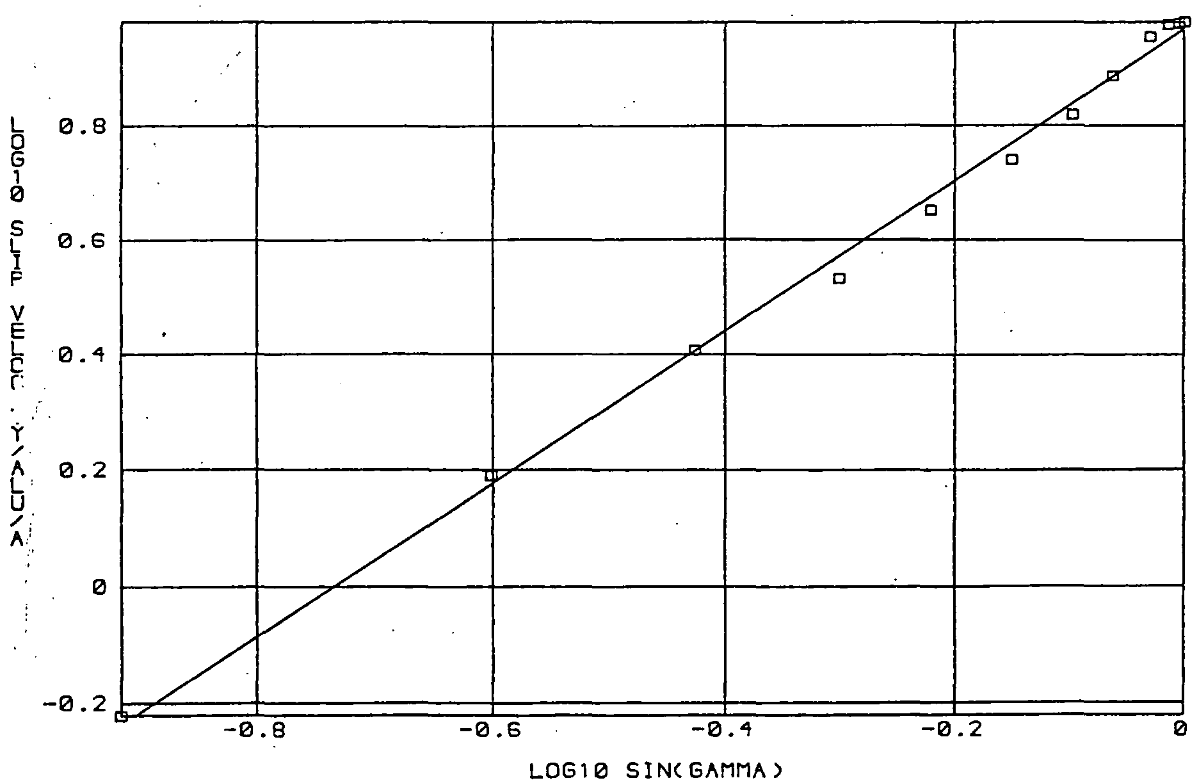

Figure 5.21 Velocity vector plot for a compressible Glen rheology with χ = 1 alu²/bar.a and v_d = 100 alu/a (Case 31).

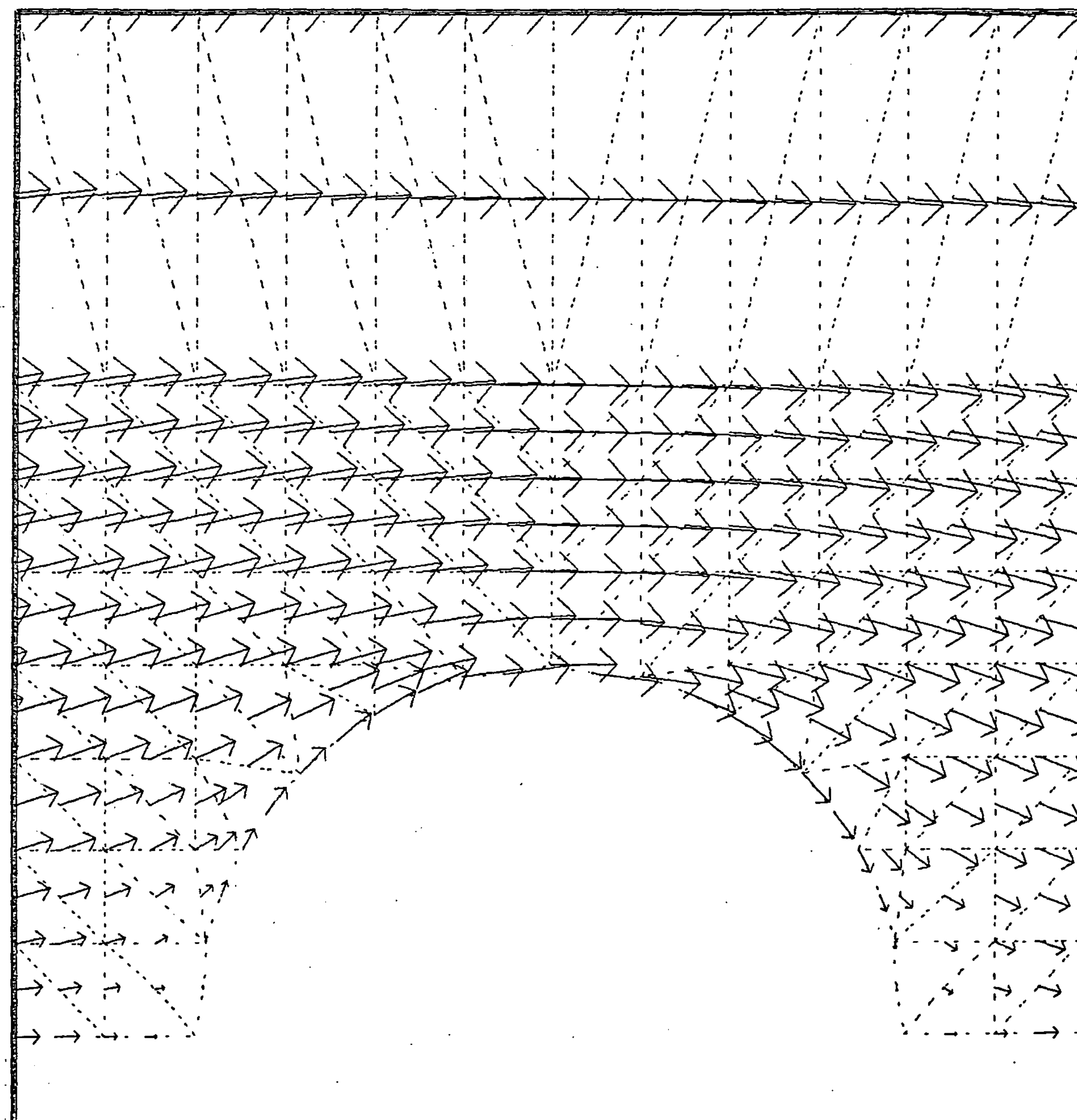

Figure 5.22 v_τ against $\sin\gamma$ for a compressible Glen rheology with χ = 1 alu²/bar.a and v_d = 200 alu/a (Case 32).

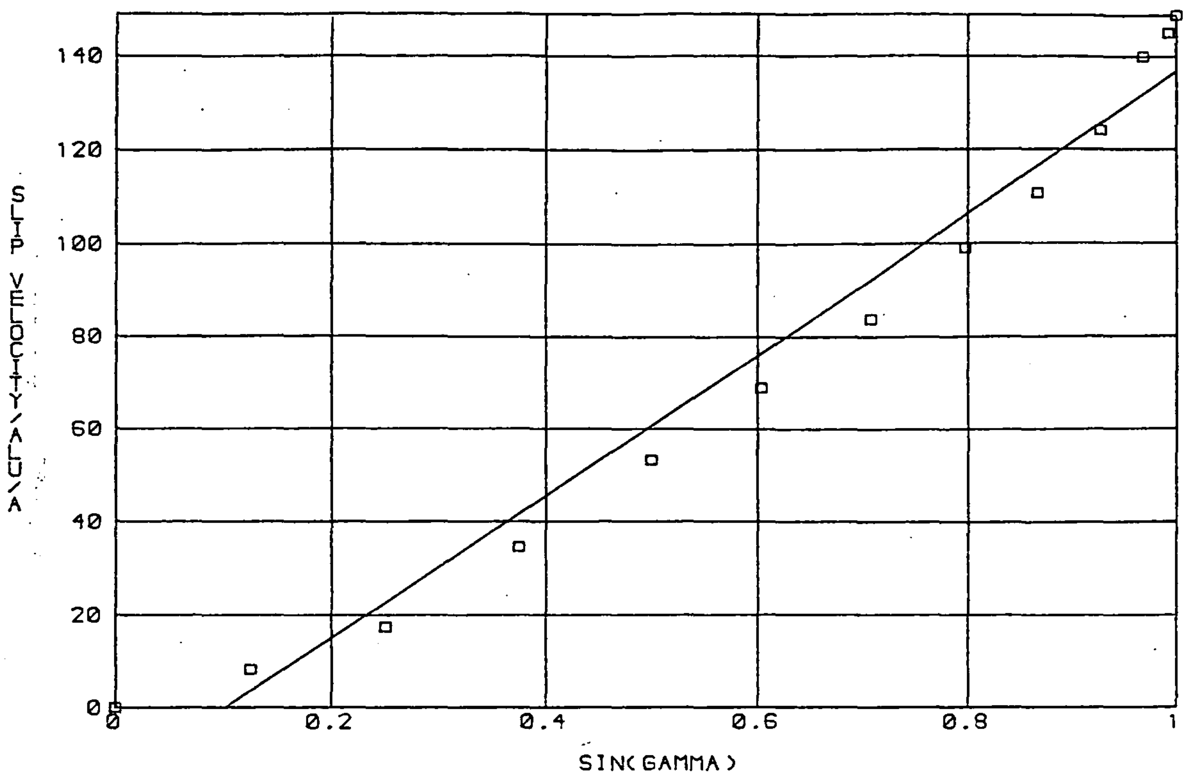

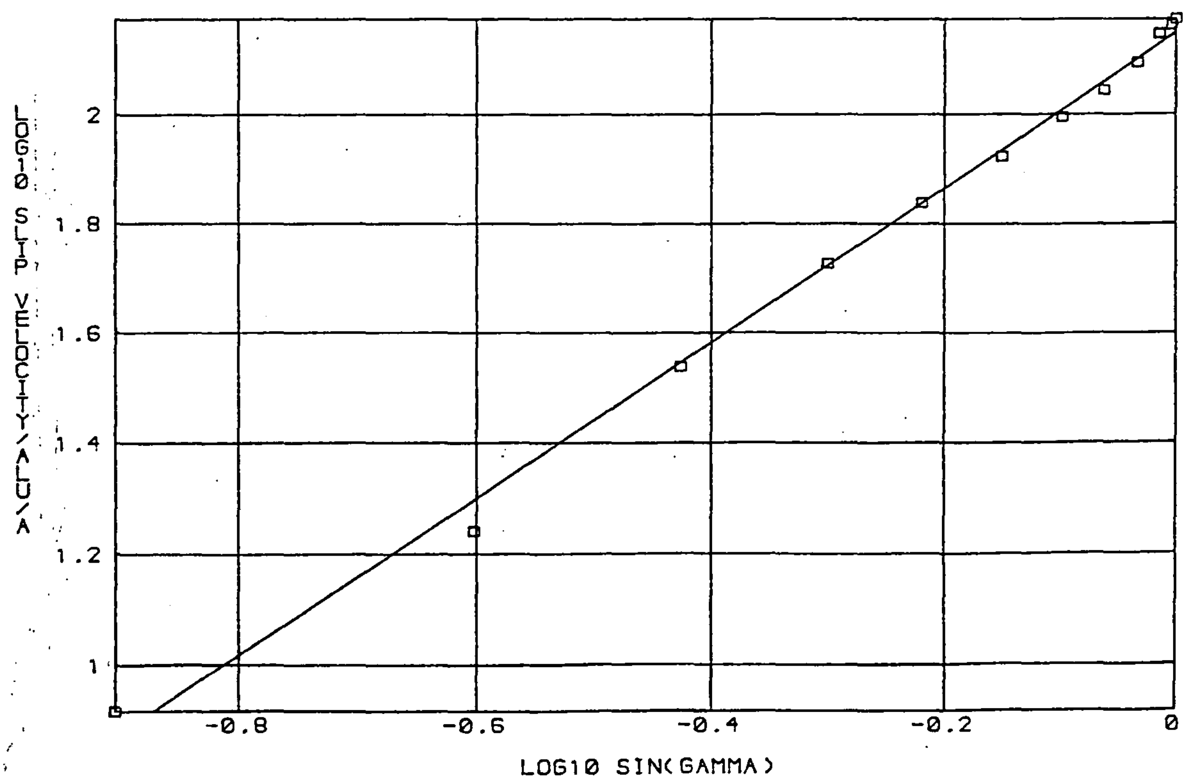

Figure 5.23 v_τ against $\sin\gamma$ for an incompressible Glen rheology with bed $S = 10$ alu/bar.a and $v_d = 10$ alu/a (Case 34).

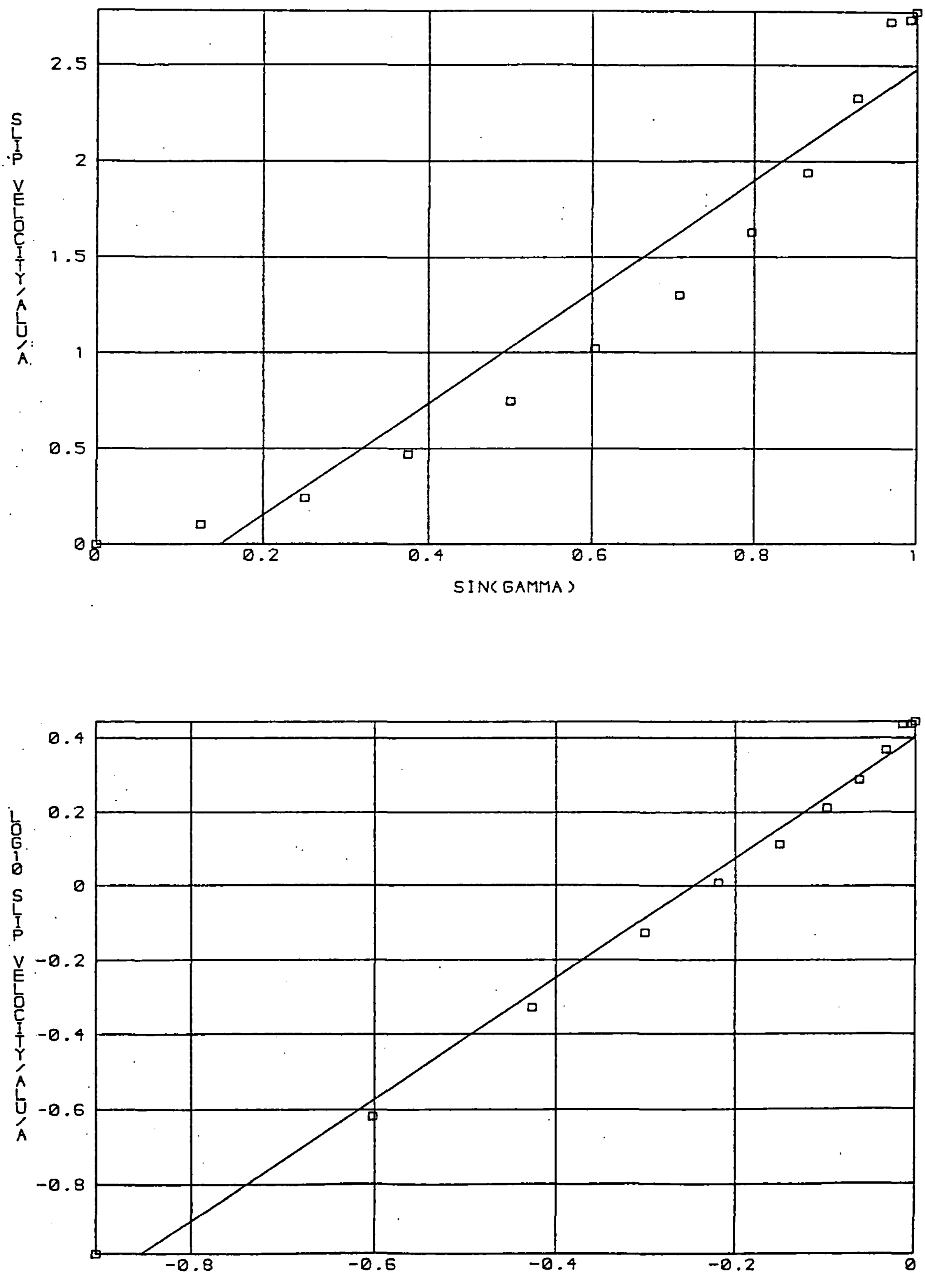

Figure 5.24 Velocity vector plot for an incompressible Glen rheology over a truncated sine ridge with v_d = 100 alu/a (Case 47).

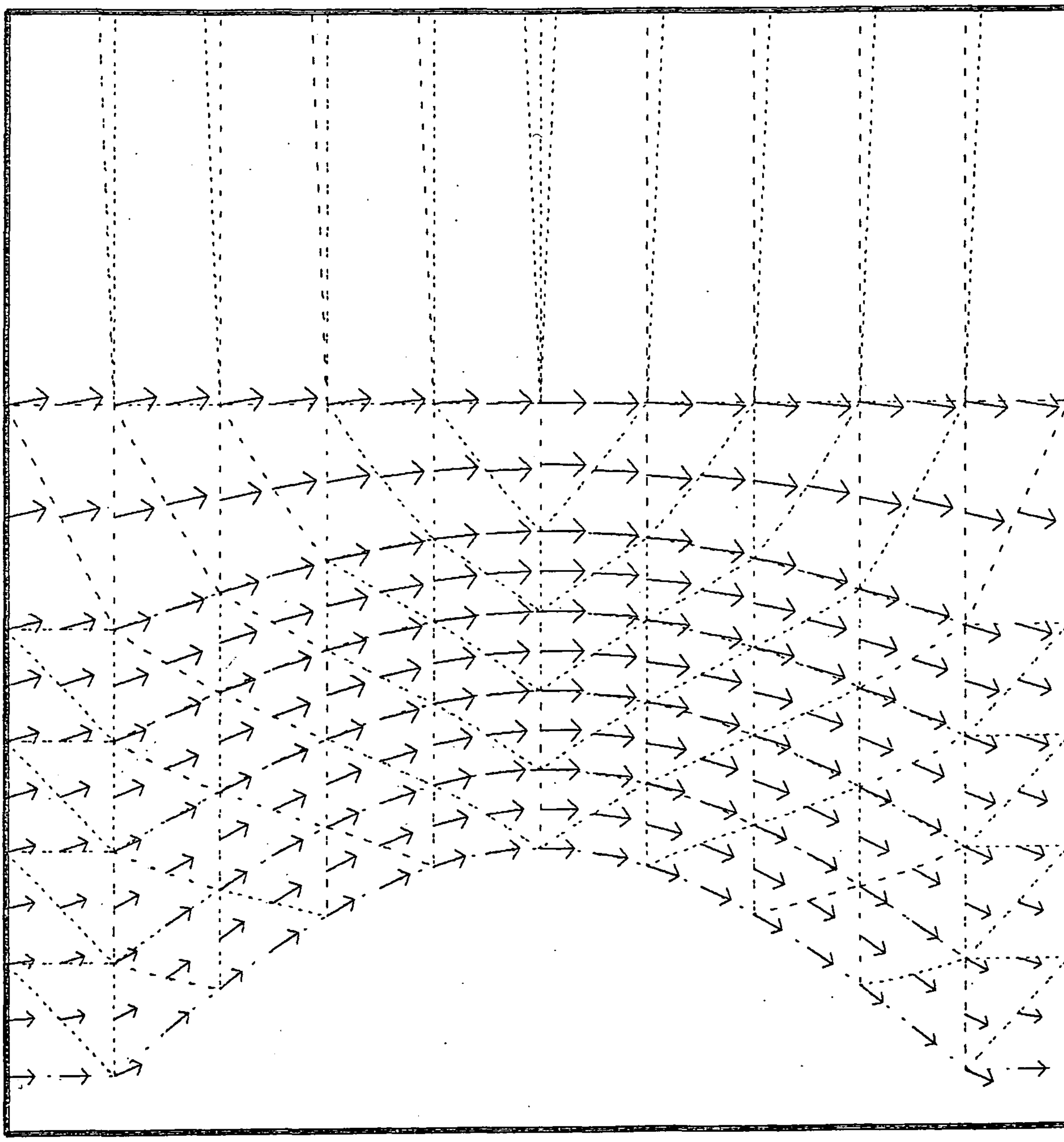

Figure 5.25 v_τ against position for flow over a truncated sine ridge (Cases 40 - 49): Glen rheology

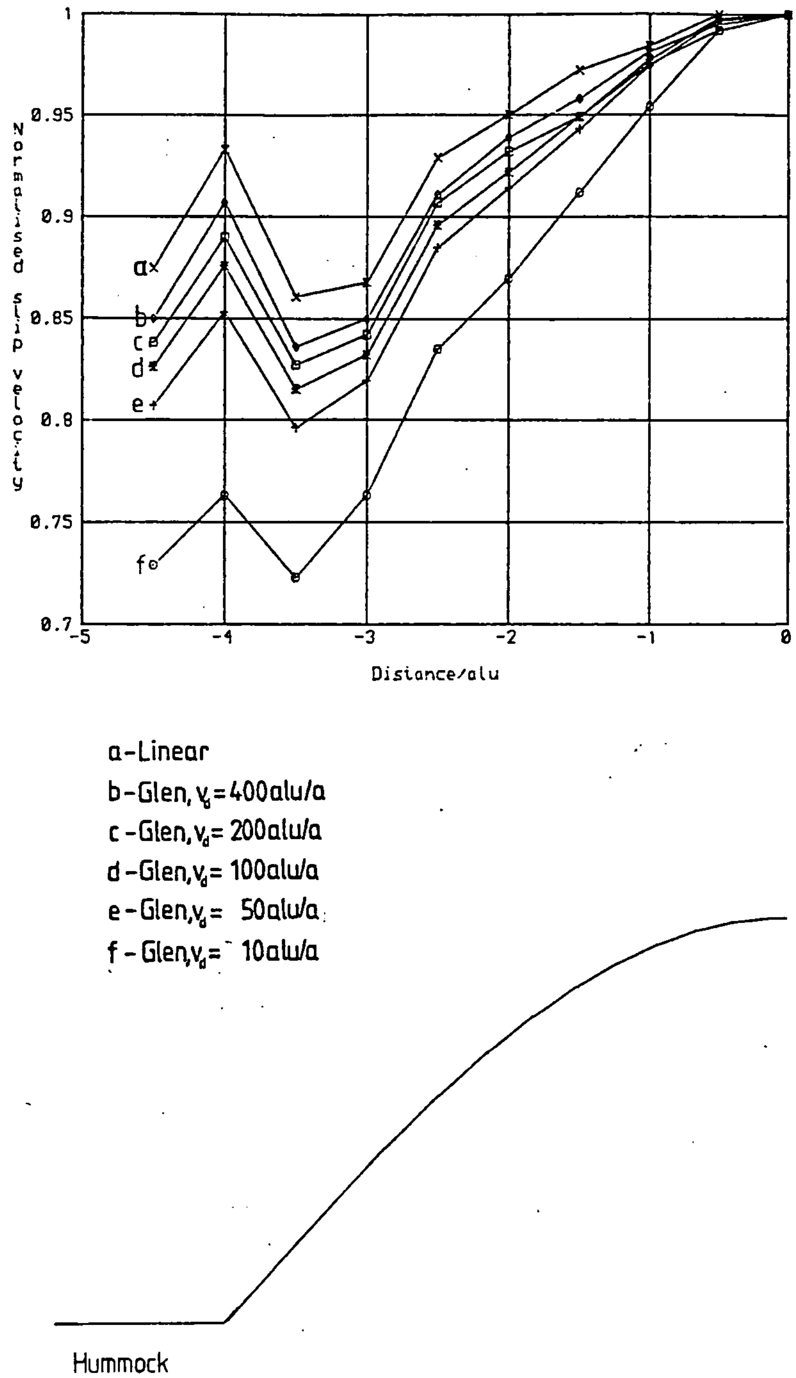

Figure 5.26 Regression coefficients from v_τ against v_d against position for flow over a truncated sine ridge (Cases 45 - 49).

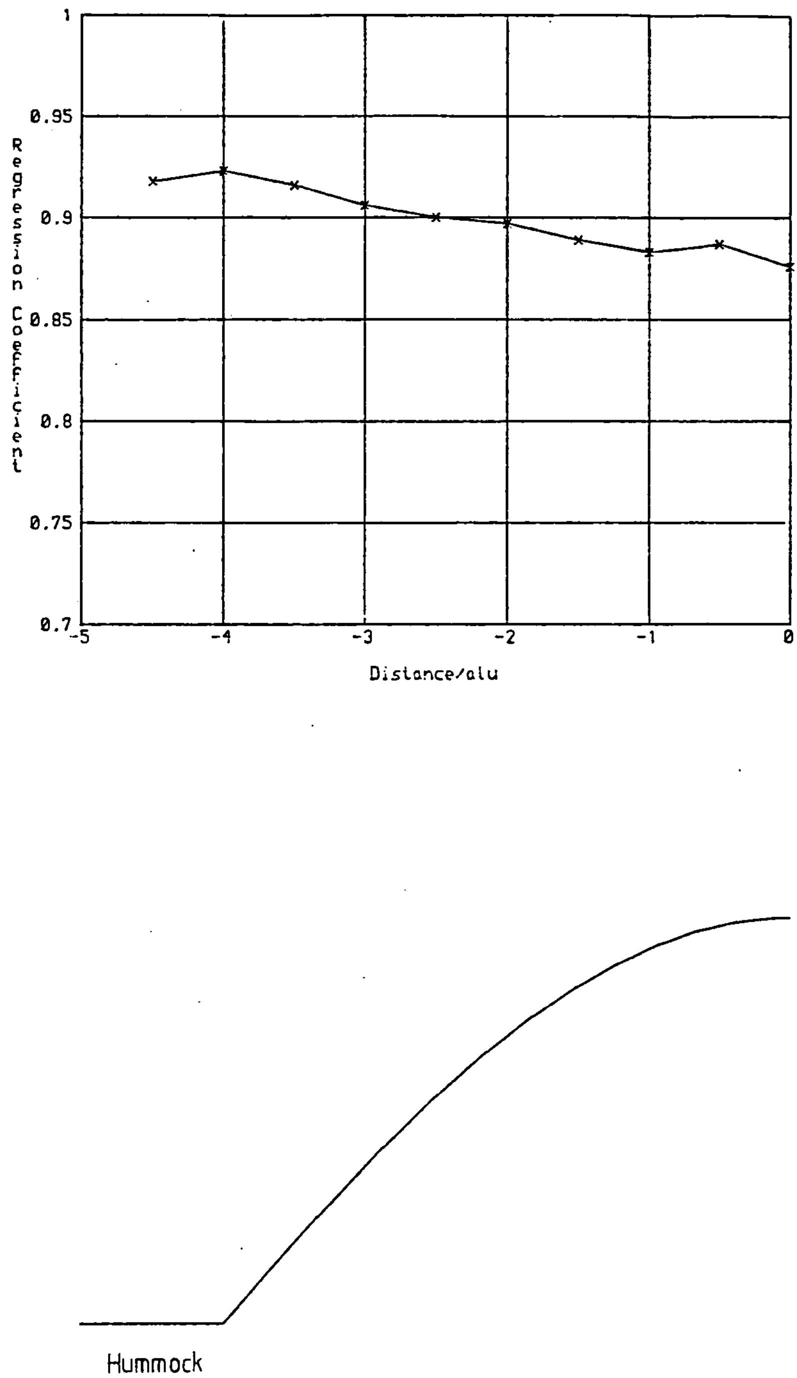

Figure 5.27 Pressure contours in bar for an incompressible linear rheology with v_d = 100 alu/a (Case 3).

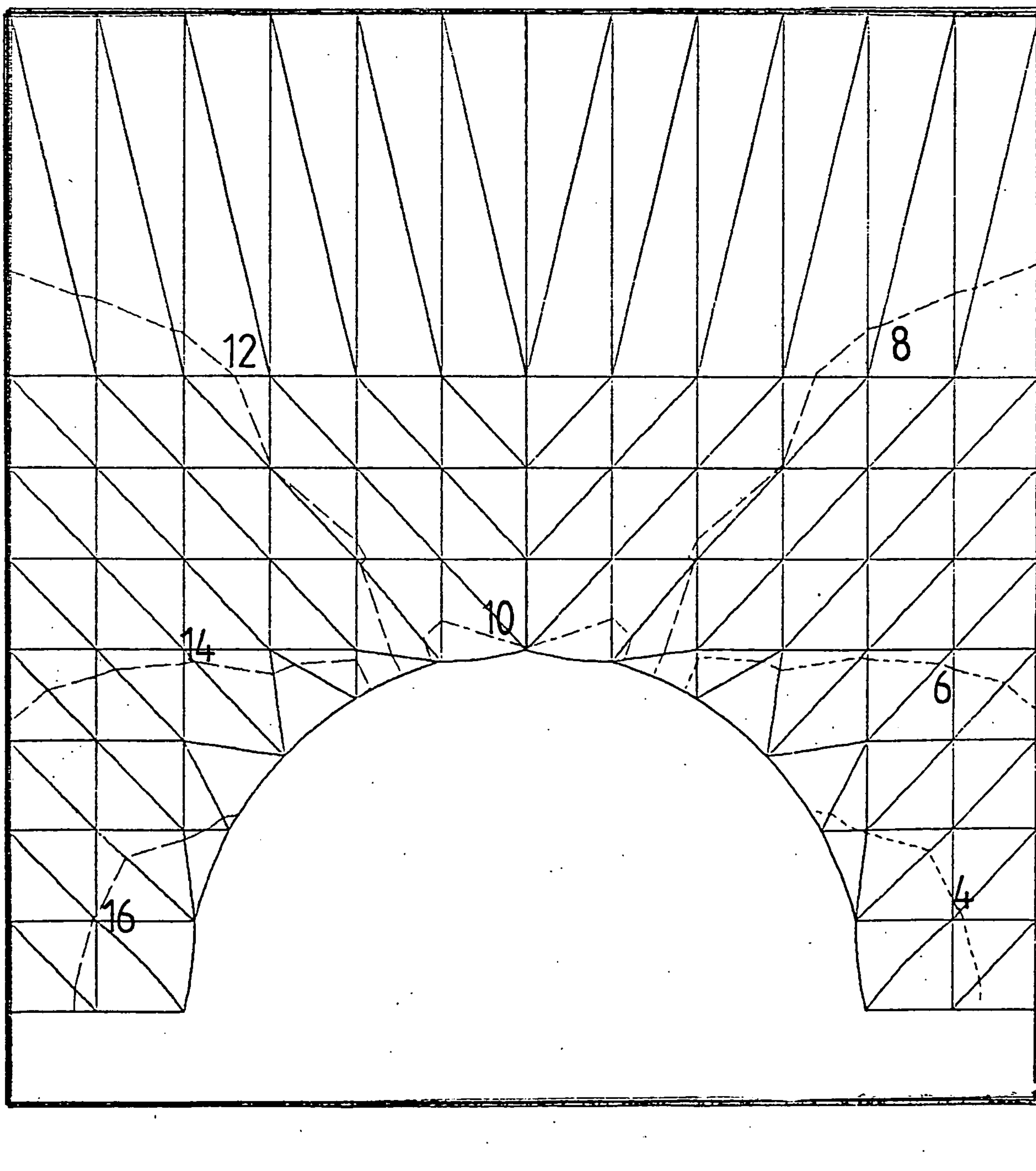

Figure 5.28 p' against $\cos\gamma$ for an incompressible linear rheology with v_d = 400 alu/a (Case 1).

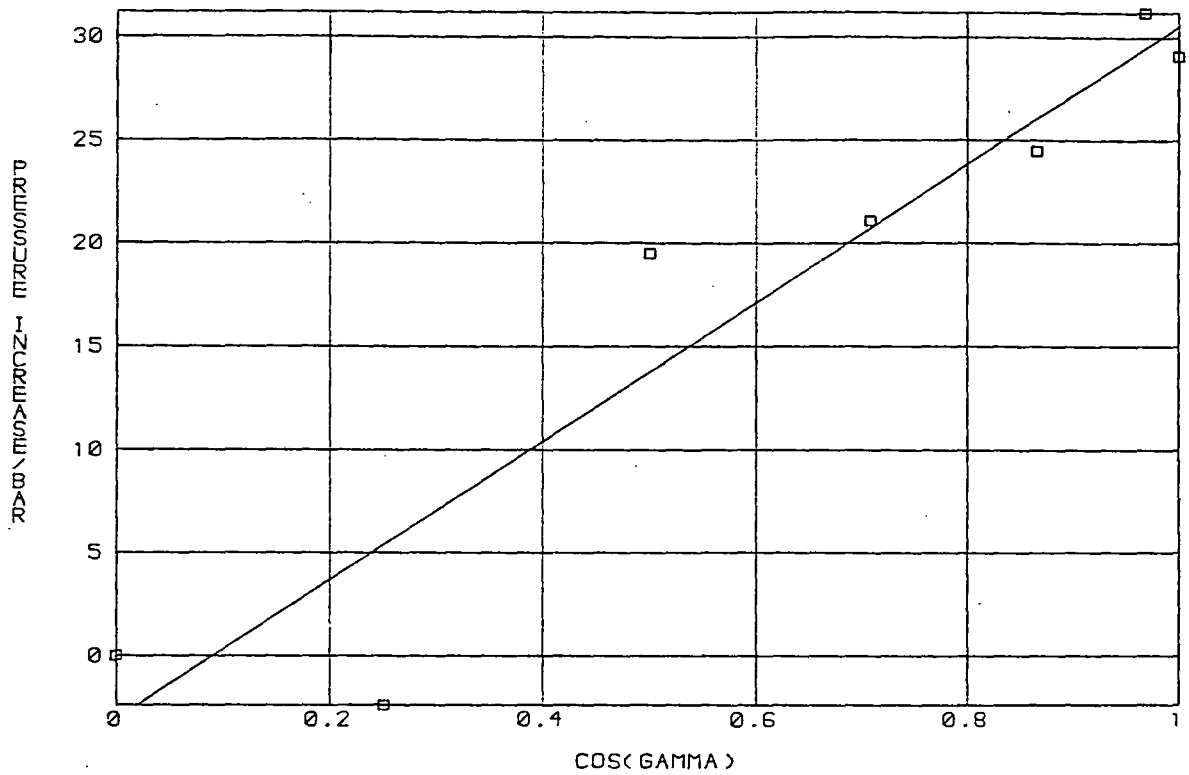

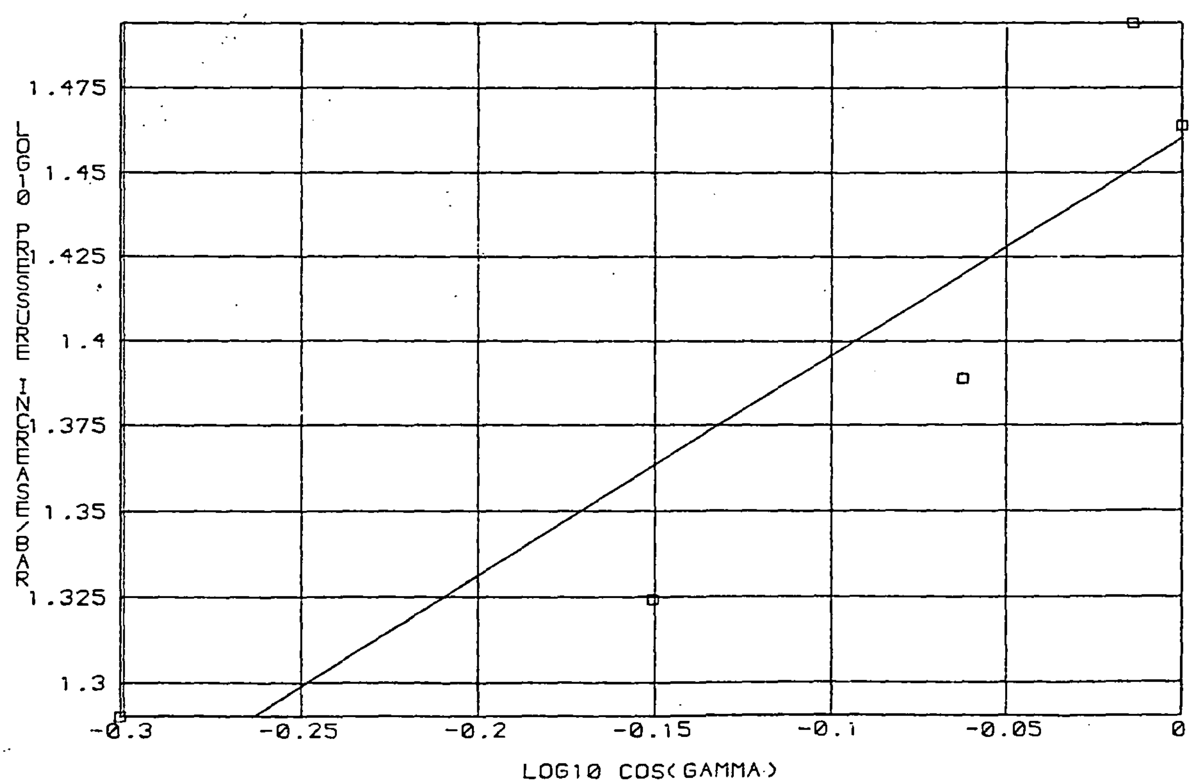

Figure 5.29 p' against $\cos\gamma$ for an incompressible linear rheology with a cavity and v_d = 400 alu/a (Case 5).

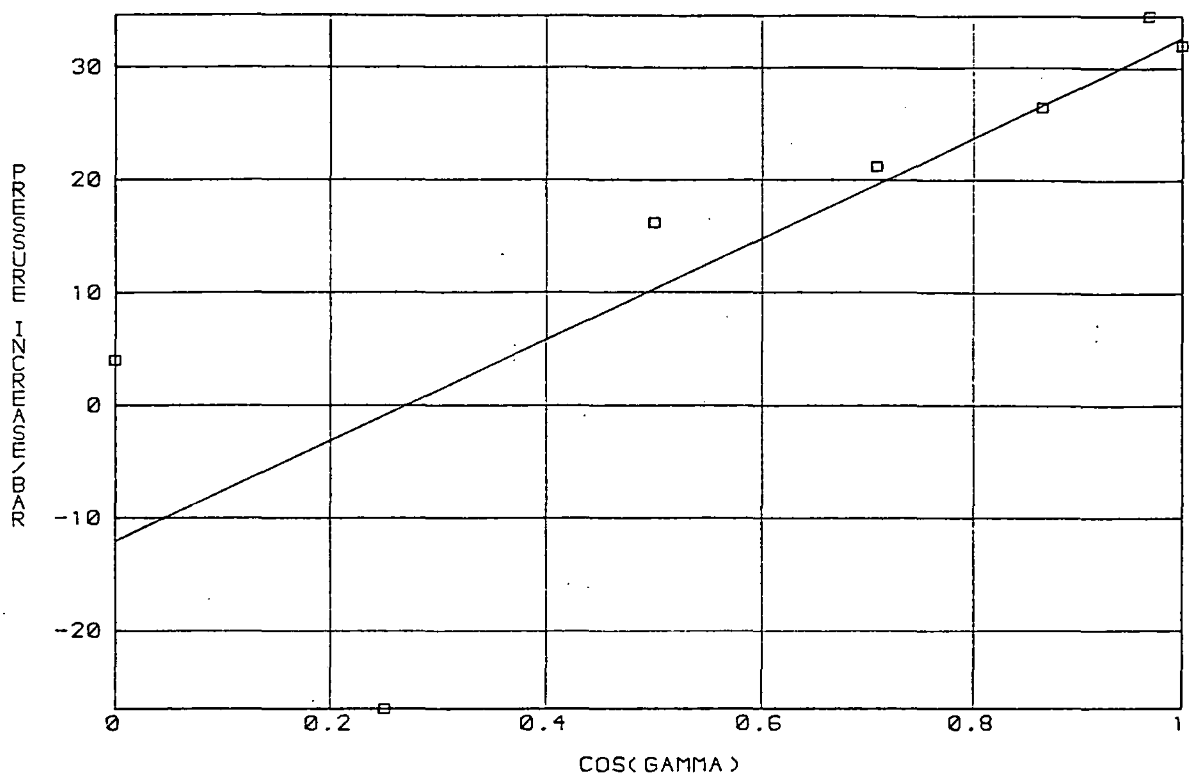

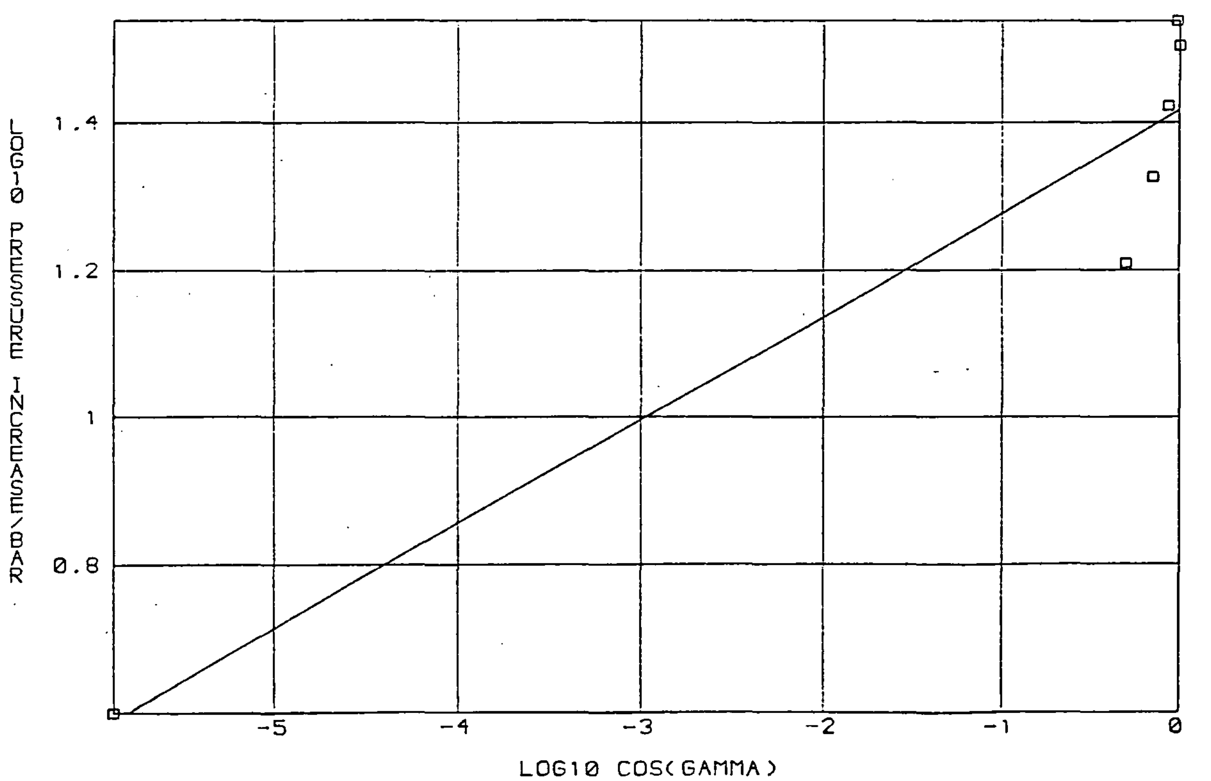

Figure 5.30 p' against $\cos\gamma$ for a compressible linear rheology with χ = 1 alu²/bar.a and v_d = 400 alu/a (Case 12).

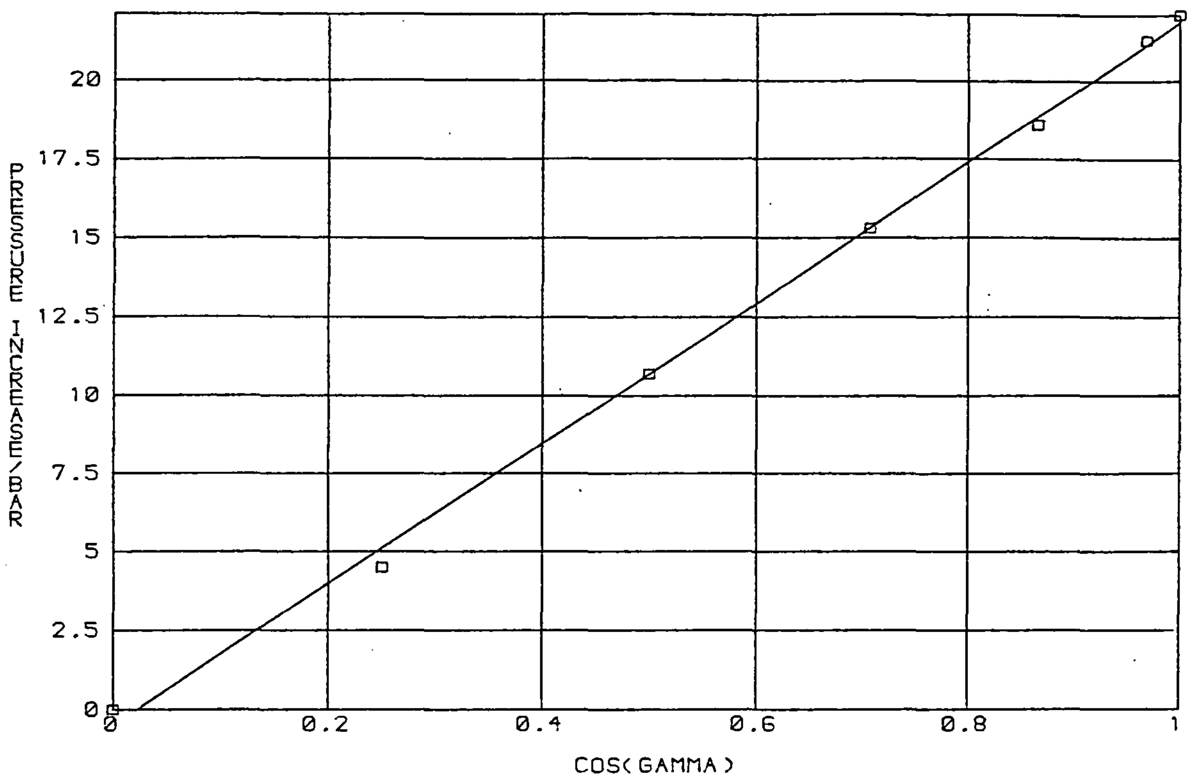

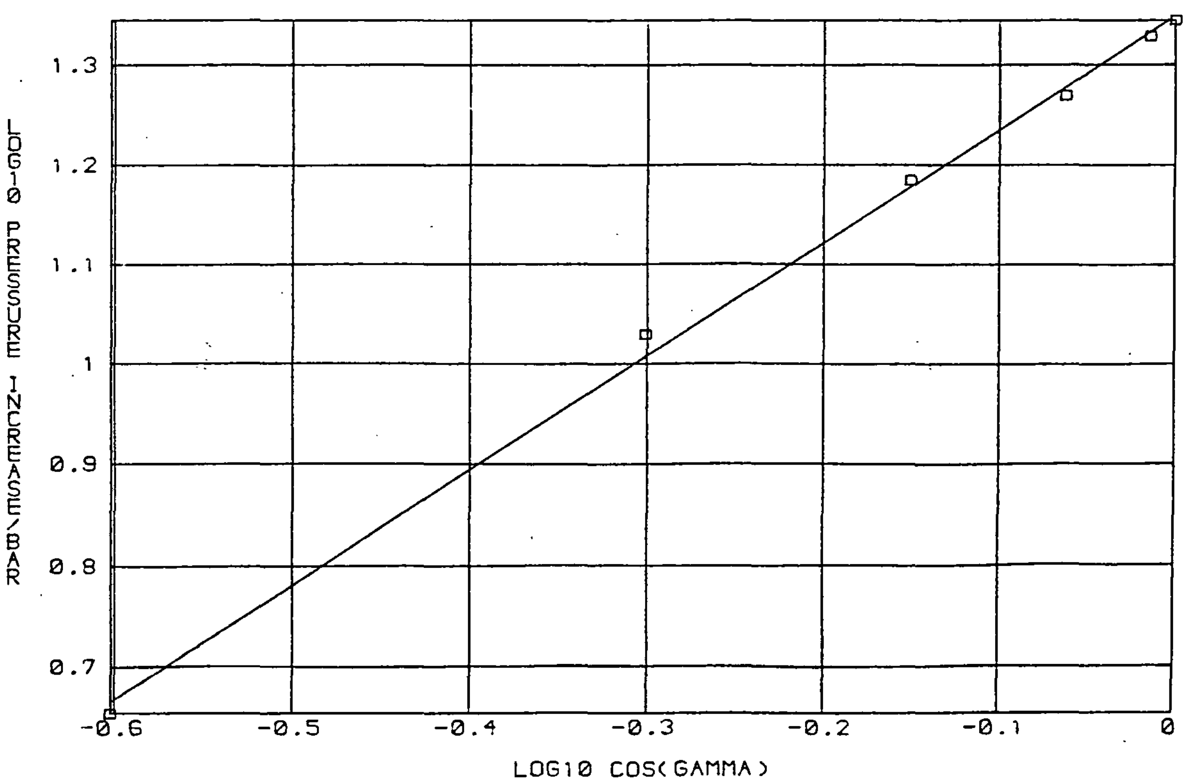

Figure 5.31 Pressure contours in bar for a compressible linear rheology with $\chi = 10\ alu^2/bar.a$ and $v_d = 400\ alu/a$ (Case 17).

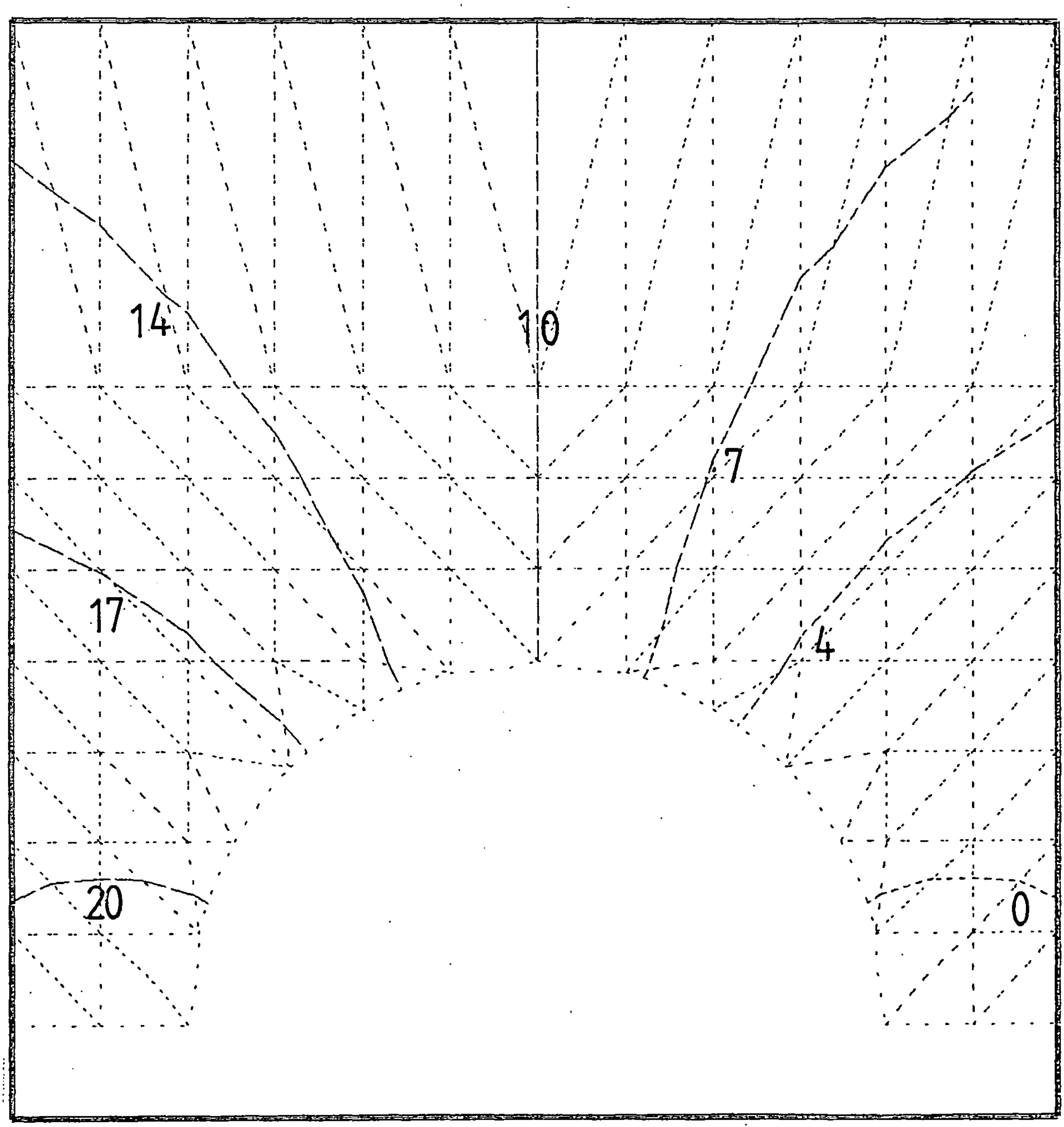

Figure 5.32 p' against $\cos\gamma$ for a compressible linear rheology with χ = 10 alu²/bar.a and v_d = 200 alu / a (Case 16).

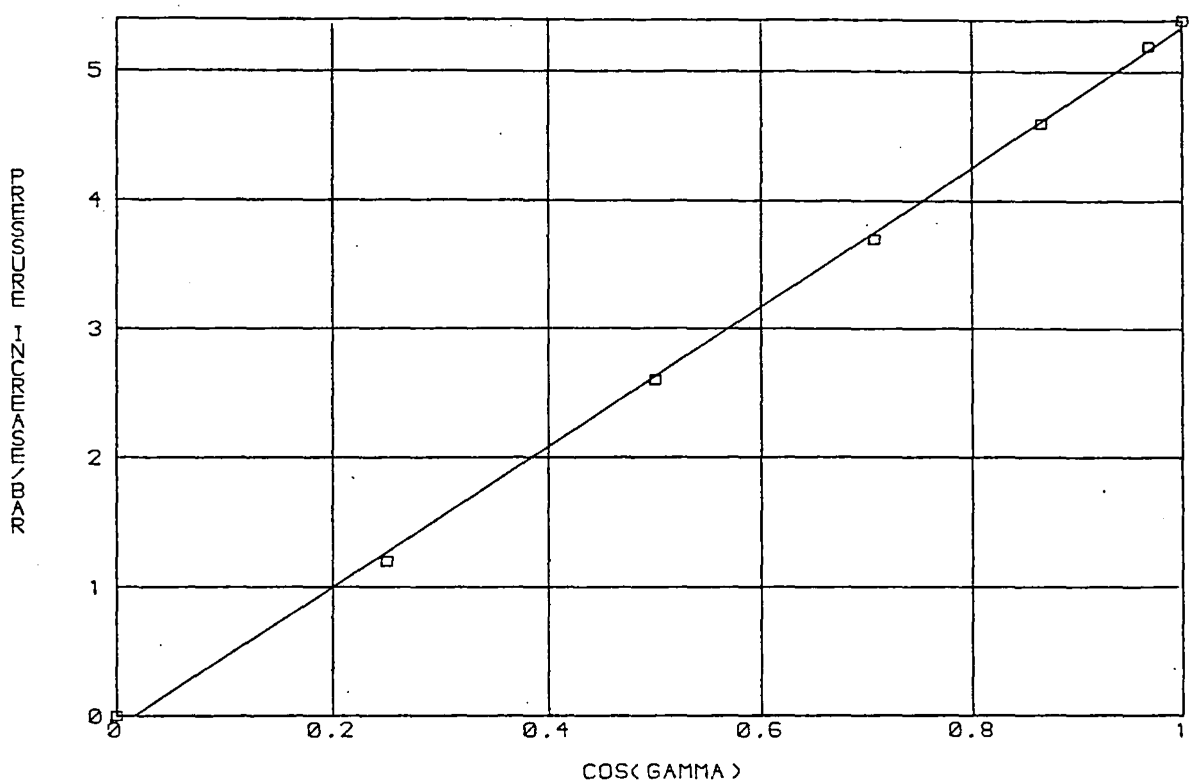

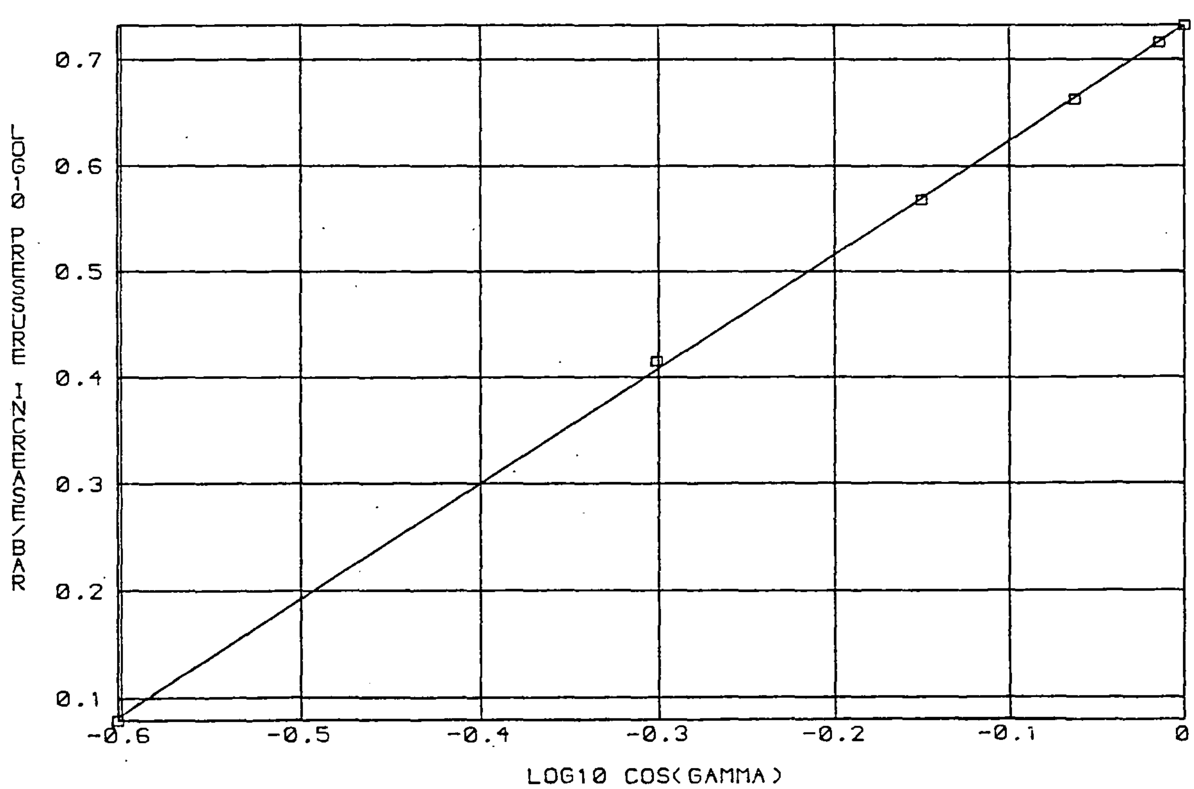

Figure 5.33 Pressure contours in bar for an incompressible linear rheology with bed of S = 100 alu /bar.a and v_d = 100 alu / a. (Case 20).

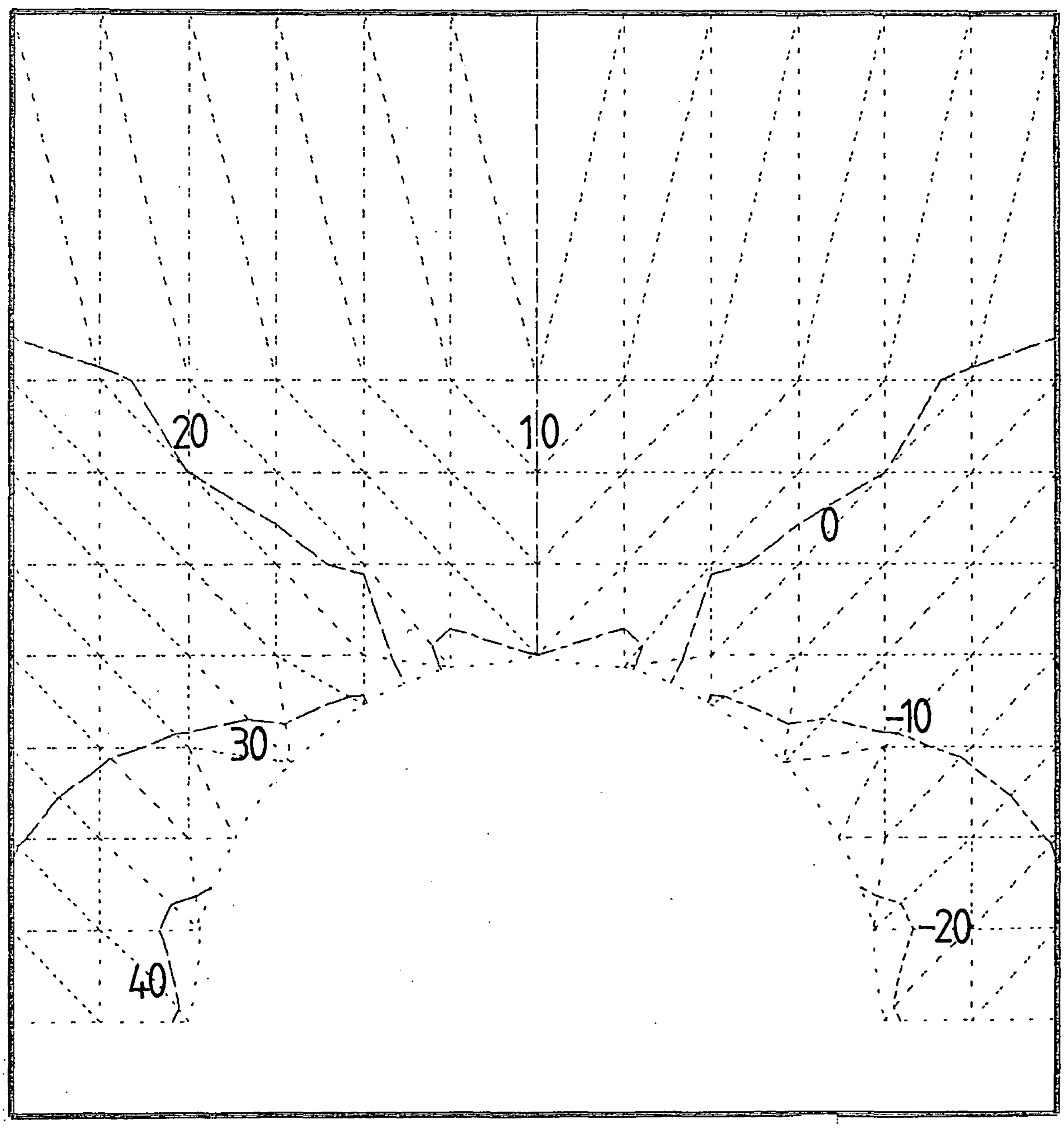

Figure 5.34 p' against cosγ for an incompressible linear rheology with bed of S = 10 alu /bar.a and v_d = 10 alu / a (Case 18).

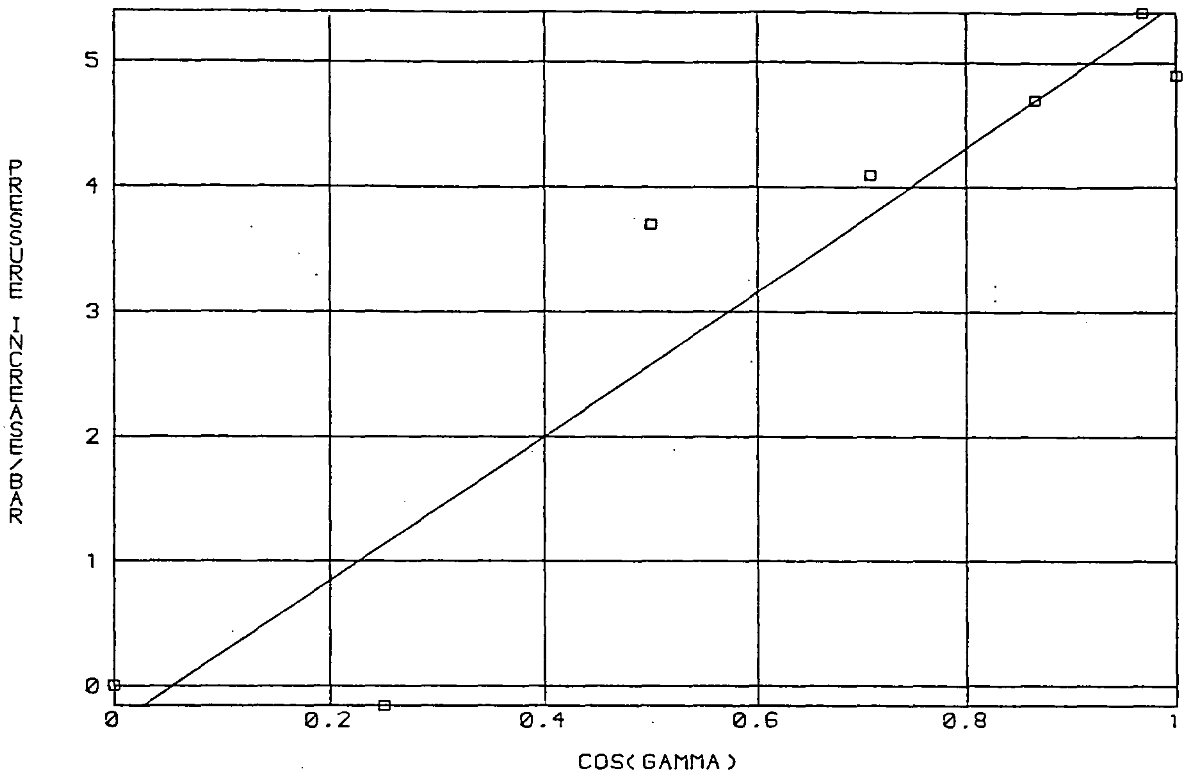

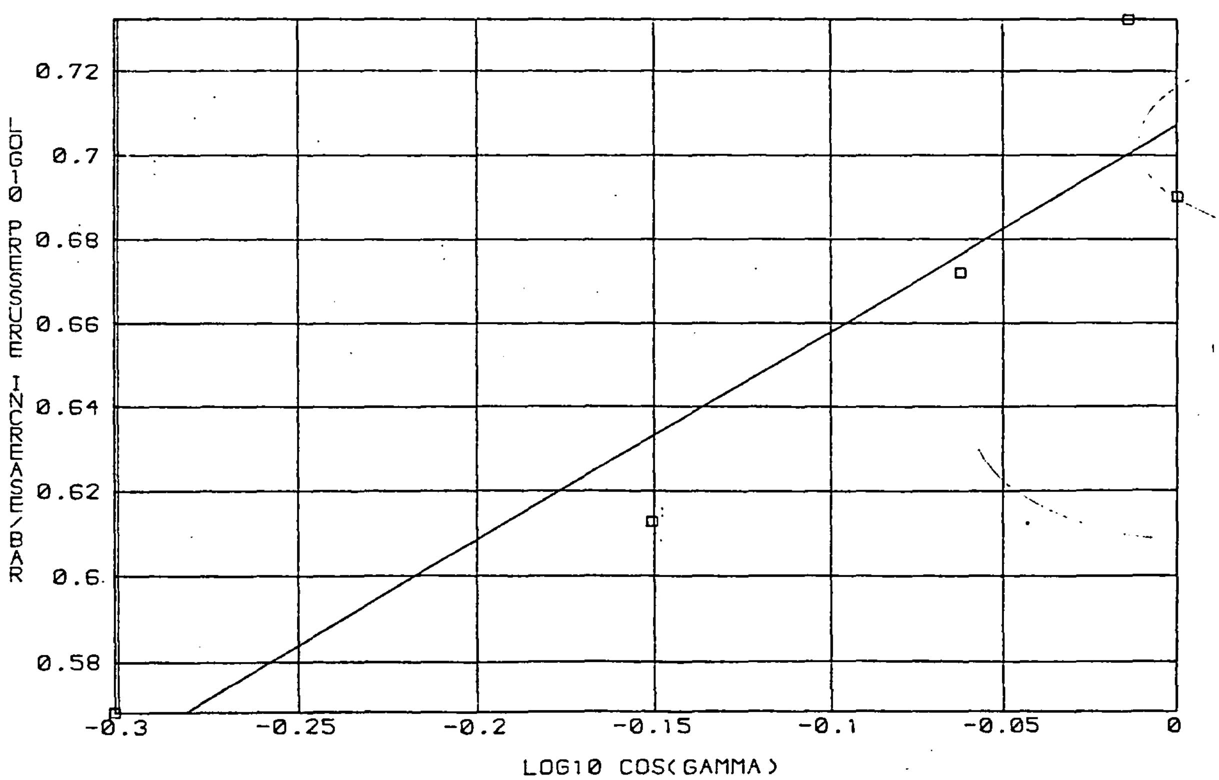

Figure 5.35 p' against $\cos\gamma$ for an incompressible linear rheology with bed of S = 400 alu /bar.a and v_d = 400 alu / a. (Case 22).

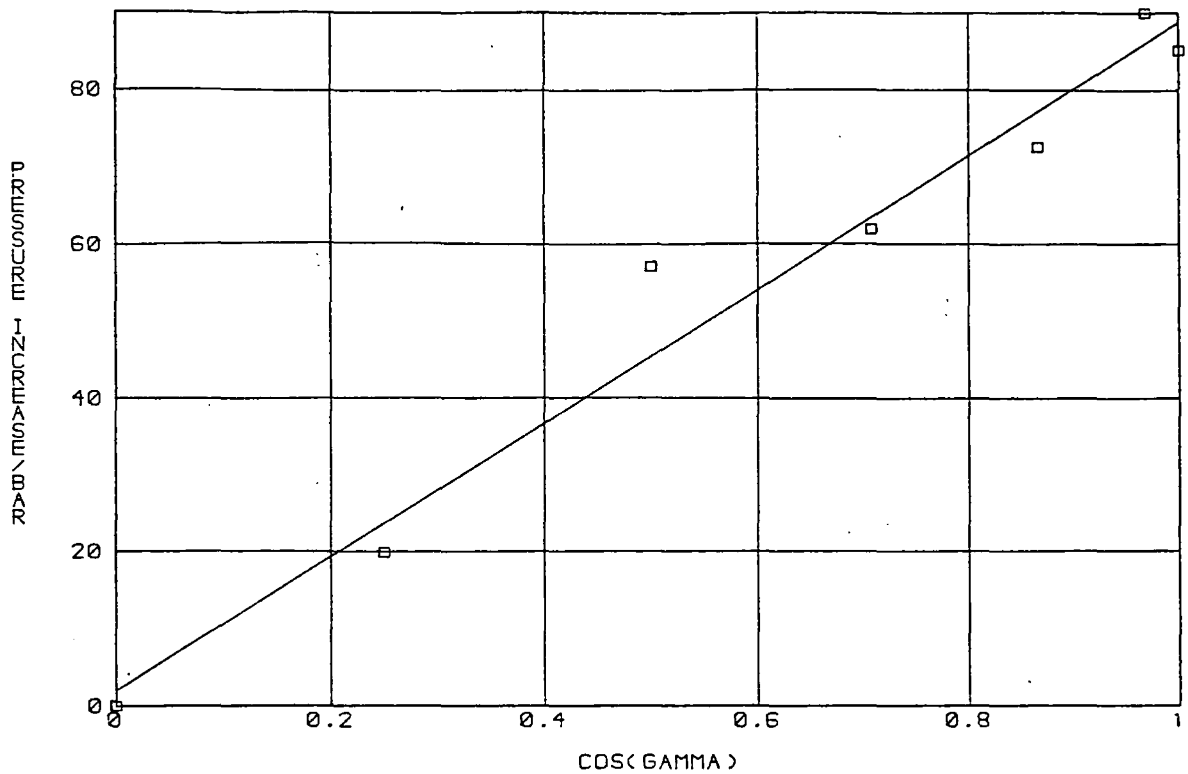

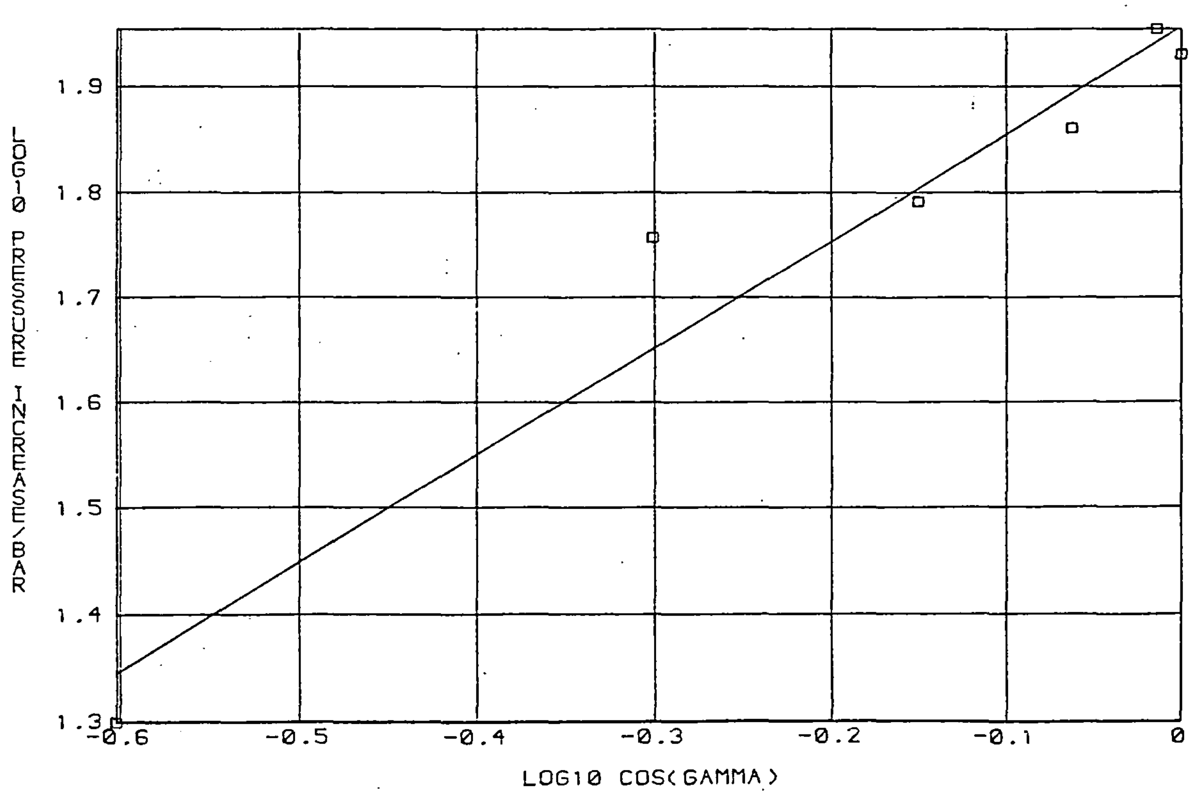

Figure 5.36 Pressure contours in bar for an incompressible Glen rheology with v_d = 200 alu/a (Case 25).

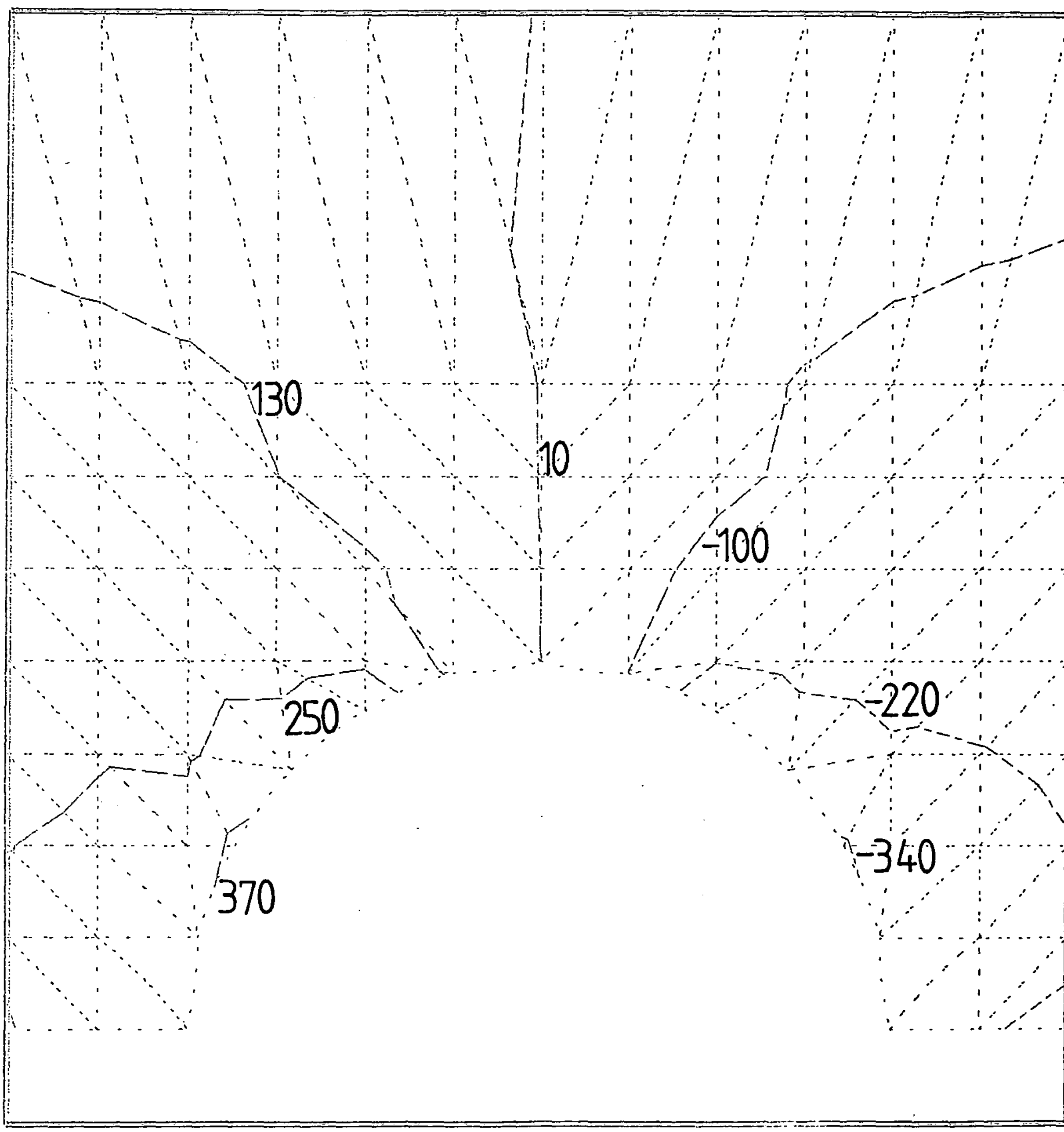

Figure 5.37 p' against $\cos\gamma$ for an incompressible Glen rheology with v_d = 10 alu/a (Case 23).

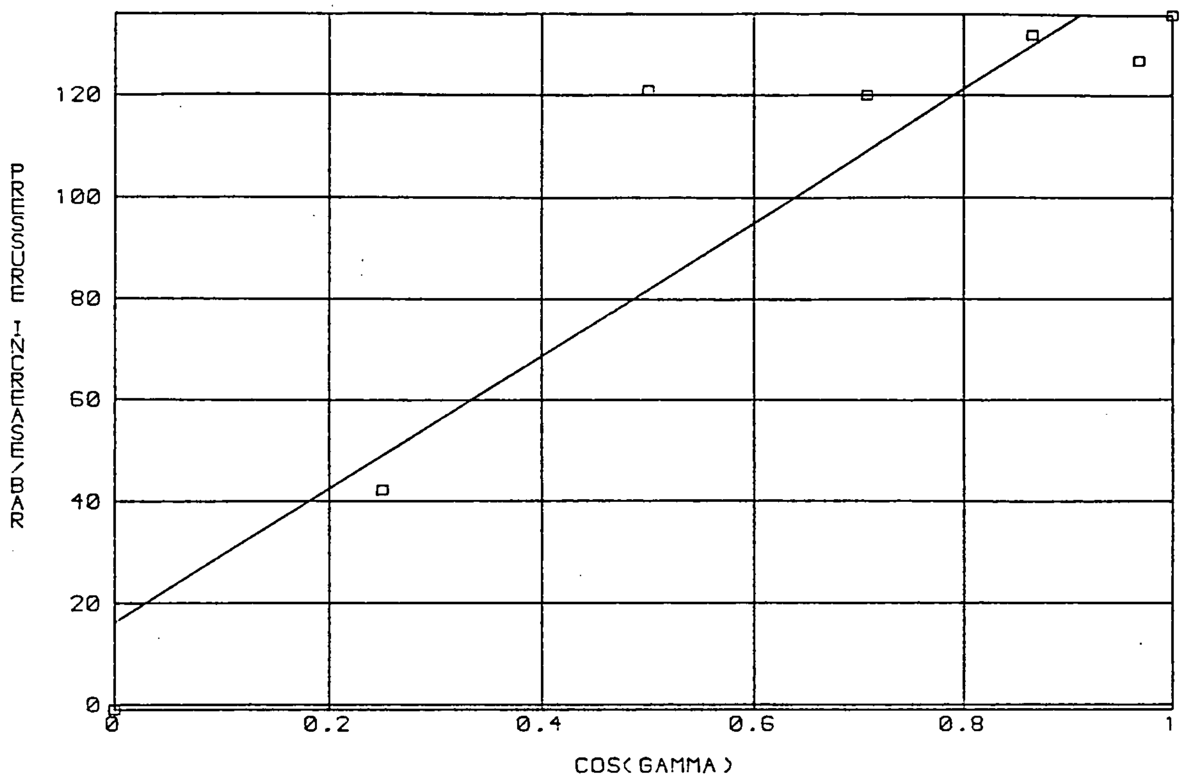

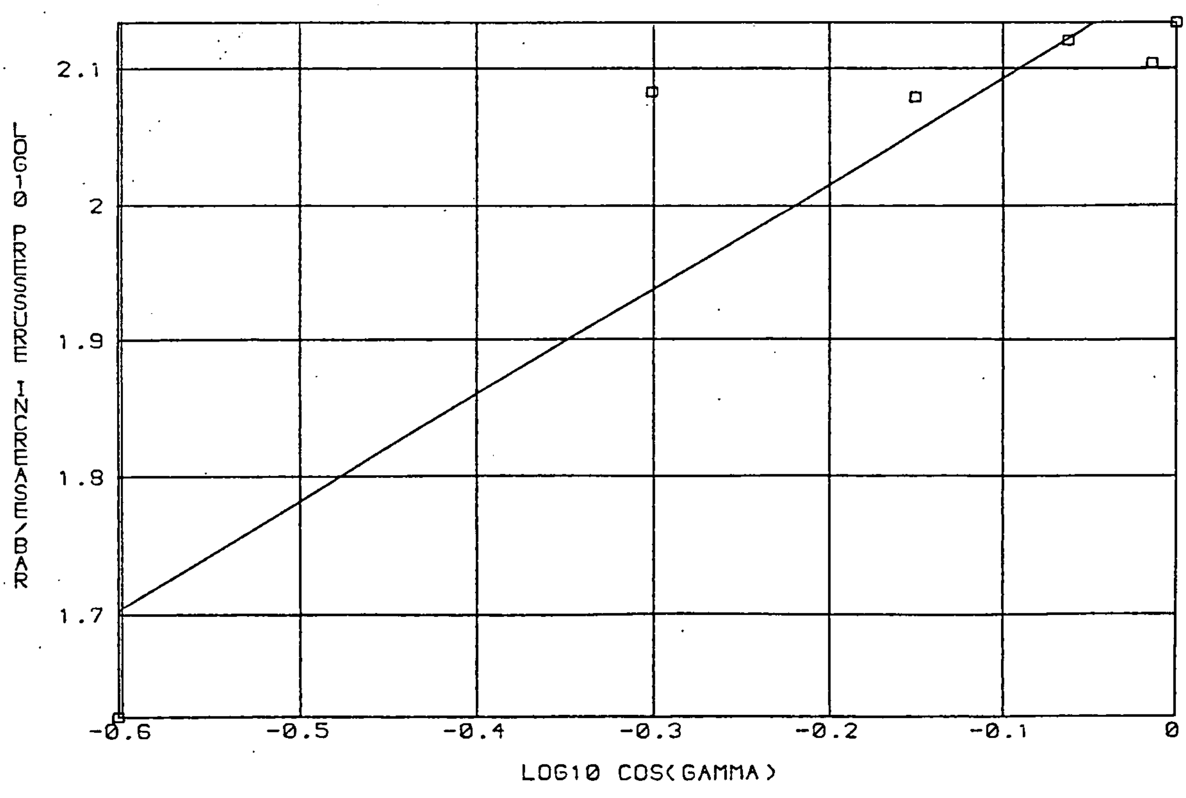

Figure 5.38 p' against $\cos\gamma$ for an incompressible Glen rheology with v_d = 400 alu/a (Case 27).

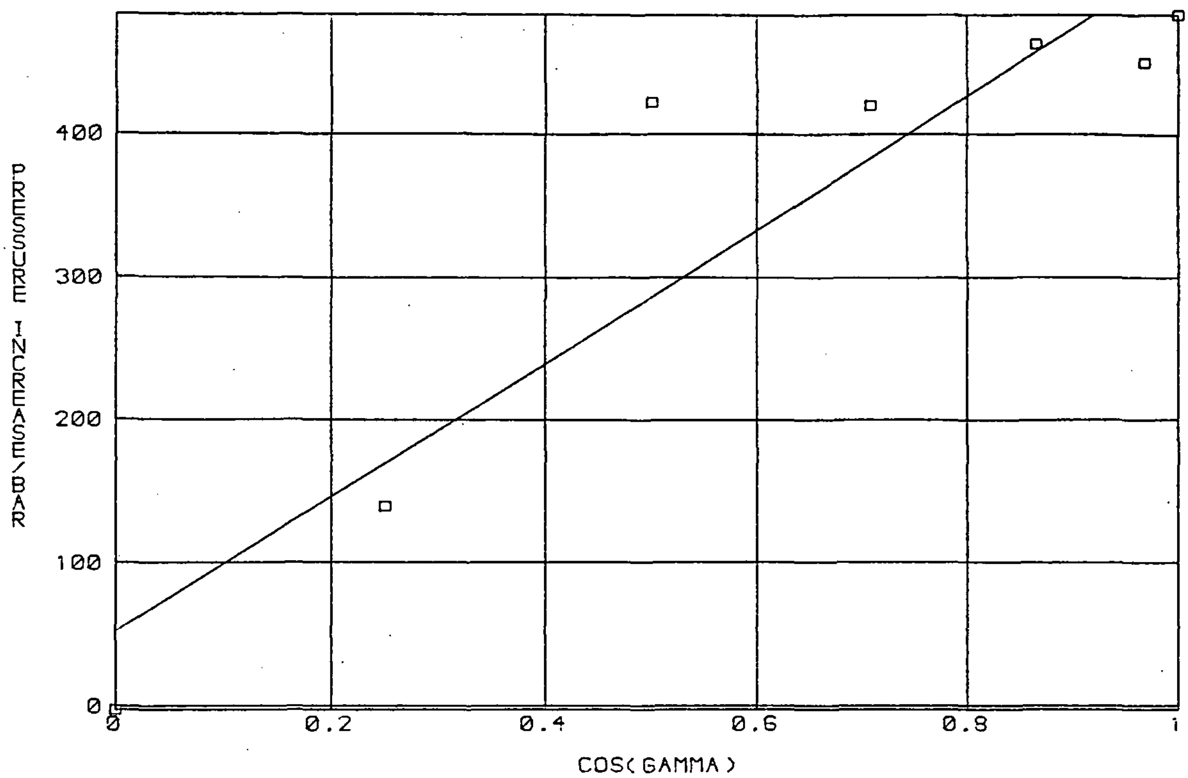

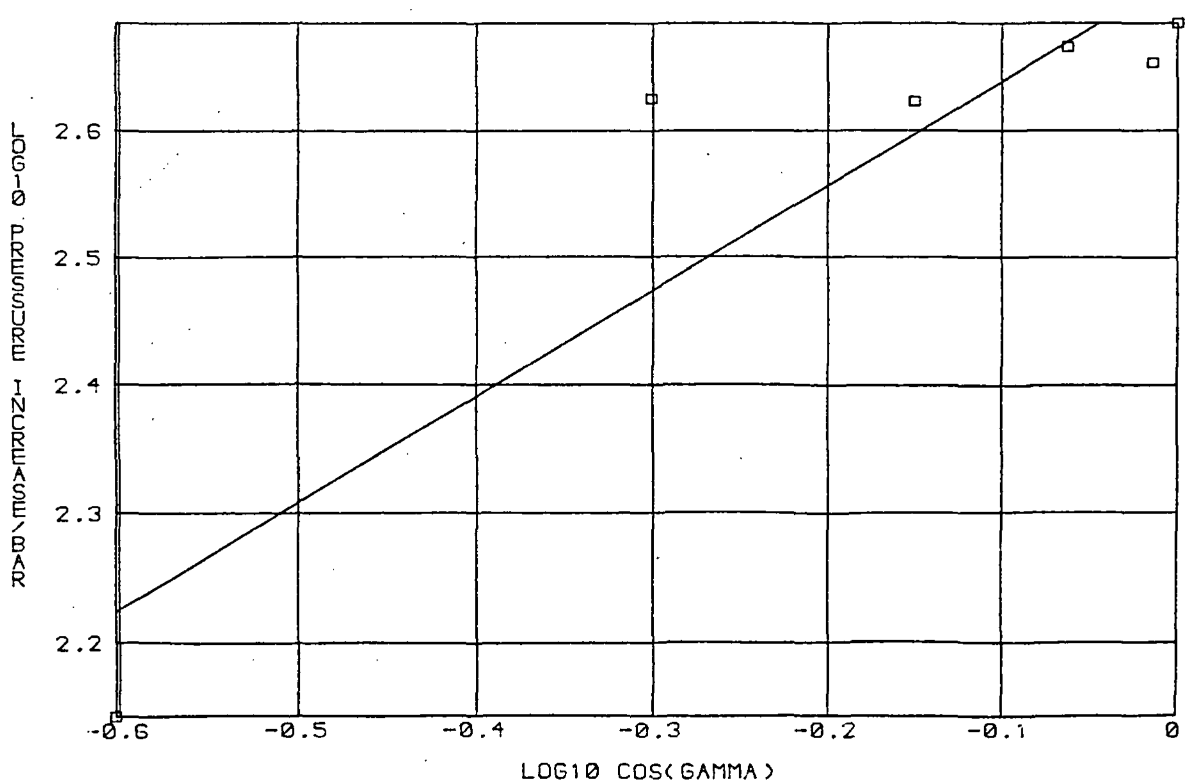

Figure 5.39 Pressure contours in bar for an incompressible Glen rheology with a cavity and v_d = 10 alu/a (Case 27).

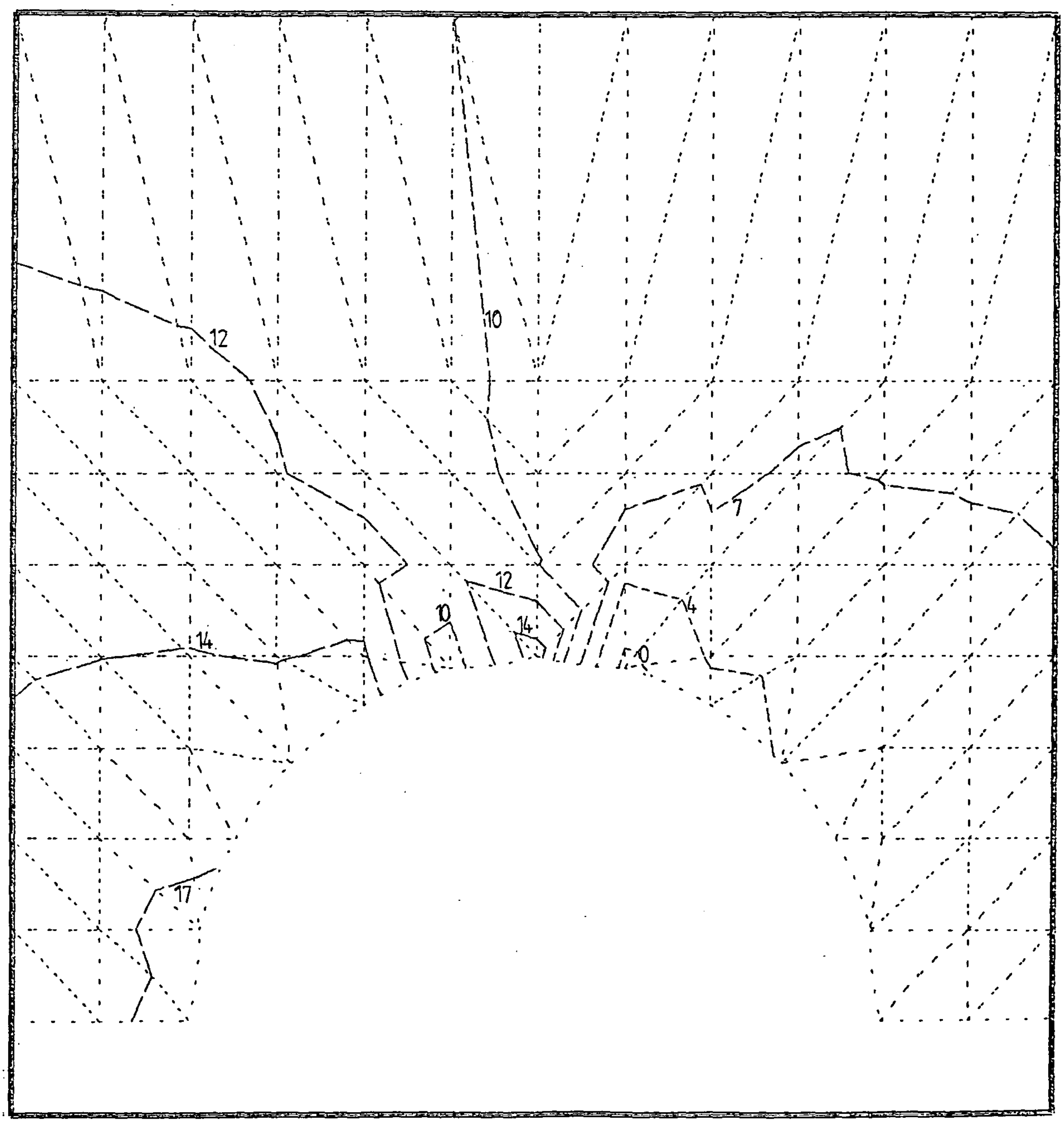

Figure 5.40 p' against cosγ for an incompressible Glen rheology with a cavity and v_d = 10 alu/a (Case 27).

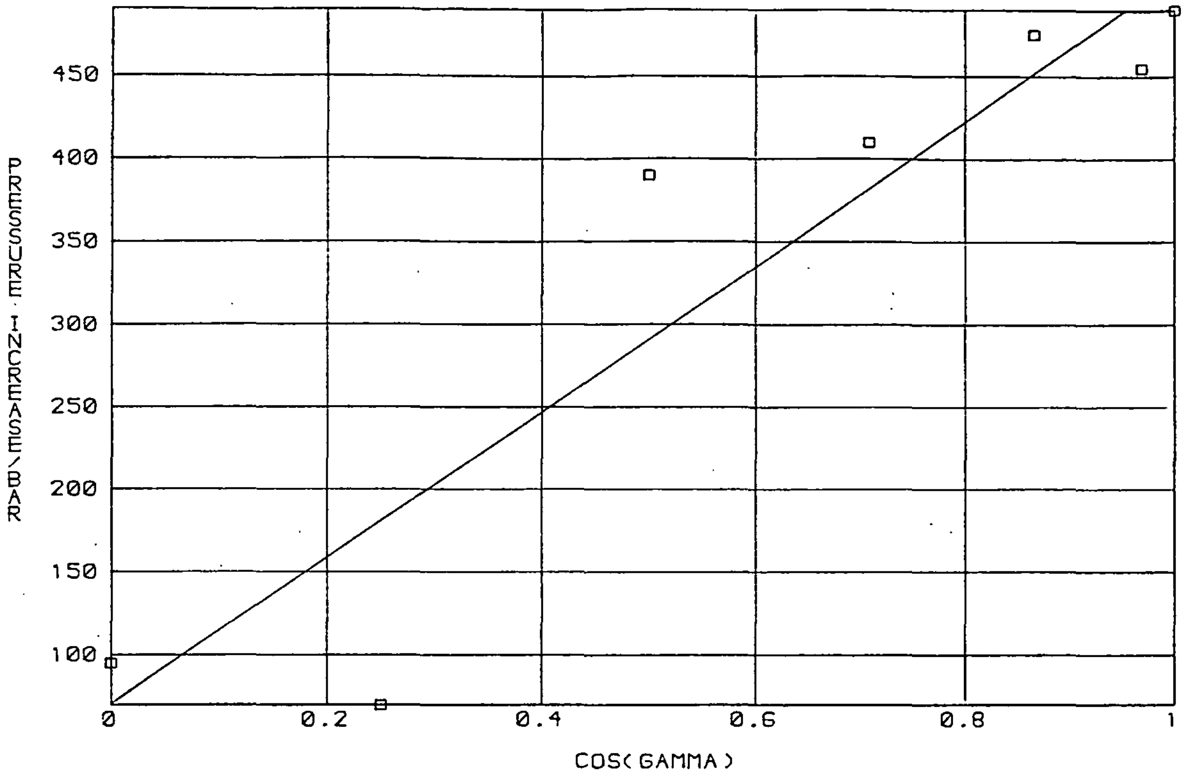

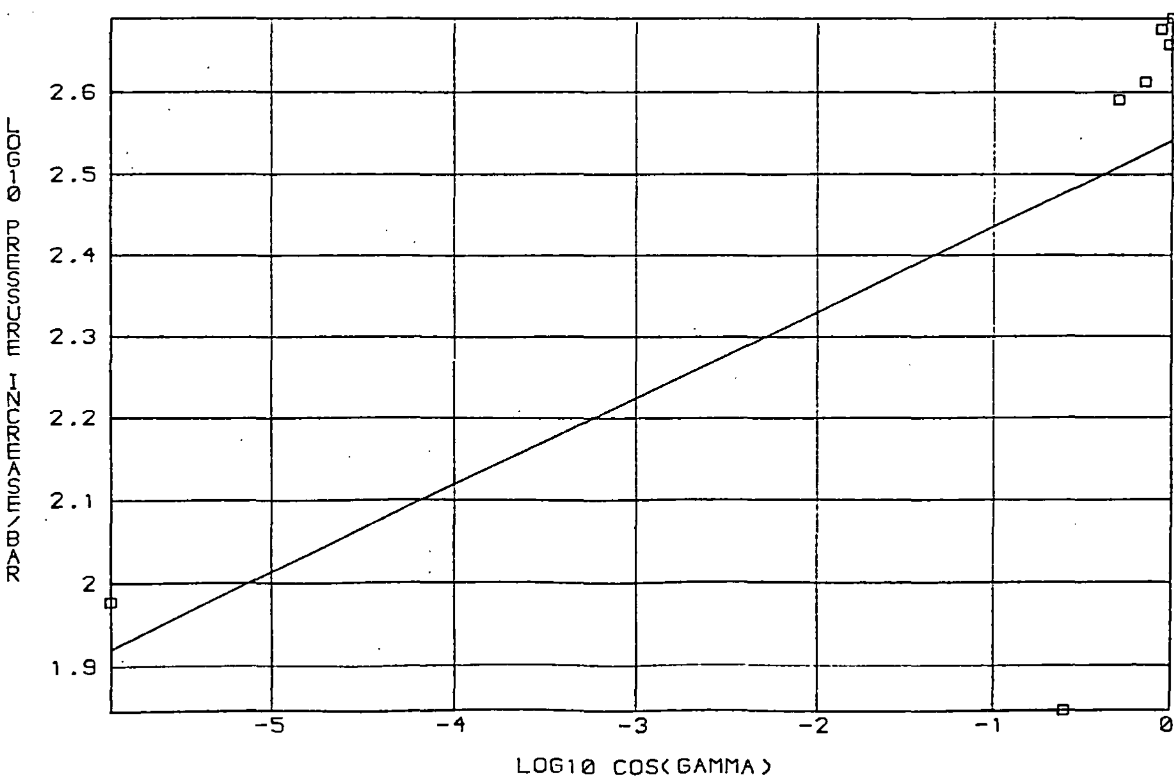

Figure 5.41 Pressure contours in bar for a compressible, Glen rheology with χ = 1 alu²/bar.a and v_d = 100 alu/a (Case 29).

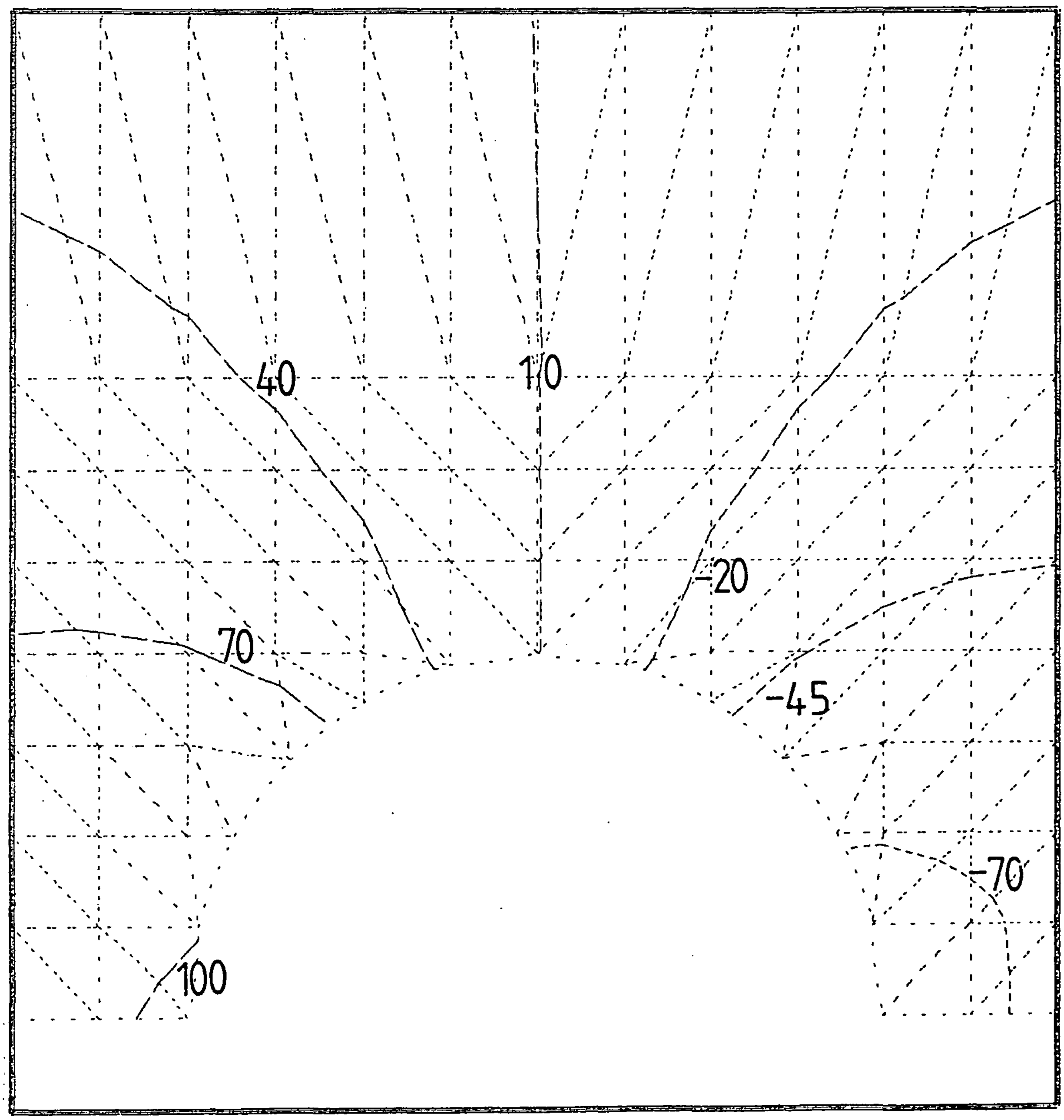

Figure 5.42 p' against $\cos\gamma$ for a compressible Glen rheology with χ = 1 alu²/bar.a and v_d = 200 alu/a (Case 30).

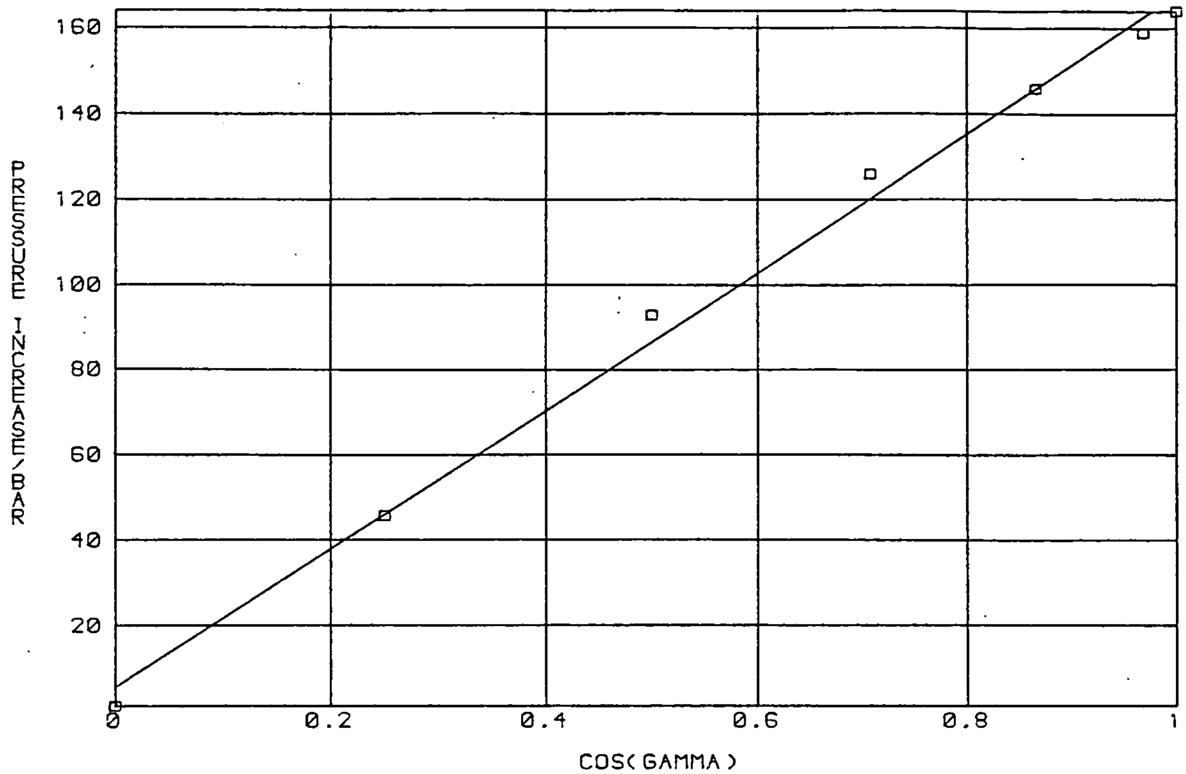

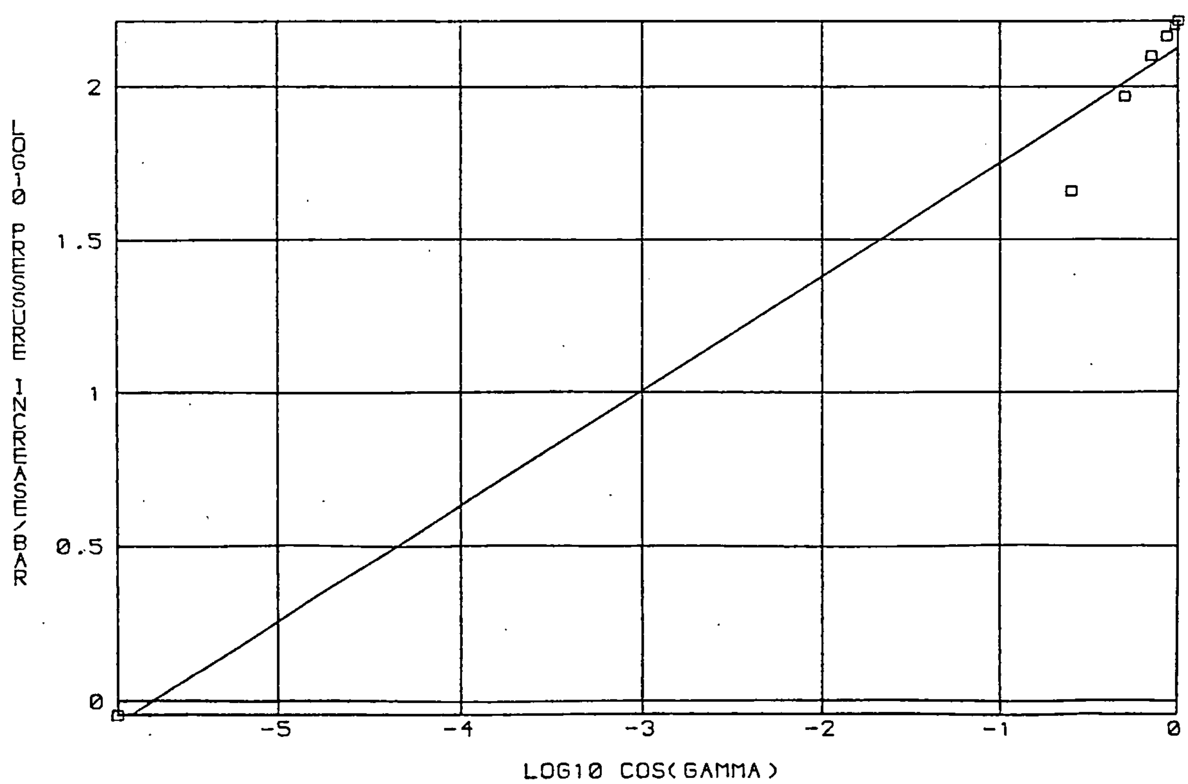

Figure 5.43 p' against $\cos\gamma$ for an incompressible Glen rheology with bed of $S = 10$ alu/bar.a and $v_d = 10$ alu/a (Case 34)

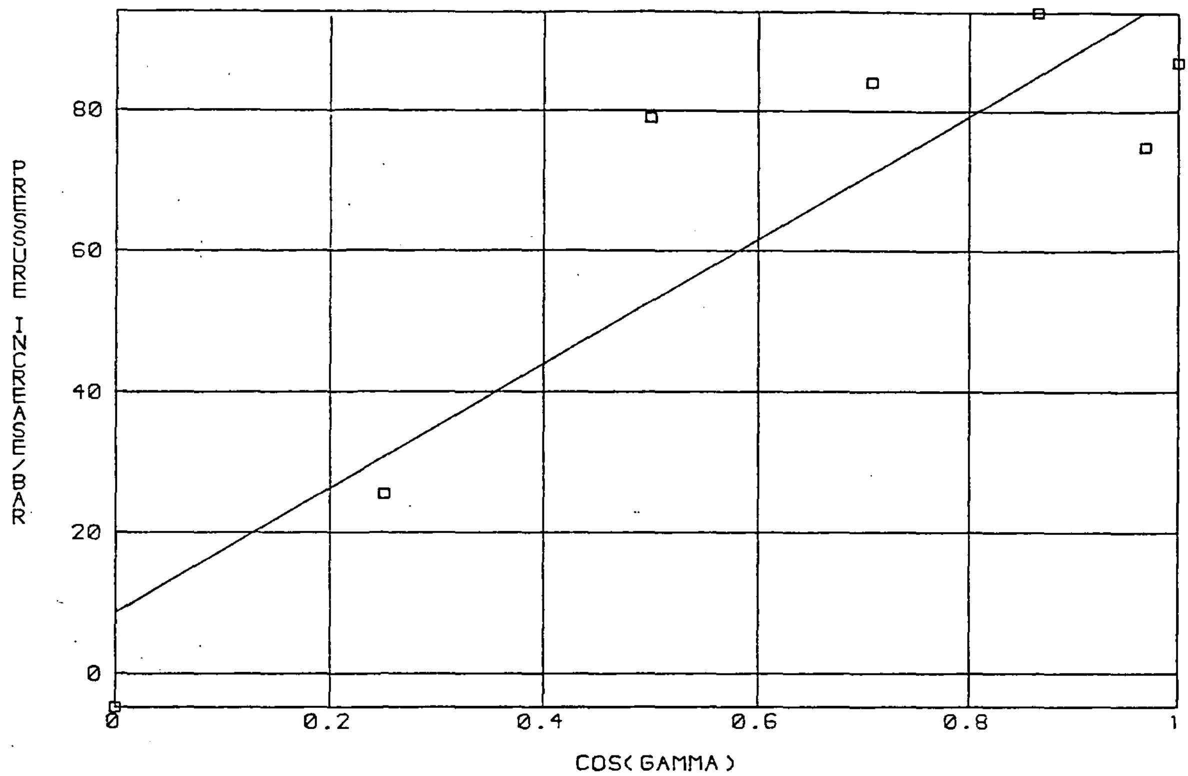

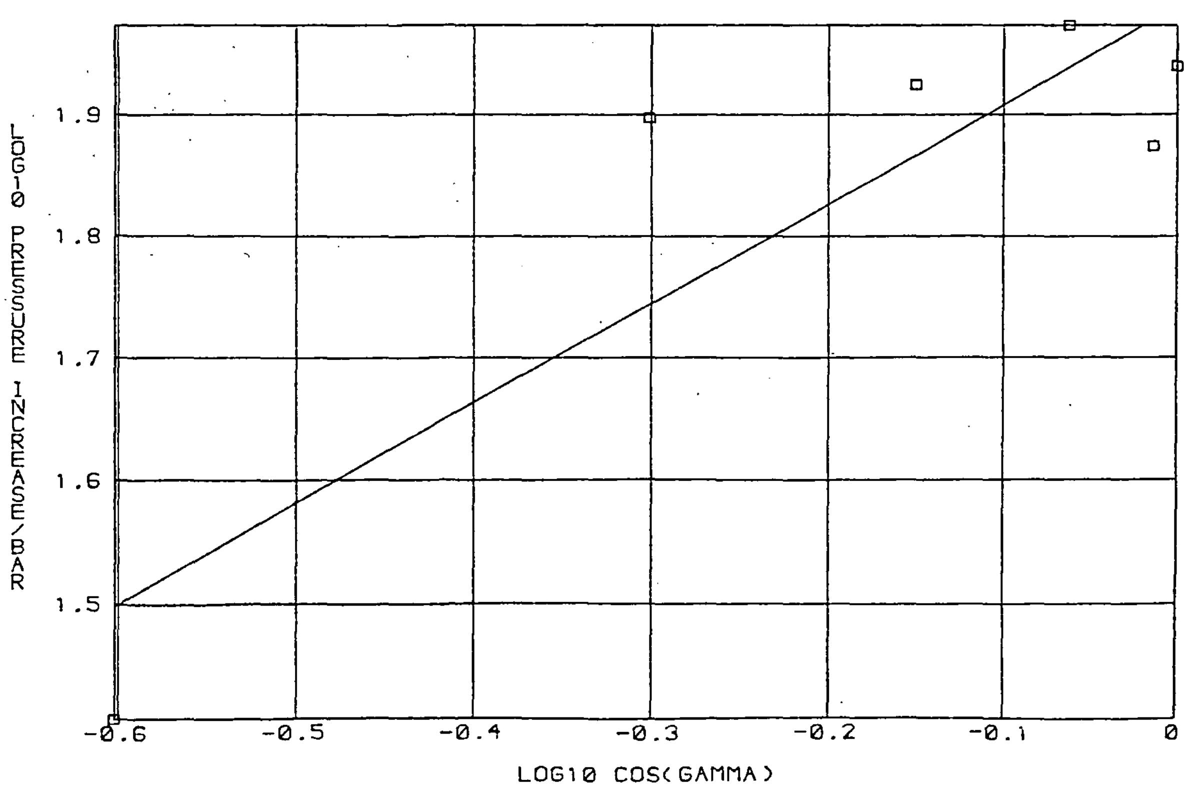

Figure 5.44 p' against position for flow over a truncated sine ridge (Cases 40 - 49).

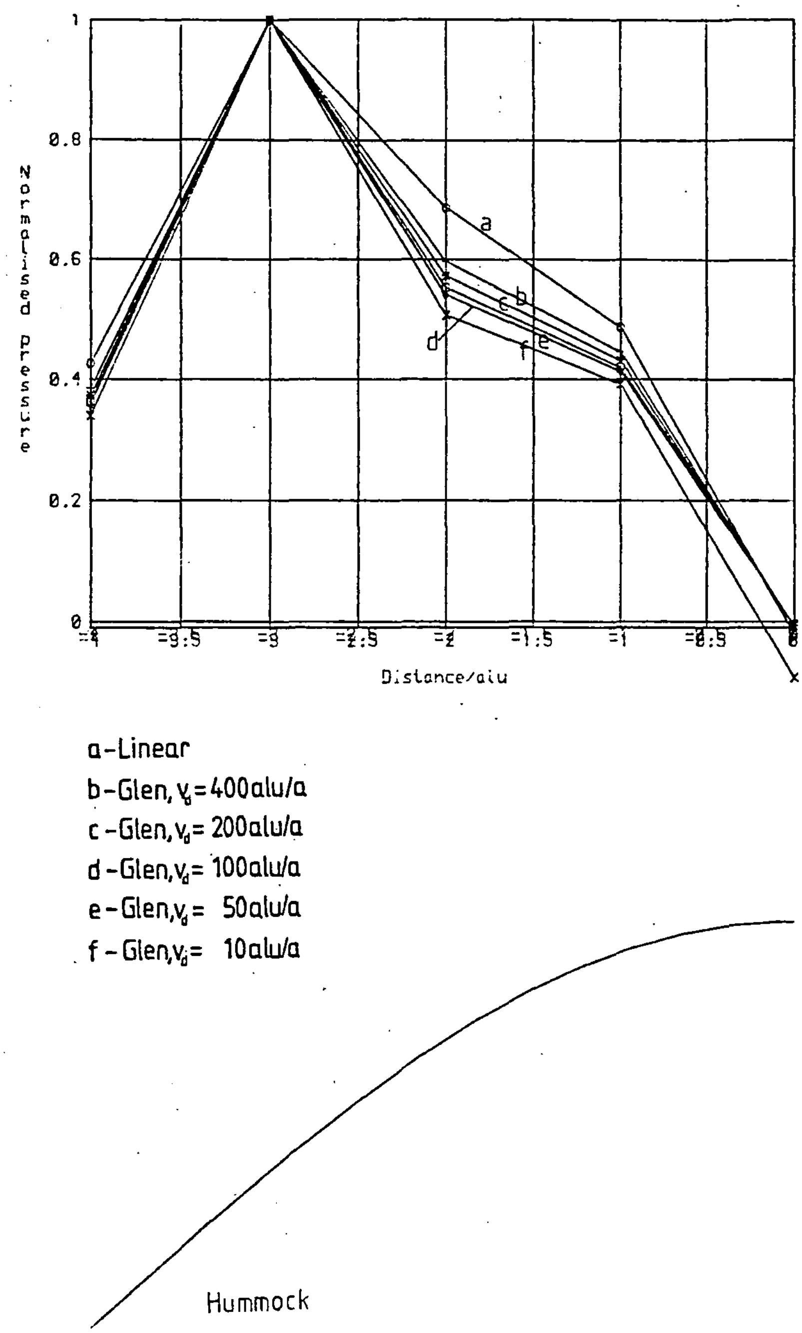

Figure 5.45 Pressure contours in bar for an incompressible Glen rheology with v_d = 100 alu/a for flow over a truncated sine ridge (Case 47).

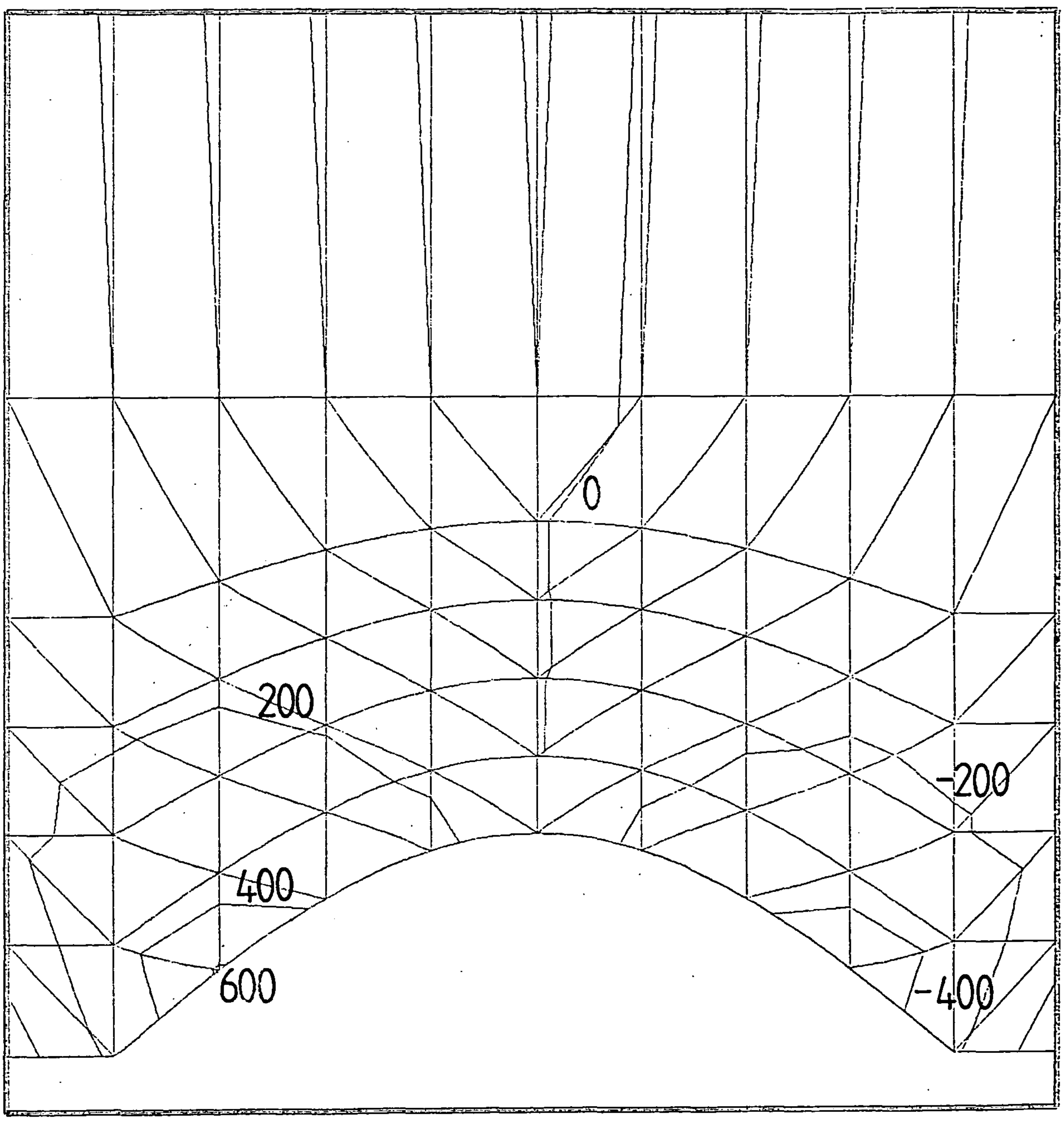

Figure 5.46 $\dot{\varepsilon}_v$ in a^{-1} for a compressible linear rheology with χ = 1 alu²/bar.a and v_d = 400 alu/a (Case 12).

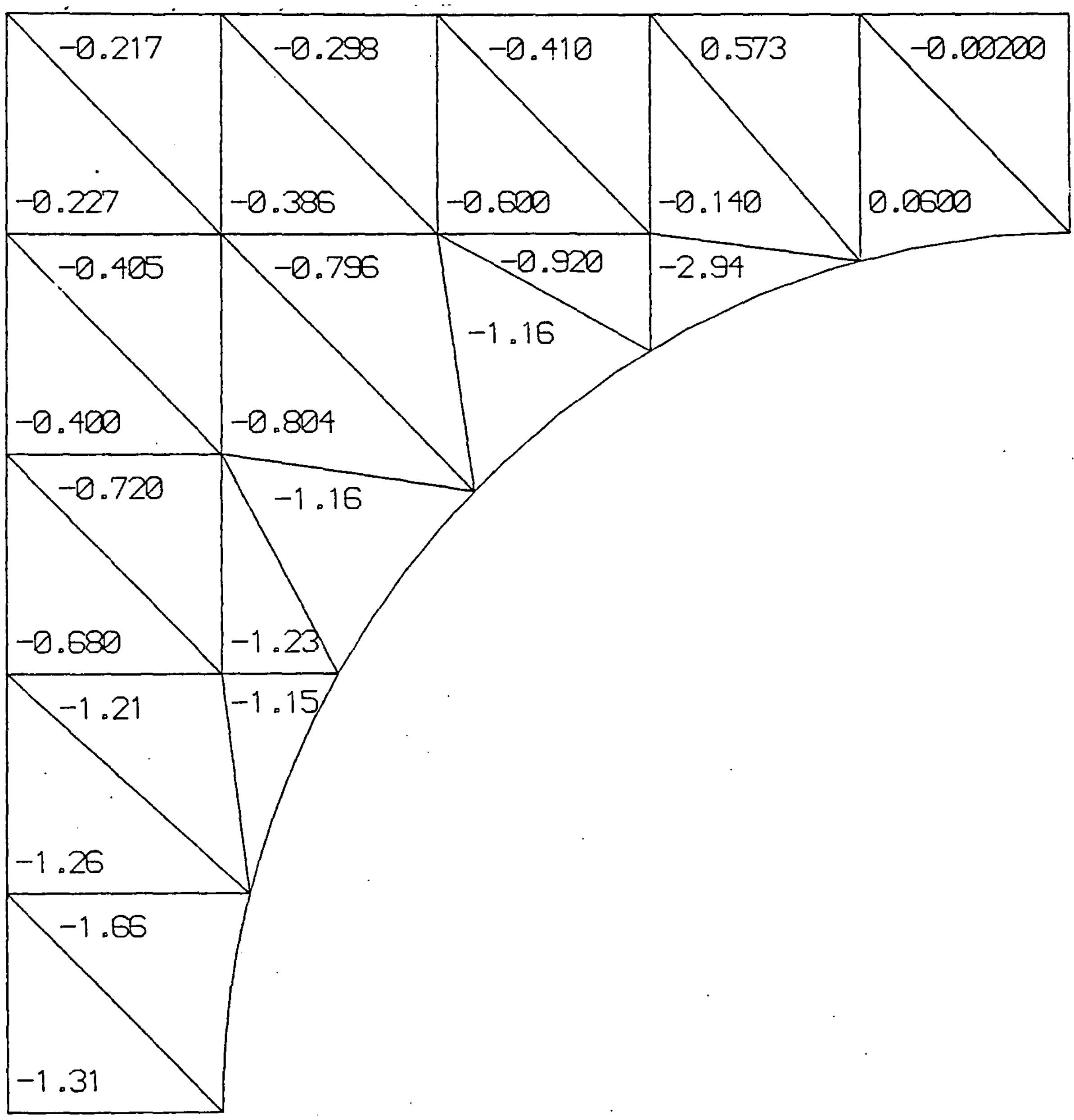

Figure 5.47 $\dot{\varepsilon}_v$ in a^{-1} for a compressible linear rheology with χ = 10 alu²/bar.a and v_d = 200 alu/a (Case 16).

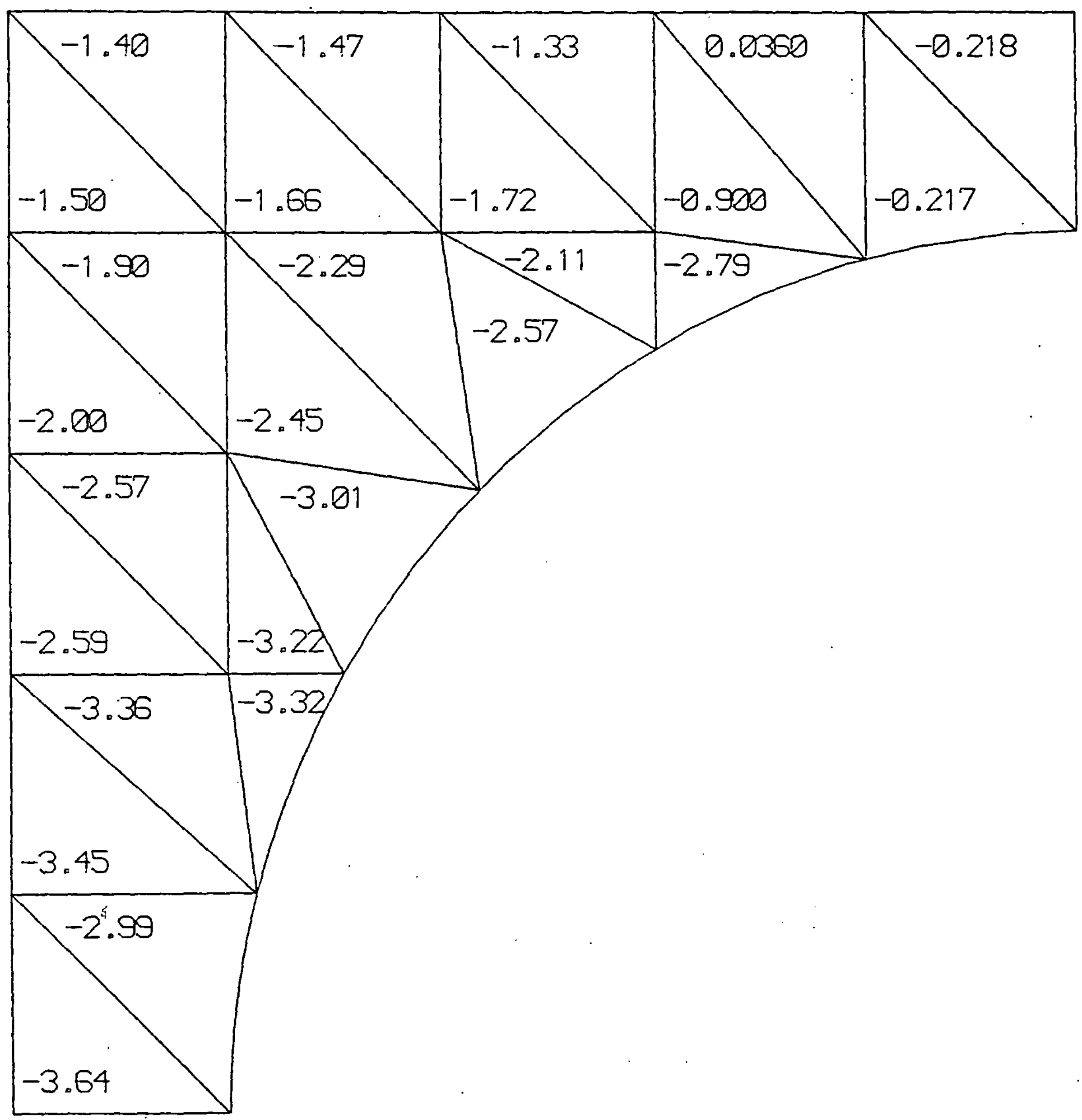

Figure 5.48 $\dot{\varepsilon}_v$ in a^{-1} for a compressible Glen rheology with χ = 1 alu²/bar.a and v_d = 10 alu/a (Case 29).

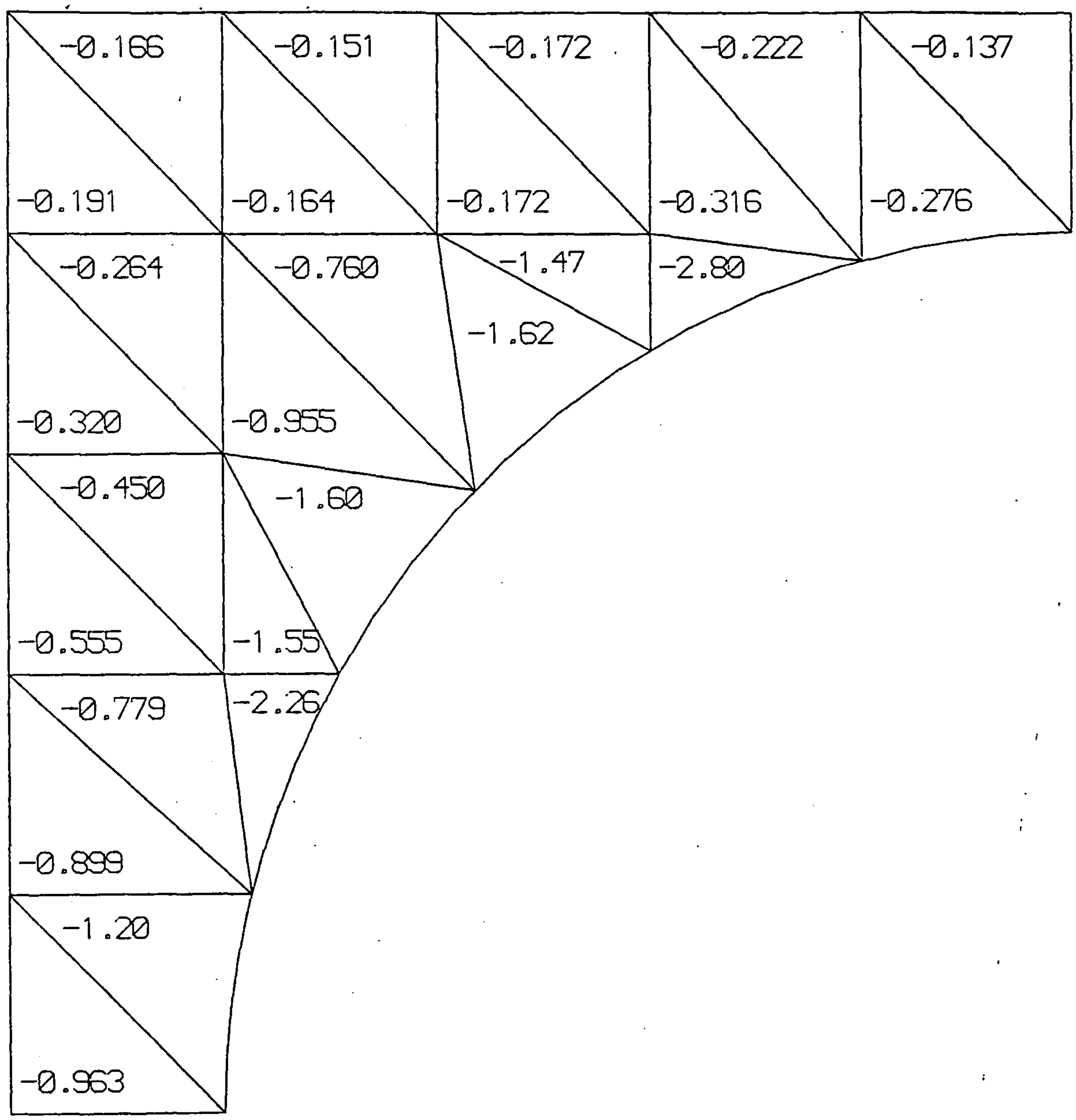

Figure 5.49 $\dot{\varepsilon}_v$ in a^{-1} for a compressible Glen rheology with χ = 1 alu²/bar.a and v_d = 400 alu/a (Case 33).

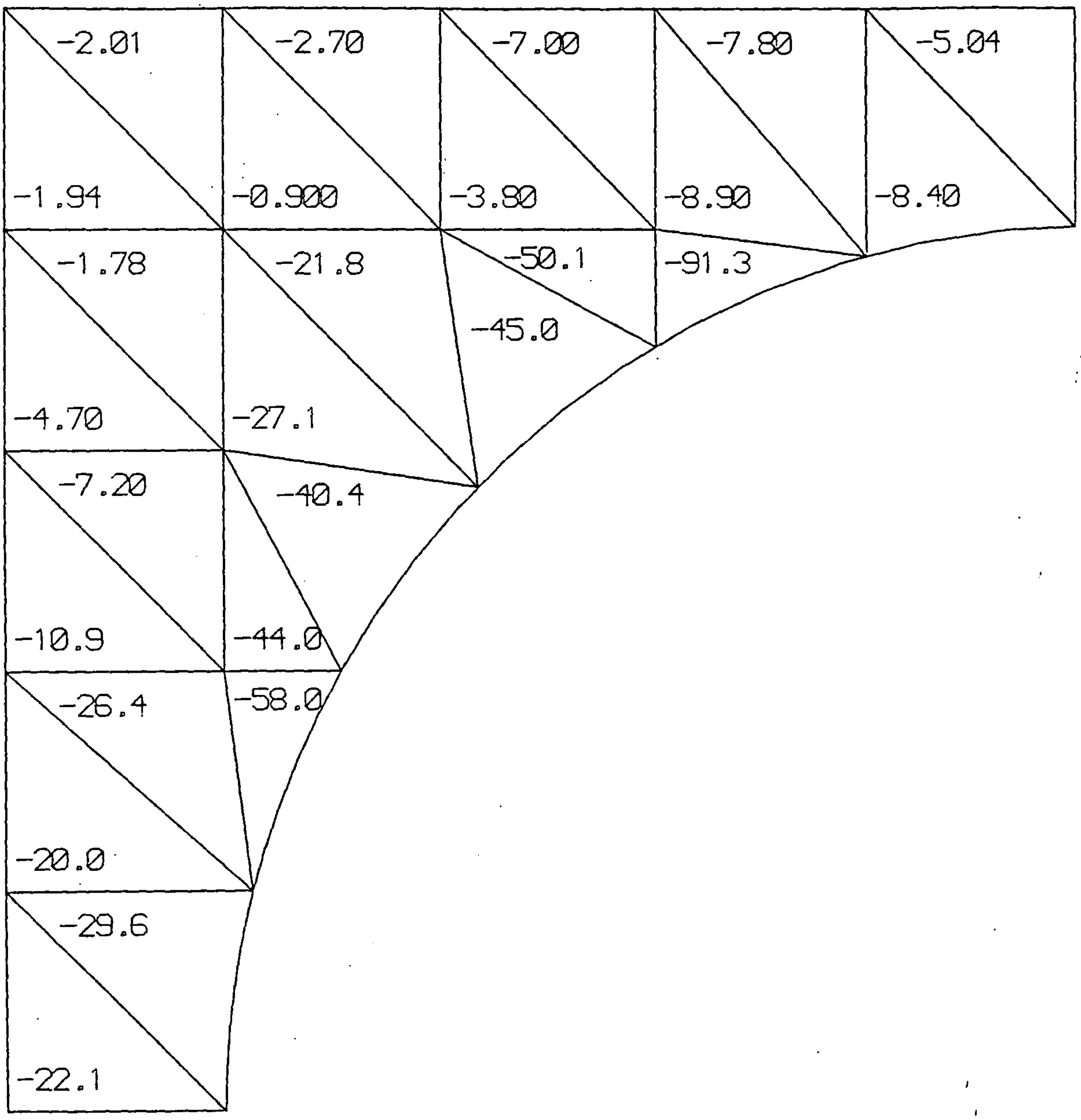

Figure 5.50 Regression exponent for $\dot{\varepsilon}_v$ against v_d for a compressible Glen rheology with χ = 1 alu² /bar.a (Cases 29 - 33).

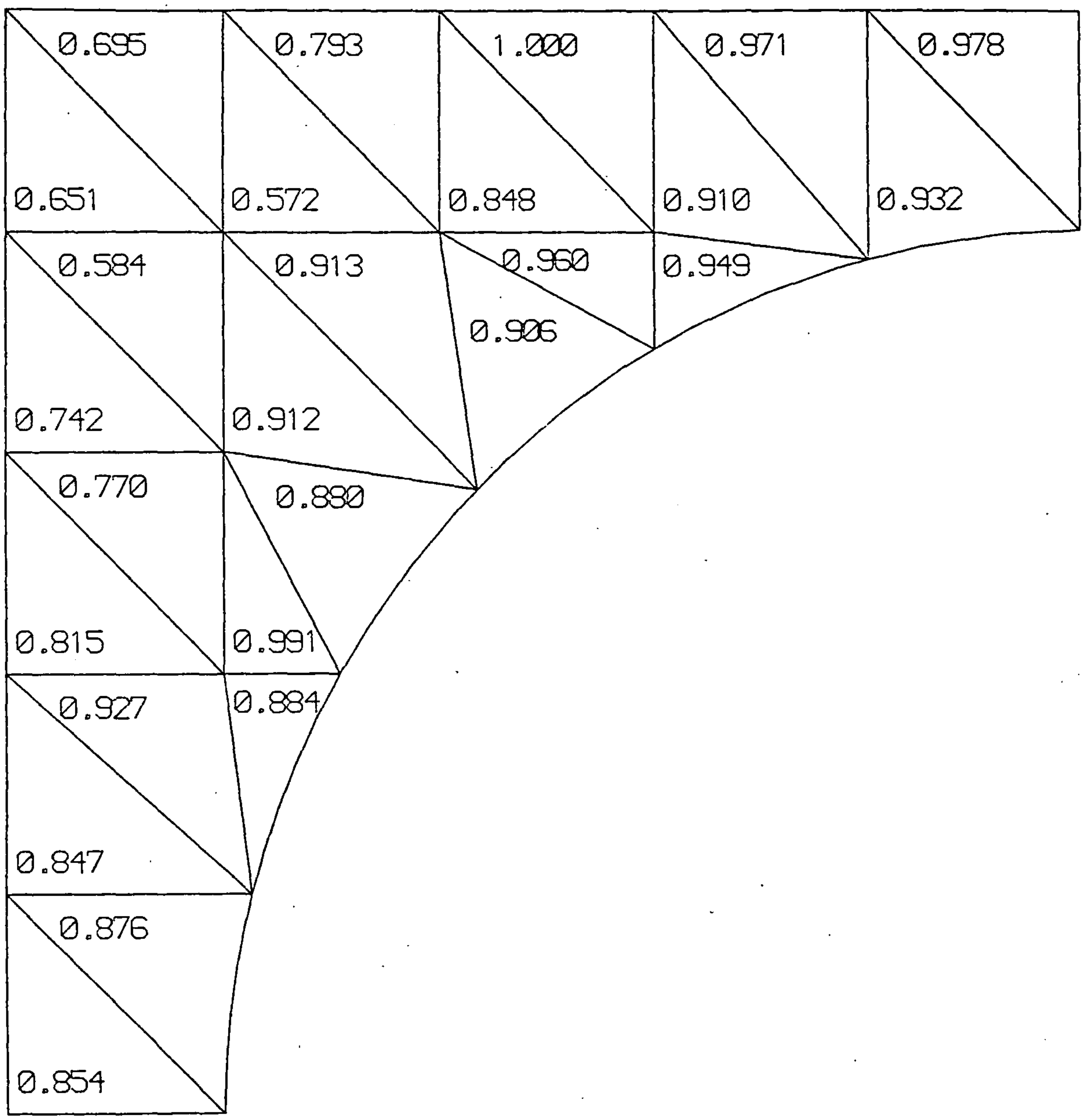

Figure 5.51 μ in bar.a for an incompressible Glen rheology with v_d = 10 alu/a (Case 23).

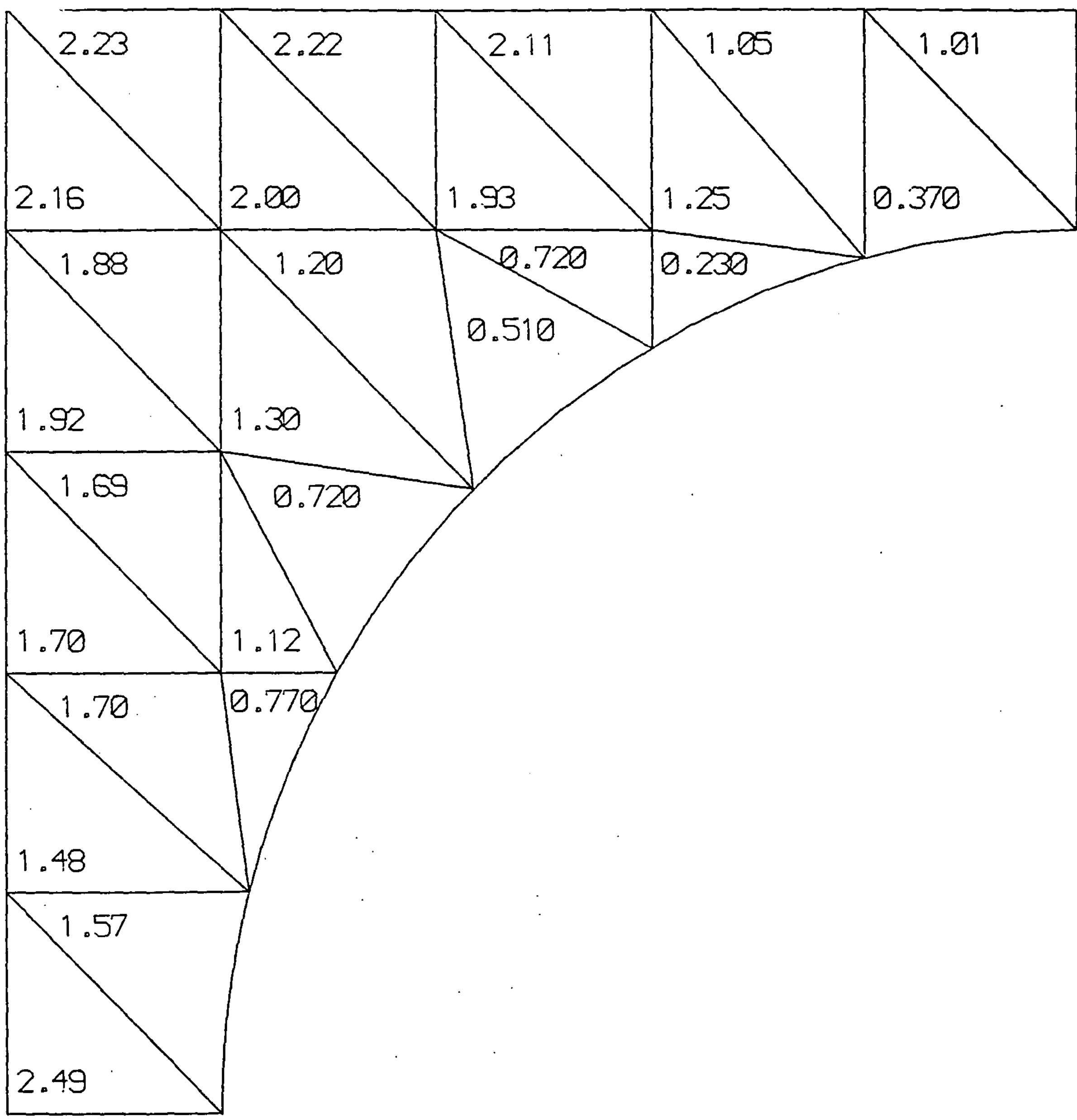

Figure 5.52 μ in bar.a for an incompressible Glen rheology with v_d = 400 alu/a (Case 26).

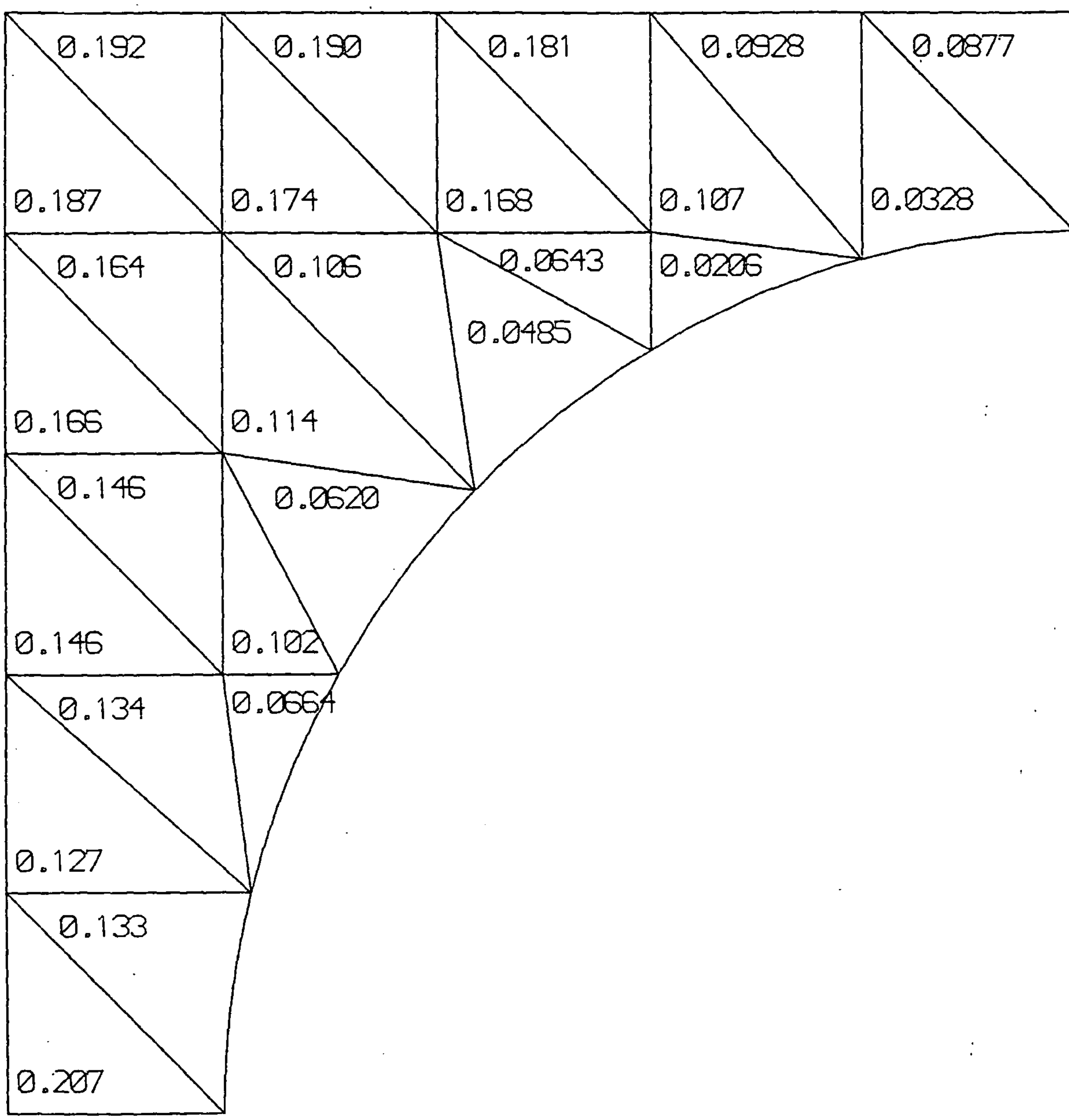

Figure 5.53 μ in bar.a for an incompressible Glen rheology with a cavity and v_d = 10 alu/a (Case 27).

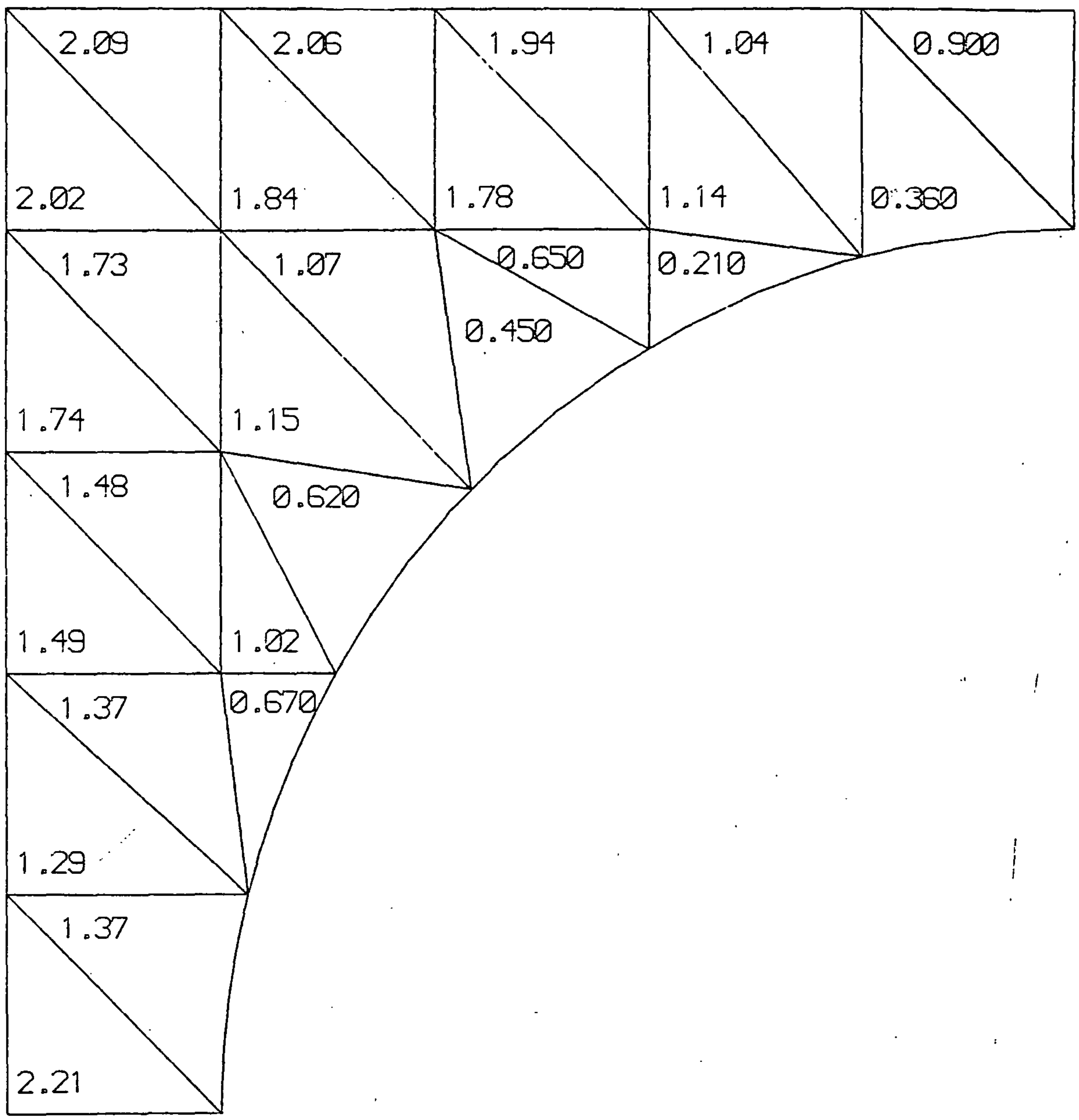

Figure 5.54 μ in bar.a for a compressible Glen rheology with χ = 1 alu²/bar.a and v_d = 10 alu/a (Case 29).

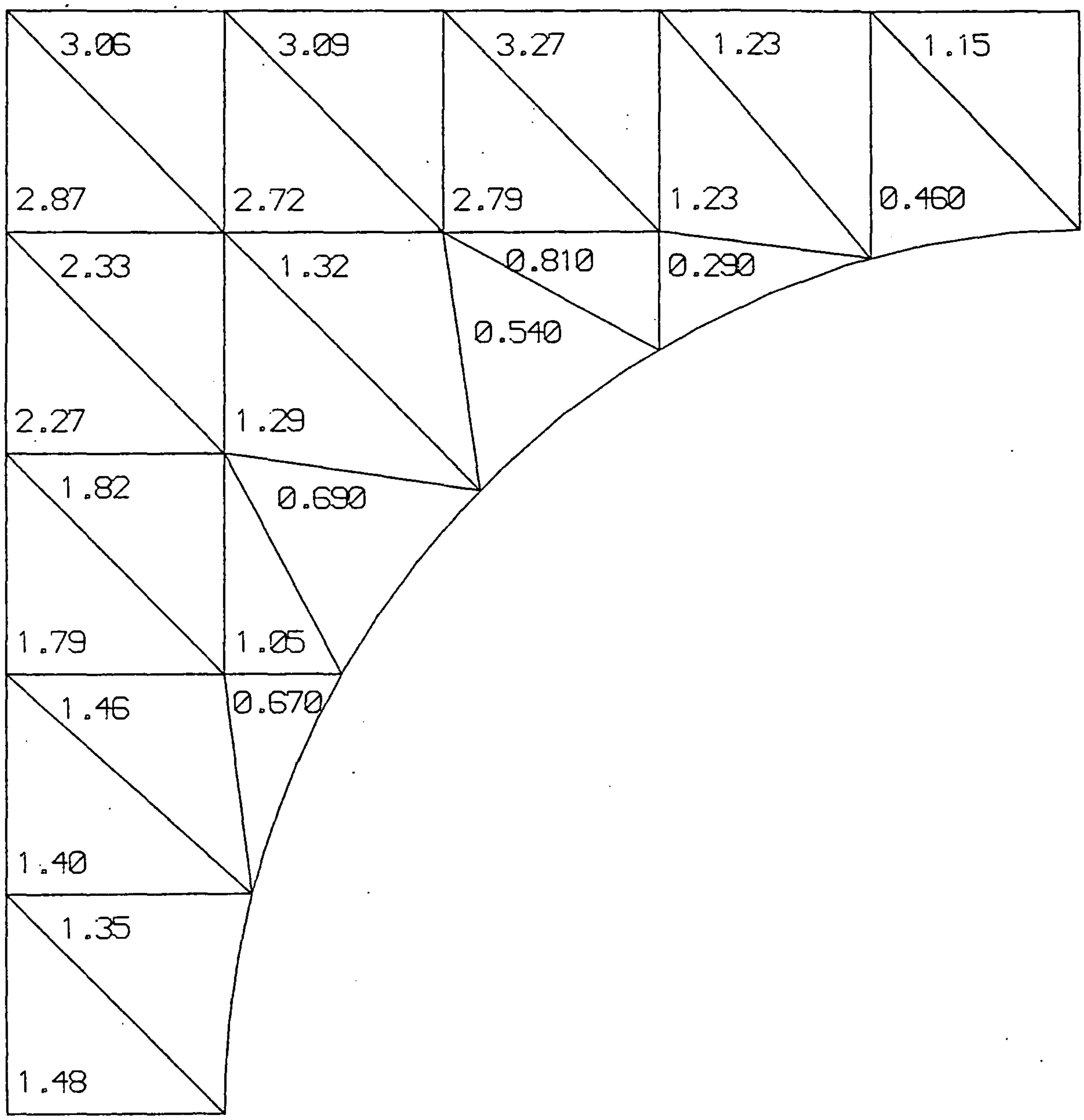

Figure 5.55 μ in bar.a for a compressible Glen rheology with χ = 1 alu²/bar.a with v_d = 400 alu/a (Case 33).

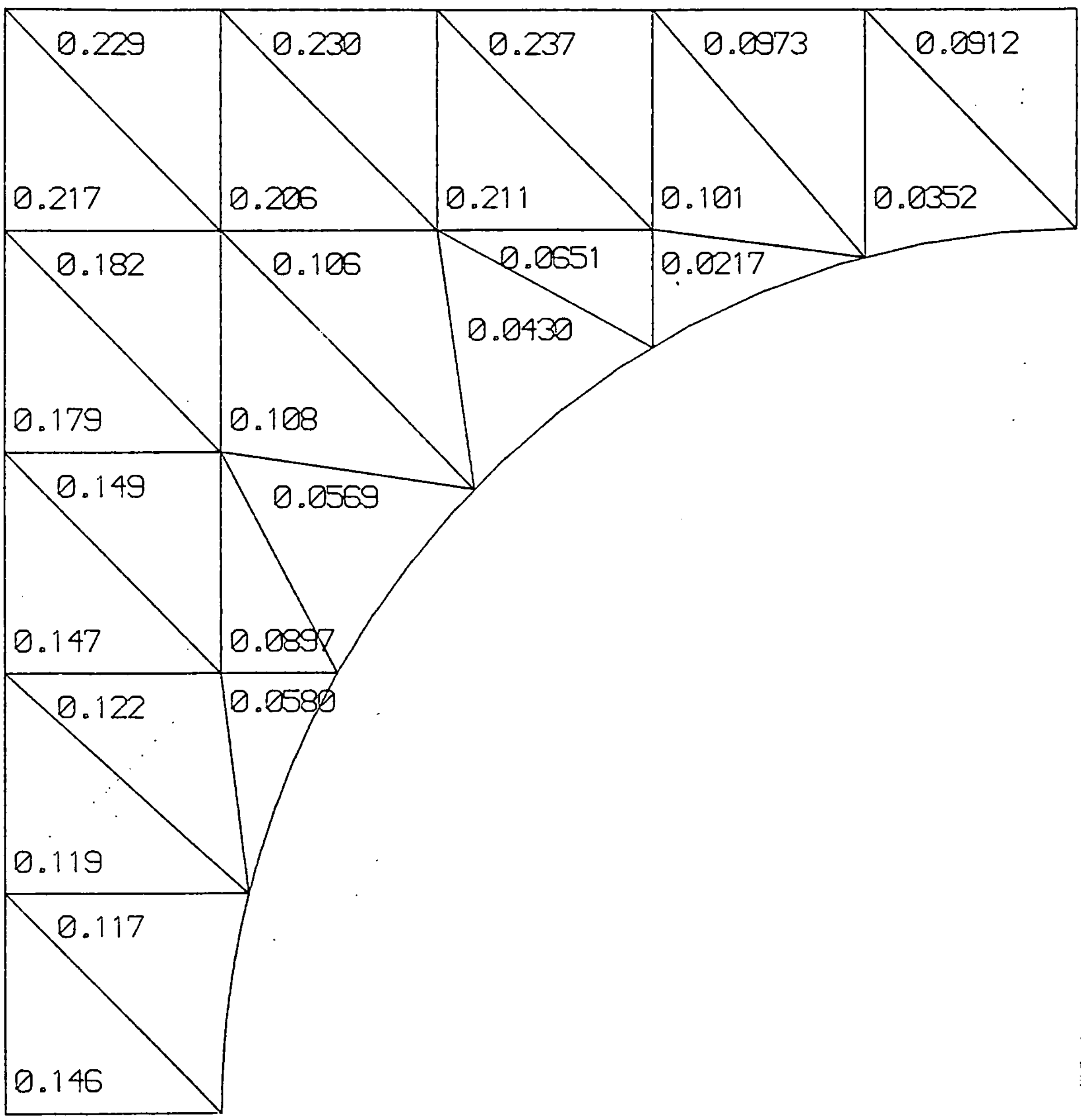

Figure 5.56 μ in bar.a for an incompressible Glen rheology with S = 10 alu/bar.a and v_d = 10 alu/a (Case 34).

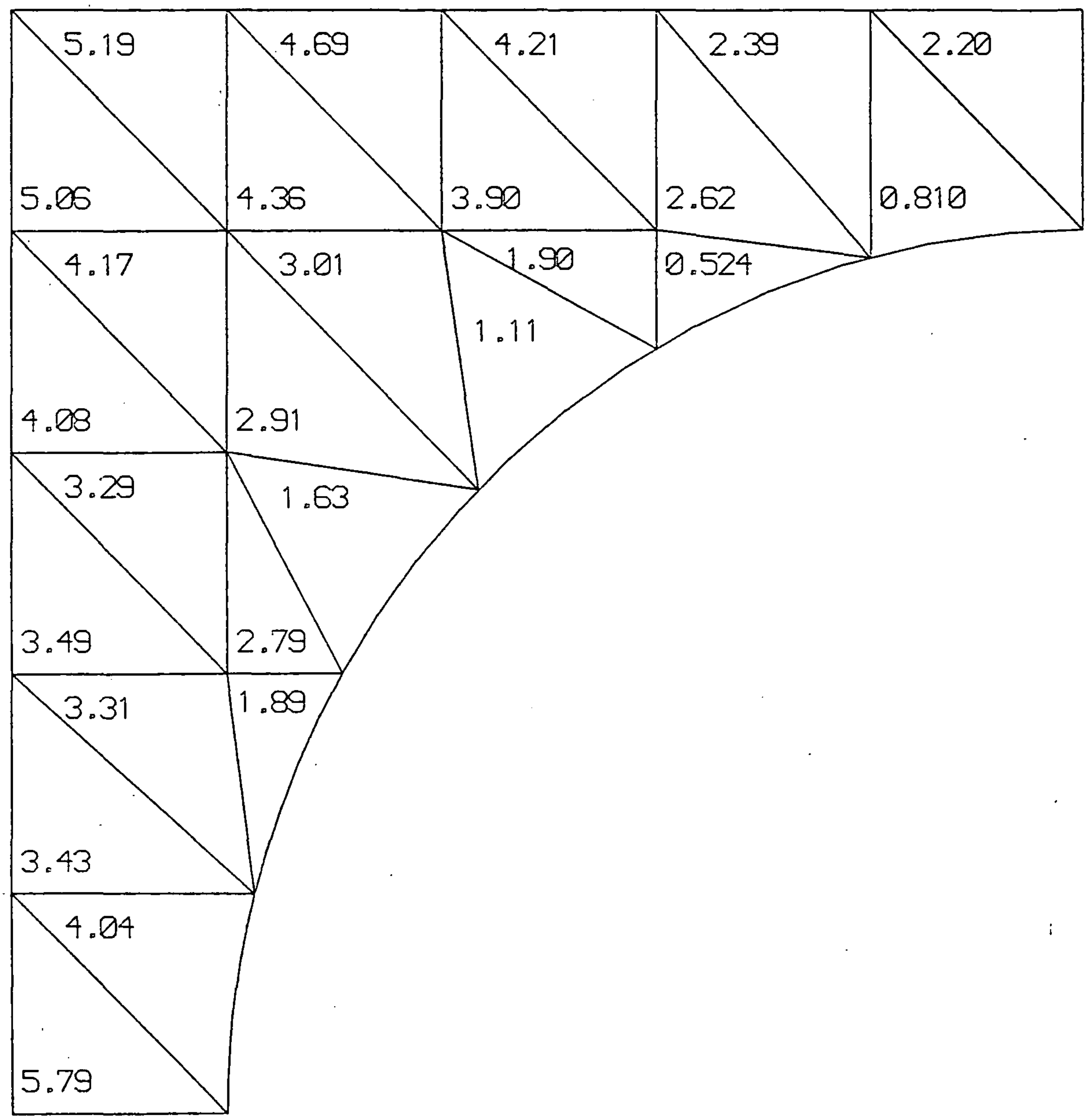

Figure 5.57 μ in bar.a for an incompressible Glen rheology with v_d = 10 alu/a for flow over a truncated sine ridge (Case 45).

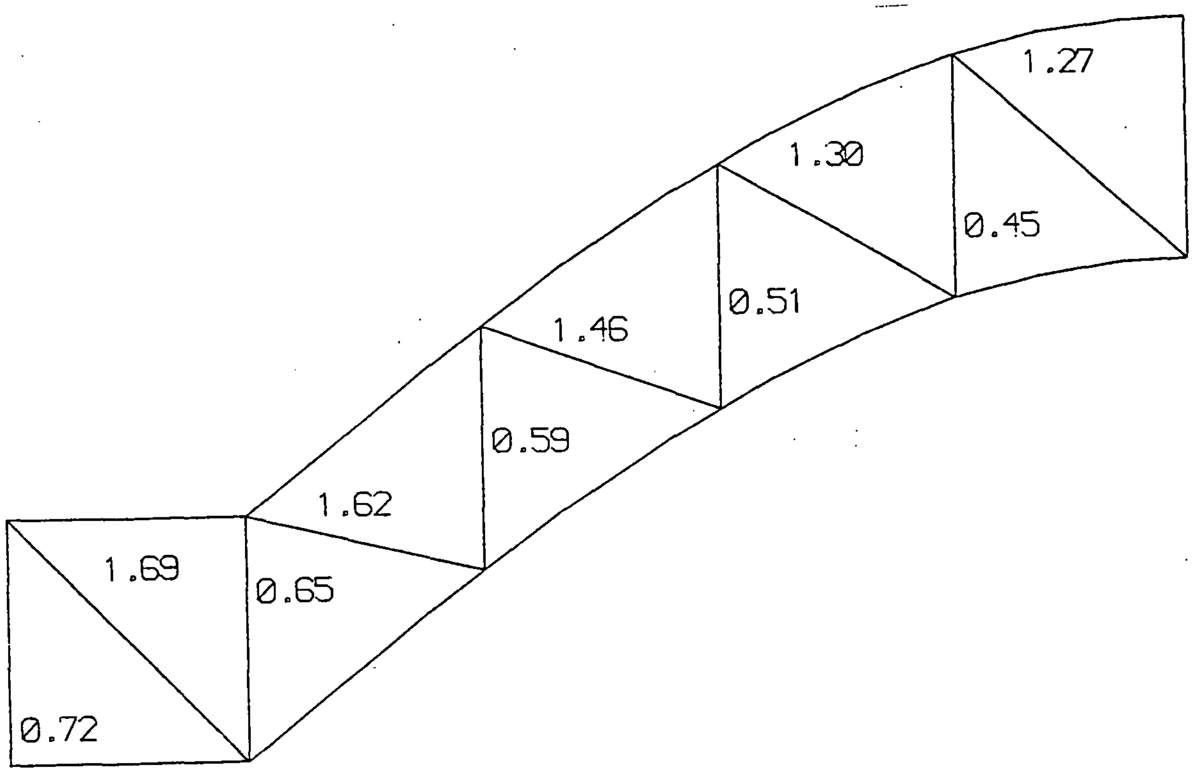

Figure 5.58 μ in bar.a for an incompressible Glen rheology with v_d = 400 alu/a for flow over a truncated sine ridge (Case 49).

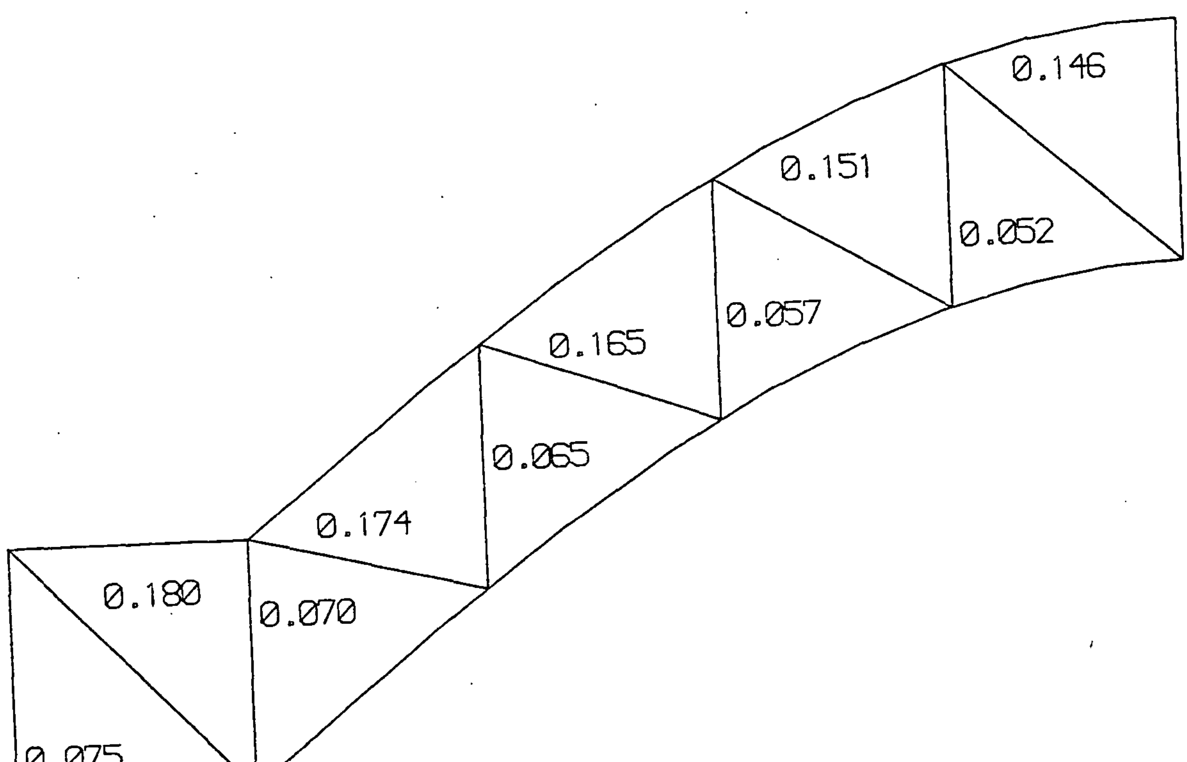

Figure 5.59 Regression exponent of μ against v_d for flow over a truncated sine ridge (Cases 45 - 49).

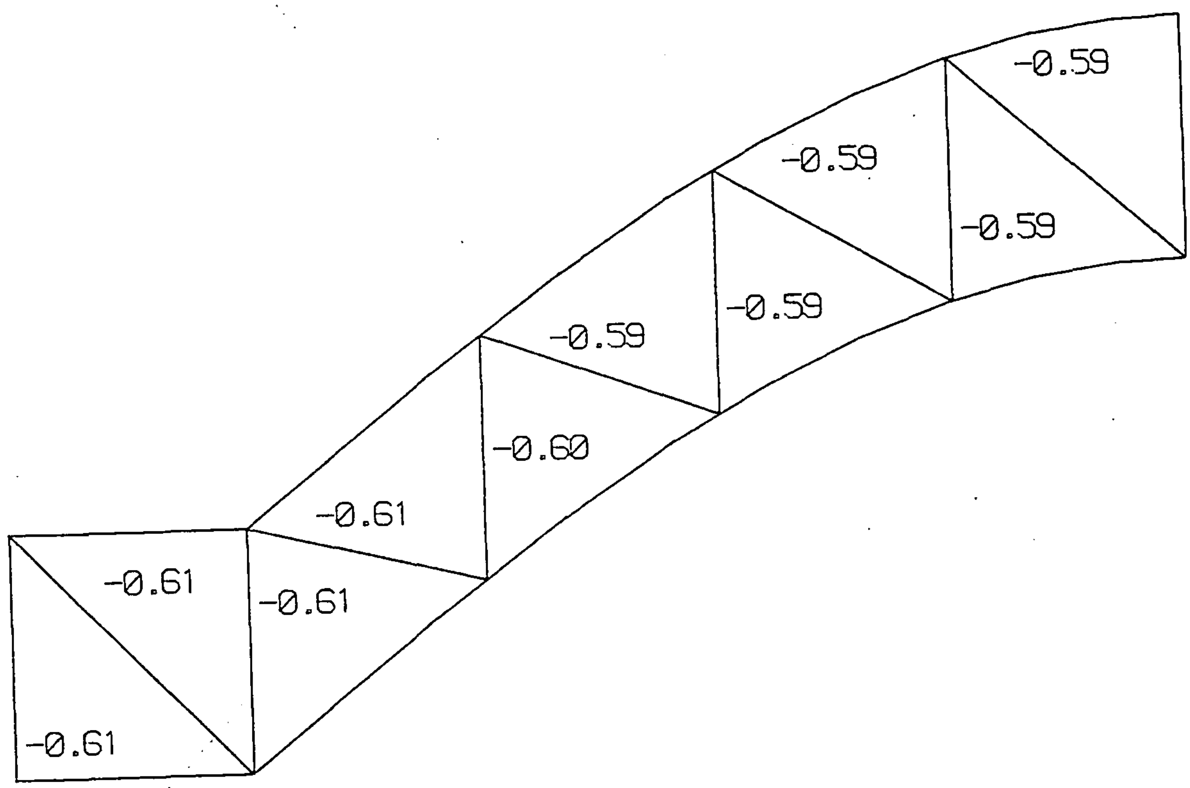

Figure 5.60 Semi-analytic interfacial stress for incompressible linear rheology with v_d = 10 alu/a.

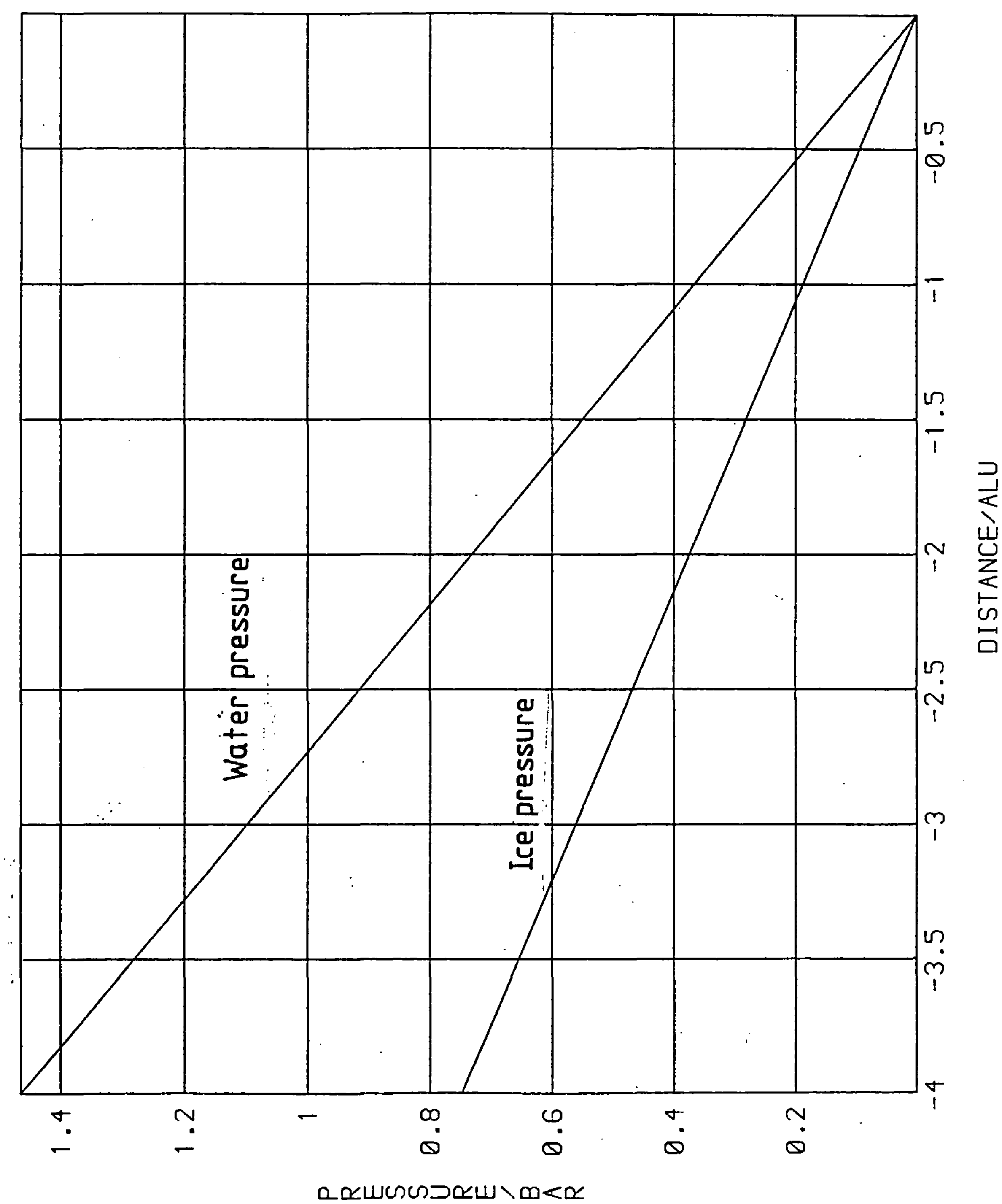

Figure 5.61 Semi-analytic interfacial stress for compressible linear rheology with χ = 1 alu²/bar.a and v_d = 10 alu/a.

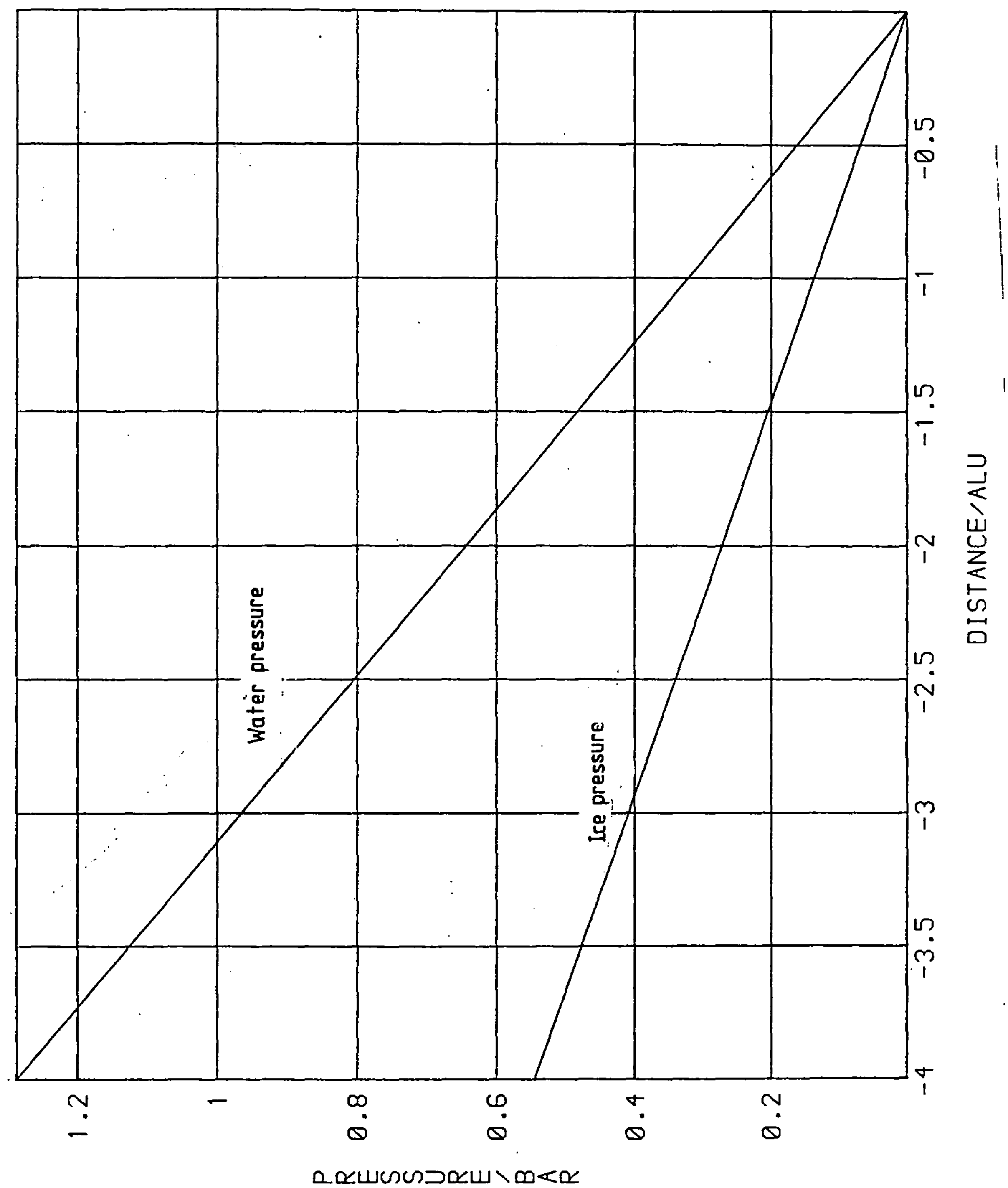

Figure 5.62 Semi-analytic interfacial stress for compressible linear rheology with χ = 10 alu² /bar.a and v_d = 10 alu/a.

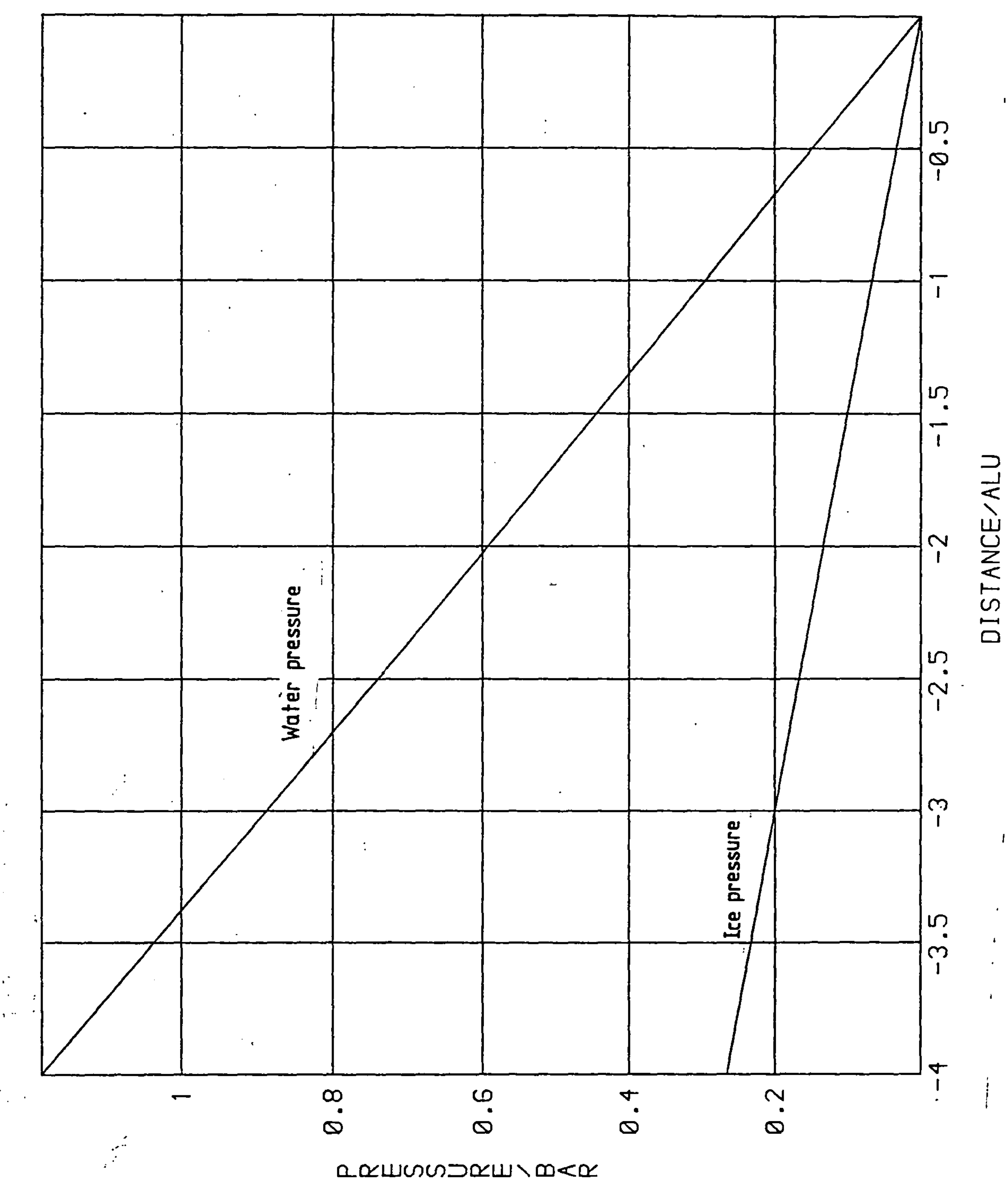

Figure 5.63 Semi-analytic interfacial stress for incompressible Glen rheology with v_d = 10 alu/a.

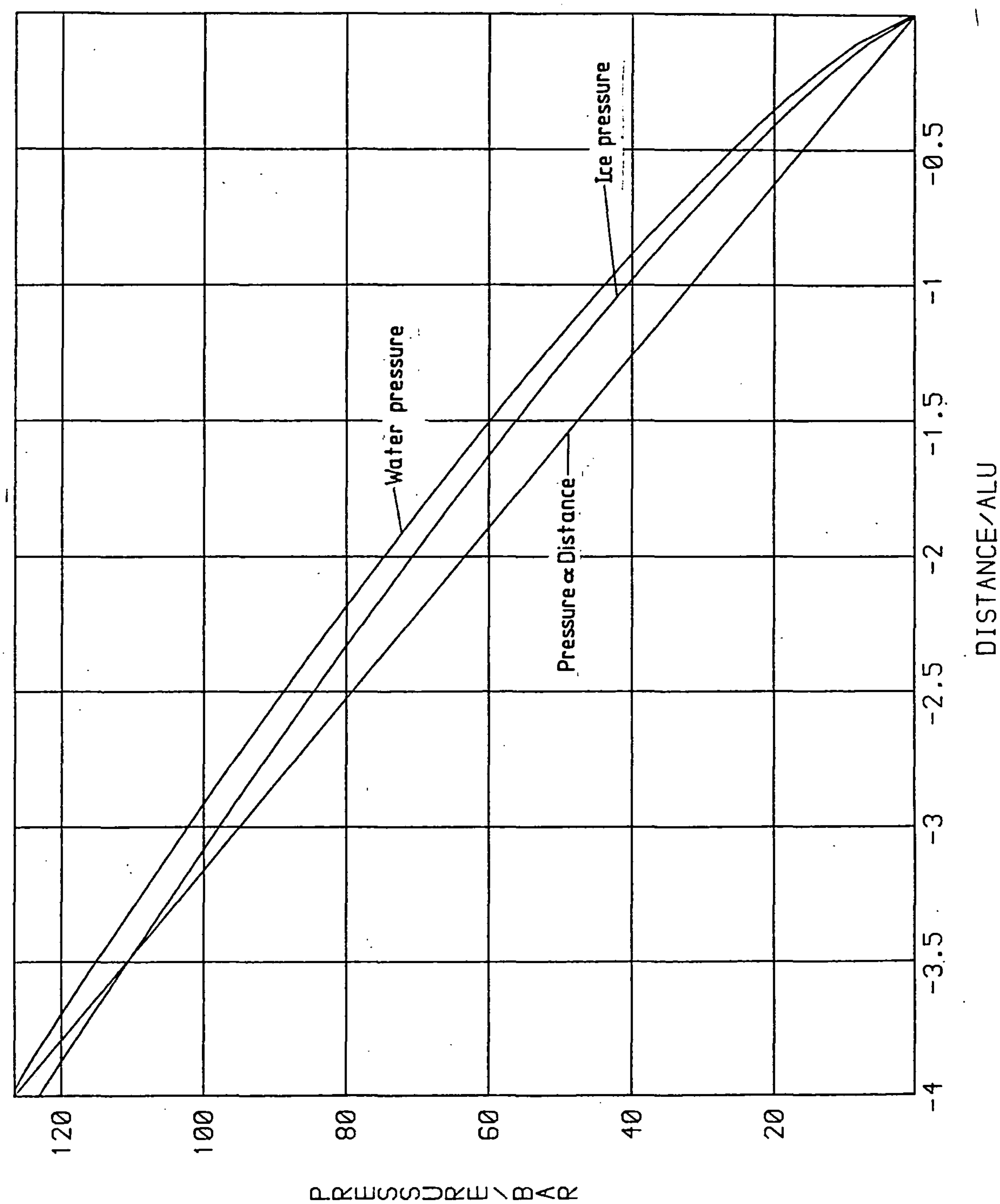

Figure 5.64 Semi-analytic interfacial stress for compressible Glen rheology with χ = 1 alu²/bar.a and v_d = 10 alu/a.

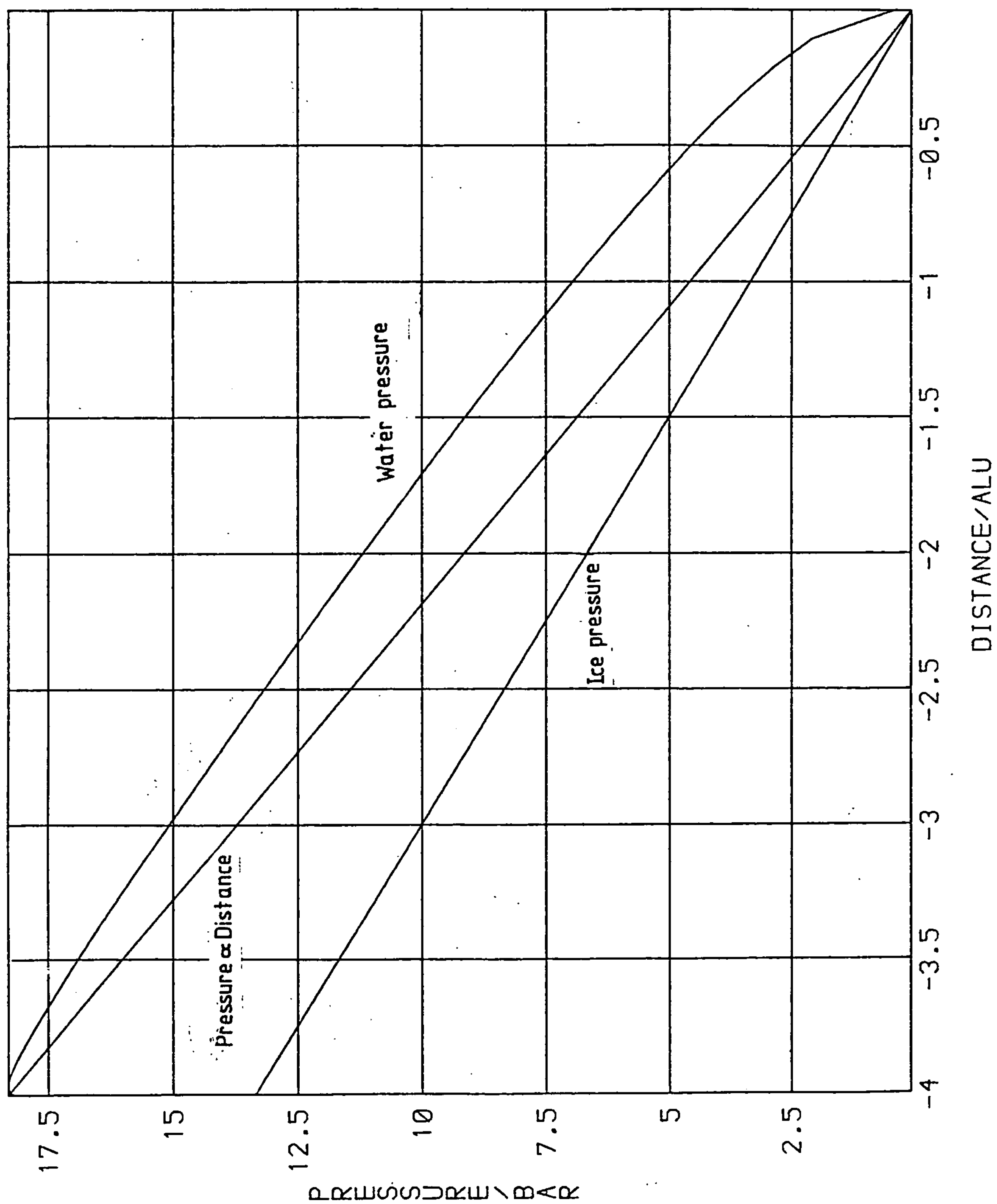

Figure 5.65 Finite element mesh for uni-axial flow modelling.

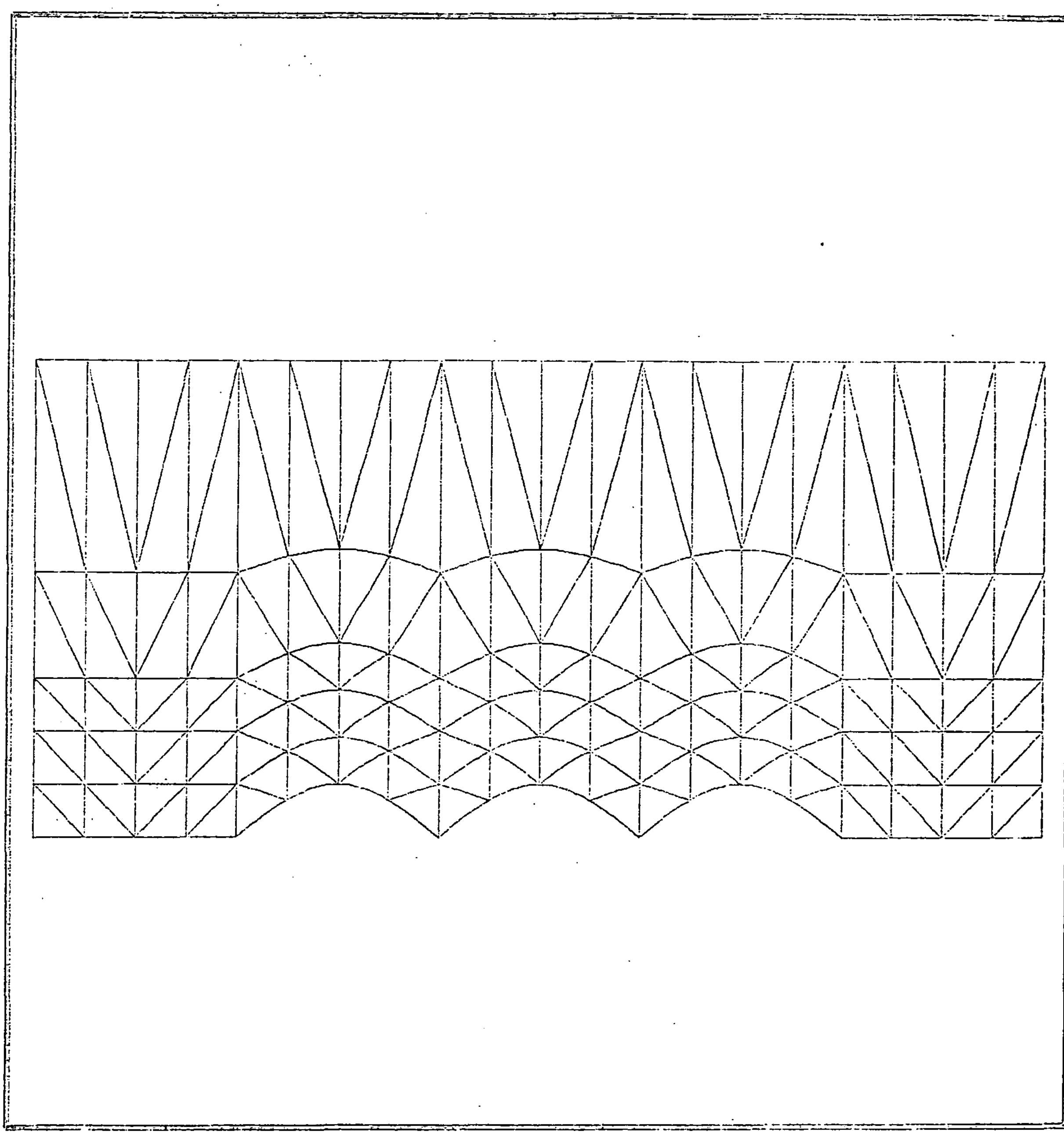

Figure 5.66 Velocity contours in alu/a for v_d = 10 alu/a and a bed of S = 0·002 alu/bar.a, wide-hummocked case.

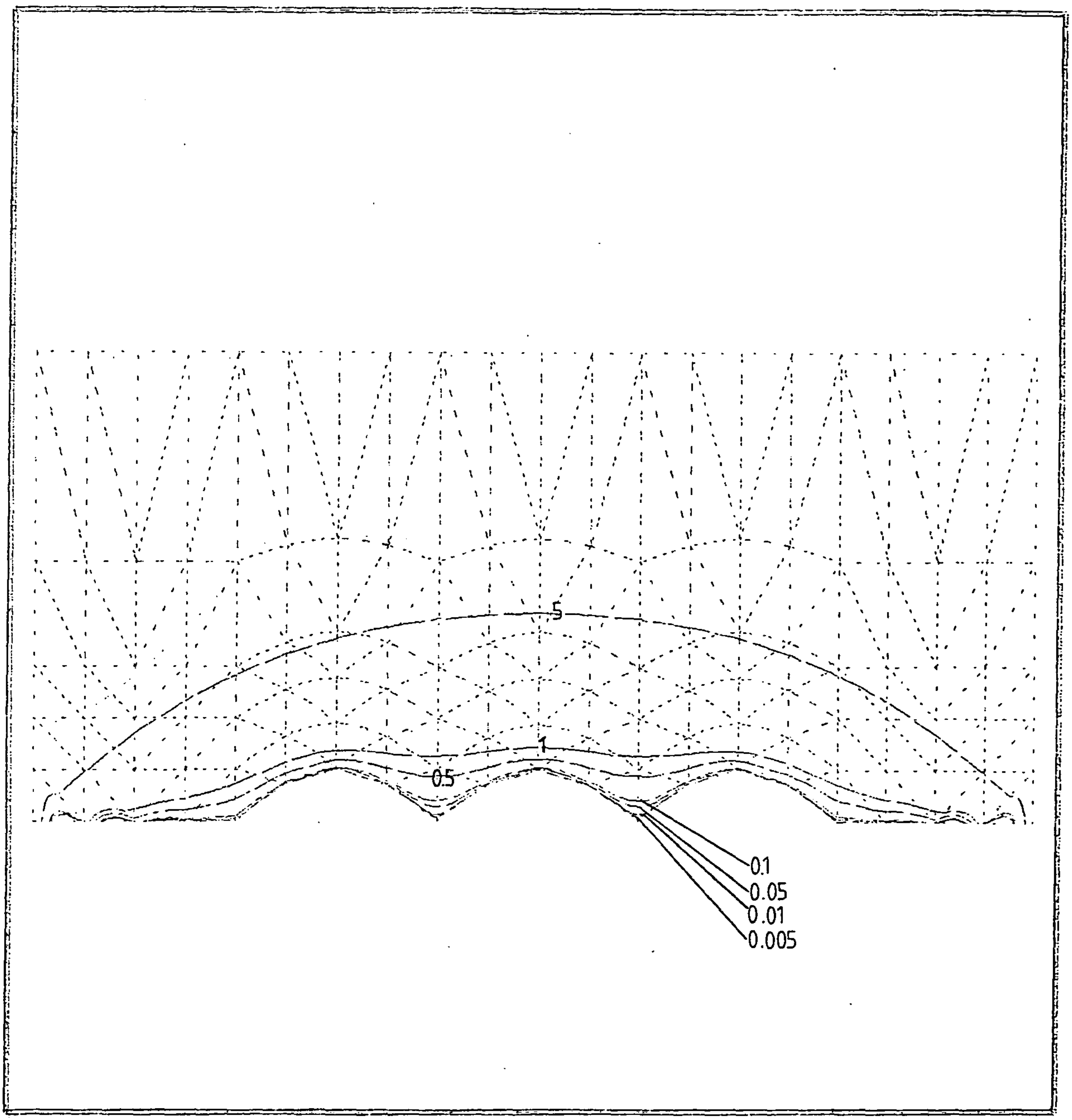

Figure 5.67 Velocity contours in alu/a for v_d = 10 alu/a and bed of S = 0·01 alu/bar.a, wide-hummocked case.

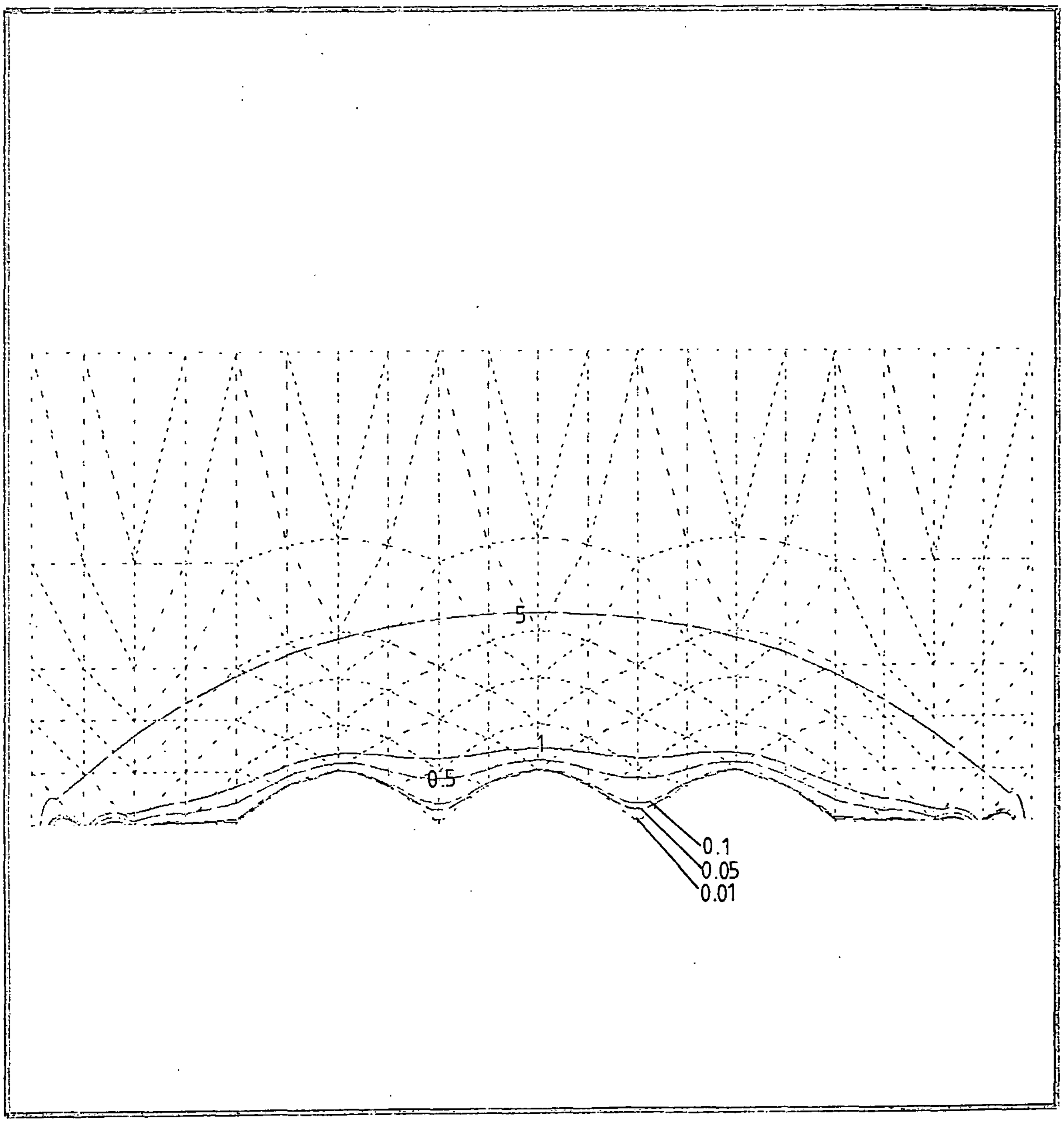

Figure 5.68 Velocity contours in alu/a for v_d = 10 alu/a and a bed of S = 0·02 alu/bar.a, wide-hummocked case.

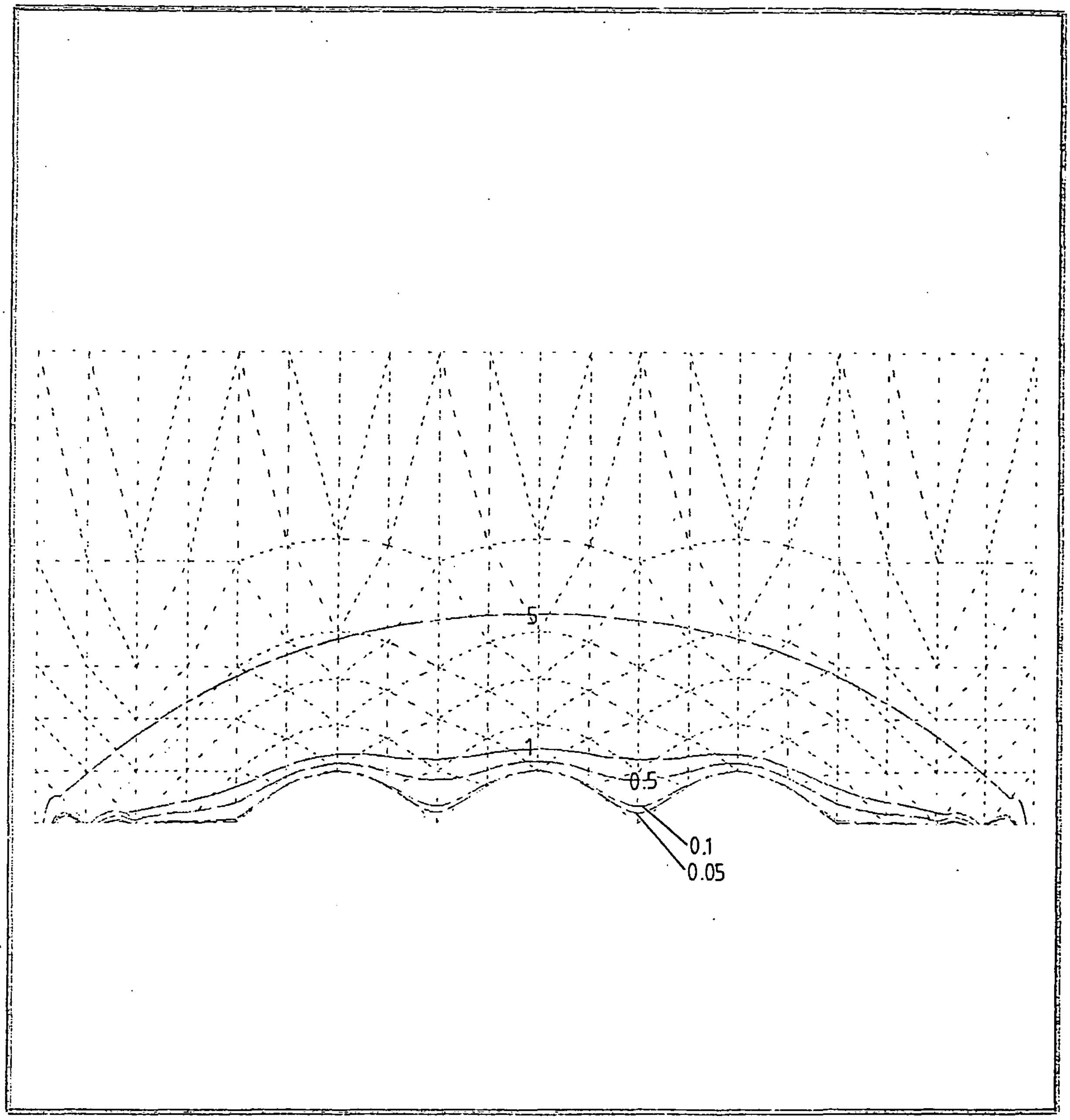

Figure 5.69 Velocity contours in alu/a for v_d = 10 alu/a and a bed of S = 0·1 alu/bar.a, wide-hummocked case.

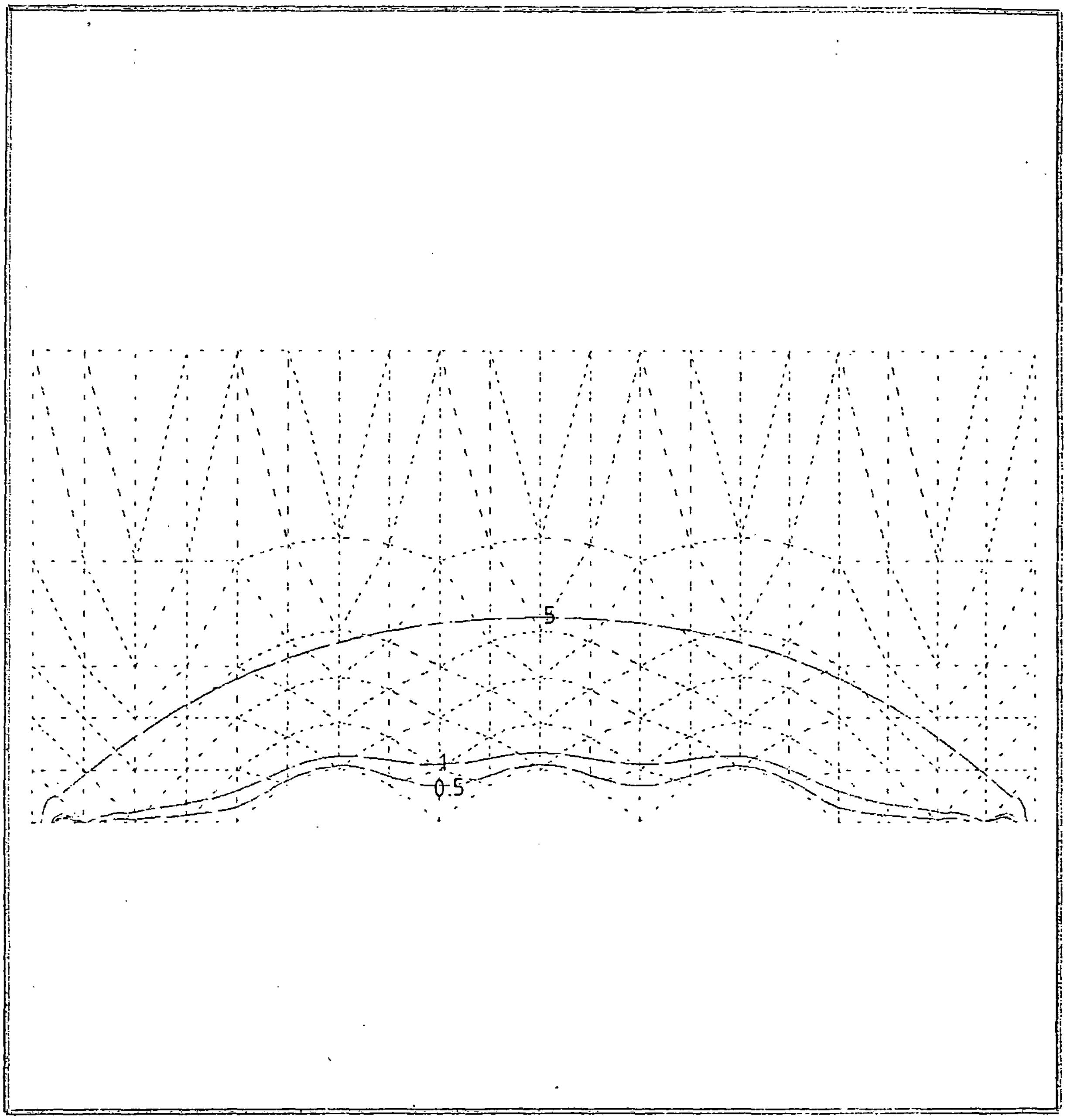

Figure 5.70 Velocity contours in alu/a for v_d = 10 alu/a and a bed of S = 0·2 alu/bar.a, wide-hummocked case.

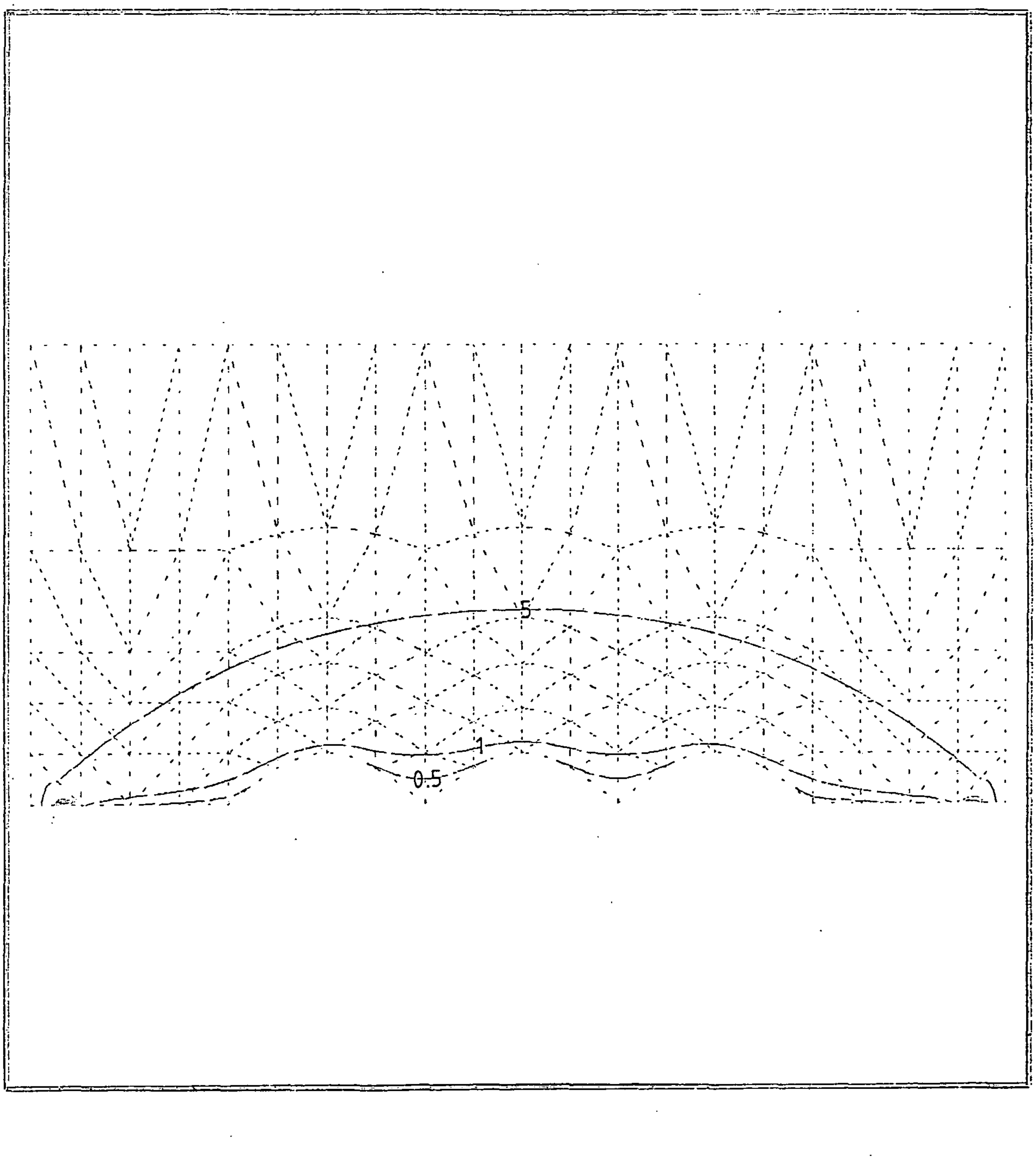

Figure 5.71 Velocity contours in alu/a for v_d = 10 alu/a, and a bed of S = 1 alu/bar.a, wide-hummocked case.

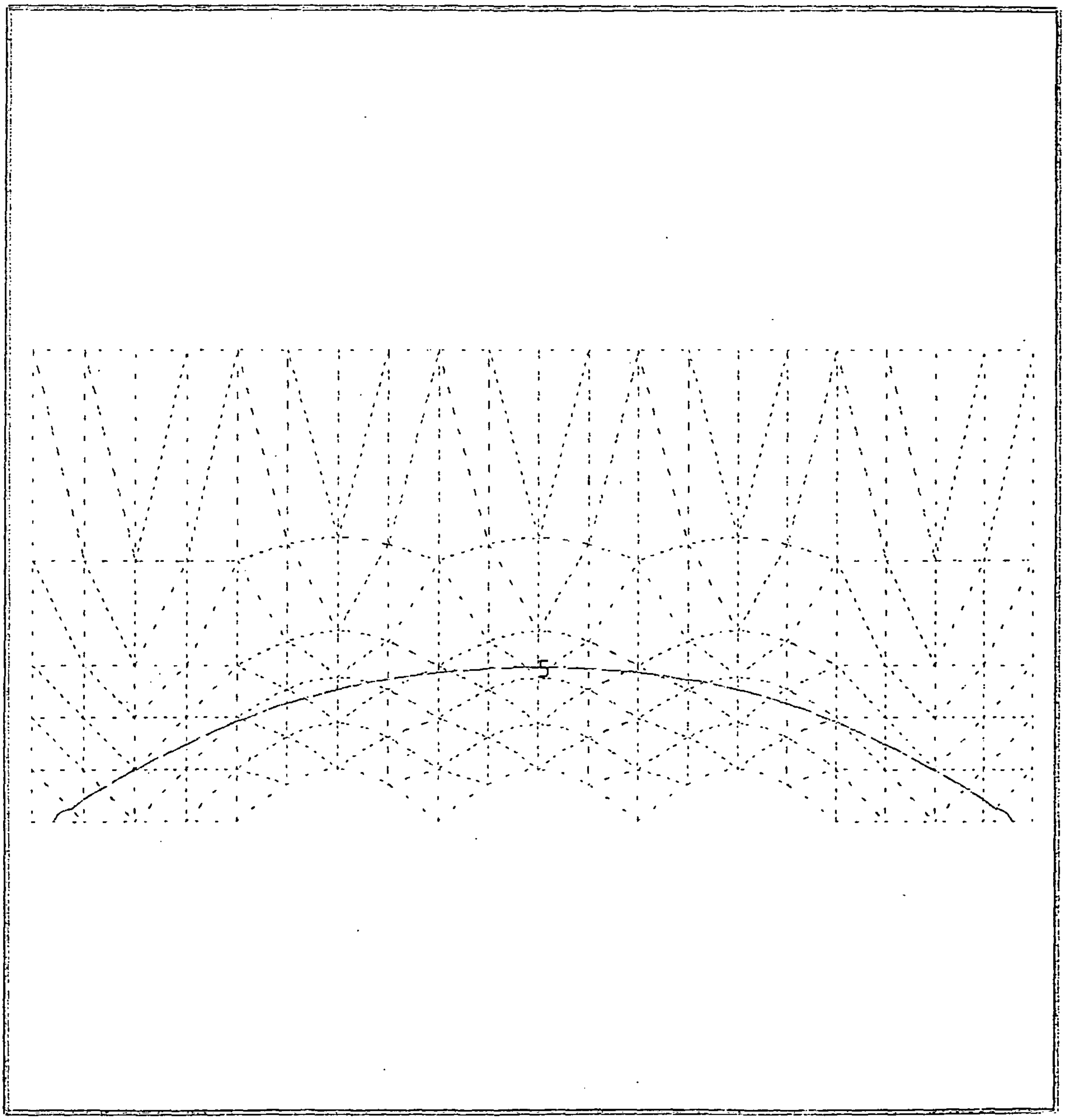

Figure 5.72 Velocity contours in alu/a for v_d = 10 alu/a and a bed of $\underset{\sim}{S}$ = 2 alu/bar.a, wide-hummocked case.

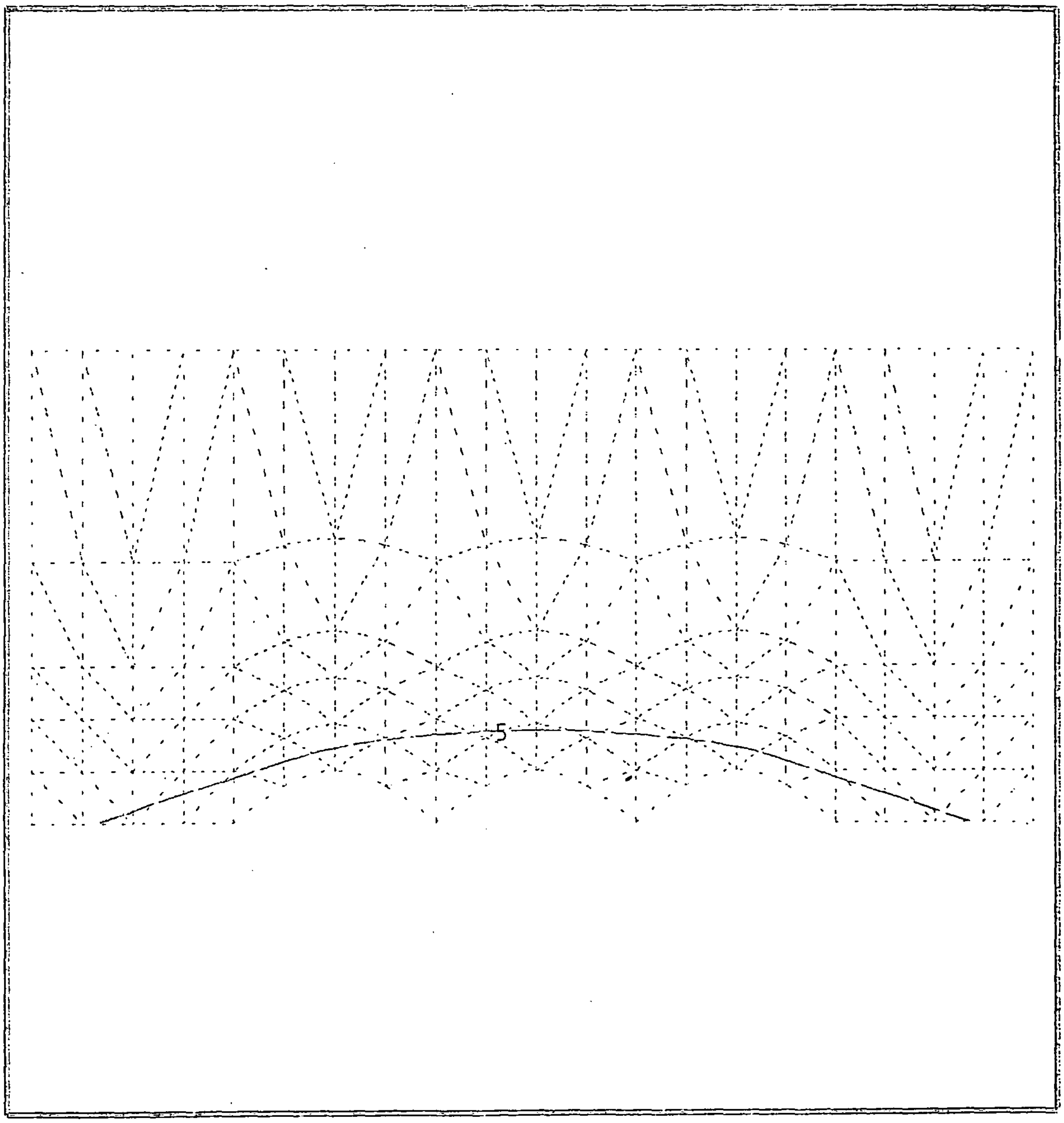

Figure 5.73 Velocity contours in alu/a for v_d = 50 alu/a and a bed of S = 0·01 alu/bar.a, wide-hummocked case.

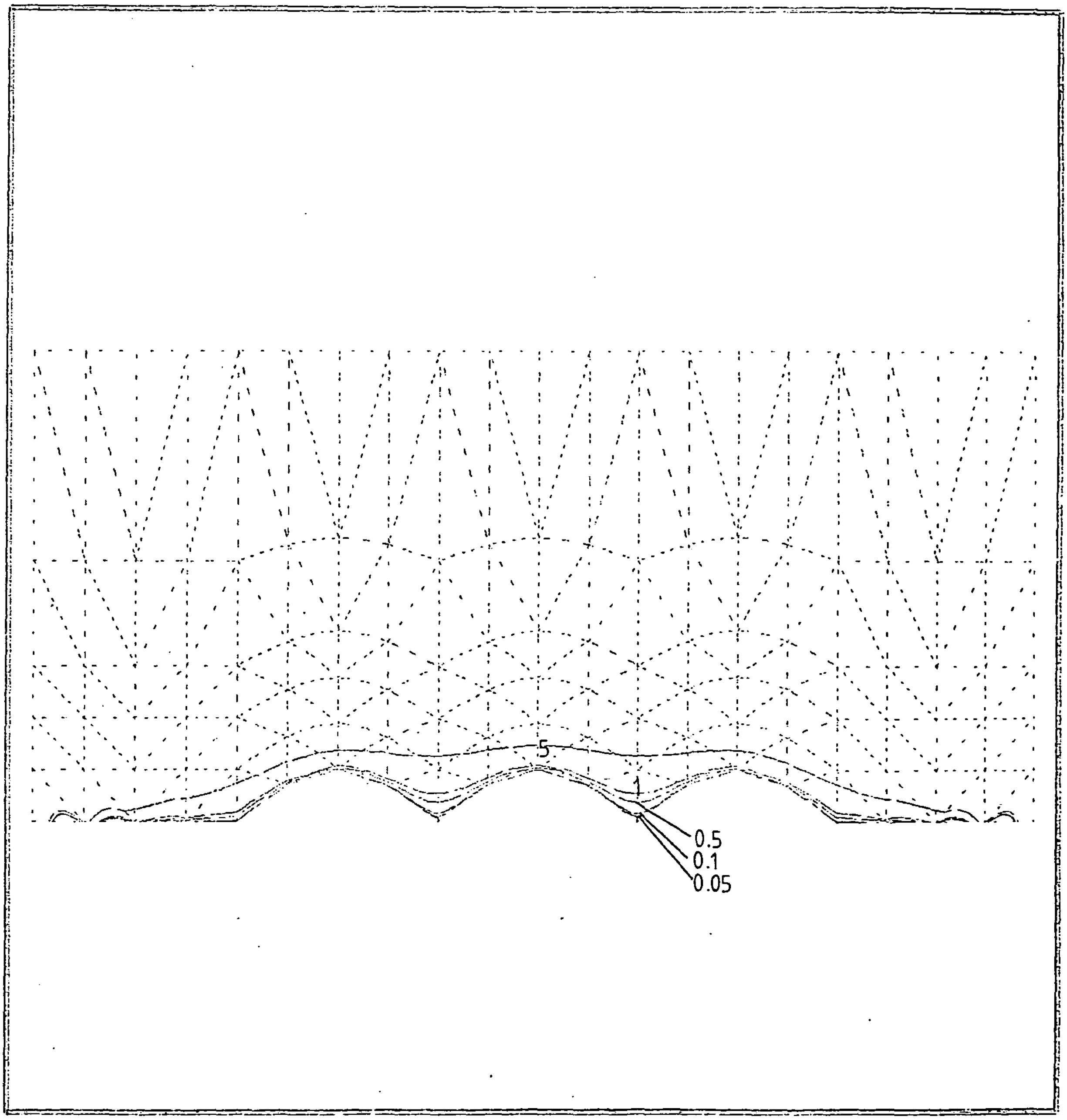

Figure 5.74 Velocity contours in alu/a for v_d = 100 alu/a and a bed of S = 0·01 alu/bar.a, wide-hummocked case.

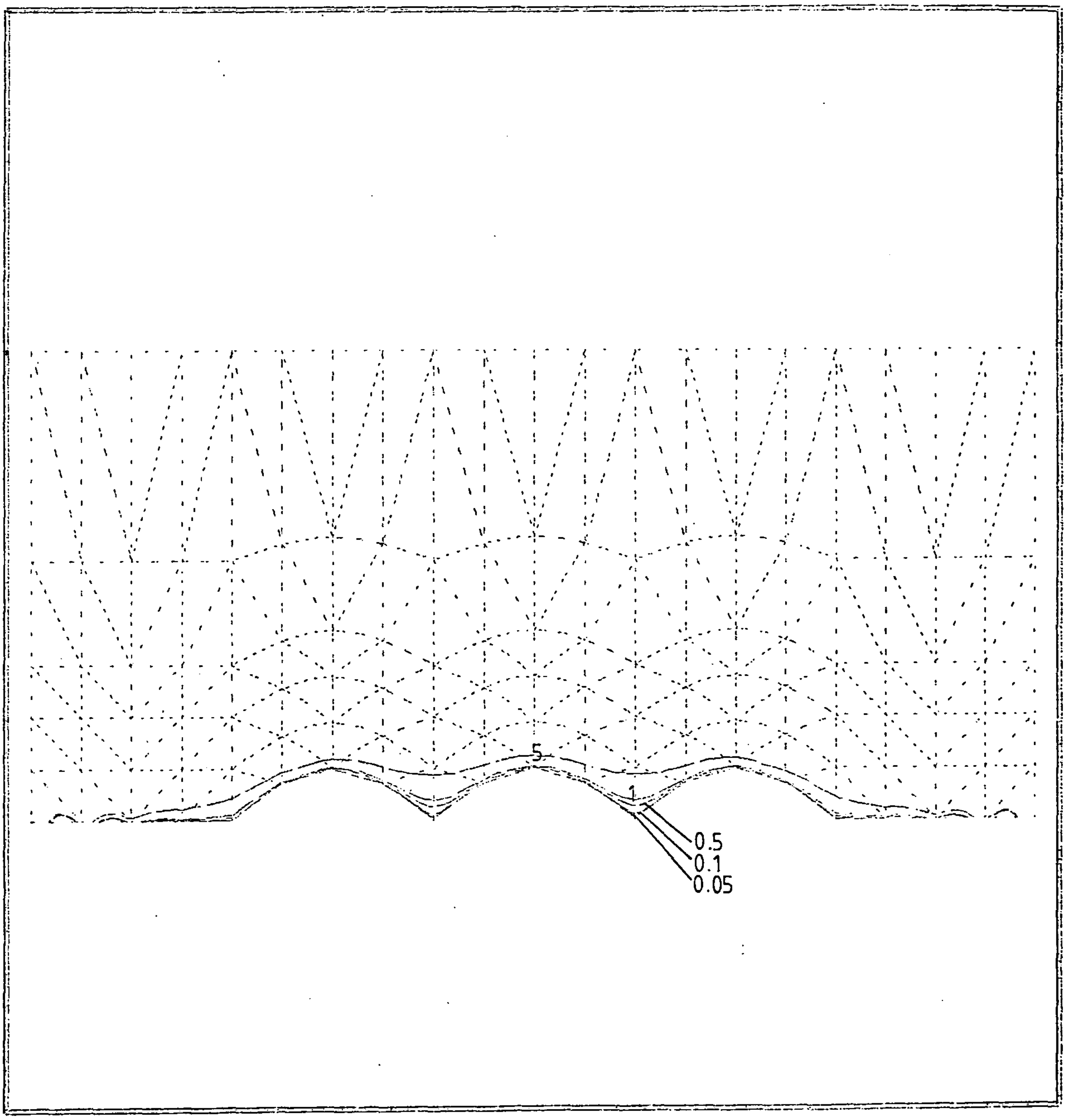

Figure 5.75 Velocity contours in alu/a for v_d = 200 alu/a and a bed of S = 0·01 alu/bar.a, wide-hummocked case.

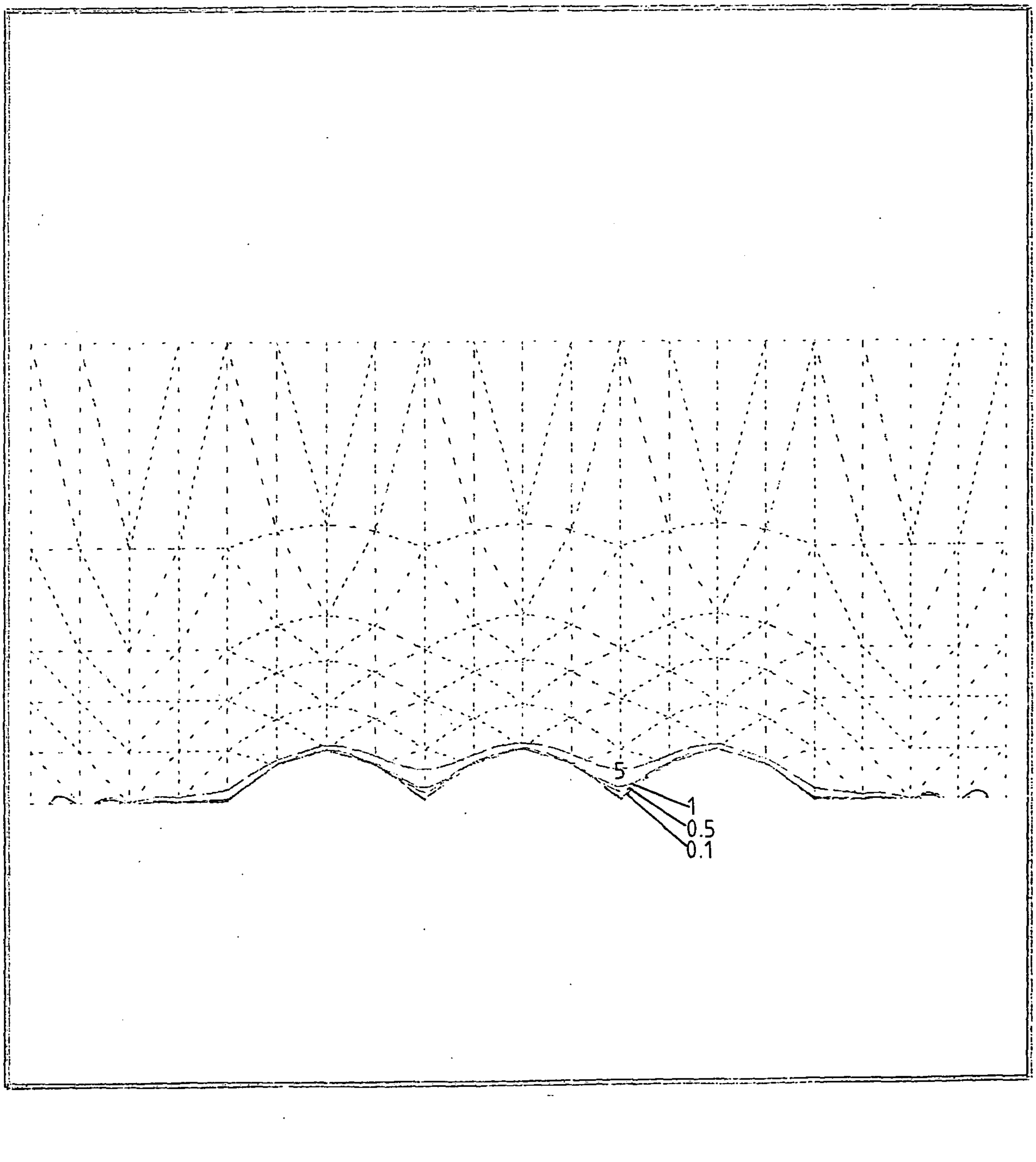

Figure 5.76 Velocity contours in alu/a for v_d = 10 alu/a and a bed of S = 0·02 alu/bar.a, narrow-hummocked case.

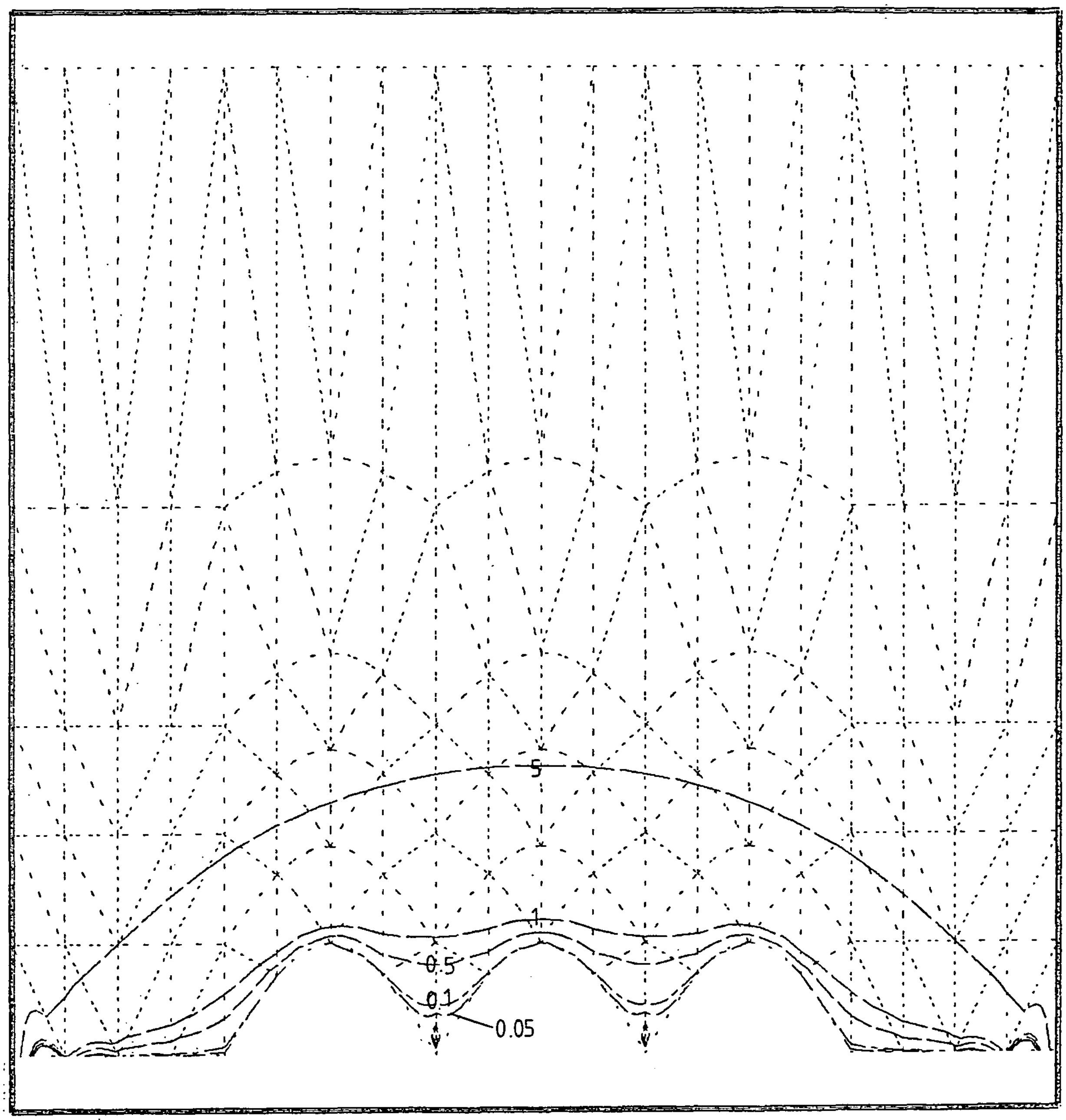

Figure 5.77 Velocity contours in alu/a for v_d = 10 alu/a, bed of S = 0·002 alu/bar.a, narrow-hummocked case.

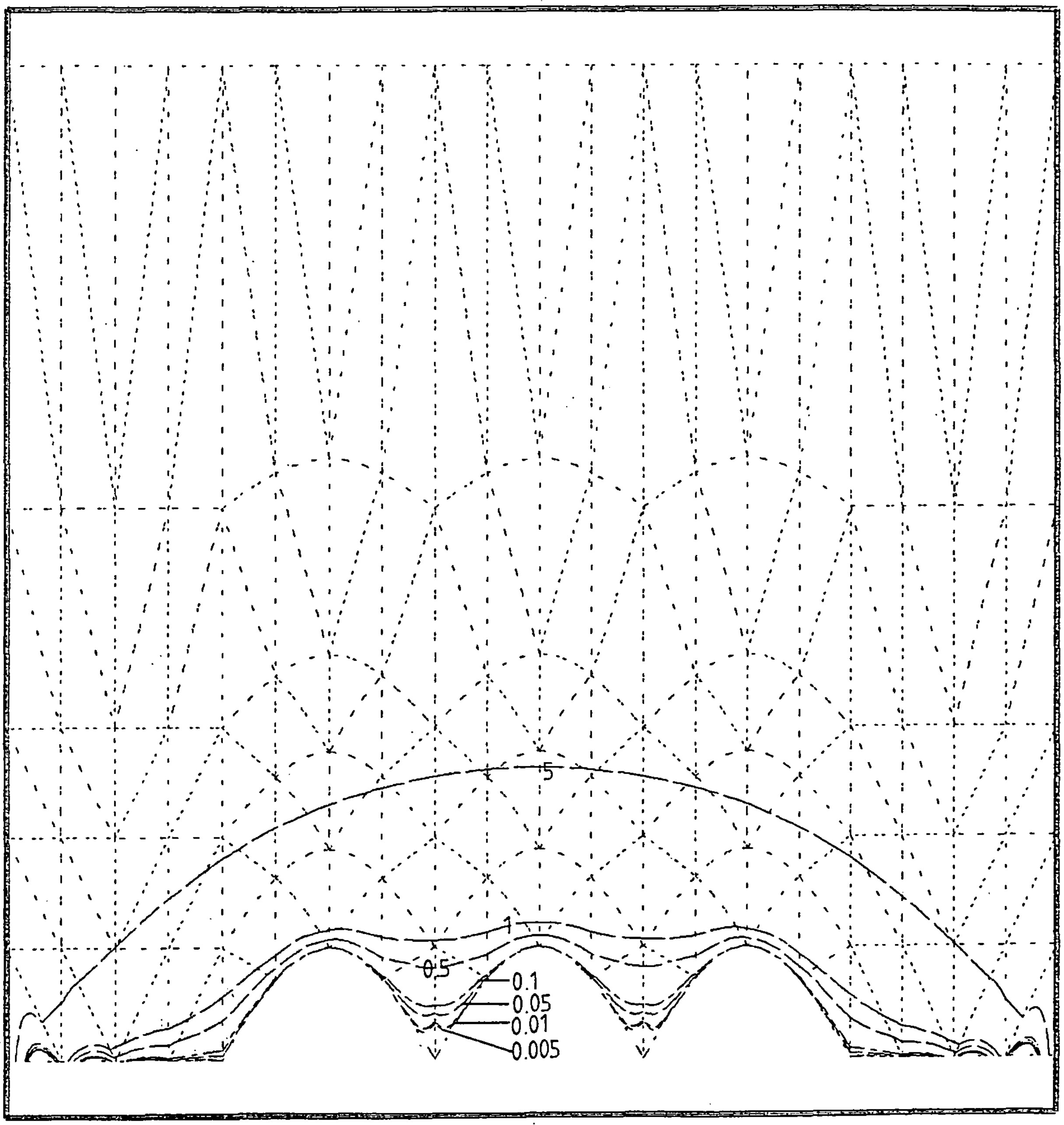

Figure 5.78 Velocity contours in alu/a for v_d = 400 alu/a, bed of S = 0·02 alu/bar.a, narrow-hummocked case.

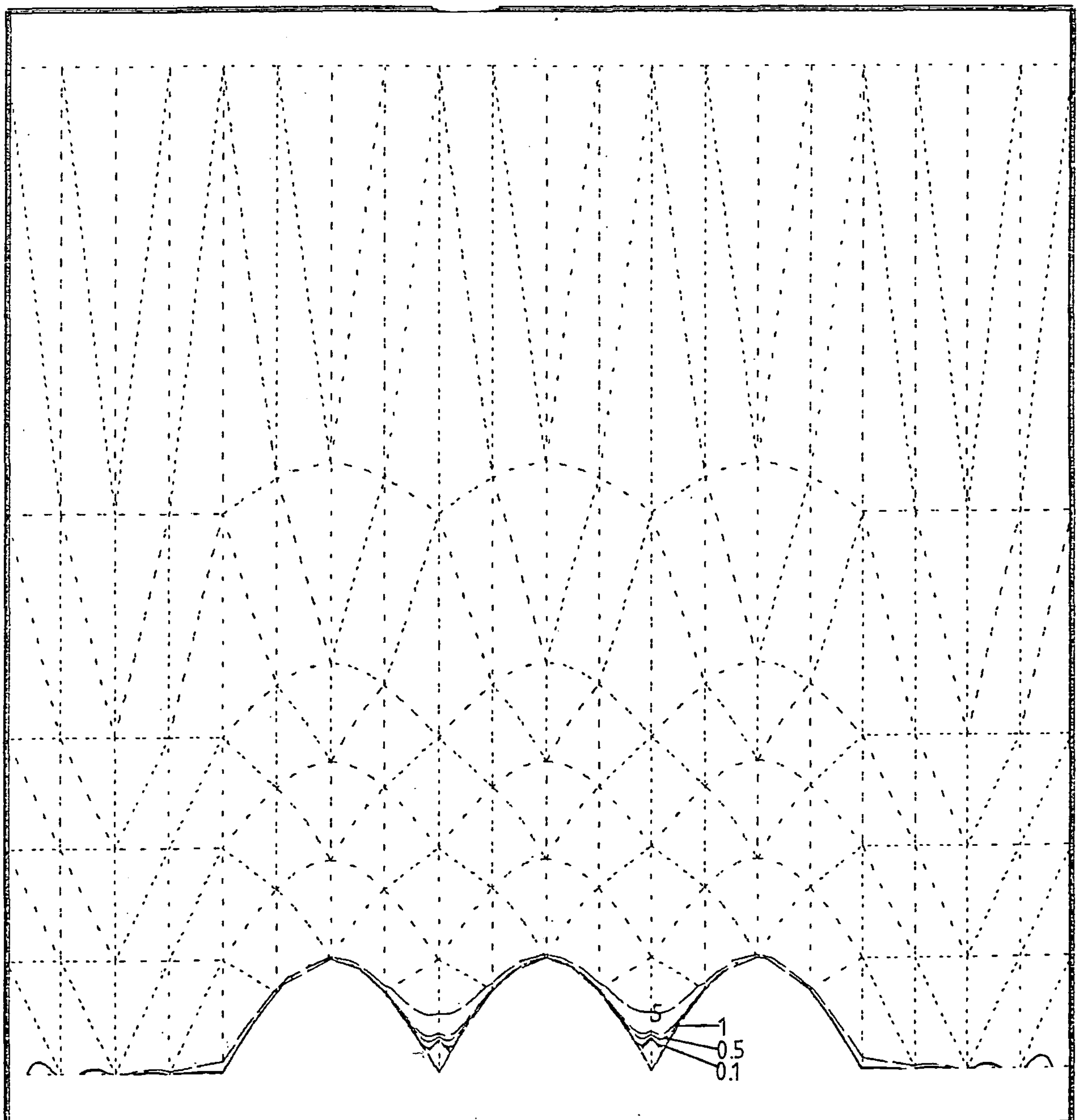

Figure 5.79 Velocity contours in alu/a for v_d = 10 alu/a, bed of maximum S = 0·02 alu/bar.a, smoothed-crested case.

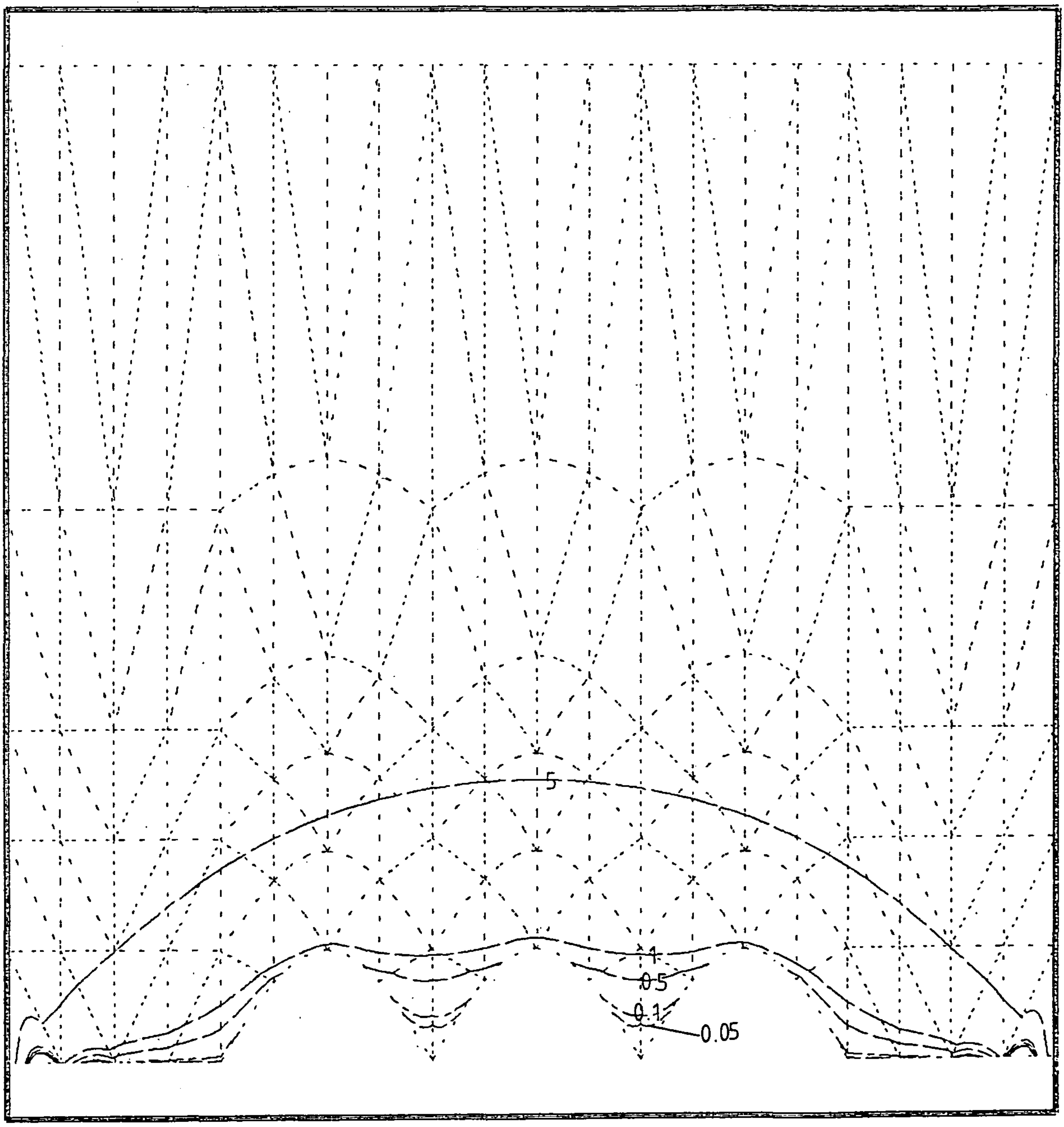

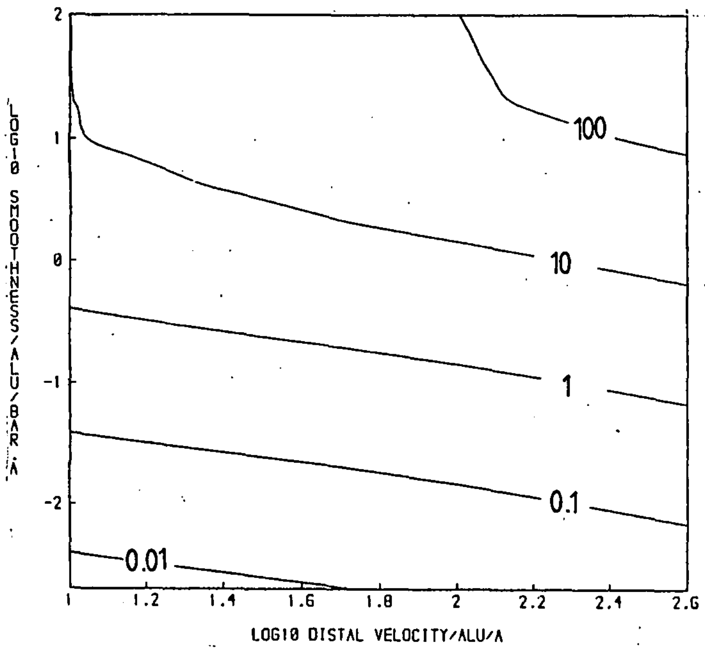

Figure 5.80 Crestal velocities in alu/a for the wide-hummocked case.

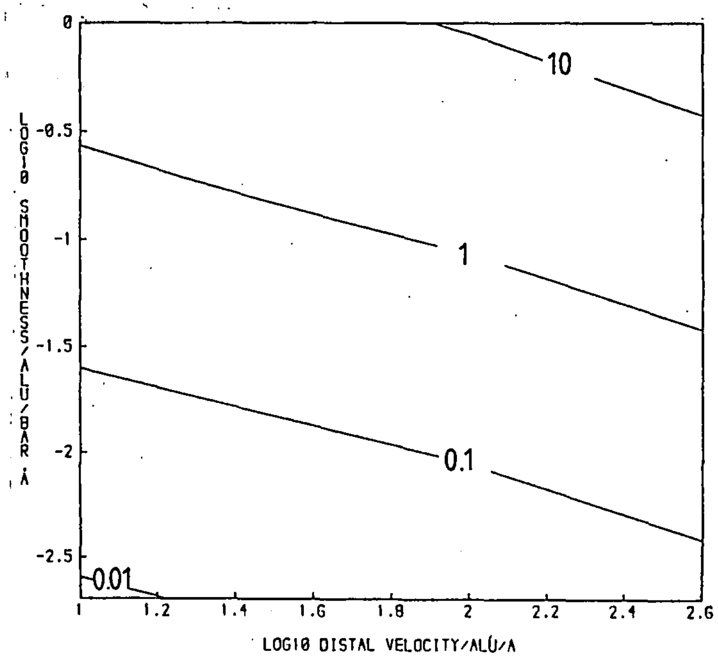

Figure 5.81 Crestal velocities in alu/a for the narrow-hummocked case.

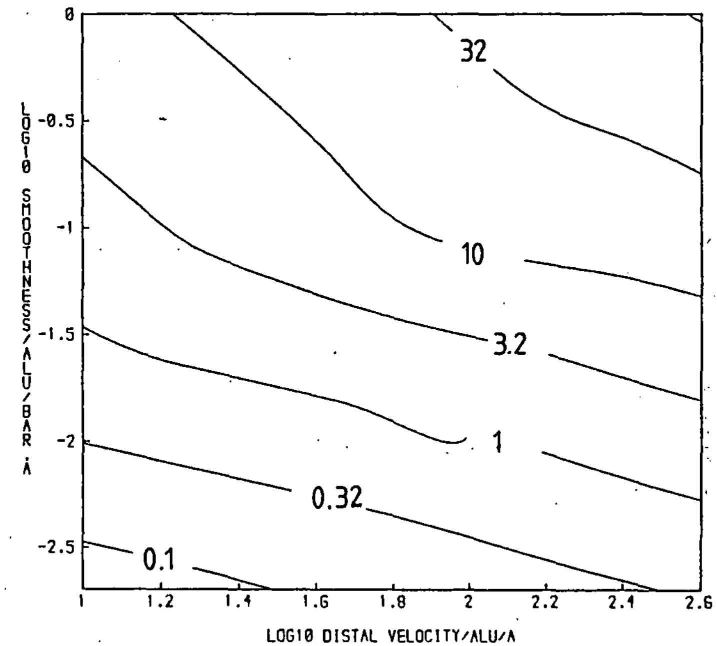

Figure 5.82 Crestal velocities in alu/a for the smooth-crested case.

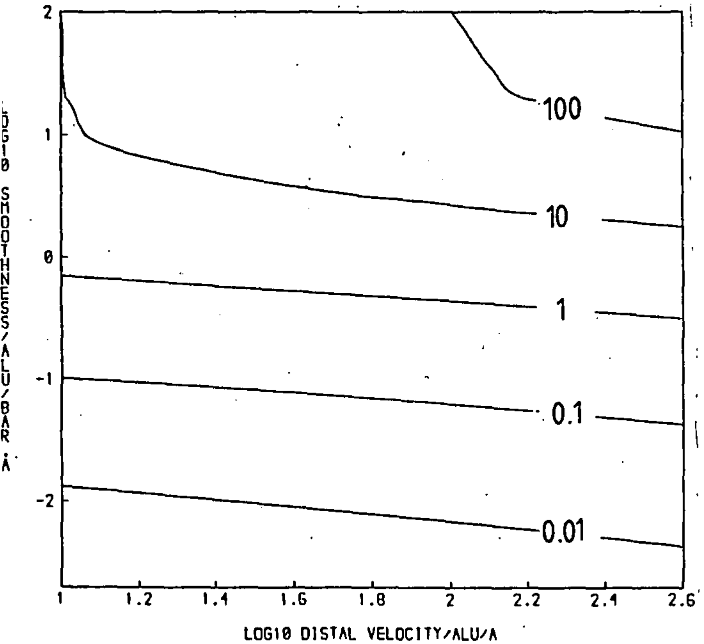

Figure 5.83 Trough velocities in alu/a wide-hummocked case.

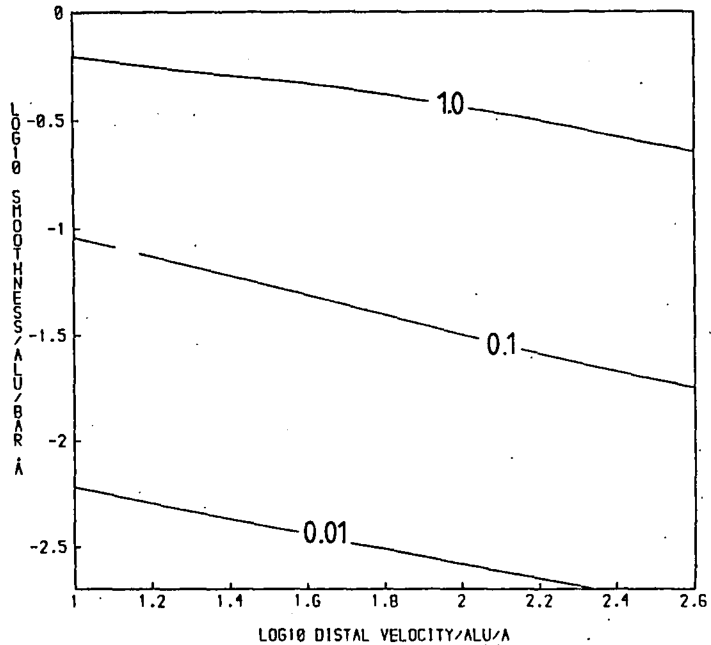

Figure 5.84 Trough velocities in alu/a for the narrow-hummocked case.

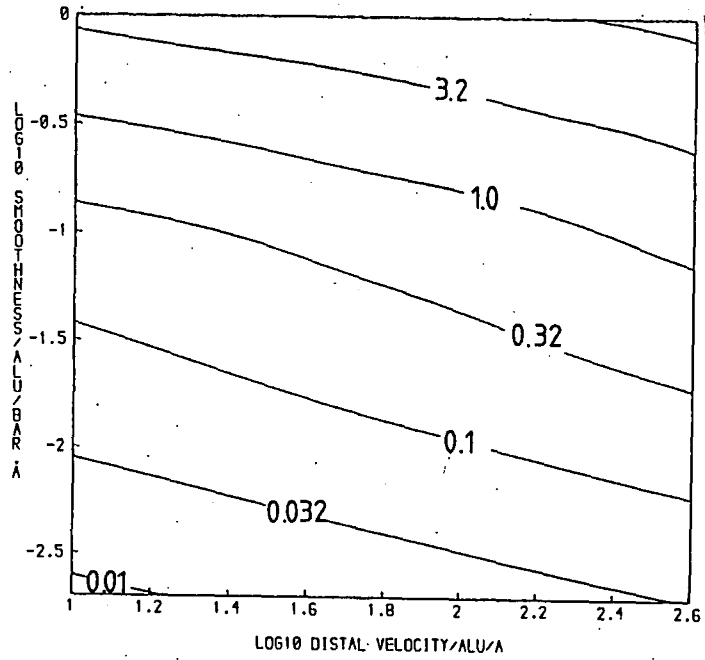

Figure 5.85 Trough velocities in alu/a for the smooth-crested case.

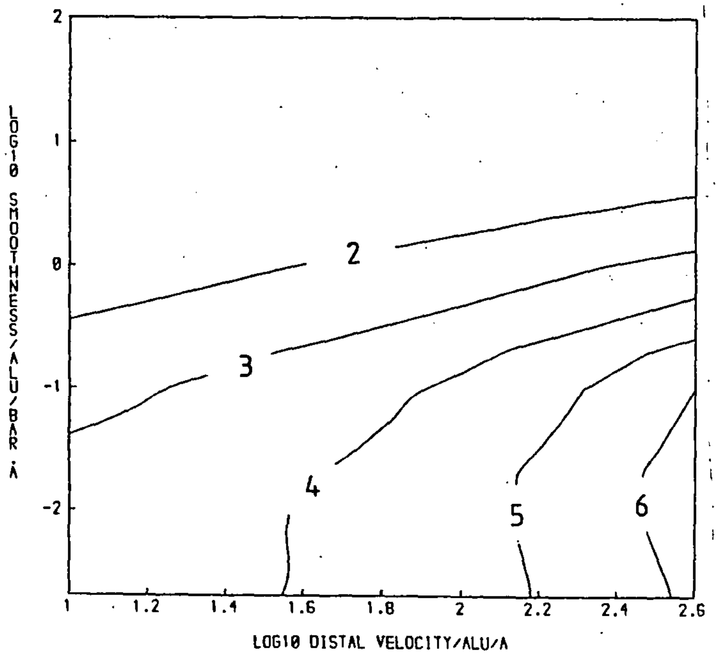

Figure 5.86 Crest/trough velocity ratios for the wide-hummocked case.

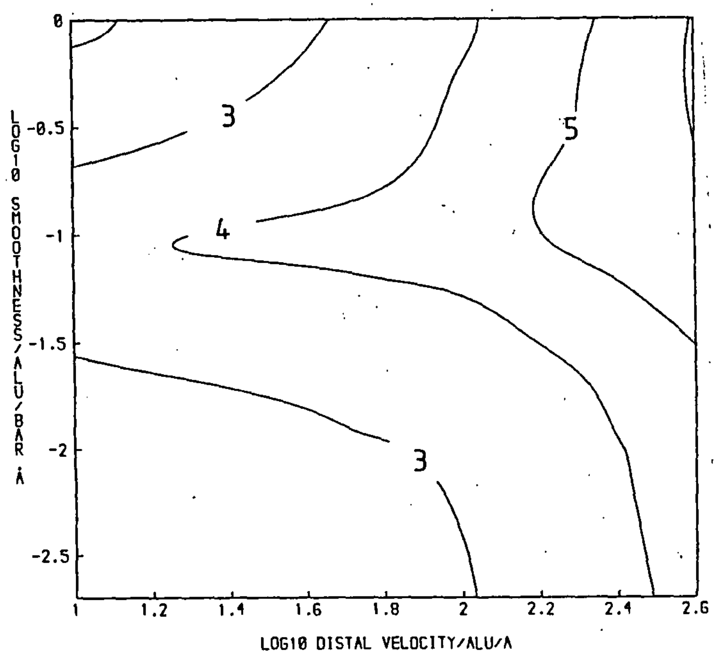

Figure 5.87 Crest/trough velocity ratios for the narrow-hummocked case.

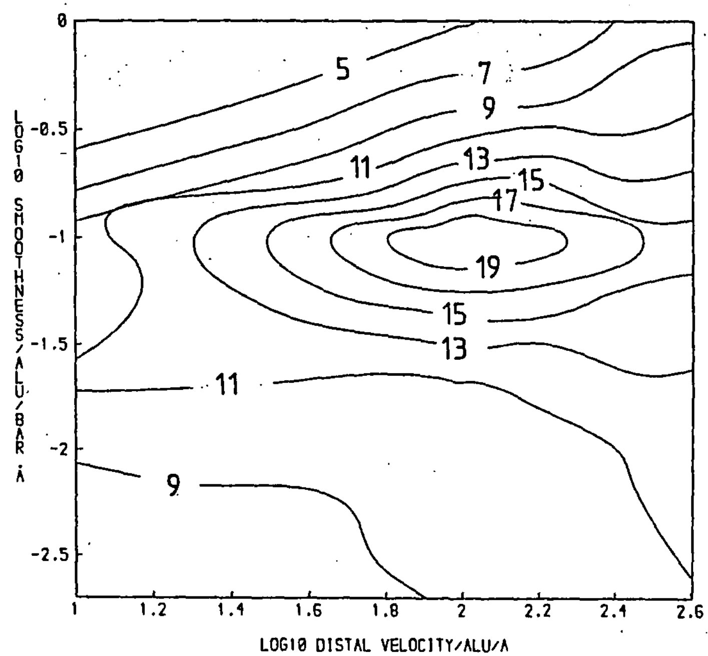

Figure 5.88 Crest/trough velocity ratios for the smooth-crested case.

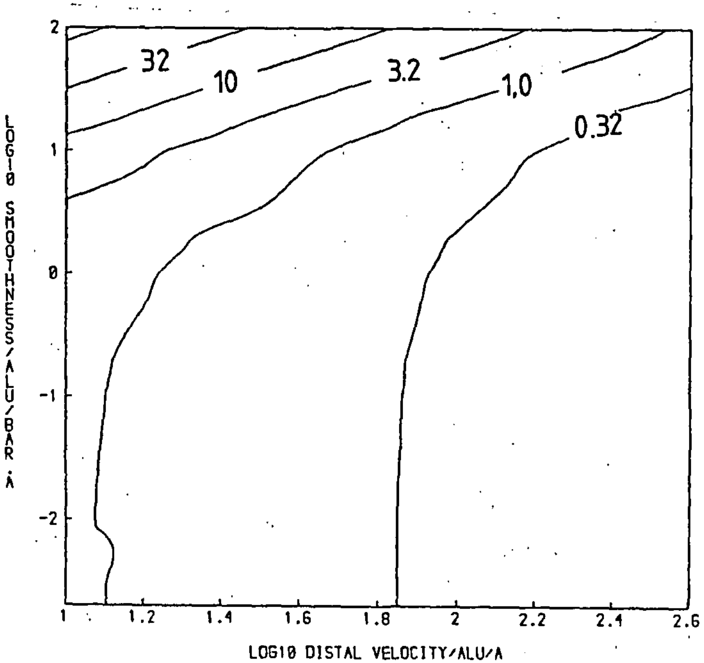

Figure 5.89 Crestal viscosity in bar.a for the wide-hummocked case.

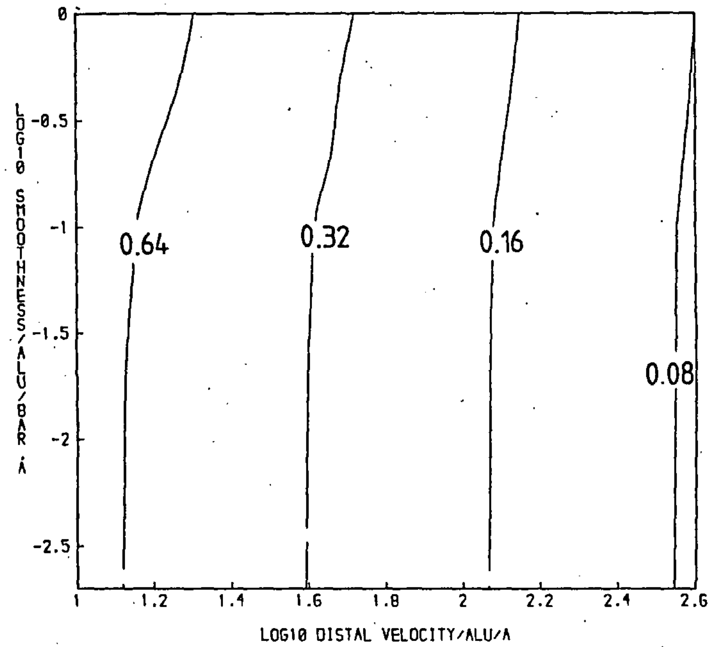

Figure 5.90 Crestal viscosities in bar.a for the narrow-hummocked case.

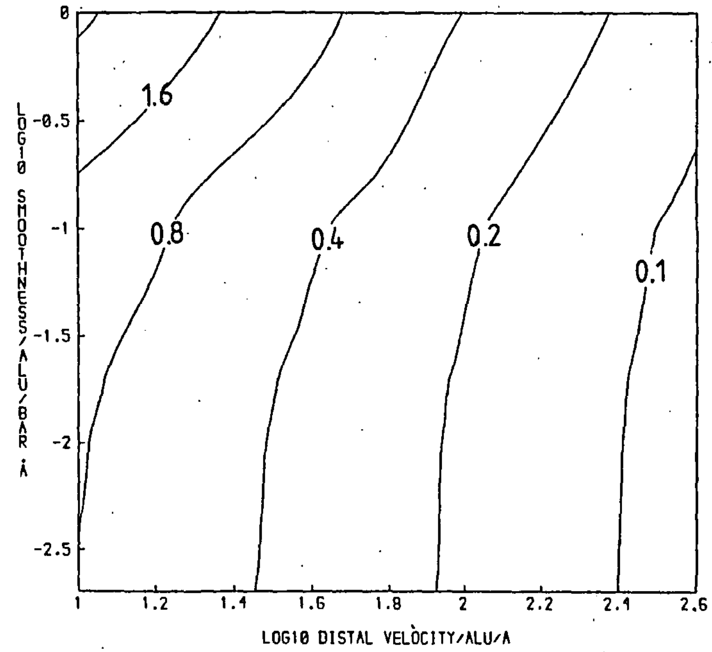

Figure 5.91 Crestal viscosities in bar.a for the smooth-crested case.

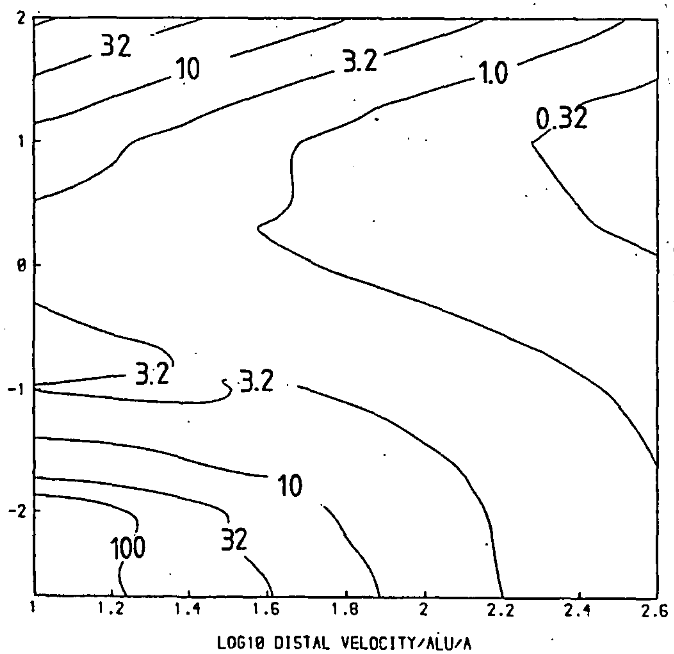

Figure 5.92 Trough viscosities in bar.a for the wide-hummocked case.

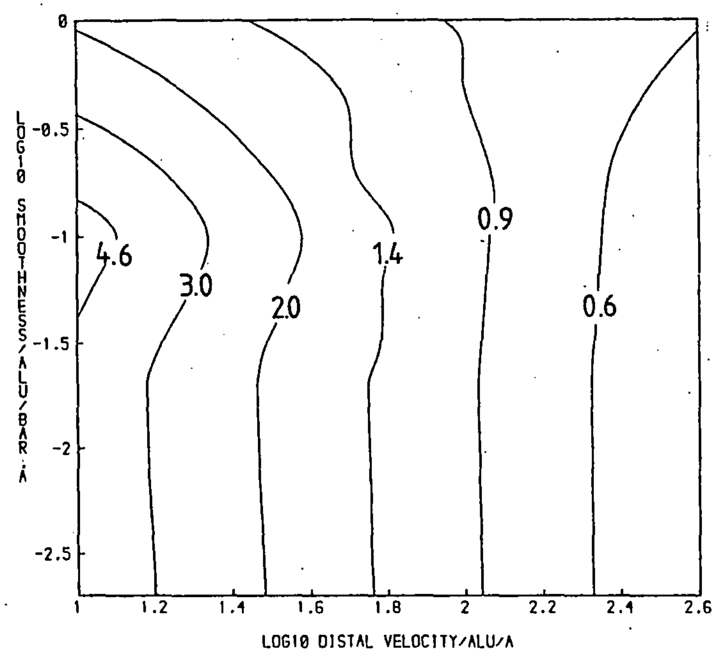

Figure 5.93 Trough viscosities in bar.a for the narrow-hummocked case.

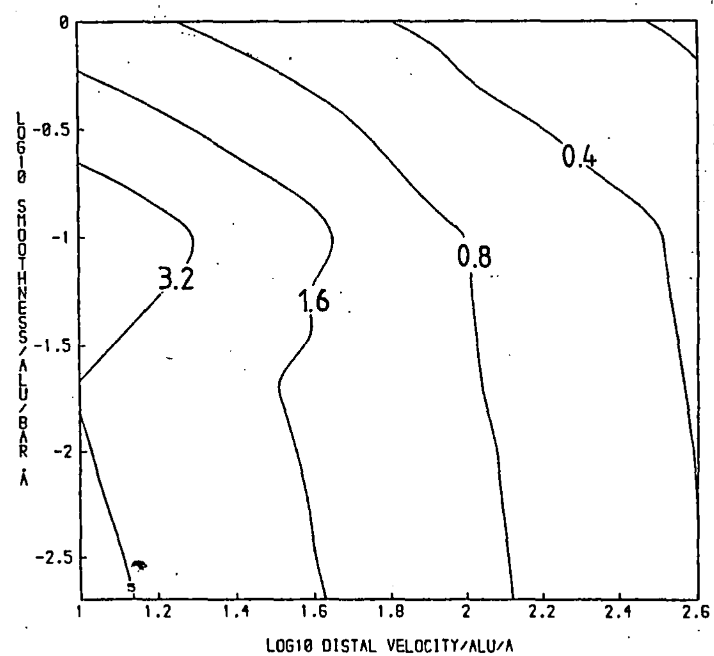

Figure 5.94 Trough viscosities in bar.a for the smooth-crested case.

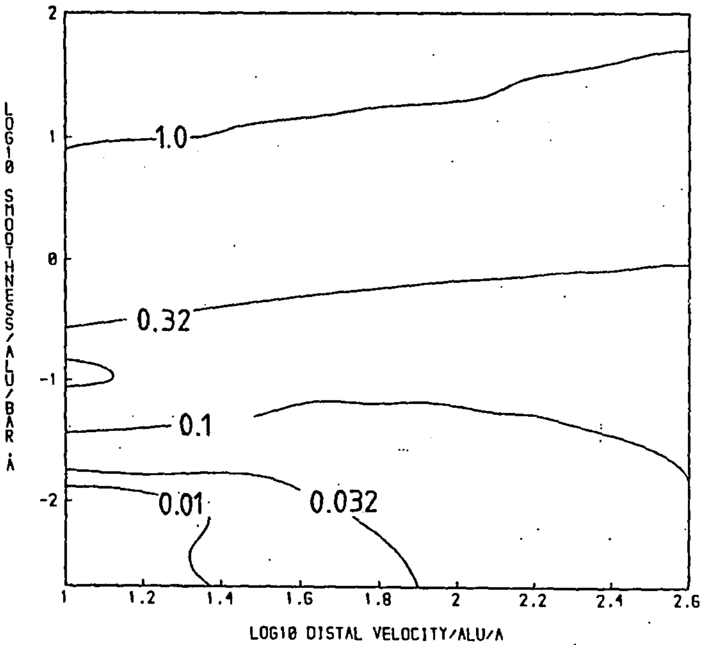

Figure 5.95 Crest/trough viscosity ratios for the wide-hummocked case.

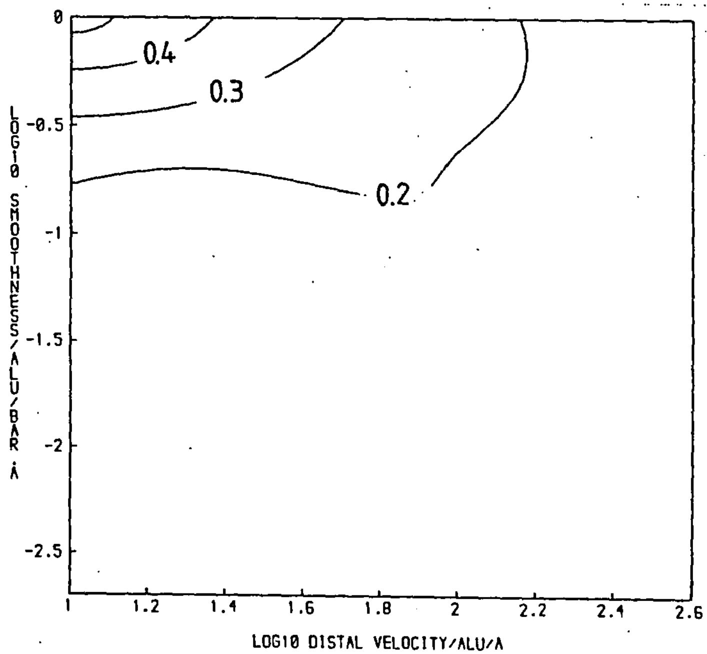

Figure 5.96 Crest/trough viscosity ratios for the narrow-hummocked case.

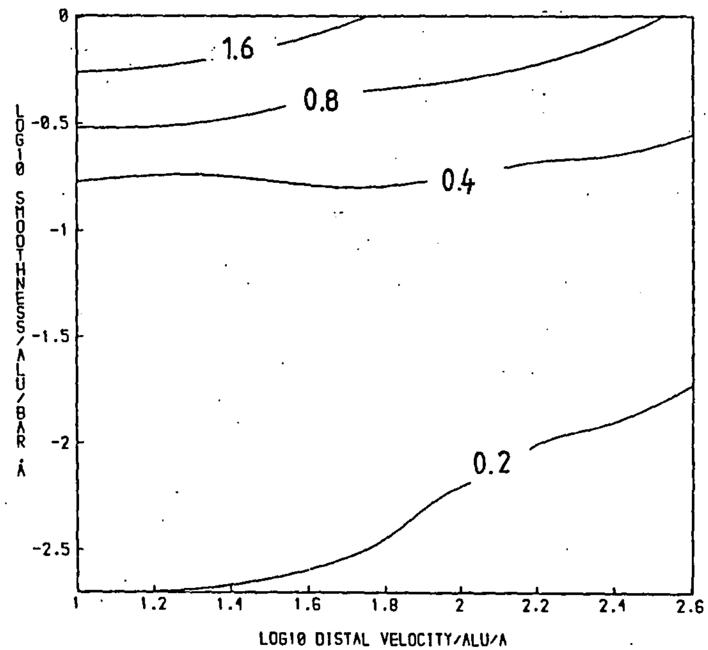

Figure 5.97 Crest/trough viscosity ratios for the smooth-crested case.

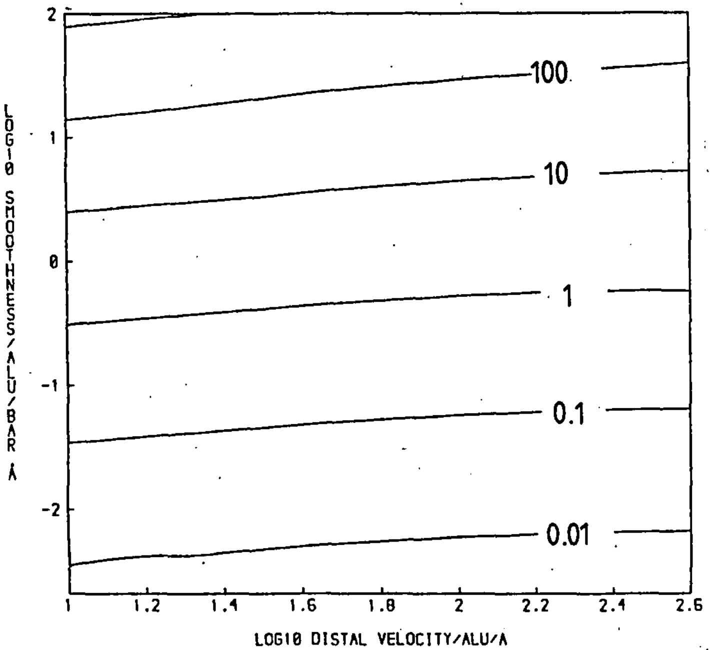

Figure 5.98 Crestal viscosity x velocity in bar.alu for the wide-hummocked case.

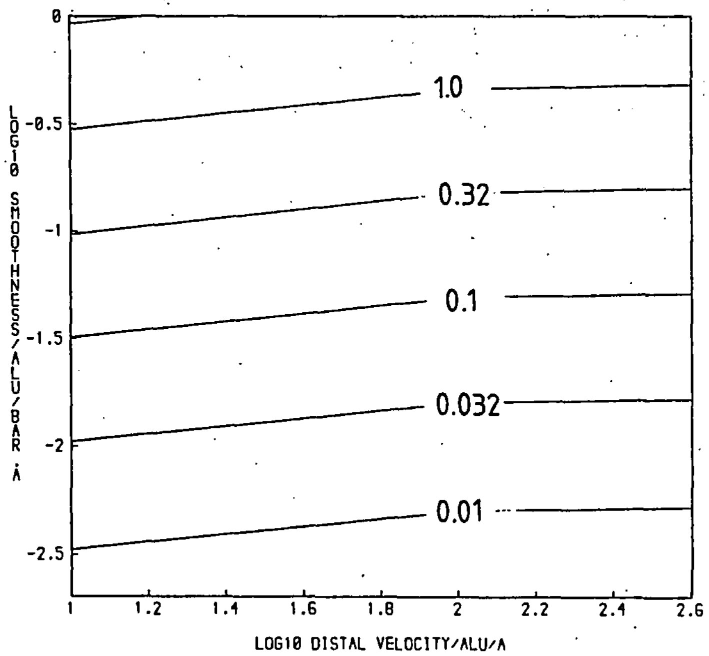

Figure 5.99 Crestal viscosity x velocity in bar.alu for the narrow-hummocked case.

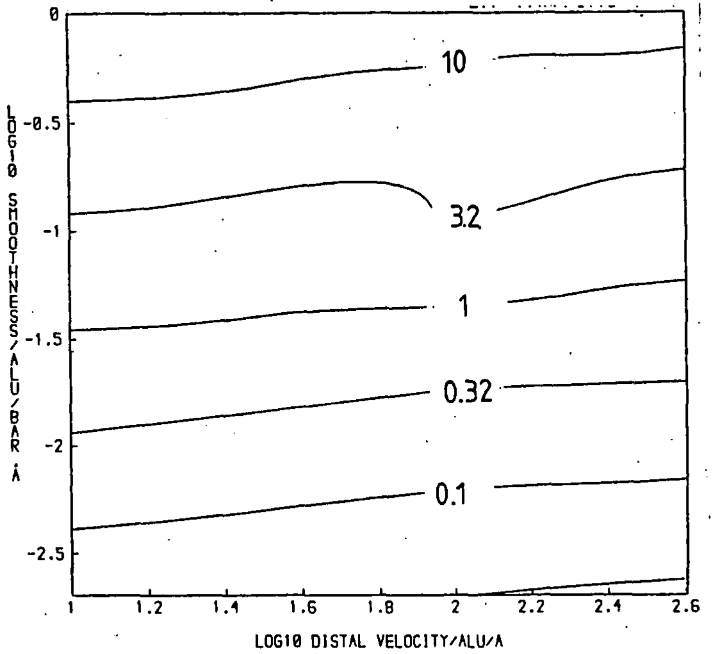

Figure 5.100 Crestal viscosity x velocity in bar.alu for the smooth-crested case.

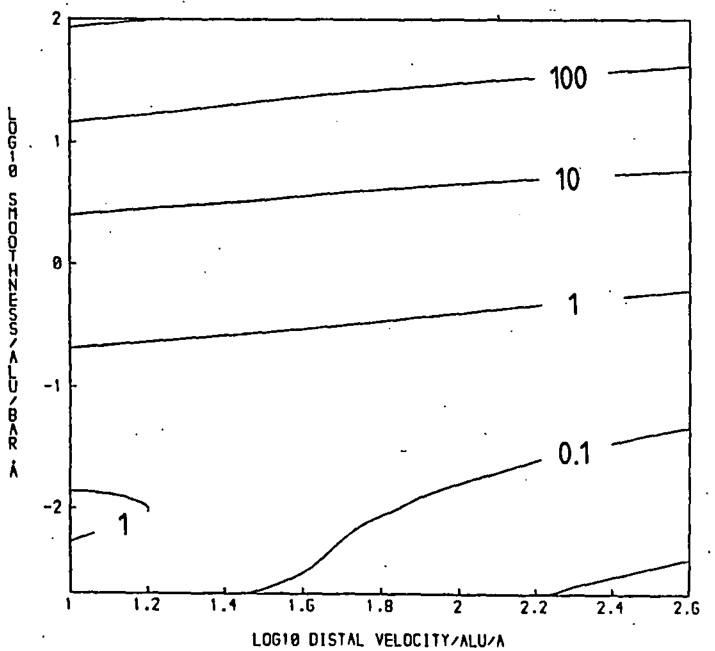

Figure 5.101 Trough viscosity x velocity in bar.alu for the wide-hummocked case.

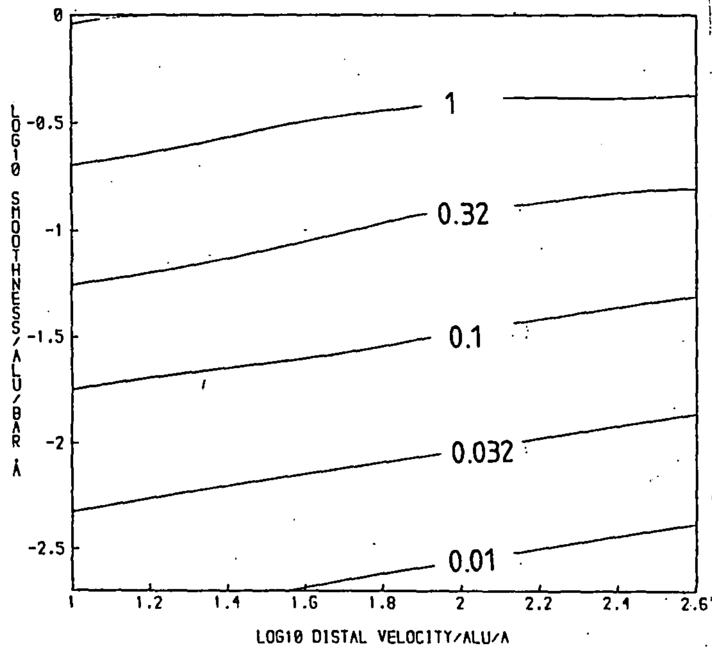

Figure 5.102 Trough viscosity x velocity in bar.alu for the narrow-hummocked case.

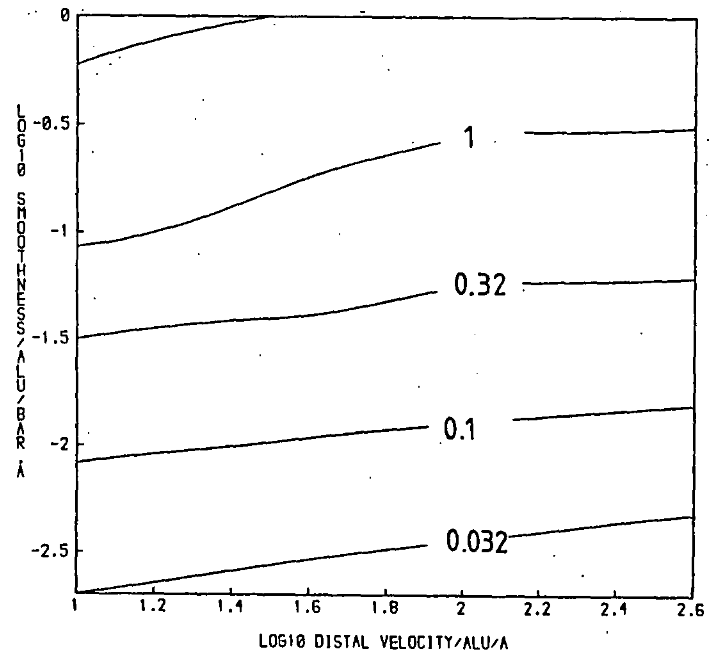

Figure 5.103 Trough viscosity x velocity in bar.alu for the smooth-crested case.

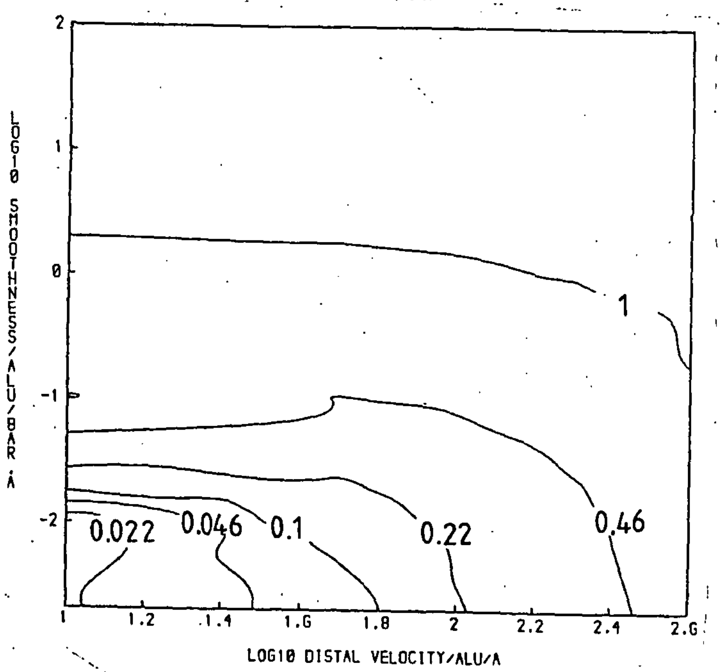

Figure 5.104 Crest/trough viscosity x velocity ratio for the wide-hummocked case.

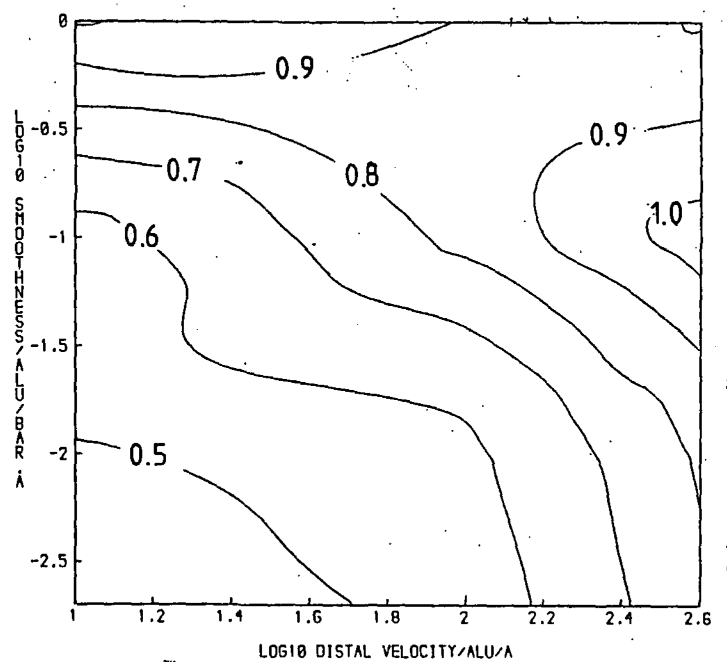

Figure 5.105 Crest/trough viscosity x velocity ratio for the narrow-hummocked case.

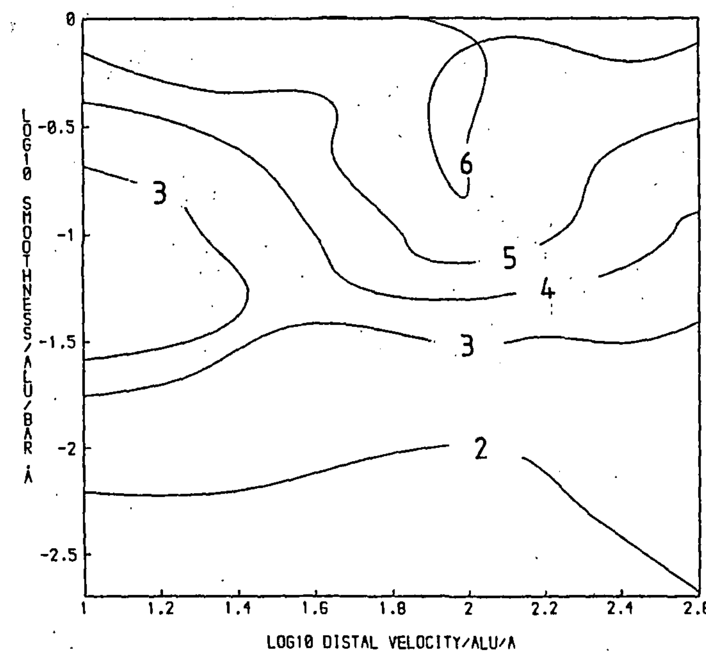

Figure 5.106 Crest/trough viscosity x velocity ratio for the smooth-crested case.

Figure 6.1

Clast at the base of a temperate glacier.

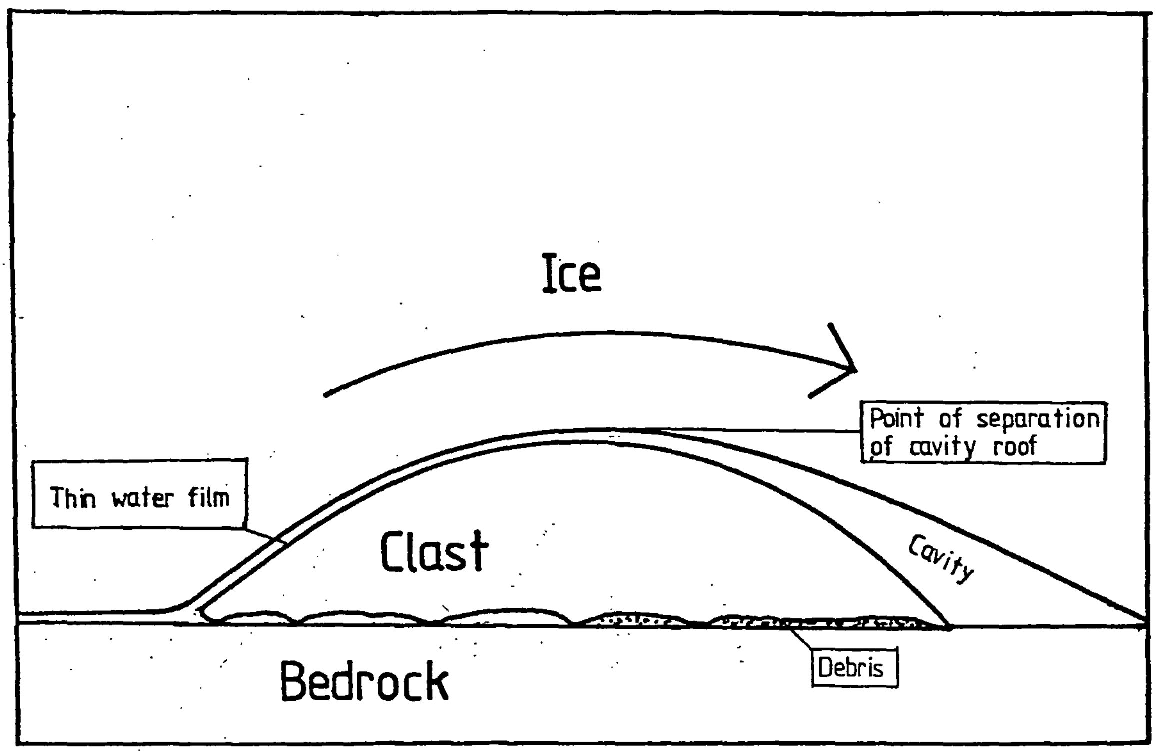

FIGURE 6.2 ICE-CLAST CONTACT GEOMETRIES

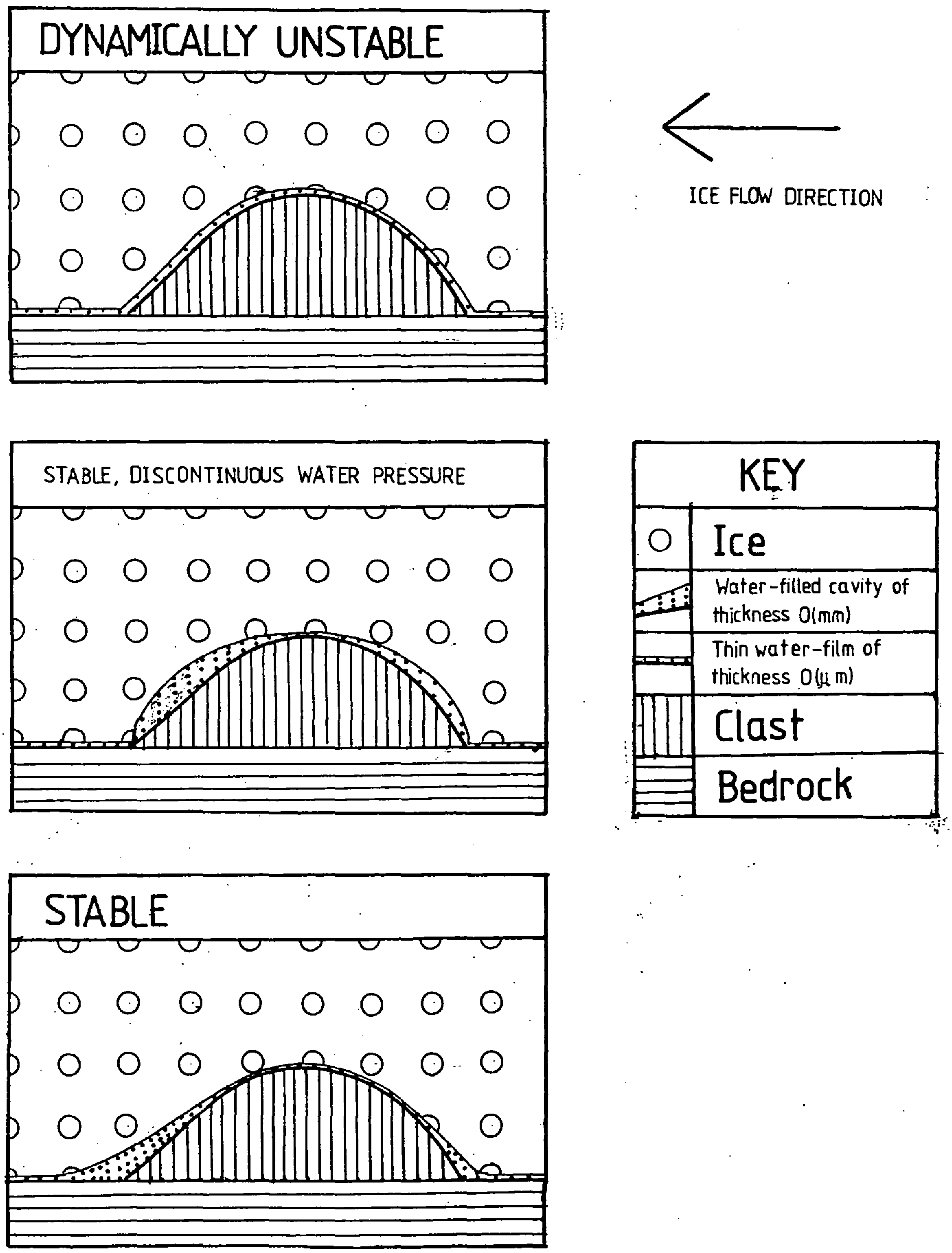

Figure 6.3 The effect of ice-clast contact geometries on the water pressure beneath the clast.

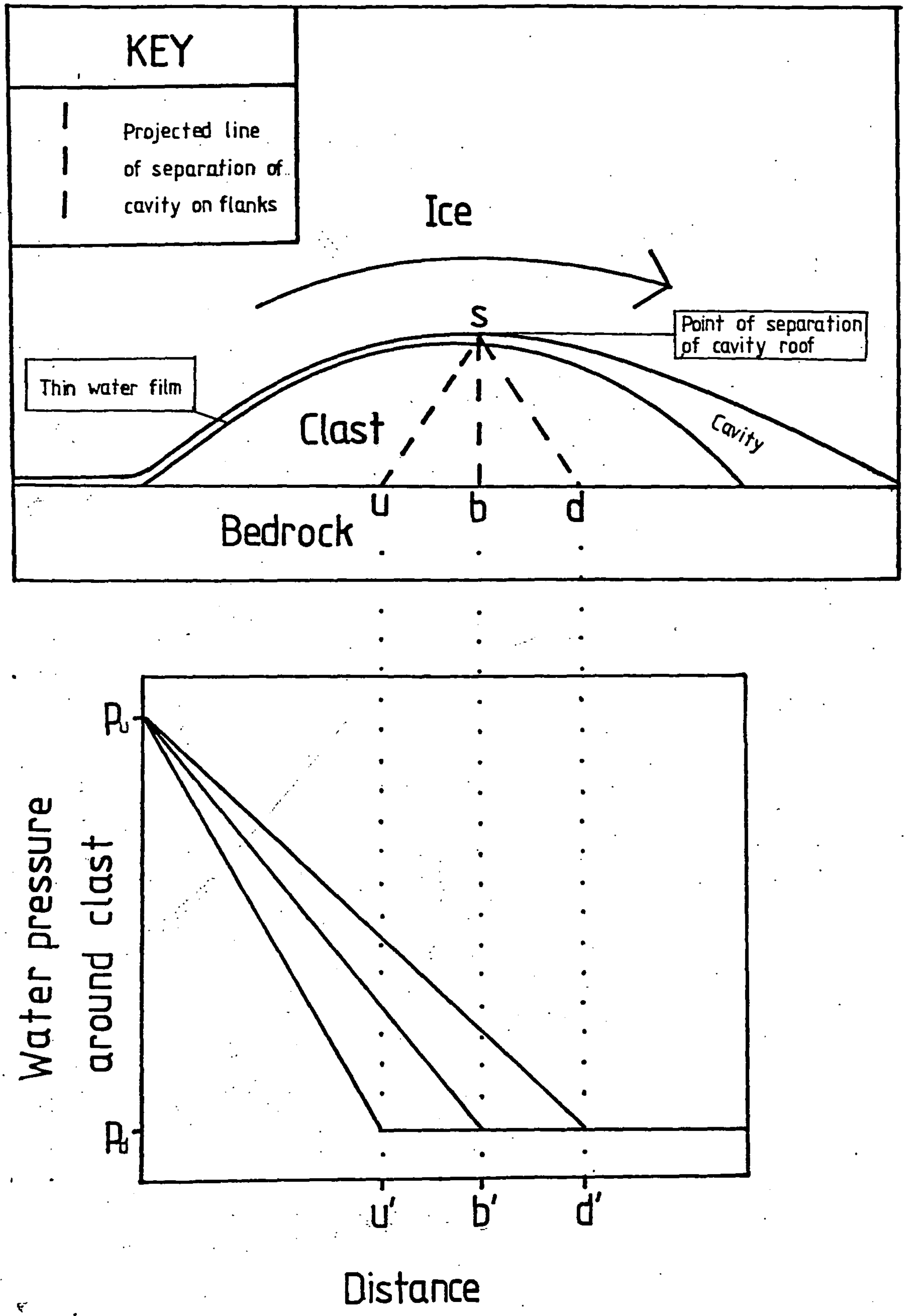

Figure 6.4 The effect of a generalised normal velocity on water pressure.

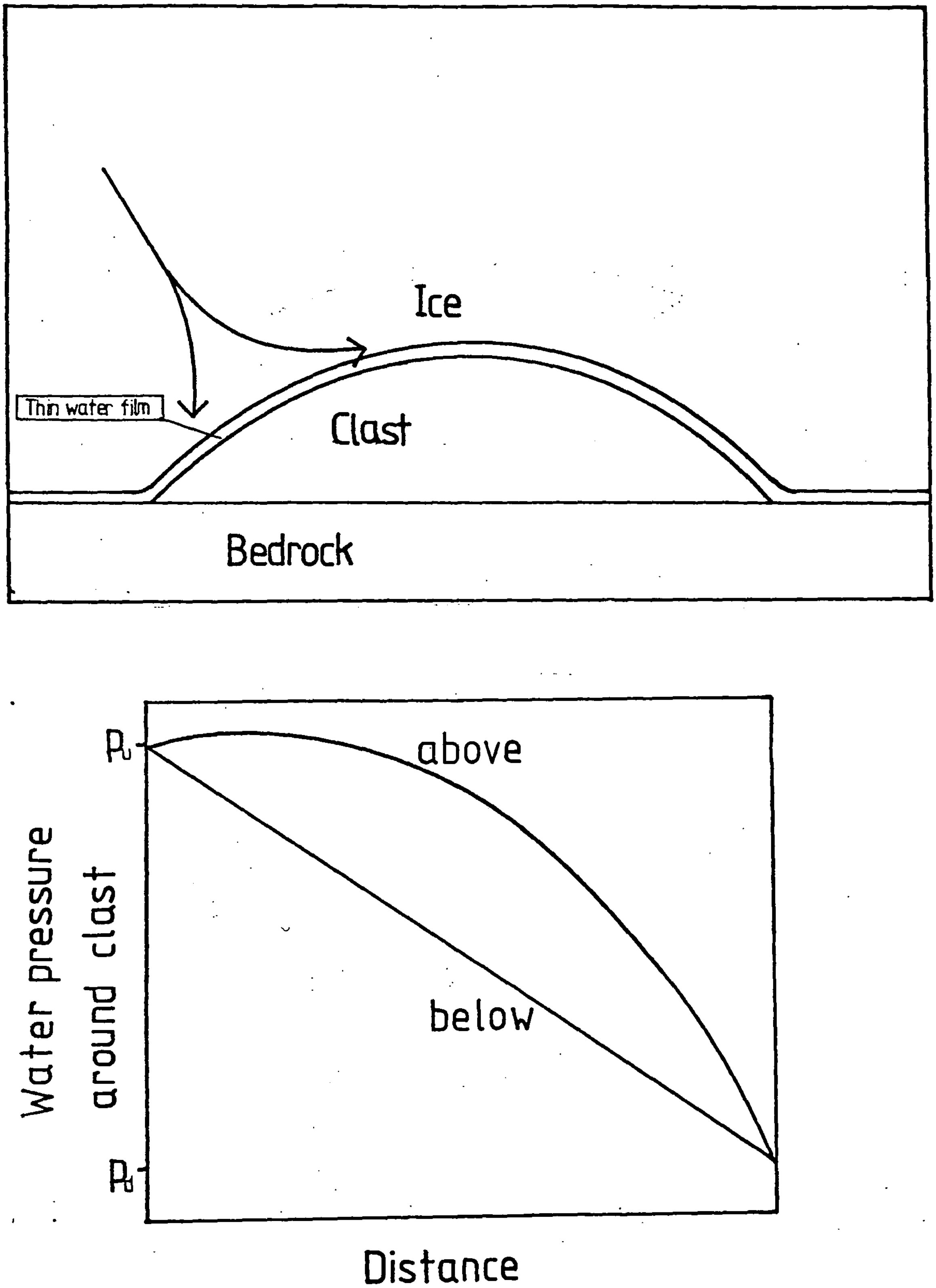

Figure 6.5 The effect of having pressure turning-points away from the clast edge.

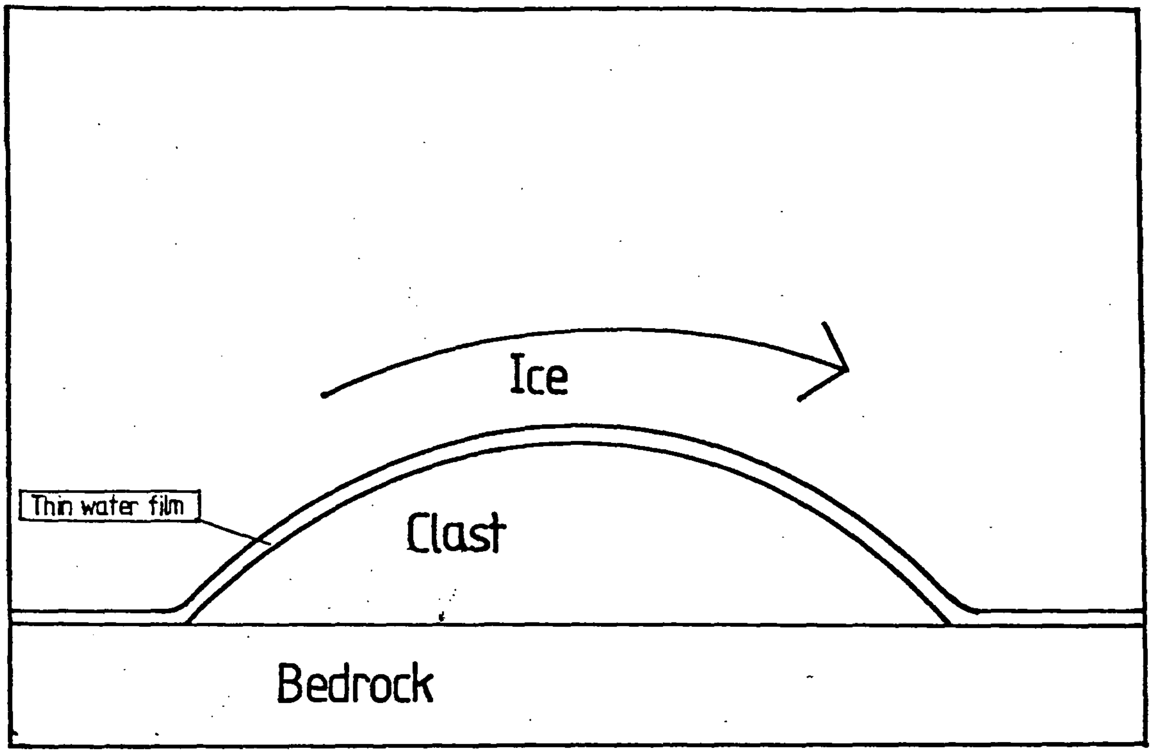

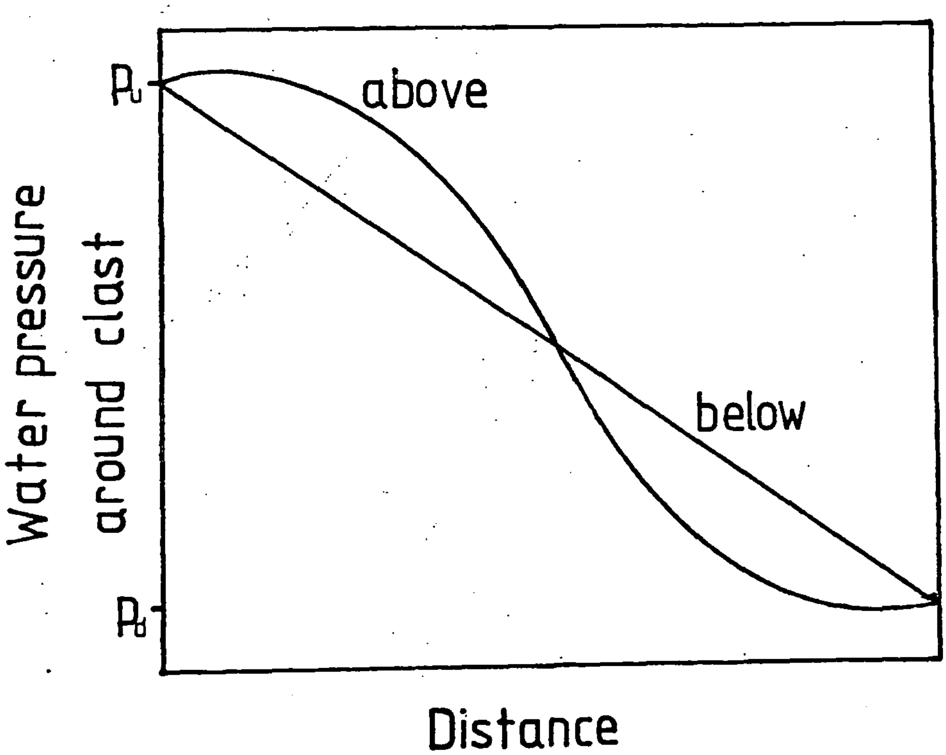

Figure 6.6 The effect of having a pressure turning point away from the clast-edge when a cavity exists.

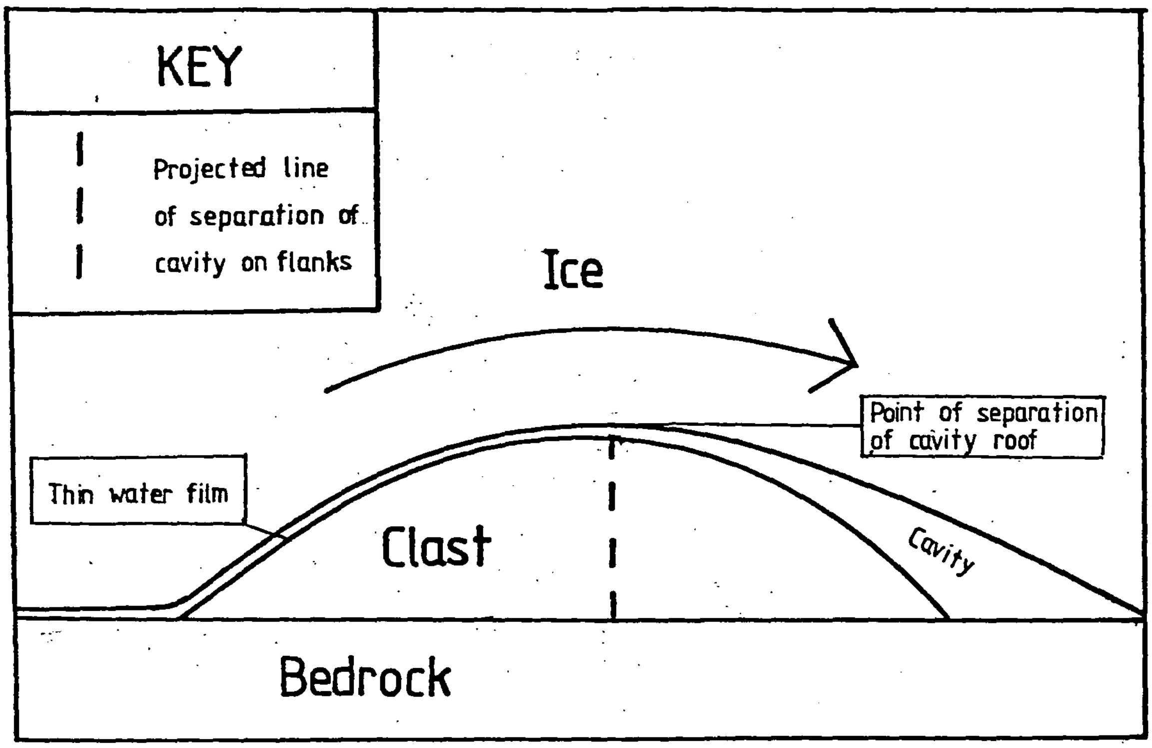

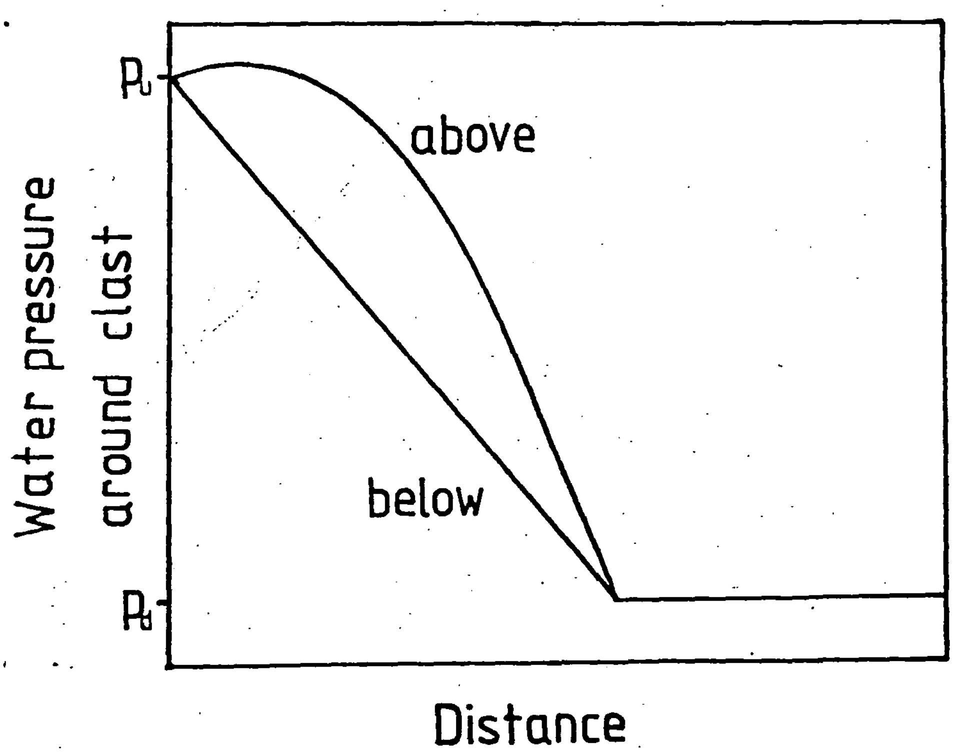

Figure 6.7 Sub-clast water pressures when the upstream end is less transmissible.

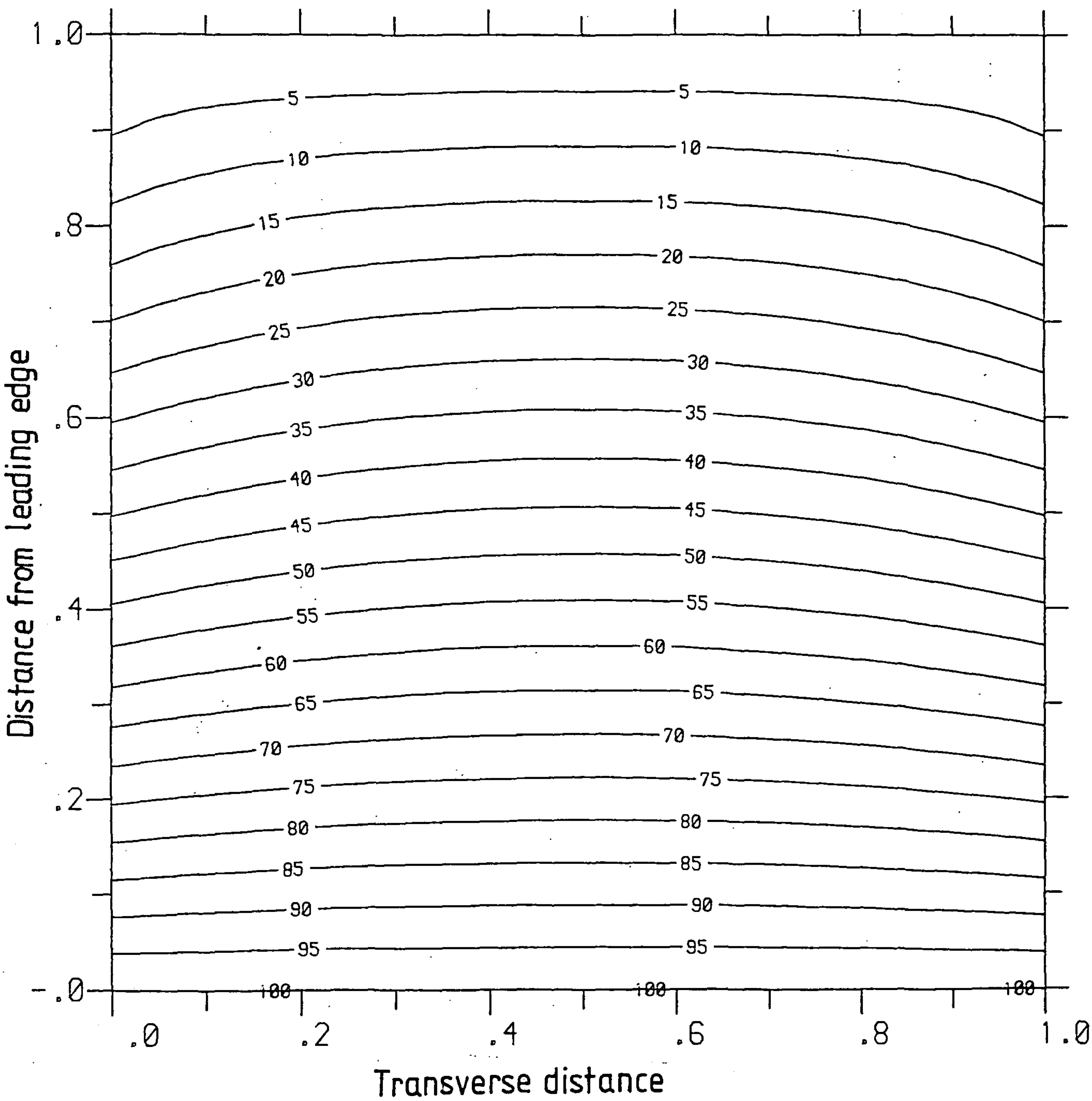

Figure 6.8 Sub-clast water pressures when the downstream end is less transmissible.

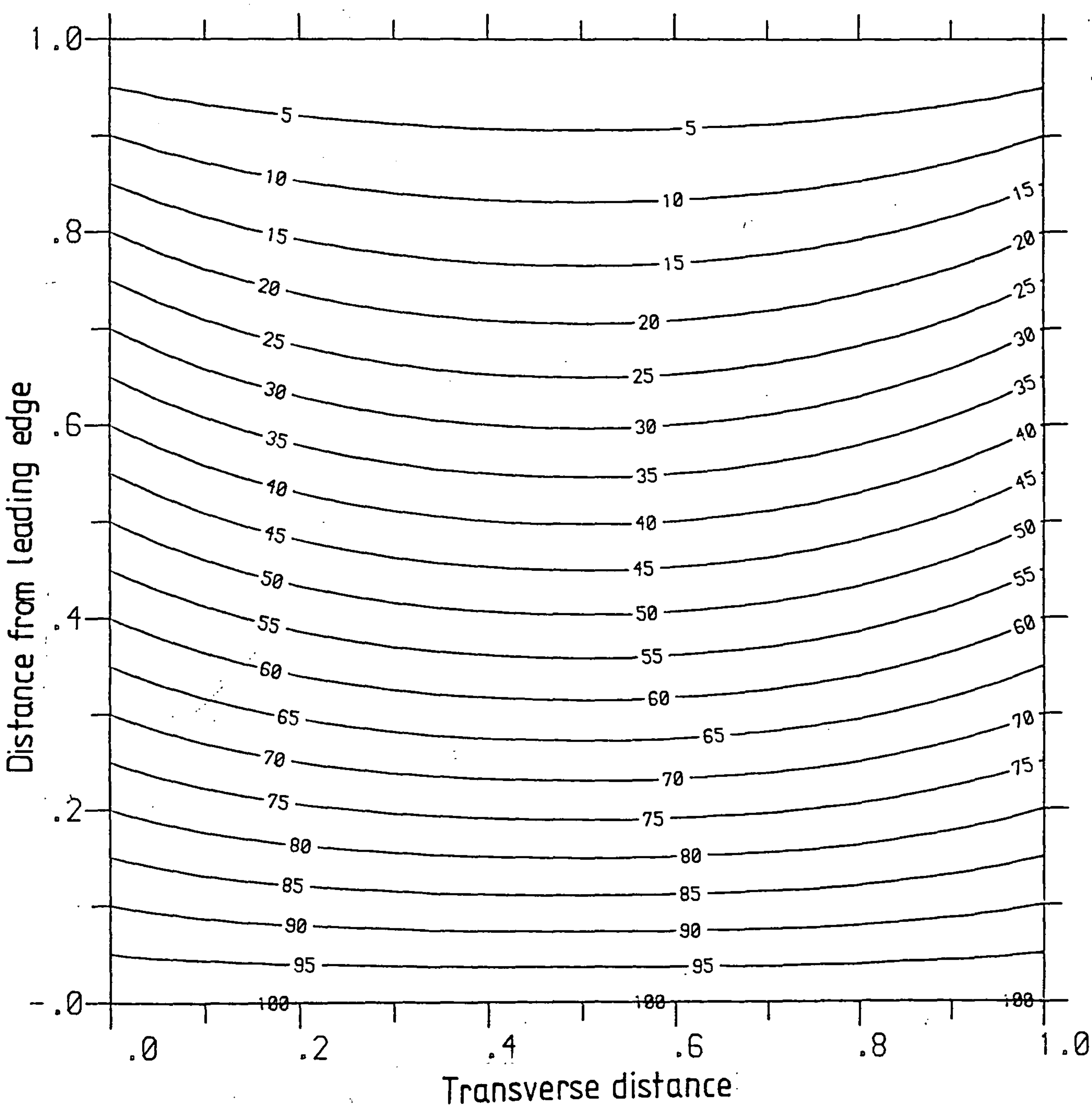

Figure 6.9 Sub-clast water pressures when the boundary pressure decline is slower than linear.

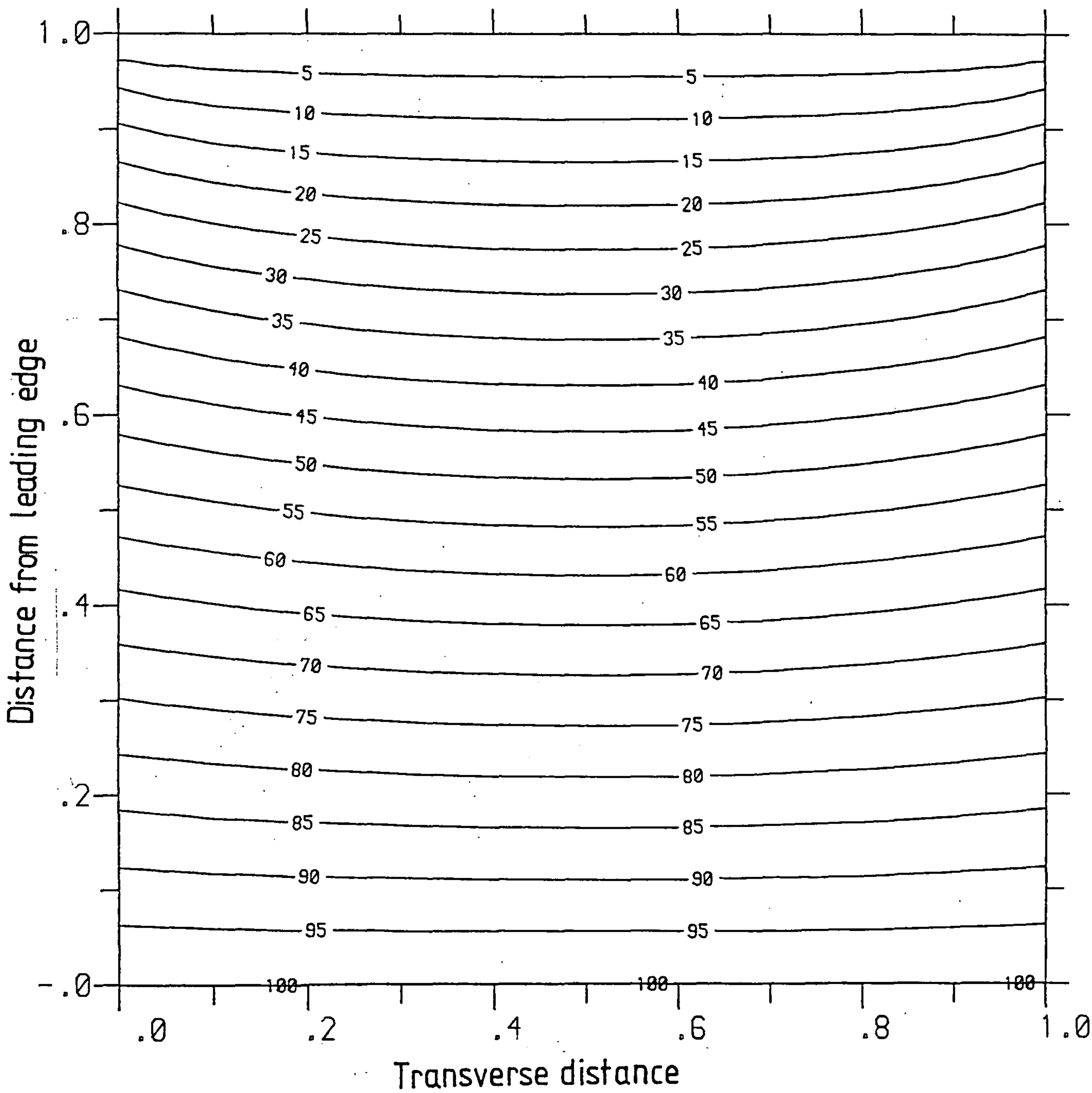

Figure 6.10 Sub-clast water pressures when the boundary pressure decline is faster than linear.

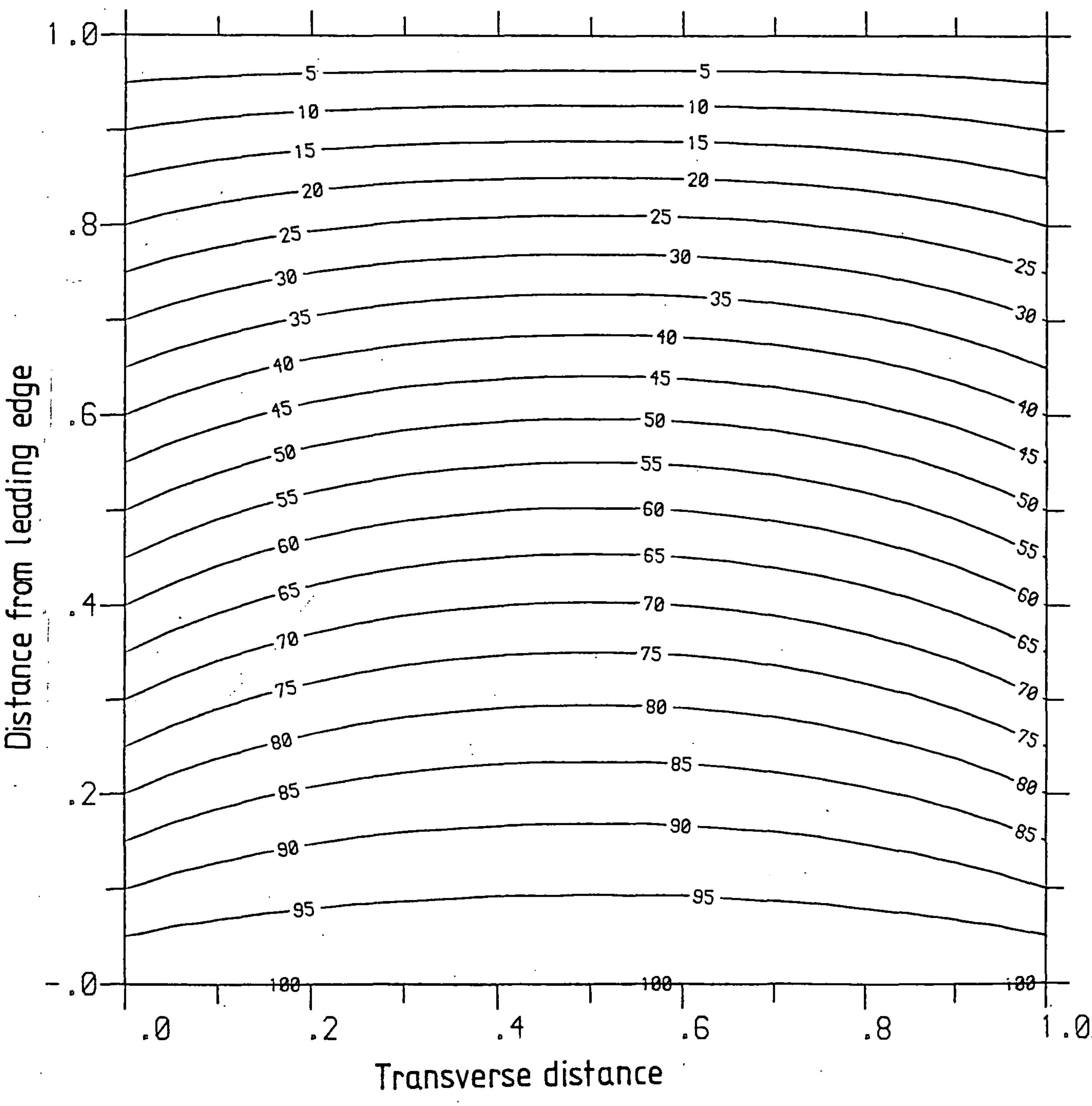

Figure 6.11 Dependence of abrasion rate on velocity and pressure.

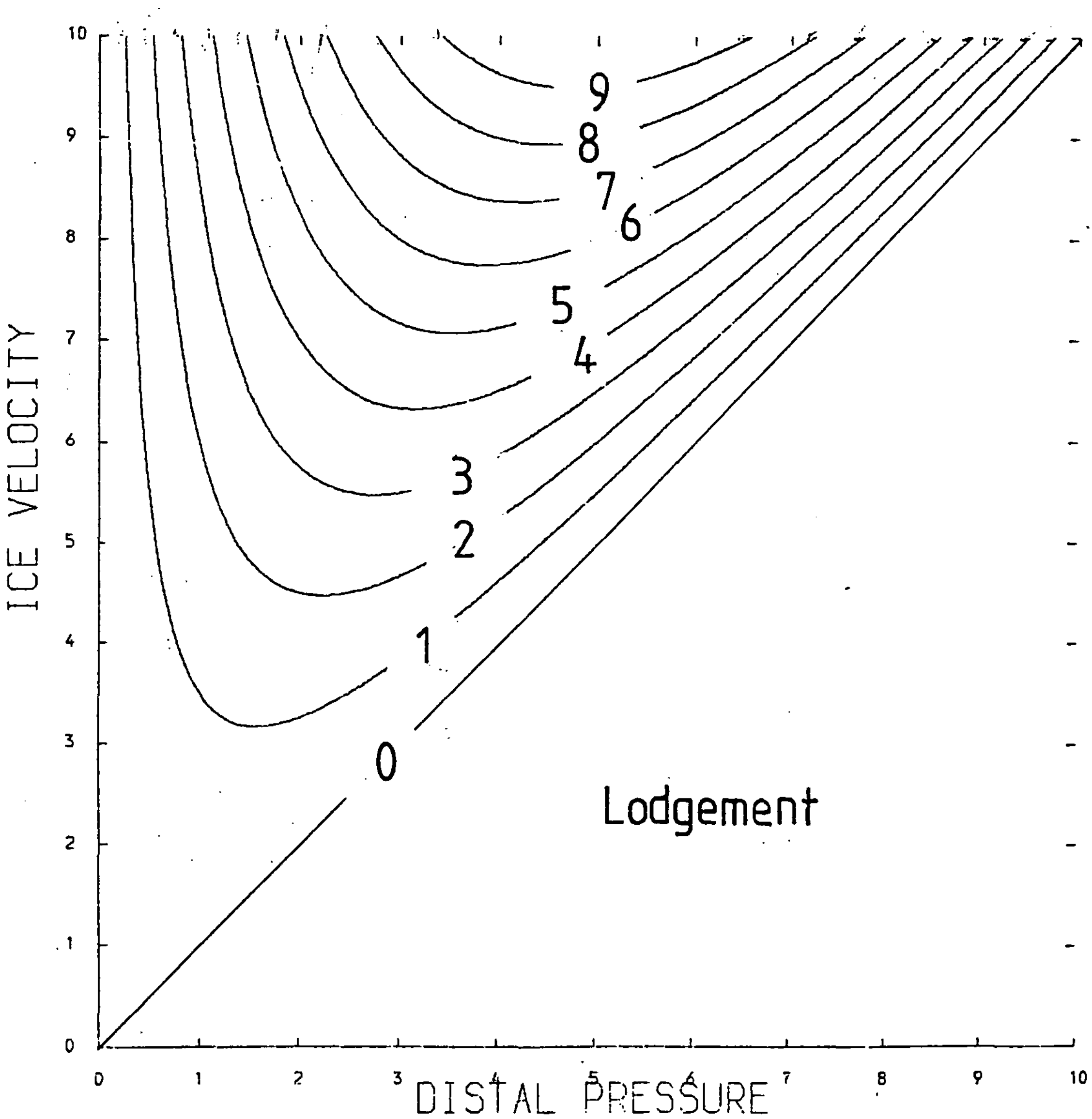

Figure 8.1 Three species mass-balance analysis

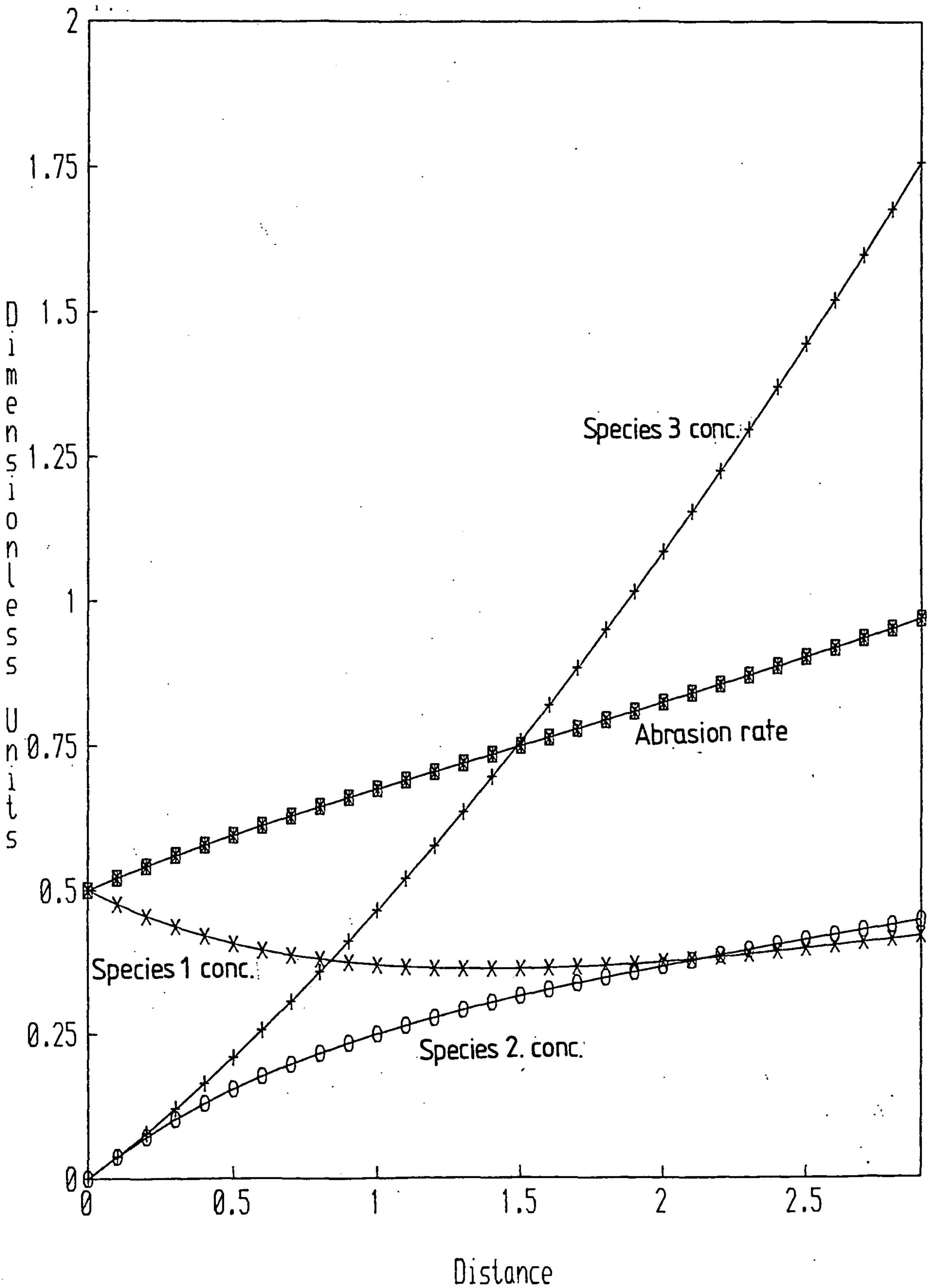

Figure 8.2 Four species mass-balance analysis.

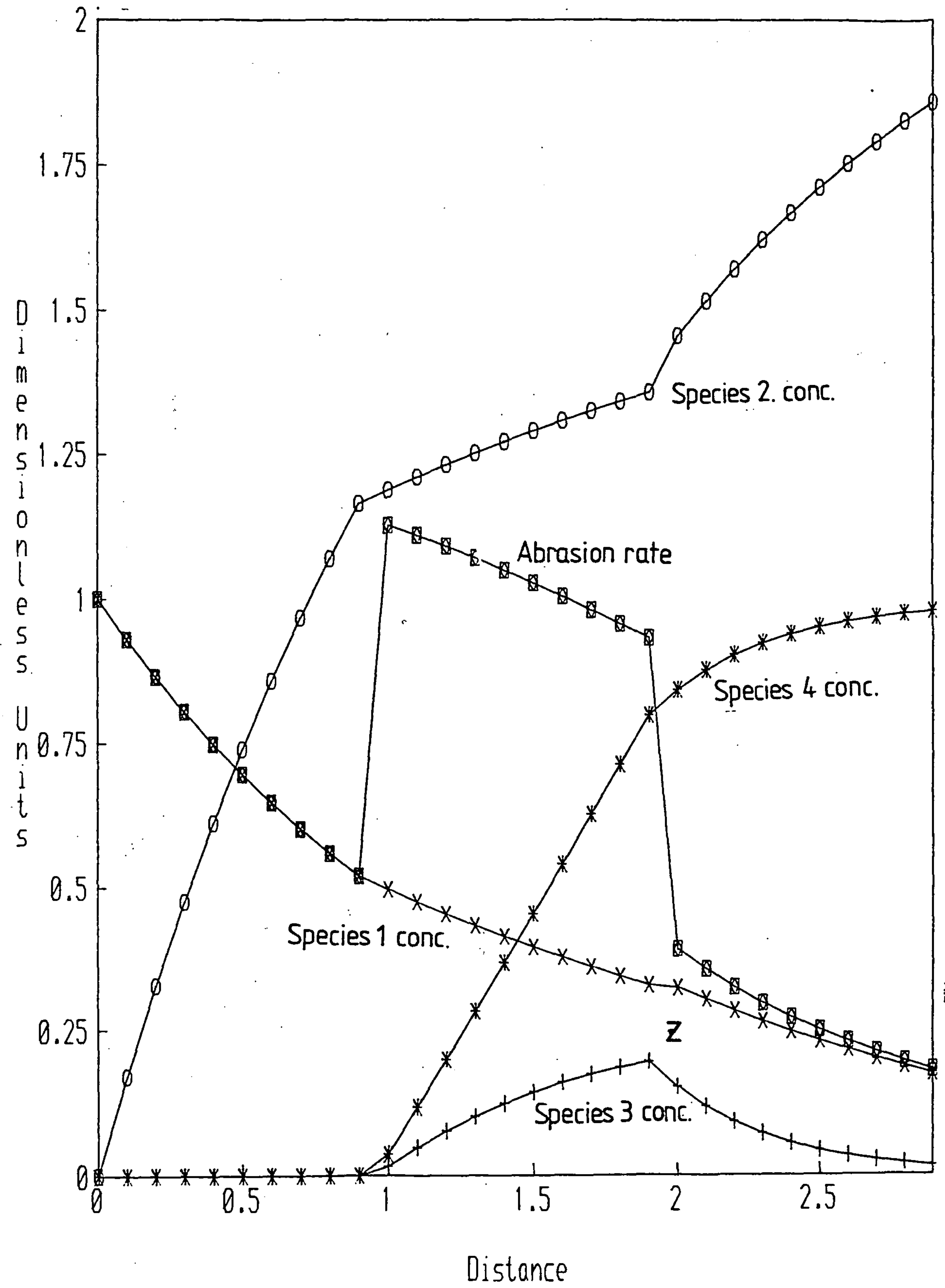

Figure 8.3 Four species mass-balance analysis with tool supply independent of abrasion rate.